Thermal Transport in Nanofluids: Boiling heat transfer

Sanjeeva Witharana

Submitted in accordance with the requirements for the degree of

Doctor of Philosophy

The University of Leeds

School of Process, Environmental and Materials Engineering

January, 2011

Abstract

This thesis is constructed around the topic of thermal transport in nanofluids, with special emphasis of boiling heat transfer. Nanofluids boiling, as it is popularly known, have been researched nearly for two decades. While some controversies surrounding the boiling mechanisms had been sorted out, others still remained. The aim of this thesis is to address the remaining concerns. For the best treatment of the research problem, the experimental work was divided into three segments.

Time-resolved **small angle x-ray scattering studies** of nanofluids were focused to examine the nanoparticle aggregation in liquid media. These were conducted at two national synchrotron facilities located at Daresbury Laboratory and Diamond Light source in Oxford, UK. In-situ experiments were conducted with static and convective nanofluidic samples. Types of nanofluids and the experimental conditions were chosen to cover a broad range of practical applications. Water based nanofluids of spherical particles of aluminium oxide (Al_2O_3) and titanium dioxide (TiO_2) and acicular particles of aluminium oxide (Al_2O_3) were exposed to 1Ă wavelength x-ray beam for varying duration of times at a frame rate of 10miliseconds. Data analysis was conducted using the Dream and SAXS Utilities software. Signs of change in particle size were discovered with the near-IEP nanofluids. For further clarification of these SAXS observations, microscopic and photography studies were conducted in the laboratory. SEM studies were supported by optical microscopy. It helped to estimate the aggregate sizes and porosity within aggregates. The settling rates were determined by still photography, which were subsequently compared with the prediction of Stoke's settling theory. At the end of data and image analysis, it was discovered that the x-ray beam had successfully predicted the settling rates of nanoparticle aggregates. Although SAXS has long been used to analyse particulate systems, for the best of the knowledge of this author, this is the first time its capability as a tool to estimate particle settling rates in nanofluids has been showcased. Furthermore, by fine tuning the present methodology, it seems possible to determine the nanoparticle aggregation rates in a nanofluid.

Saturated **pool boiling of nanofluids** was experimentally investigated under the atmospheric pressure. A boiling test rig was designed and constructed for this purpose in the Leeds University. Water based and water-ethylene glycol (WEG) based nanofluids were examined for boiling heat

transfer on flat copper substrates. The substrates were resistively heated from the bottom, providing surface heat fluxes up to 189kW/m^2. Boiling heat transfer coefficients were calculated using the measured temperature differences between substrate and the boiling liquid at each surface heat flux. All nanofluids in general displayed deterioration in boiling heat transfer. Moreover all substrates were found fouled with nanoparticles after boiling. SEM observation on fouled substrates revealed the presence of structures consisting of sub-micron size cavities and pores, which are possibly interconnected by sub-surface network of channels. By measuring their surface roughness, it was further understood that the degree of change of roughness due to boiling depended upon its initial roughness, the particle concentration in the nanofluid, as well as the shape of nanoparticles. This study also points to an interval of roughnesses that gives optimum boiling heat transfer performance. Further experiments are recommended to focus on this aspect. Also to avoid in future is the bubble nucleation in the periphery of the copper substrates that became a major obstacle to visualise bubbles in the middle.

The need to explore the **bubble nucleation phenomena on at sub-micron size cavities** was inspired by the presence of such cavities on nanofouled substrates. Moreover in literature sometimes the inconsistencies on the degree of enhancement or deterioration were attributed to hitherto-unknown boiling phenomena at these length scales. Two key challenges were to create very small cavities on a smooth substrate and to conduct phenomenally clean boiling experiments on them. In principle there should not be a foreign particle inside the boiler which is larger than the cavity mouth. The biggest challenge however was to find a technique to measure the temperature of the liquid layer on top of the cavities. The infrared thermometry facility at the Nuclear Science and Engineering Department of the Massachusetts Institute of Technology (MIT) was used as a part of research collaboration. Tiny cavities were machined on ultra smooth silicon substrate using the focus ion beam (FIB) technology at the University of Leeds and at Harvard Centre for Nanoscale Systems. The mouth diameters of conical cavities were ranging from 0.6µm to 4.5µm. A boiling test rig was simultaneously developed at MIT. Heating to the liquid was provided by a halogen spot heater. The cleanliness of the test rig was successfully proved by reaching the heterogeneous nucleation superheat of liquid methanol on a silicon wafer. Water and a water based dilute SiO_2 nanofluid were boiled in this novel test rig. Temperature profiles of bubble evolution were captured using the IR thermometry. Also the superheated liquid layer temperatures were measured. It was found that the measured values were in good agreement

with Young-Laplace theory. Moreover the SiO_2 0.01wt%-water nanofluid in most cases demonstrated boiling heat transfer enhancement up to 40% above water. With this work, for the first time the classical Young-Laplace theory was proved for sub-micron cavities. It further removed the suspicion that there might be a different phenomenon governing the bubble nucleation on nanofouled substrates.

Contents

List of Figures

List of Tables

List of Abbreviations

ASTM	American Society for Testing and Materials
CNT	Carbon nanotubes
CHF	Critical Heat Flux
DLS	Dynamic Light Scattering
EG	Ethylene Glycol
EMT	Effective Medium Theories
FIB	Focus Ion Beam
G-W	Griffith-Wallis
H-C	Hamilton-Crosser
IEP	Iso-Electric Point
IR	Infrared
LOM	Light Optical Microscope
NF	Nanofluid
PC	Personal Computer
SAXS	Small-Angle X-ray Scattering
SEM	Scanning Electron Microscope
TEM	Transmission Electron Microscope
THW	Transient Hot Wire
VDU	Visual Display Unit
WEG10	Water 90wt%+EG 10wt%
WEG25	Water 75wt%+EG 25wt%
Y-L	Young-Laplace

Nomenclature

h	Heat transfer coefficient	W/m^2K	***Subscripts***	
I	Intensity		b	Bubble
k	Thermal conductivity	W/mK	eff	Effective
Nu	Nusselt number		L, l	Liquid
Pe	Peclet number		NF, nf	Nanofluid
Pr	Prandtl number		S, s	Solid
Q	Heat rate	W	Sat	Saturation
q	Scattering vector		W	Water
q''	Heat flux	kW/m^2		
Ra	Rayleigh number			
Re	Reynolds number			
T	Temperature	K or °C		
U_t	Settling velocity	m/s		
vol%	volume percentage			
wt%	mass percentage			
Δ	Difference			
κ	Boltzmann constant			
μ	Dynamic viscosity	Pas		
ν	Kinematic viscosity	mm^2/s		
ρ	Density	kg/m^3		
σ	Surface tension	N/m		
ϕ	Volume fraction			

CHAPTER 1

Introduction

This Doctoral Thesis addresses the research question of thermal transport in nanofluids with emphasis on boiling heat transfer. Being a topic vigorously examined during the past decade, the thermal characteristics of nanofluids have been reasonably well documented. Experimentally obtained data under given test conditions have been published along with justifications. Thermal conductivity was leading the nanofluids research for it standing on its own as a heat transport mechanism and also for its strong influence on convective and boiling heat transfer. Today it has come to a point where the research community is convinced that the effective medium theories sufficiently accurately predict the experimental data for dilute suspensions. Therefore controversies on thermal conduction behaviour of nanofluids are coming to a closure. However questions on convective and boiling heat transfer are still at large.

A nanoparticle is distinct from a large particle in its surface area to volume ratio. In a nanoparticle, this ratio is far larger. As a consequence, the number of atoms or molecules on the nanoparticle surface is larger too. Consider the graphical illustration given in figure 1.1 for two molecular sizes; $0.05nm^3$ and $0.1nm^3$. It turns out that below 100nm, the number of molecules on the surface becomes significant.

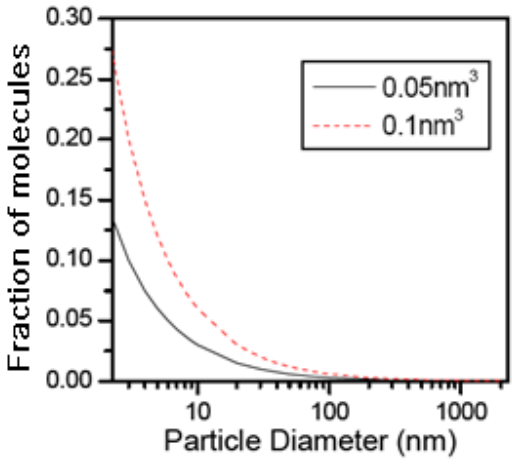

Figure 1.1: Fraction of molecules on particle surface for two molecular sizes

In chemical reactions involving solid materials, the surface area to volume ratio is an important factor for reactivity. Materials with large *s* to *v* ratios react much faster because more surface molecules are available for reaction. This makes nanoparticles highly reactive with surroundings and to exhibit different properties from its bulk material.

Boiling heat transfer is a two-phase phenomenon that has inherent capability to move large quantities of heat across small temperature differences. Consider figure 1.2 that illustrates a thermodynamic cycle on a temperature-entropy diagram. Boiling occurs at the bottom half of the cycle, where a liquid is being held at its boiling temperatureT_2 by transferring heat from a source at T_{source}.

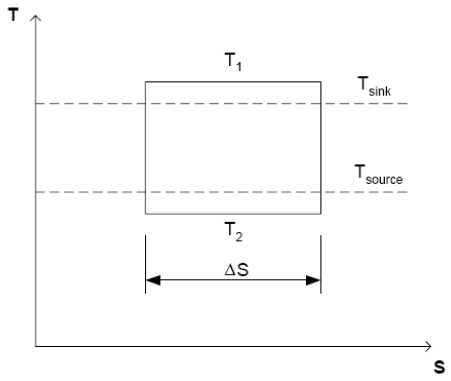

Figure 1.2: Phase change heat transfer

Hallmark of boiling heat transfer is the occurrence of vapour bubbles on heater surface. The larger the number of bubbles, the higher the amount of heat transferred. Efficient heaters are therefore expected to consist of a large number of sites which facilitates bubble formation. The classical boiling theory pioneered by W.M. Rohsenow and subsequently modified by others correlates the transferred heat quantity to the temperature difference, number of active bubble sites, and physical properties of the boiling liquid and surface-liquid interactions. Six decades on, manufacturing of the optimized boiling surface remains a mission to accomplish.

The scenario of boiling of a nanofluid involves a third phase in addition to the liquid and vapour. That is the solid nanoparticles. Modeling of such systems is a great challenge as reflected by the fact that almost all of published work in boiling of nanofluids is experimental. Also there is significant scatter in experimental data and so is the opinion on the underlying mechanism. The common consensus is that the nanoparticle deposition on heater plays a major role in controlling the boiling performance.

Thermal transport in nanofluids should therefore be ideally addressed along three distinct lines. Broadening the knowledge on the particle structuring and agglomeration should be one part of the study. This will help to bridge the knowledge gap in the aggregation kinetics of nanoparticles

in boiling conditions, a crucial element missing in literature. One part of the study should address the nanoscale boiling phenomena to help understand the activities occurring on a nanofouled heater. Nanofluids boiling experiments itself are suggested as the third part of study. Rationale behind is to acquire a broader view of various interacting parameters.

This thesis opens with a literature review in ***Chapter 2***. Starting with a general introduction to nanofluids, the chapter evolves through the synthesis, characterization and thermo-physical properties of nanofluids. It is followed by the thermal conductivity, convective heat transfer and boiling characteristics. The review of nanofluids literature identifies two directions for further research; firstly the gap of knowledge in nanoscale boiling, secondly, the importance of disclosing the nanoparticle aggregation kinetics in liquids. In order to set the stage for further research, the chapter moves on to review the work on small angle x-ray scattering and boiling of liquids on artificial cavities. It is demonstrated that novel approaches are needed to apply these techniques in order to resolve boiling heat transfer of nanofluids.

Chapters 3 through 6 are respectively titled as the Results and Discussion I-IV. ***Chapter 3*** is on Materials and Methods that sets preamble to the experimental chapters. Various types of nanofluids formulated in our laboratories are introduced and the formulation and stabilization techniques are discussed in detail. Instrumentation and methods for characterization of nanofluids on particle size (Zetasizer), shape (Electron microscopy), thermal conductivity (KD-2 probe, 3-Ω device and λ-meter), viscosity and rheology (u-tube viscometer and rotational rheometer), and wetting and spreading (geniometer) are presented. Recent experimental data are elaborated. Latter parts of the chapter are dedicated to the introduction of experimental facilities for SAXS synchrotron radiation, pool boiling, and the boiling on artificial cavity. In the closure of ***Chapter 3*** it is pronounced the criticality of aggregation kinetics which opens the avenue for the following chapter.

Chapter 4 is on small angle x-ray scattering experiments. Three rounds of SAXS investigations were conducted at two UK national facilities viz. Daresbury Laboratory and Diamond Light Source in Oxford. The objectives of the experiments were to examine the aggregation kinetics of nanoparticles in suspension. Water-based and water-ethylene glycol-based nanofluids of spherical particles of titanium dioxide, and spherical and acicular particles of aluminum oxide of varying mass concentrations were studied at 20°C and 60°C temperatures. Nanofluid samples

were prepared in a range of pH values some of which were near the iso-electric point (IEP). The X-ray scattering patterns are featured and the data are analyzed in detail. In order to further interpret the SAXS data and to elaborate the observed trends, several supplementary experiments were conducted in our Leeds university laboratories with samples similar to SAXS nanofluids. Settling and light scattering experiments, SEM and optical microscopy imaging and Brownian diffusion calculations were performed. Finally it was found that SAXS experiments had successfully captured the settling dynamics of nanoparticle aggregates. Despite the fact that settling experiments have been known for decades of years, to the best knowledge of this author this is the first time the small angle x-ray scattering has been reported as a tool to measure nanoparticle settling. This pioneering work is expected to open up new directions for future research on nanofluids with the help of synchrotron radiation.

Having examined the kinetics of nanoparticles in foregoing chapter, the ***Chapter 5*** is written on pool boiling of nanofluids. These nanofluids comprised water based and water-ethylene glycol based Al_2O_3, TiO_2, CNT nanoparticles. This is the first time the boiling of water-ethylene glycol based nanofluids is documented. All experiments were conducted on flat heaters mounted on a custom-built test rig under atmospheric pressure and with heat fluxes up to 189kW/m^2. The heaters were made of copper and stainless steel. Desired heater roughnesses were obtained by mechanical grinding and a systematic polishing procedure. It was found that the nanofluids deteriorated the boiling heat transfer under the conditions of experiments. The degree of deterioration depends on the type and shape of nanoparticles and the base liquid. Also found from the experiments was the deposition of nanoparticles on heater surfaces. These deposits were of different porosities and altered the surface roughness of heaters. The data suggest that there is an interval of roughnesses that may yield optimum boiling heat transfer. Two extremes of this interval to be approximately R_a=50 and R_a=1000nm. In the backdrop of present findings and the revelation of tiny cavities on nanofouled surfaces, it is suggested at the end of the chapter to examine the Young-Laplace bubble nucleation theory for sub-micron length scales.

Chapter 6 of this thesis discusses the experiments on boiling on small artificial cavities. Focused Ion Beam (FIB) device was used to create artificial cavities of sub-micron sizes on smooth silicon wafers. The mouth diameters of conical cavities were ranging from approximately 0.5µm to 4.5µm. The aim of this work was to validate the Young-Laplace theory for nanoscale bubble nucleation. Experiments were conducted at the Massachusetts Institute of Technology. A

contaminant-free ultraclean test rig and procedure was developed. Its cleanliness was later proved by attaining the homogeneous nucleation temperature for methanol. Bubble visualization and temperature measurements were conducted using the Infra Red thermometry assisted by image analysis software. Due to the accurate use of IR filters, the temperature of a 3µm thin superheated liquid layer was successfully captured. Bubble cycles on artificial cavities were recorded by IR videos of frequency up to 1000Hz. By subsequent image analysis, the time-resolved temperature distribution on cavities was reproduced. Experimentally obtained temperature data for water were plotted with Young-Laplace predictions. It is shown that the two sets are in excellent agreement thereby proving for the first time that the two-century old classical theory stands for nanoscale boiling. As second part of these experiments water based dilute silica nanofluids were boiled on artificial cavities. In all but one experiment, the boiling heat transfer was found to be far superior to water.

The thesis is summed up in ***Chapter 7*** under Conclusions and Recommendations. In here the important findings and the original contributions are revisited. Valuable experiences gained as a result of the work done for this thesis are discussed. From the lessons learnt, recommendations are made for the follow on work in view of carrying forward the presented work in a more efficient and systematic way.

CHAPTER 2

Literature Review

Nanofluids, also referred to as nanoparticle suspensions or nanocolloidal suspensions, have been at the centre point of heat transfer applications in recent times. It was nearly fifteen years ago when the first technical publication on nanofluids was released from Argonne National Laboratory , USA [3]. It was claimed that stably suspended aluminum oxide nanoparticles in water exhibited anomalous enhancement in thermal conductivity in comparison to water. Incidentally this became the first publication to have used the term 'nanofluids. Despite the claim of anomalous enhancement being fiercely debated in subsequently years, the concept of nanofluids did achieve overwhelming popularity due to their display of superior thermal properties. The outcome of this is reflected by the exponential growth in related publications. For instance, figure 2.1 illustrates the number of journal articles and patents containing the term "nanofluid" according to SciFinder Scholar database.

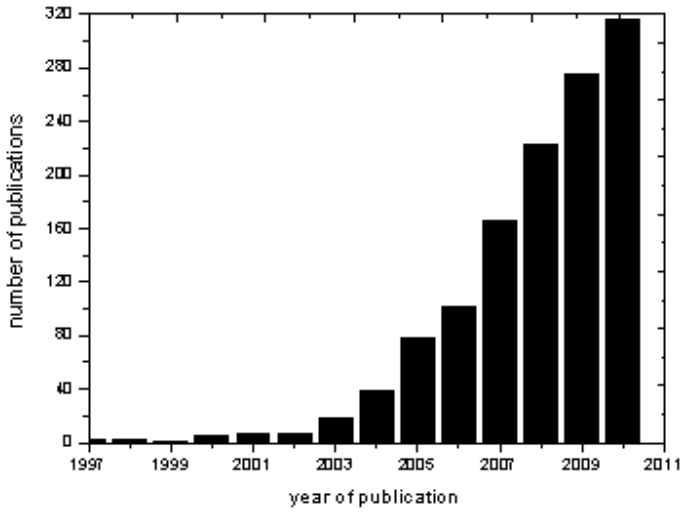

Figure 2.1: Number of publications containing the term 'nanofluid' [4]

A nanofluid is often defined as a stable suspension of nanometer-size particles in conventional heat transfer liquids such as water, ethylene glycol, engine oil etc., where at least one dimension of particles is less than 100nm. For example, the length of carbon nanotubes is usually in the order of one micrometer. It is their tubular cross section which is few nanometers in diameter qualifies them to be called nanoparticles. Naturally nanoparticles prefer to form particle clusters rather than stand as individuals. The smallest dimension of a cluster may easily surpass 100nm lengthscale. Sometimes these clusters are called aggregates or agglomerates. However there are instances they are referred to as nanoparticles, which might confuse the reader. In this report

therefore, whenever a contrast has to be made between individual nanoparticles and nanoparticle clusters, the former will be called ‘primary particles’.

Forthcoming discussion is primarily a review of literature on thermal transport in nanofluids, with high emphasis on thermal conductivity and boiling heat transfer. It further addresses a range of related topics from formulation and characterization to measurement. There are brief reviews on classical bubble nucleation and x-ray scattering. In fact being existent for many decades and extensively researched, the number of technical papers, books, and reviews on classical bubble nucleation and x-ray scattering are astronomical. The overall discussion in this chapter is tailored to highlight the need to conduct further research to resolve controversies in thermal transport in nanofluids.

2.1 Synthesis of nanoparticles and nanofluids

Principal features expected from a successful nanoparticle synthesis technique are its ability to produce clean nanoparticles of well-defined size and shape. Commercially available nanoparticles however exhibit a wide spread of sizes. Figure 2.2 shows scanning electron microscopy (SEM) images of commercial aluminum oxide powder supplied by Nanophase Technologies and silicon dioxide suspension supplied by W.R. Grace & Co. Primary particle sizes were claimed as 46nm and 22nm respectively by the suppliers.

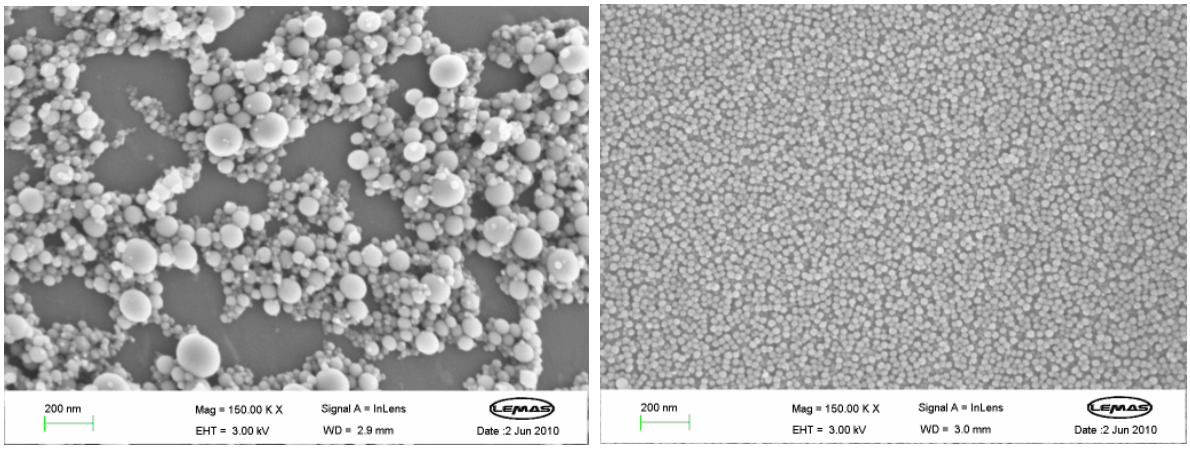

Figure 2.2: Left-NanoTek Alumina, Right-Ludox TM-50 Silica dispersed in distilled water

NanoTek alumina is produced by NanoArc synthesis method, which is understandably based on electric arc vaporization-condensation technique. Ludox TM-50 Silica which is nearly monodisperse in figure 2.2, is claimed to be synthesized by ion exchange of sodium silicate solution. Details of commercial nanoparticle synthesizing processes are however often not disclosed but are declared as proprietary by manufacturers. A brief outline of nanoparticle synthesis methods follows.

In general, nanoparticle synthesis techniques can be classified as physical and chemical methods. The chemical methods of producing nanoparticles are inclusive of chemical vapour deposition (CVD), chemical vapour condensation [5-6], chemical precipitation (sol-gel processing), thermal spraying & spray pyrolysis [7]. Meanwhile, the most popular physical methods are the grinding with high energy ball milling and inert gas condensation which is also known as IGC [8-10]. IGC happens to be the most common nanoparticle production method.

Nanoparticles synthesized as such can then be suspended in a liquid, popularly known as host liquid, in order to obtain a nanofluid; first produce the nanoparticles, then suspend them in a host liquid. Suspension of dry particles in a host liquid in this way is called the two-step method. Major advantage associated with two-step method is that nanoparticle synthesis facility does not need to be a part of the nanofluid formulation process. Two steps can be conducted at two locations, under two conditions. Over the time, two-step method has become the preferred sequence to obtain nanofluids.

There is a one-step formulation process for nanofluids, where the nanoparticle synthesis and nanofluid formulation are achieved simultaneously. One-step method is preferred for production of moderate quantities of nanofluids of highly oxidizing particles. The bulk material is first vaporized and then condensed into a low vapour pressure liquid, in a process known as the direct evaporation technique. Two factors that impose technical limitations are identified; the thermo-physical properties of the material heavily influence the vaporization process. Moreover, the host liquid needs to have a low vapour pressure. It is nonetheless reported that the particle size variation was narrow and the stability of nanofluids was superior when the one-step method was followed [3, 11].

Among those who employed chemical vapour condensation method to synthesize nanoparticles were Hong et al.. [6]. They produced nanocrystalline Fe powder of spherical shape by using iron carbonyl as a precursor under flowing helium atmosphere, a process previously reported by Dong et al. [12]. Subsequent TEM images had confirmed uniformly distributed particle clusters, each of approximately 10nm diameter.

Brust et al. [13], Patel et al. [14] and Zhu et al. [15] provide further examples of applying chemical methods to synthesize nanoparticles. Brust et al. [13] produced metal nanoparticles with a monolayer of octadecanethiol in the form of a powder. The monolayer acted as a coating that improved the stability of particles in the suspended form. Patel et al. [14] reported that silver and gold nanoparticles were produced by reduction of chloroauric acid and silver nitrate respectively in a sodium citrate environment. Meanwhile copper nanoparticles were synthesized by Zhu et al. [15] by reducing copper sulphate pentahydrate in sodium hypoposphite environment. TEM images given in figure 2.3 illustrate the capability of these methods to successfully produce nanoparticles of good monodispersity.

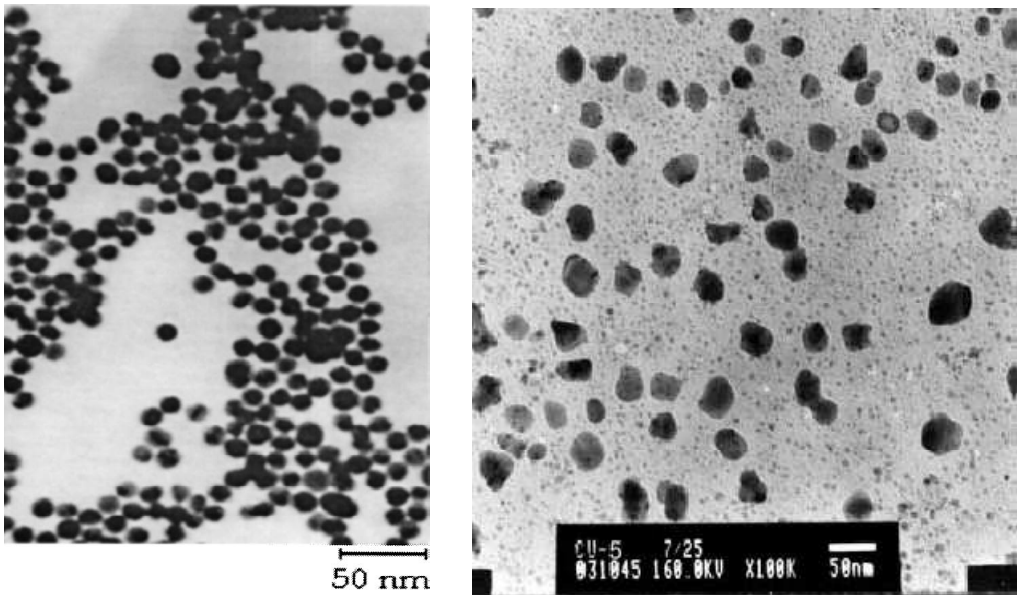

Figure 2.3: Left-Ag nanoparticles produced by citrate method [14], Right-Cu nanoparticles produced by reduction method [15]

Submerged arc nanoparticle synthesis under vacuum conditions is a technique successfully applied to produce nanofluids with different morphologies. Lo et al. [16] followed this route to synthesize ethylene glycol based copper and copper oxide nanofluids. They depicted TEM images

given in figure 2.4 to demonstrate the uniform distribution of particles and a low degree of aggregation. In the above work, Lo et al. [16] also synthesized needle-like and polygon shapes, which were later repeated by Jwo et al. [17] and Chein and Chuang [18] for acicular CuO nanoparticles.

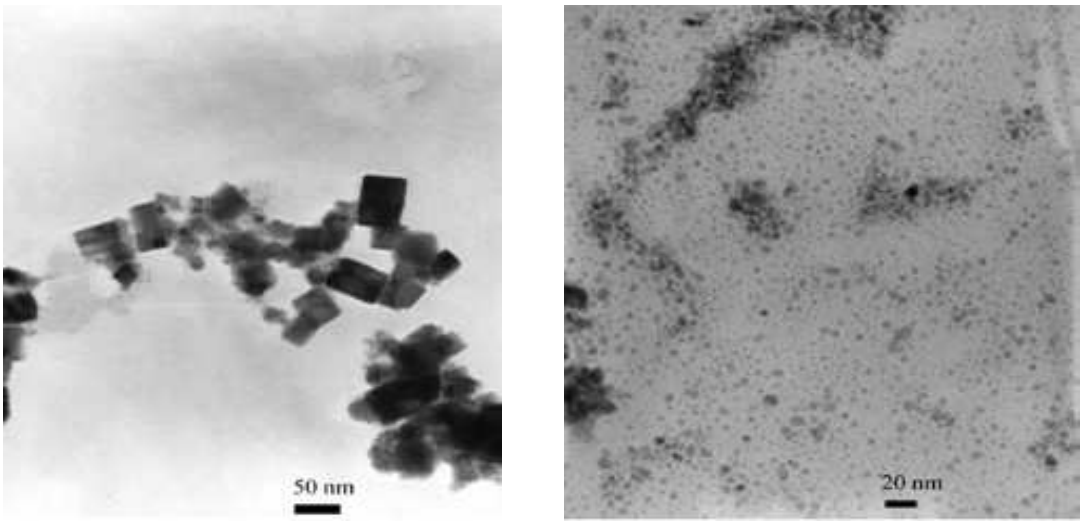

Figure 2.4: Left-Cu_2O nanoparticles produced in 70% Ethylene glycol, Right-Cu nanoparticles in pure ethylene glycol [16]

A co-precipitation method was followed by Zhu and co-workers [19] to prepare aqueous Fe_3O_4 nanofluids. They blended aqueous solutions of ferric chloride and iron chloride tetrahydrate in a flask and subjected the mixture to a sequence of chemical and mechanical means to obtain a precipitate. Later they dispersed this precipitate in distilled water to obtain nanofluids of desired particle concentration. Electron microscopy and x-ray diffraction examinations confirmed the Fe_3O_4 particles were spherical in shape with an average size of approximately 10nm. The drawback with the co-precipitation method was its inability to control the degree of particle aggregation.

2.2 Achieving the stability of nanofluids

Consider nanofluid samples given in figure 2.5. One is visually “stable”, while the particles have visibly separated from the liquid in the other. There is no clear definition for a stable nanofluid. Nevertheless there is a wide agreement that a nanofluid is “stable” if it stays as one entity for a considerable period of time, usually in the order of three months or more from the date of preparation.

Figure 2.5: Stable and unstable nanofluids

The reason for the particles to separate from liquid and settle on the bottom is the gravitational force. Stoke's settling theory in eq 2.1 explains the physical background of particle settling when gravitational acceleration and viscous force are the only forces acting on particles. For heat transfer applications the nanoparticles are denser than host liquid $(\rho_s > \rho)$, hence they may settle with time. However, this effect is counterbalanced by their tiny sizes (x), making the settling velocities (U_t) very small and hence the time scales are very large. A problem arises when nanoparticles flock together and make aggregates which are heavy enough to settle faster.

$$U_t = \frac{x^2(\rho_s - \rho)g}{18 * \mu} \qquad \textbf{Eq 2.1}$$

Settling is desired in a variety of industrial sectors such as petroleum, mining and mineral. In nanofluids however, this is the most undesirable. In heat transfer equipment, the fluids are either stationary or moving. In a circulating nanofluid, such as forced convection in tubes, the probability of particles settling on the tube is low due to mixing. In natural convection and pool boiling environments however, the probability is high due to the stationary nature of the bulk fluid. Particles thus settled may clog fluid channels as well as adding extra thermal resistance on to the wall in cases of wall materials are highly thermal conductive. Ultimately the nanofluid may end up introducing a burden to the system instead of bringing enhancement. Having said so, it is noteworthy a positive side of this; the increase in critical heat flux is proved to be due to systematic deposition of nanoparticles on heater surface [18, 19]. This will be discussed later in this chapter.

The question is how to stabilize nanofluids for heat transfer applications? A nanofluid collapses as a result of particle settling, which in turn could be a consequence of undesired aggregation. To explore this further, the interaction between suspended particles need to be examined.

2.2.1 Interparticle interactions

Interacting forces between suspended particles have been identified to include London-van der Waals forces, electrostatic forces, hydrophilic interactions, depletion interaction and polymer-polymer interactions. In a dilute suspension of nanoparticles which a nanofluid often belongs to, the dominant types of interparticle interactions are the London-van der Waals attraction and the electrostatic repulsion. These forces are respectively represented by the Hamaker constant and the Debye length. The classical DLVO theory suggests that the stability of a colloidal suspension is governed by the net effect of these two forces [20].

The key to obtain a stable nanofluid is to make the magnitude of repulsive forces larger than the attractive forces. This can further be explained using figure 2.6; the distance between colloids should be made larger than the 'energy trap' zone. For an aqueous solution, one way to do this is to change the pH of the suspension and the ionic strength. This technique is known as electrostatic stabilization. Another way is to modify the particle surface properties by adding a surfactant or by adsorption of polymers. This is known as steric stabilization. A third technique, depletion stabilization, is to introduce free polymer into the dispersion medium. The second and third methods together are also called polymeric stabilization.

However the most preferred method is the adjusting of solution pH. As it does not introduce foreign materials, the system is clean and the interpretation of its response is less complicated [21]. In doing so, the pH is brought to a value far away from the iso-electric point (IEP). The iso-electric point is the value of solution pH where the zeta potential is zero. Closer to the IEP, lower is the zeta potential and larger is the interparticle attraction. Therefore near-IEP nanofluids collapse very soon. Figure 2.7 illustrates the shape of a typical titration curve for a nanoparticle suspension.

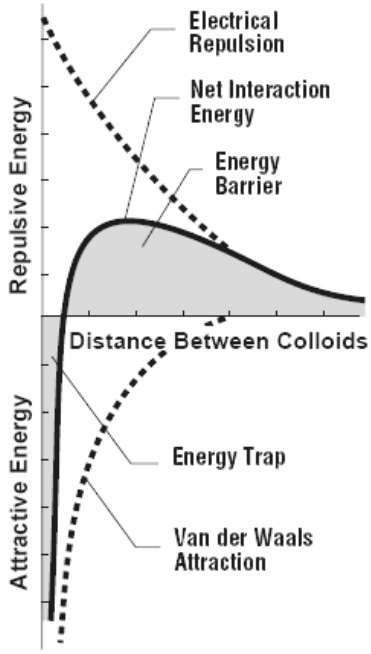

Figure 2.6: Interparticle interaction in a suspension

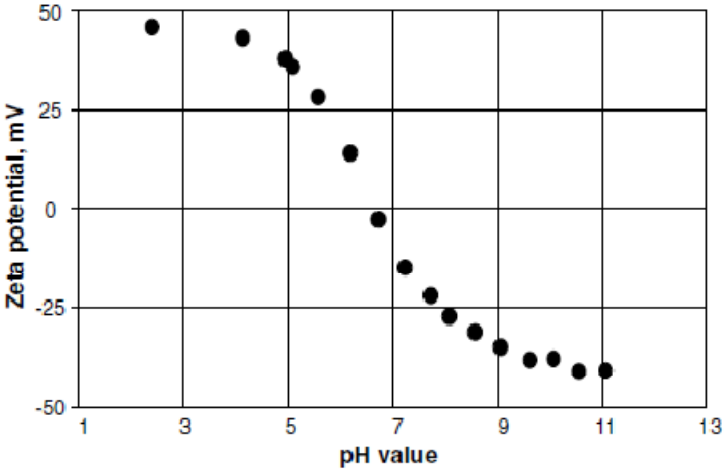

Figure 2.7: Zeta potential of TiO_2-Water nanofluid [22]

It is known that the IEP of solids depends on a variety of factors including the synthesis process, stoichiometry, crystal structure, degree of surface hydration and the presence of impurities. Moreover, a recent study conducted by Gulicovski et al. [23] highlighted the influence of experimental protocol on IEP. Initially they prepared two samples of 99.99% pure α-alumina

particles in KNO_3. One sample was equilibrated at pH3.5 for 24hrs, while the other was at pH9.1 for a similar duration. Then these samples were titrated with 0.1M KOH and 0.1M HNO_3 respectively. As shown in figure 2.8, there were two titration curves with two IEPs. In the base titration, the obtained value of 8.6 was close to the IEP of $Al(OH)_3$. This suggests that the starting pH of solution is a major deciding factor of IEP of certain materials.

Due to the dependence of IEP on several factors as such, it is customary to give a narrow band of values for IEP, instead of a single value [24].

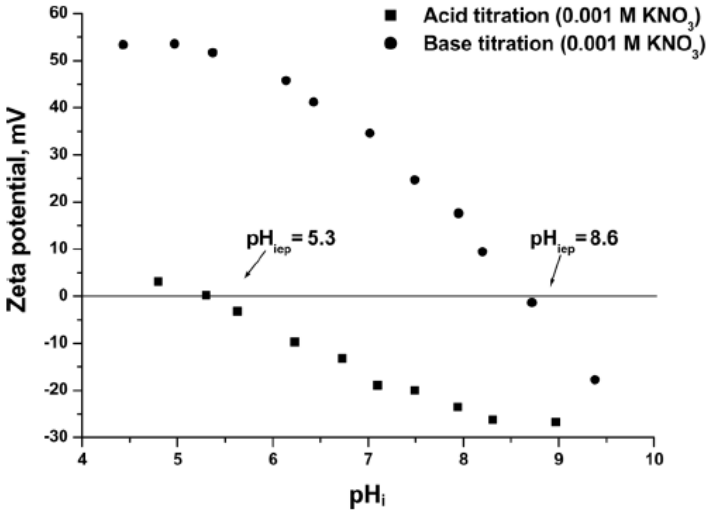

Figure 2.8: α-Al_2O_3 in KNO_3 at different pH [23]

Having said so much on electrostatic stabilization, it should also be noted that this is not a universally applicable technique. For example, some nanofluid applications demand a particular pH which may be close to IEP. In some cases, solution pH changes with time due to reactions between constituents. Consider two nanofluids for instance; titania-water and CNT-water. The aqueous titania nanofluid can be brought to stability by adjusting the pH [25]. However aqueous CNT nanofluid needs pH adjustment and a surfactant [26].

Two particles in a suspension attached with polymers or functional groups are represented by figure 2.9. Assume for this particular case the thickness of polymer layers is t and the particle separation is s. When s becomes smaller than 2t, the polymers will touch each other resulting attraction.

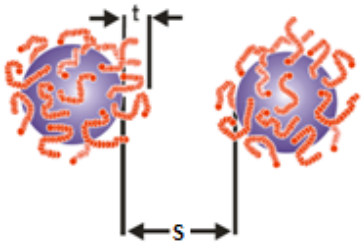

Figure 2.9: Steric stabilization

The Gibbs free energy change ΔG of the overlap interaction of the adsorbed layers can be expressed as $\Delta G = \Delta H - T\Delta S$. For a stable suspension, the value of ΔG should be positive in order to avoid the energy trap shown earlier. ΔH and ΔT are respectively the enthalpy and entropy change.

One theory that explains the steric stabilization mechanism is the entropic stabilization theory. It assumes that a second surface approaching the adsorbed layer is impenetrable. The adsorbed layers will therefore get compressed and the polymer segments present in the interaction region lose configurational entropy. Reduction in entropy will increase ΔG, producing the net effect of repulsion between the particles, thus preventing them from flocculating. The entropic stabilization theory neglects the enthalpic interaction between the adsorbed molecules and the dispersion medium [27].

Steric stabilization has several advantages over electrostatic stabilization. The steric stability is effective in both aqueous as well as nonaqueous media, yet reversible by simple dilution. Moreover sterically stabilized suspensions are relatively insensitive to electrolyte concentration.

Sodium dodecylbenzene sulfonate (SDBS) is a popular surfactant associated with nanofluids. Wen and Ding [28] added a small amount of SDBS to stabilize aqueous γ-alumina nanofluid. Worsely et al. [29] used SDBS to stabilize aqueous suspensions of double-walled carbon nanotubes. However, historically Gum Arabic has been the most popular dispersant with CNT-water nanofluids [26, 30-31].

2.3 Nanoparticle characterization techniques

Knowledge of particle size and shape is an important part in characterization of nanofluids. In ideal conditions nanoparticles are expected to be monodispersed. In practice however polydispersity is widely observed. Forthcoming discussion is about various particle

characterization techniques. Higher attention will be paid to describe characterization techniques used in the present study.

Particles suspended in nanofluids are normally of few tens of nanometers in size. These sizes should hence fit into several techniques outlined in figure 2.10. X-ray and neutron scattering, static and dynamic light scattering, and electron microscopy are covering the range of sizes of interest.

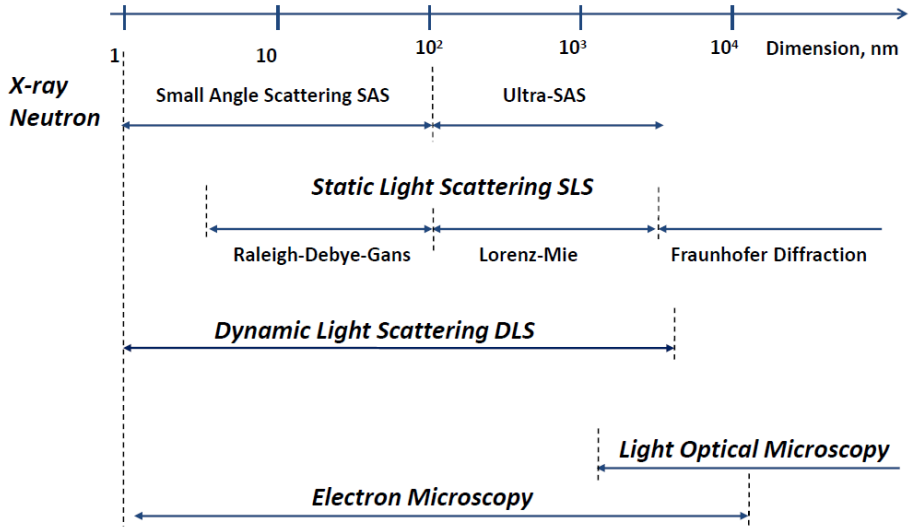

Figure 2.10: Techniques for sizing of colloidal systems. Modified from Glatter [32]

As much as technological capability, a favorable technique should offer ease of operation and cost effectiveness. These are the reasons for SLS and DLS to have become popular. Electron microscopy however offers the unique capability of visualizing particle shapes.

2.3.1 Light scattering techniques

The principle behind light scattering particle size measurement techniques is essentially the capturing and analyzing of the diffraction pattern of a beam of light shone on a particle suspension. An illustration is given in figure 2.11. Static light scattering is when the analysis is based on time-averaged intensity whereas dynamic light scattering is based on the intensity fluctuations with time at a given detector angle (θ), for series of angles. These techniques are ideally recommended for dilute suspensions in order to avoid the risk of multiple scattering.

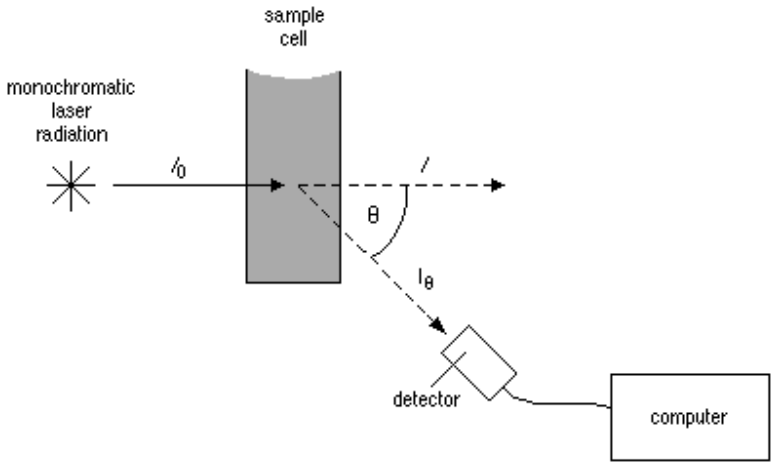

Figure 2.11: Light scattering on a suspension [33]

Instrument manufacturers often refer to ISO 13320:2009 [34] for it provides guidelines on instrument qualification and size distribution measurement of particles in many two-phase systems, e.g. powders, suspensions and emulsions, through the analysis of their light-scattering properties. ISO 13320:2009 is primarily applicable to particle sizes ranging from approximately 0.1µm to 3mm. However with special instrumentation and conditions, ISO recommends the applicable size range to be extended above 3mm and below 0.1µm.

2.3.1.1 Dynamic Light scattering

This technique uses the Stokes-Einstein equation for diffusion of spherical particles through liquid with a low Reynolds number.

$$D = \frac{\kappa T}{6\pi\mu R} \qquad \textit{Eq 2.2}$$

where *D* is diffusivity, *κ* is Boltzmann's constant, *T* is the absolute temperature, *μ* is dynamic viscosity of liquid, and *R* is the radius of spherical particle.

The particle diameter obtained from this technique is the diameter of a sphere that has the same diffusion coefficient as the particle. The diffusion coefficient *(D)* depends on the size of particle core as well as its surface structure and ionic strength of medium. Therefore the DLS size of a particle of the shape shown on figure 2.12 will be bigger than the size of particle core.

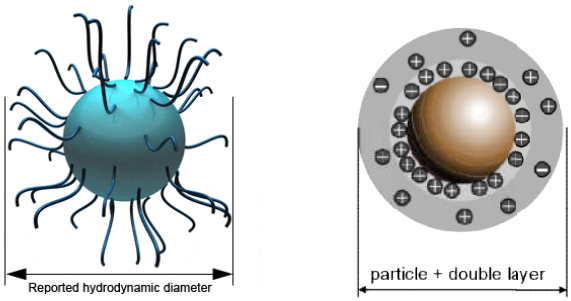

Figure 2.12: Actual size and DLS size of particles

A similar explanation goes for the ionic strength. The ions in the medium and the total ionic concentration can affect the particle diffusion speed by changing the thickness of the electric double layer. The thickness increases in lower conductivity media reducing the diffusion speed and resulting in a larger apparent hydrodynamic diameter. The opposite will happen with higher conductivity media.

2.3.1.2 Static light scattering

In SLS the intensity of the scattered light is measured, averaged over time as a function of the scattering angle. The intensity data is then fitted into a suitable model such as Guinier [35], Debye [36] or Zimm [37], and the information such as the size and the molar mass of a sample is extracted. Glatter et al. [32] provide useful guidance for mathematical treatment and interpretation of SLS data.

2.3.1.3 Small angle x-ray scattering

The principle of operation of SAXS is fairly similar to other light scattering techniques. The main difference is, in SAXS the incident beam of x-rays is very powerful that the wavelength can be as small as 1Ă. Small wavelength light offers the unique capability to see through tiny objects of the same order-of-magnitude lengthscales. In addition to this, the scanning speed is very rapid in a SAXS machine. Small angle x-ray scattering is therefore a very useful tool to obtain information on the particle size, shape, and interparticle distances in millisecond intervals. Upon collection of realtime scattering data, various software are available to analyze it and extract finer details.

2.3.2 Microscopy

Microscopy and image analysis are valuable tools for particle size characterization. There is a range of options from optical microscopy to electron microscopy classified upon the degree of resolution. Although labour-intensive unlike light scattering techniques, microscopy images

provide the user the confidence of directly observing the actual particle sizes, shapes and their distribution.

2.3.2.1 Optical microscopy

Optical microscopy has developed for over 400 years in association with great names such as Galileo Galilei, Marcello Malpighi, George Bass, Carl Zeiss and Louis Pasteur. It is by far the most widely used technique today to magnify and observe objects which lie beyond the capacity of the naked eye. The smallest object that can be comfortably seen through a modern optical microscope is in the order of 1 micron. Figure 2.13 depicts popular microscope configurations employed for particle visualization. Shown in the insets are Zeiss Axioskope and Nikon Eclipse TE2000 respectively to represent each configuration.

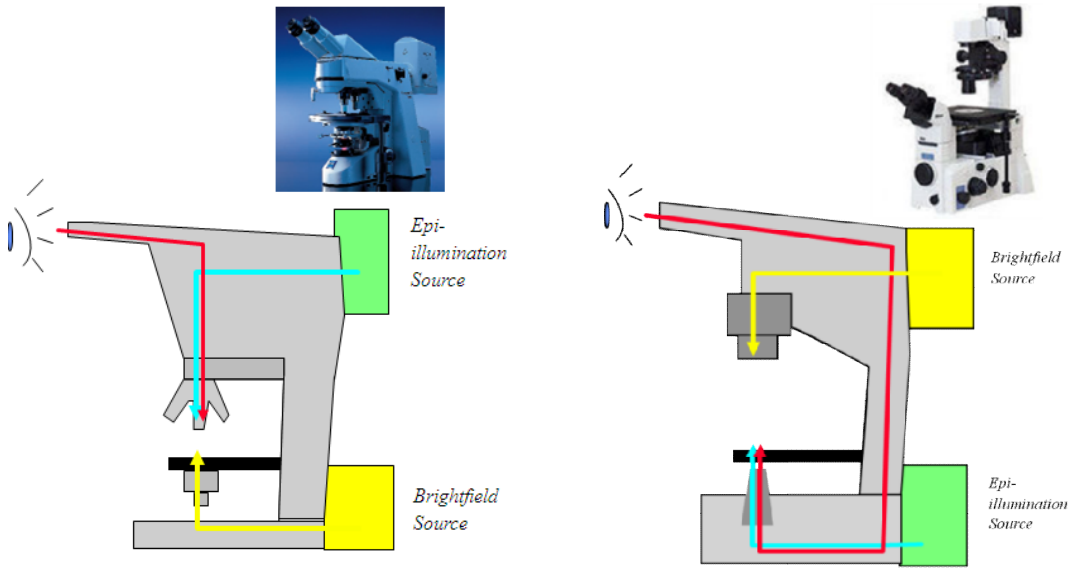

Figure 2.13: Left-upright, Right-inverted microscope configurations. Modified from [38]

The samples to be observed under the inverted microscope should be deposited on optically transparent substrates to make passage for the light to travel through. Advantage with the upright configuration is that it offers the possibility of observing samples deposited on opaque substrates.

2.3.2.2 Electron microscopy

Instruments that use a focused beam of highly energetic electrons to examine very fine objects are called electron microscopes. Further to providing size and shape information of extremely tiny

objects, these instruments are also capable of analyzing the material composition of specimens. They are classified into two groups; scanning electron microscopy (SEM) and transmission electron microscopy (TEM). As the names suggest, the incident electron beam scans the top surface of the sample in SEM whereas it transmits through the sample in TEM. Nevertheless they have several features in common, as seen from figure 2.14.

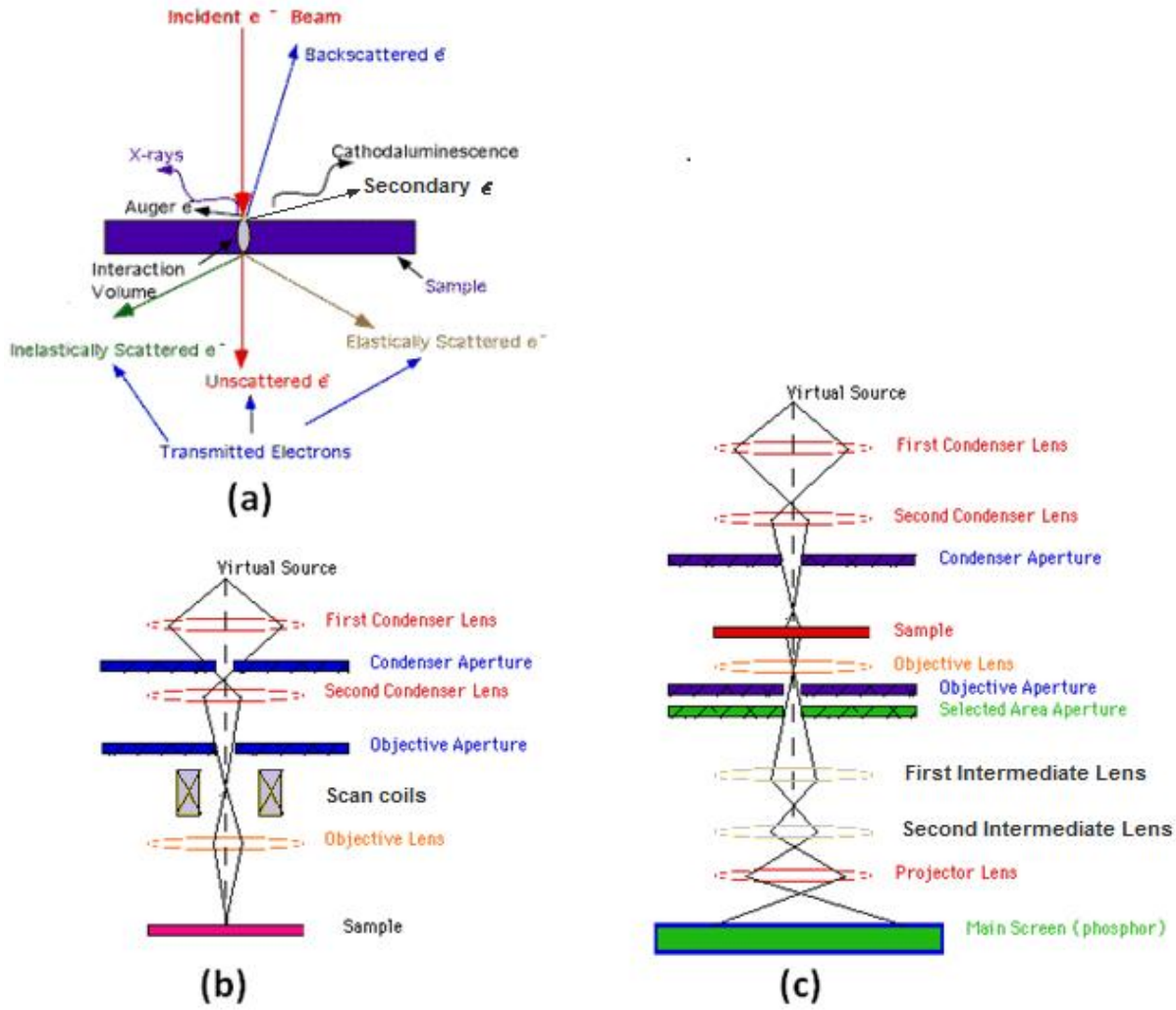

Figure 2.14: (a) striking electron beam, and interior of (b) SEM (c) TEM. Modified from [39]

When a powerful beam of electrons strikes a substrate, various interactions occur. One such reaction is the release of electrons from the substrate. SEM imaging uses the electrons emitted by the top surface of specimen, known as secondary electrons. As the electron beam scans surface of

the sample in a raster pattern, the detectors build up an image by mapping the detected signals with beam position.

If the sample is sufficiently thin, the electron beam partially transmits through the sample carrying the information about the structure of sample. TEM uses this principle to build images. The spatial variation in this information is then magnified by a series of magnetic lenses until it is recorded by hitting the main screen. The image detected by the main screen is displayed in real time on a visual display unit.

A common feature to electron microscopy is the necessity of the sample to be dried before observation. From the point of view of nanofluids, this is unfavourable. Nanoparticles are often in the form of aggregates in a wet state. These aggregates may change their sizes and shapes while drying. The microscopy images therefore may not represent the genuine conditions the observer is interested of.

Consider the example in Figure 2.15. These images are from a sample of alumina-water nanofluid obtained using Malvern Zetasizer (a DLS technique) and a Philips FEGSEM (electron microscopy).

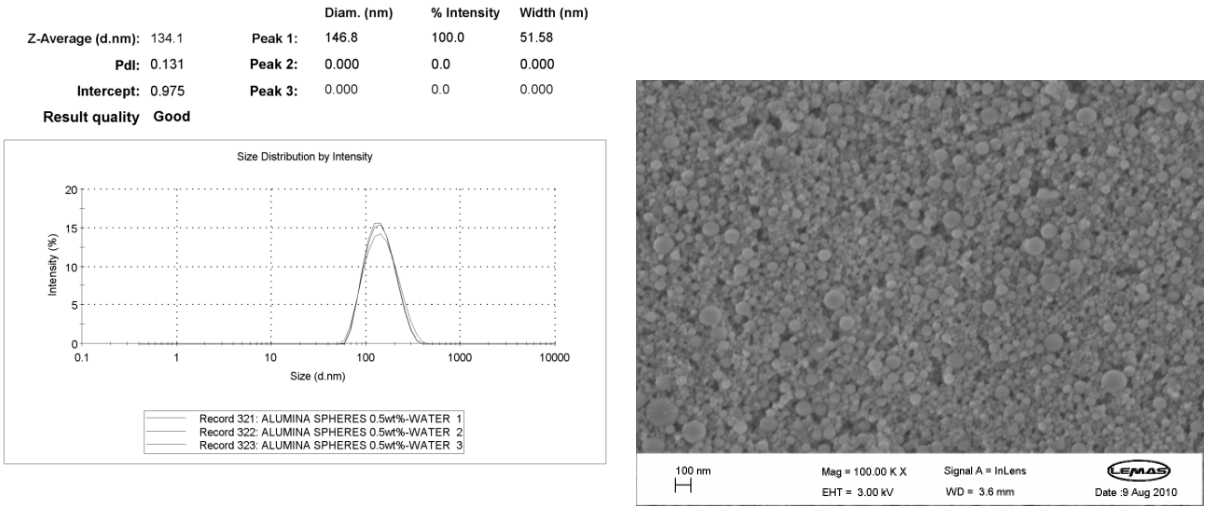

Figure 2.15: A comparison of DLS and EM techniques

The SEM image provides shape and size information at a glance on figure 2.15. The particles are spherical in shape and a vast majority of them are less than 100nm in size. Meanwhile on the DLS graph, the average diameter is stated as 134.1nm, with peaks near 146.8nm. The most likely

reasons for the disparity could be the particles being in the form of aggregates in a wet measuring condition and also the hydrodynamic effect associated with DLS.

2.4 Thermal conduction in nanofluids

The first few publications on nanofluids were successful in giving the impression that these types of heat transfer fluids demonstrate anomalous enhancement in thermal conductivity. The degree of enhancement was defined as the thermal conductivity ratio between the nanofluid and base liquid (k_{nf}/k_L). This value was as large as 140% in some cases, despite the presence of nanoparticles was less than 10% of the total volume of suspension [3, 5, 11, 40] . It was shown that the classical effective medium theories (EMTs) such as written by Maxwell [41] and followers [42-44] were under-predicting the experimental data. During the course of the last fifteen years since the pioneering publications, a controversy was brewing. Investigators on one side were supporting the claim of anomalously, while the investigators on the other side were contradicting it. Keblinski et al. [45] in their article titled 'Thermal conductance of nanofluids: is the controversy over?' convincingly demonstrated that all the published data except a few sets, lie within Hashin-Shtrikman [46] effective medium bounds. They were on the opinion that the disagreement between the data and the theories was an artifact caused by resorting to a particular EMT. Yet the strongest ever evidence emerged through the recently-concluded international nanofluid properties benchmarking exercise (INPBE). Upon the experimental data analysis of thermal conductivity measurement of nanofluids by over 30 organizations worldwide, INPBE ruled out anomalously and concluded that the effective medium theory predicts the experimental data sufficiently accurately. Following is an effort to highlight the important landmarks in the development of the thermal conductivity side of the story of nanofluids.

2.4.1 Classical theories

Effective medium theories (EMT) predict thermal conductivity of composites. A composite consists of a matrix and insertions. First and foremost of EMTs was authored by Maxwell in 1881 [41]. For low volume fractions of well dispersed non-interactive spherical particles, the thermal conductivity of the composite (k_{eff}) is determined by the thermal conductivities of the matrix (k_L), the insertions (k_s) and the volume fraction of insertions (φ_s). Maxwell correlated these parameters in the following manner.

$$k_{eff} = k_L \left[\frac{k_s + 2k_L + 2(k_s - k_L)\phi_s}{k_s + 2k_L - (k_s - k_L)\phi_s} \right] \qquad \textbf{Eq 2.3}$$

Bruggeman in 1935 [42] modified Maxwell's equation to include higher particle concentrations when interparticle interactions cannot be neglected. As φ_s increases, the interparticle interactions become prominent. The new correlation given in eq 2.4, accounted for this aspect. Bruggeman's contribution was therefore significant in the development of EMTs.

$$k_{eff} = k_L \frac{\left[(3\phi_s - 1)k_s/k_L + (2 - 3\phi_s) + \sqrt{\Delta} \right]}{4} \qquad \textbf{Eq 2.4}$$

where $$\Delta = (3\phi_s - 1)^2 \left(k_s/k_L \right)^2 + (2 - 3\phi_s)^2 + 2\left(2 + 9\phi_s - 9\phi_s^2\right)\left(k_s/k_L \right)$$

To generalize Maxwell's correlation furthermore, Hamilton and Crosser [43] studied heterogeneous two-component systems of aluminum and balsa wood particles in rubber. The particle shapes were spherical, cylindrical, disk, cubic and parallelepiped. The particle sizes ranged between millimeters and micrometers. Their experiments led to a modified version of Maxwell's correlation as follows.

$$k_{eff} = k_L \left[\frac{k_s + (n-1)k_L - (n-1)(k_L - k_s)\phi_s}{k_s + (n-1)k_L + (k_L - k_s)\phi_s} \right] \qquad \textbf{Eq 2.5}$$

The term *'n'* is the parameter that accounts for the shape of particle and the ratio k_s/k_L. It had been defined as n=3/ψ, where ψ was called 'sphericity'. The sphericity is the ratio of the surface area of a sphere with a volume equal to that of the particle, to the actual surface area of the particle. For spherical particles therefore ψ =1, that will make n=3, and the eq 2.5 will reduce to eq 2.3. The underlying message of Hamilton and Crosser's work is this; the shape effect plays a role only when $k_s/k_L > 100$. As long as the case is otherwise, the eq 2.3 holds.

Hashin and Shtrikman [46] removed the restriction on particle volume fraction in Maxwell's model. Their correlation, stated as equation 2.6, gained more prominence as a tool for nanofluids analysis when Keblinski et al. [45] demonstrated that most of experimental data fall within the

lower and upper limits predicted by this correlation, popularly known as H-S bounds. The lower H-S bound corresponds to Maxwell's prediction given in equation 2.3.

$$k_L\left(1+\frac{3\phi_s(k_s-k_L)}{3k_L+(1-\phi_s)(k_s-k_L)}\right)\le k_{eff}\le k_s\left(1-\frac{3(1-\phi_s)(k_s-k_L)}{3k_s-\phi_s(k_s-k_L)}\right) \qquad \textbf{Eq 2.6}$$

Yet equations 2.3, 2.4 and 2.5 fail to account for another important parameter, namely the interfacial thermal resistance. This is a phenomenon that describes the resistance to heat flow in the interface of two neighboring materials. In 1987, Hasselman and Johnson [44] investigated the interfacial thermal resistance for spherical shapes, circular cylinders oriented perpendicular to heat flow, and for flat plate shapes oriented perpendicular to heat flow. In order to eliminate the interactions between the temperature fields of neighbouring dispersions, they assumed the condition of low particle concentrations. Given in equation 2.7 is their derivation for spherical particles. The appearance of particle radius (a) on the equation suggests the effect of size on k_{eff}. The term h_c represents the boundary conductance. Note the use of symbol *'a'* for particle radius instead of *'R'* used before. This is to avoid it conflicting with the boundary resistance R_{Bd}.

$$k_{eff}=k_L\frac{\left[2(\frac{k_s}{k_L}-\frac{k_s}{ah_c}-1)\phi_s+\frac{k_s}{k_L}+\frac{2k_s}{ah_c}+2\right]}{\left[(1-\frac{k_s}{k_L}+\frac{k_s}{ah_c})\phi_s+\frac{k_s}{k_L}+\frac{2k_s}{ah_c}+2\right]} \qquad \textbf{Eq 2.7}$$

Every et al. [47]recently rearranged the equation 2.7 by introducing a term α calling it the ratio of Kapitza radius to particle radius i.e. $\alpha=a_k/a$. Furthermore it was stated that $a_k=R_{Bd}k_L$ where R_{Bd} was described as the boundary resistance. Then the new correlation took the following form:

$$k_{eff}=k_L\left[\frac{k_s(1+2\alpha)+2k_L+2[k_s(1-\alpha)-k_L]\phi_s}{k_s(1+2\alpha)+2k_L-[k_s(1-\alpha)-k_L]\phi_s}\right] \qquad \textbf{Eq 2.8}$$

It would be very handy to have a tool like equation 2.8 for analysis of dilute nanofluids. In practice however there exists very limited data for R_{Bd}. This hinders accurate calculation of α and hence restricts wide usage of the equation.

The presentation of equations 2.3 through 2.8 was aimed at abstracting the historical development of several theories that were later used to analyze thermal properties of nanofluids.

Interestingly none of these theories was initially developed for particle suspensions. All of them were developed with the aim of accurately predicting the thermal conductivity of solid-solid composites. Therefore there was no account for particle Brownian motion in any of these theories.

2.4.2 Experimental work

Experimental investigations of thermal conductivity were overwhelming dominating the nanofluids literature. This has led to the development of a comprehensive databank. A thorough literature survey shows that the experimental work can be finely categorized based upon the particle size, particle shape, particle material, base liquid, particle concentration and experimental conditions. A general summary is provided in Table 2.1.

Table 2.1: Experimental data on nanofluids thermal conductivity

Particle material	Size* (nm)	Base liquid	Enhancement#
Al_2O_3	33[3]	Water	29% at 5vol%
	24.4, 38.4[9]	Water	10% at 4vol%
		EG	17% at 5vol%
	28[40]	Water	12% at 3vol%
		EG	40% at 8vol%
		EO	50% at 7vol%
	38.4[48]	Water	24.3% at 4vol% at 51°C
	12.2-302[49]	Water, EG, PO	Up to 30% at 5vol%
	36[50]	Water	29% at 10vol% at 34.7°C
	27-56[28]	Water	10% at 1.6vol%
	48[51]	Water	4% at 1vol%
	20[52]	Water	20% at 14.5vol% & 50°C
	110-210[53]	Water	0% at 0.1vol%
	36 & 47[54]	Water	28% & 26% at 6vol% and 35°C
	8-282[1]	Water	18% at 4vol%
	12-282[1]	EG	16% at 3vol%
	36 & 47[55]	Water	30% at 18vol% and 47nm
CuO	36[3]	Water	60% at 5vol%
		Transformer oil	44% at 5vol%
	18.6, 23.6[9]	Water	12% at 3.5vol%
		EG	20% at 4vol%
	23[40]	Water	12.3% at 4.5vol%
		EG	12.5% at 6vol%
	28.6[48]	Water	36% at 4vol% at 51°C
	29[50]	Water	58% at 6vol% at 36°C
	33[52]	Water	18% at 5vol% & 30°C
	33[56]	Water	5% at 1vol%
		EG	9% at 1vol%
	29[55]	Water	8% at 3.3vol%
	L=50-100[17]	Water	9.6% at 0.4vol%
	L=80, W=20[18]	Water	8.3% at 0.4vol%
TiO_2	15, 10*40 rods[57]	Water	30, 33% at 5vol%
	165[58]	Water	6.5% at 0.72vol%
	40[52]	Water	6% at 2.5vol% & 40°C
	95[59]	Water	22% at 2vol%
	25[51]	Water	14.4% at 1vol%
	21[60]	Water	6.9% at 3vol%

Fe_3O_4	9.8[19]	Water	38% at 5vol%
WO_3	38[51]	EG	14% at 0.3vol%
ZrO_3	20[52]	Water	15% at 10vol%
	110-250[53]	Water	0% at 0.1vol%
SiO_2	20-40[53]	Water	0% at 0.1vol%
	12[61]	Water	3% at 1vol%
Cu			
	<10[11]	EG	40% at 0.3vol%
	100[10]	Water	75% at 7.5vol%
		Transformer oil	44% at 7.5vol%
	50-100[62]	Water	23.8% at 0.1vol%
Fe	10[6]	EG	18% at 0.55vol%
	10[63]	EG	18% at 0.2vol%
	10[51]	EG	18% at 0.55vol%
Ag, Au	10-20[14]	Water	4% at 0.001vol% at 60°C
		Toluene	9% at 0.011vol% at 60°C
Au	2[64]	Toluene	1.5% at 0.04vol%
	4[64]	Ethanol	1.4% at 0.03vol%
Fullerene(C60-C70)	0.5-0.6[64]	Toluene	~0% at 0.8vol%
	10[56]	Mineral oil	6% at 5vol%
DWCNT	D=5 L=20microne[65]	Water	7.6% at 1vol%
MWCNT	D=25 L=50microne[66]	Water	38% at 0.6vol%
	D=10-30,L=10-50microne[61]	EG, Water	30, 10% respectively at 1vol%
	D=25, L=50microne[5]	Synthetic poly oil	250% at 1vol%
	D=15 L=50microne[67]	Water, EG & Decane	7, 13 & 19% respectively at 1vol%
	D=70nm, L=2microne[7]	PAO oil	23.6% at 0.2vol% at 90°C
SWCNT	D~1.1nm, L>100nm	Epoxy	70% at 0.9vol%
Bi_2Te_3 Nanorods	D=20nm, L=170nm[68]	FC-72	8% at 0.8vol%
		Oil	6% at 0.8vol%

** refers to particle size given by the authors. However in many cases it was not clear if the stated size was primary particle size or the size of aggregates.# at room temperature unless otherwise stated*

As far as the base liquid is concerned, water has been the most popular. Vast areas of usage, high specific heat and favorable boiling point, low viscosity, chemical stability with varieties of nanoparticle materials, safe to handle, and cost effectiveness are among the attractive features of water. Ethylene glycol and propylene glycol are common industrial coolants. Transformer oil and synthetic oils are in demand for specialty applications. Although not as much as water, nanofluids based on these liquids too had gained reasonable attention.

Table 2.1 further shows that aluminum oxide, silicon dioxide, titanium dioxide and Carbon nanotubes have gained popularity later on the timeline. Oxides are more stable than pure elements in air and in liquids. Furthermore the oxygen atoms in oxide molecules trigger repulsive forces which make it relatively easier to disperse and stabilize oxide nanoparticles in liquids.

2.4.2.1 Parametric analysis

Forthcoming discussion is dedicated to analyze the experimental data from the viewpoint of several influential parameters. It should be mentioned the excellent review articles periodically published by various authors [69-75] have summed up the data along with excellent graphics. Their work helps to keep this presentation short and concise.

Firstly, the **particle concentration** parameter will be explored. When a medium of higher thermal conductivity in sufficient amount is embedded in a medium of lower thermal conductivity, it is intuitive to expect the thermal conductivity of the mixture to increase. In fact this was the case with nanofluids. Figure 2.16 helps to demonstrate it. This diagram was extracted from Ding et al. [73], while the respective datasets are given in table 2.1. These nanofluids were based on water, ethylene glycol, oils, and epoxy.

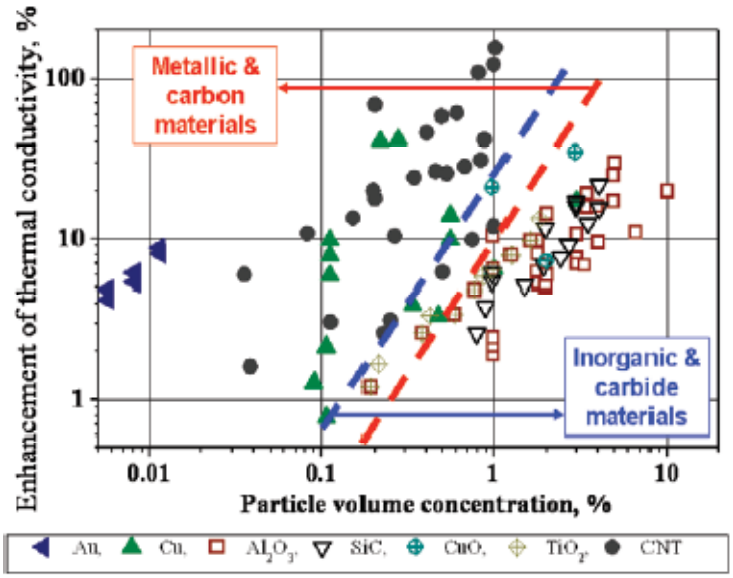

Figure 2.16: Effect of nanoparticle concentration [73]

Even with very low particle presence, there appears to be certain percentage of enhancement *(k_{nf}/k_L*100)* in thermal conductivity. The enhancement has increased nearly linearly with concentration irrespective of the particle material, an observation further consolidated by the INPBE [76]. Having said so, it remains as a fact that there were few instances where very low particle presence was insufficient to exhibit a measurable enhancement. Kim et al.'s aqueous ZrO_3

and SiO_2 suspensions [53] and Putnam et al.'s Fullerene-Toluene suspensions [64] can be depicted as examples.

Another parameter that triggered a debate is the **measuring temperature** of the sample. This is associated with possible effect of particle Brownian motion on the outcome. In many cases the thermal conductivity of liquids increases with the temperature. By extending this to a nanofluid, one may expect its thermal conductivity to follow the same trend. Supporting such hypothesis, there are several examples in the literature where nanofluid thermal conductivity increased with temperature. However the degree of enhancement is highly controversial, where some reports contradicted the claim of enhancement increasing with temperature. To examine the validity of these claims, few examples are brought forward.

In Yang and Han's work shown in figure 2.17, the thermal conductivity is enhanced with temperature. From 20°C onwards however, the enhancement was decreasing in par with the base liquid FC-72. Temperature dependence of alumina-water and alumina-EG nanofluids was recently investigated by Beck et al. [2]. They treated this in a wide interval of temperatures. Their data was recruited to plot the figure 2.18.

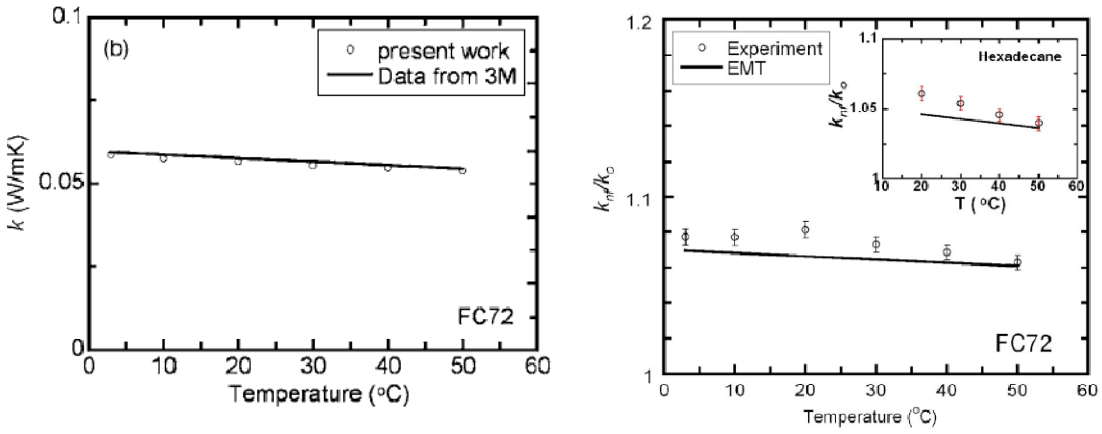

Figure 2.17: Left-FC72, Right-Bi_2Te_3 nanorods 0.8vol% in FC-72 and Hexadecane [68]

For the 5vol%-EG nanofluid, the enhancement shows a steady downward trend. The degree of enhancement is fluctuating between few percentage points for other three nanofluids. The stable or modestly downward trends seen on figures 2.17 and 2.18 are in good agreement with more recent literature, with the exception of the strong upward trend obtained for aqueous alumina

and CuO nanofluids by Das et al. [48] and Li and Peterson [50], and Wang et al. [77] for aqueous titania suspensions.

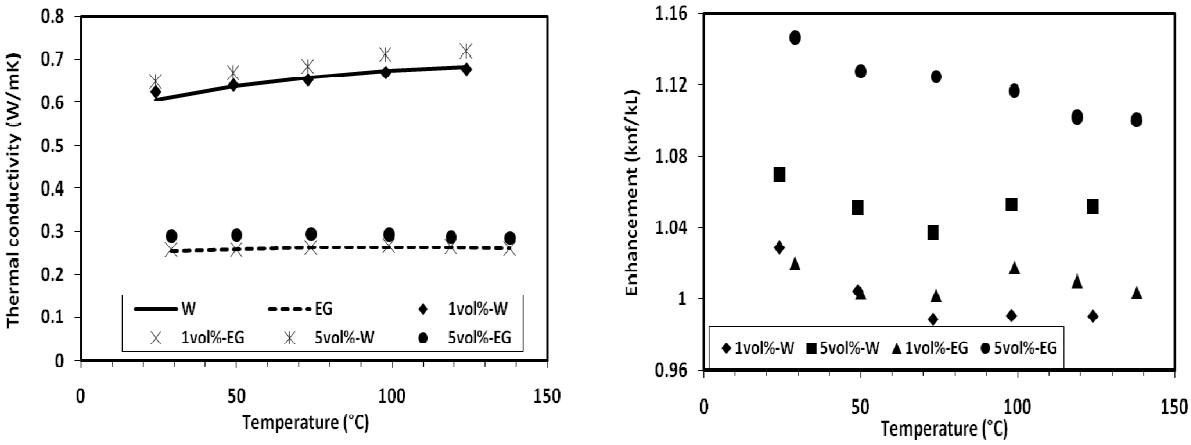

Figure 2.18: Al_2O_3 in Water and EG. Plotted using Beck et al. [2]'s data

There have been few studies dedicated to understand the **role of particle size** in determining the thermal conductivity of nanofluids. However the definition of particle size itself is ambiguous, a point previously emphasized in this report under the topic of size characterization. On one hand, the nanopowder suppliers declare a mean particle diameter as the size of their merchandise. This indicates the particles are polydisperse in reality, and also the polydispersity could either be narrow or wide. On the other hand, immediately after the nanopowder being dispersed in a liquid, the particles flock together and build clusters. This is followed by a change in the size and the size distribution. The particle size that matters is the size in suspended state. However nanofluids researchers often do not clarify what size they are referring to leaving the audience to make own judgment, or state the supplier-declared size of particles. Hence the real challenge in conducting the present size analysis is to pick a sensible size parameter that represents the actual picture. Without that piece of vital information, it would be of a little use or even misleading to analyze data and to report the trends.

Xie et al. [49] produced alumina nanopowder of five particle diameters 12.2, 12.4, 15, 26, 60.4 and 302nm. They subsequently dispersed those particles in water, EG and pump oil. When the measurements were conduced, first they observed an increase followed by a decrease in the thermal conductivity with particle size. Li and Peterson [54] studied the effect of particle size on thermal conductivity of aqueous alumina nanofluids. As illustrated on figure 2.19, they chose two

particle diameters 36 and 47nm, which presumably are primary particle sizes. It was found that the enhancement increased with decreasing particle size.

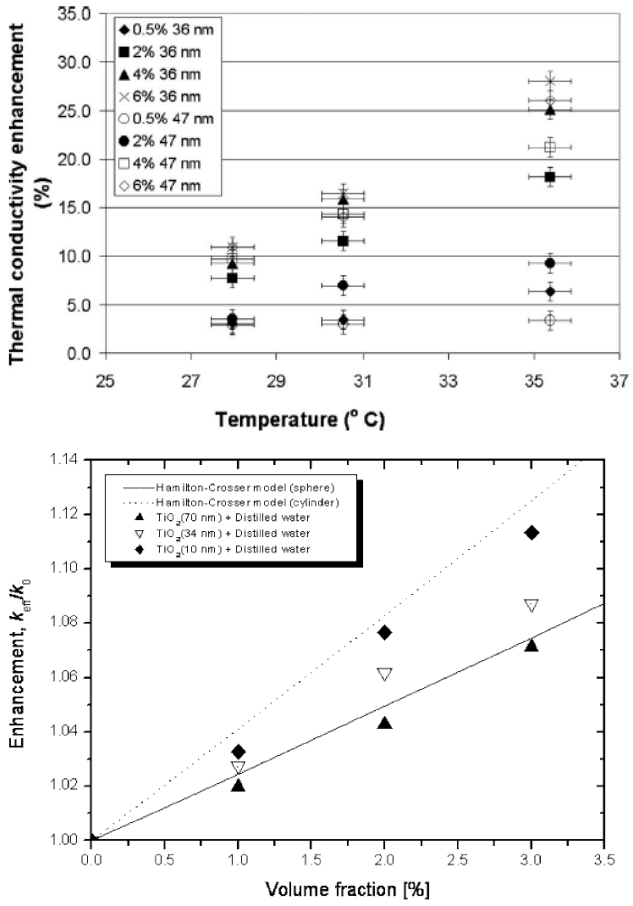

Figure 2.19: Above-aqueous alumina [54] and Below-aqueous titania nanofluids[78]

Kim et al. [78] examined aqueous and EG-based titania nanofluids. They found the size-enhancement relationship, shown on figure 2.19, similar to Li and Peterson [54]. Four datasets from literature [9, 40, 48-49] on alumina-water nanofluids were recruited by Yu et al. [79] to study the effect of primary particle size. The 28nm particles were superior in enhancement than 38nm but inferior to 60nm, suggesting there was not direct relationship between size and enhancement.

In 2008 Beck and coworkers [1] conducted a systematic investigation on the effect of particle size on the thermal conductivity of alumina-water and alumina-EG nanofluids. On top of supplier-specified size (D_s), the investigators used BET (Brunauer–Emmett–Teller) technique to measure

size (D_{BET}), TEM images to determine the standard deviation of size, and light scattering to obtain hydrodynamic diameter (D_{LS}). Presented in table 2.2, these sizes were scattering considerably. Their datasets are plotted on figure 2.20. Three trendlines are constructed for aqueous nanofluids where top-most is for 4vol% and bottom-most for 2vol%.

Table 2.2: Particle diameter (nm)

D_s	D_{BET}	D_{LS}
11	8	320
20	12	265
50	16	520
47	46	205
300	71	492
150	245	790
1000	282	522

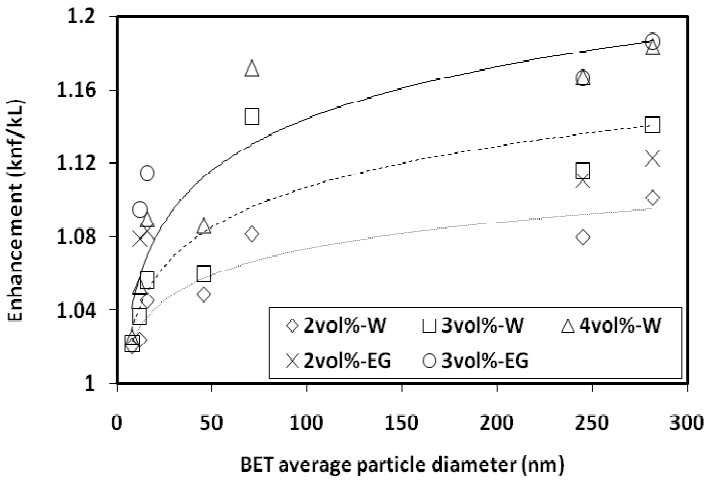

Figure 2.20: Al_2O_3 in water and EG. Data extracted from [1]

Firstly there appears a considerable degree of data scattering. Nonetheless beyond 50nm, Beck et al.'s [1] data exhibits increasing enhancement with size. Below 50nm however, the trend changed. Out of curiosity the D_{BET} in abscissa was substituted with D_{LS} and D_s, and the data were replotted. It confirmed the trends repeating, which suggests that for a qualitative analysis the sizing technique did not matter at least for this experiment. Moreover, this partly addresses the question of which size to be chosen for analysis. Previously Chen et al. [80] saw liner increase of thermal conductivity with particle size in 16vol% SiO_2-water nanofluid with size range of 10-30nm. More recently an increase in thermal conductivity enhancement with particle size was reported by Venerus and Jiang [81]. They observed this for SiO_2 particles up to 30nm in size dispersed in water with 0.16vol% nanoparticle concentration.

Figure 2.20 also helps to make a statement on the **effect of base liquid** on thermal conductivity of nanofluids. Water and EG are the two base liquids stated on the figure, and thermal conductivity of the former is higher than the latter. In order to make a comparison, consider 2vol% and 3vol% datasets. Appreciate the fact that the enhancement is superior in EG-based nanofluids for all cases under consideration. This is a trend supported by a study conducted by Xie et al. [82]. They had water, glycerol, EG and pump oil based 5vol% alumina nanofluids with particle diameter 60nm. The order of thermal conductivities of base liquids were $k_w > k_G > k_{EG} > k_{PO}$. Then the

measurements were conducted with nanofluids and found that the PO-based nanofluids were at the top end of enhancement and the water-based nanofluids were at the bottom end. Moreover the arrangement of the degree of enhancement was totally the opposite to that of respective base liquids; $(k_{nf}/k_L)_w<(k_{nf}/k_L)_G<(k_{nf}/k_L)_{EG}<(k_{nf}/k_L)_{PO}$.

A survey on the **effect of particle material** on thermal conductivity was documented by Yu et al. [79]. They reviewed water and EG based nanofluids of Al_2O_3, CuO, SiC and $Al_{70}Cu_{30}$ and plotted the graphs shown on figure 2.21. For the comparison to be done on fair ground, all other parameters but the particle materials were fixed. Generally there was sign of a clear correlation between the particle material and the degree of enhancement. This trend was closely followed by the TiO_2-water data from He et al. [25] and Turgut et al.[60]. However the metallic $Al_{70}Cu_{30}$–EG nanofluid stands out as the only exception in figure 2.21.

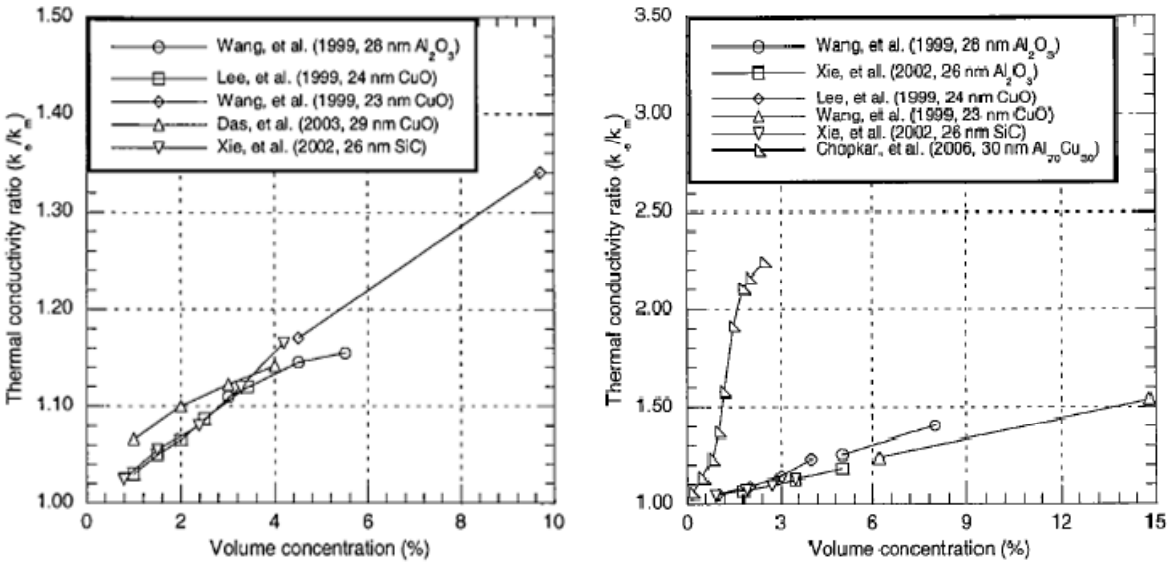

Figure 2.21: Left-water based, Right- EG based nanofluids of various particle materials [79]

To conclude the section on experimental work, it can safely be stated that the thermal conductivity enhancement had steadily increased with the nanoparticle concentration, was inversely proportional to the thermal conductivity of base liquid, and largely insensitive to the measuring temperature. Meanwhile the oxide nanoparticles did not show a noticeable difference among themselves in performance. Moreover the effect of particle size needs to be further investigated as the experimental data are equally divided into two sides.

2.4.3 Analytical work

A plausible volume of analytical work has been happening in the background of experimental work. The motivation behind was to correlate various parameters in the experimentally-obtained data and to build models which can predict the thermal conductivity in-advance. If this objective was achieved, it was believed that the application-specific (tailor-made) nanofluids could be manufactured. Moreover the nanofluids would become the next generation of coolants as initially forecasted by Eastman and Choi [5, 11, 83], who began the pioneering work in nanofluids at the Argonne National Laboratory in USA.

It is customary for modeling to start from an established theory. For nanofluids, this became the effective medium theories (EMTs). Before long however it was understood that the original form of EMTs had shortfalls in predicting the experimental data. This led the analysts to thinks that there were parameters unaccounted for in EMTs. In the meantime, a groundbreaking piece of work by Keblinski et al. in 2002 [84] listed all possible hypotheses that would govern the thermal conduction behaviour of nanoparticle suspensions. They postulated four mechanisms; particle Brownian motion in the liquid, layering of liquid molecules around particles, mode of heat transport across the particles, and particle clustering. Interestingly none of these factors were fully encountered by any single EMT. Hence it was logical to expect the EMTs to mispredict the actual data unless these missing factors are incorporated. Since the inception of the concept of nanofluids, a large number of correlations have been developed. An overall examination shows that each one of them had knowingly or unknowingly based on one or more of Keblinski et al.'s hypotheses. Although the correlations were numerous, some of them lost their versatility soon after becoming mere correlations for a selected dataset. Some correlations went a little further and accurately predicted the behaviour of certain types of nanofluids. All these efforts should be appreciated for shedding some light on the modeling stream. The forthcoming discussion is mainly focused on presenting a few carefully selected work which gradually developed into models, and are thought to have significantly contributed to the accurate modeling of thermal conductivity.

Chandrasekar and Suresh [85] recently reviewed the literature on heat conduction mechanisms in nanofluids. They divided the literature into three categories upon the possible mechanism of heat transport as stated by the corresponding authors. These categories were the influence of Brownian motion, influence of nanolayer, and influence of clustering. Particularly in a review of

analytical models, Chandrasekar and Suresh have reported that Xuan et al. [86], Jang and Choi [83], Koo and Kleinstreuer [87], Kumar et al. [88], and Prasher et al. [89] had constructed models on the base of Brownian motion, Yu and Choi [90], Leong et al. [91] and Xie et al. [92] developed models on nanolayer, and Prasher et al. [93] and Wang et al. [94] built models on clustering. Not surprisingly there were hybrids which incorporated more than one mechanism into one model. Since the influence of the mode of heat transport across the particles had already been proved trivial in the context of nanofluids, it did not gain prominence in modeling any further.

In the absence of convective currents, a nanofluid can be considered as a static body at macroscopic view. However at high temperatures, particles gain thermal energy and start to move around as described by Brownian dynamics. The diffusion coefficient D_B which is an indicator correlated to the temperature (T) and viscosity (μ) of the liquid and the particle radius (R) itself was earlier given in eq 2.2. Thus depending on the fluid temperature, a nanofluid could behave in thermal static mode or in static cum dynamic (dual) mode. Models constructed on Brownian motion precisely addressed this aspect.

S.U.S Choi and co-workers developed a model to predict thermal conductivity starting from evaluation of the role of interfacial layer [90, 95], and progressing to include the effect of the Brownian motion of nanoparticles, and heat diffusion within the particles [83]. By incorporation of all these parameters, the comprehensive model that was built was written as follows.

$$k_{eff} = k_L(1-\phi_s) + \beta k_s \phi_s + 3C\frac{d_L}{d_p} k_L \, \mathrm{Re}_{d_p}^2 \, \mathrm{Pr}_L \qquad \textbf{\textit{Eq 2.9}}$$

where β is a representation of the interfacial resistance, C is proportionality constant, d_L is diameter of liquid molecule, $\mathrm{Re}_{d_p}^2$ and Pr_L are the evaluated Reynolds and Prandtl numbers. The authors postulated that there was an ordered liquid layer surrounding each particle with a thickness equal to three times the diameter of fluid molecule. This model very closely predicted Al_2O_3-water, CuO-water, CuO-EG and Cu-water experimental data earlier obtained by them [9, 11] and the associated trends with respect to particle size and temperature. Their main argument was on the Brownian motion as a key enhancement mechanism, which they experimentally validated in a subsequent paper for Al_2O_3-water nanofluids [96]. However if their hypothesis was correct, the enhancement for a larger particle should be less than that of a smaller particle of the same

material at a given temperature. In reality it was far from truth, as discussed in the foregoing section on experimental data. Therefore this model did not accurately predict other datasets.

In the model proposed by Koo and Kleinstreuer [87], effective thermal conductivity was written as the sum of static (Maxwell) and dynamic (Brownian) contribution. Conceptual formulation is given in equation 2.10. Maxwell's theory inherently accounts for particle size, volume fraction, and particle and liquid properties.

$$k_{eff} = k_{static} + k_{Brownian} \qquad \textbf{Eq 2.10}$$

The Brownian part of the model was supposed to capture the temperature effect. The authors argued that a particle moving from hot to cold regions carries a large volume of liquid along with it. They thought the resulting micro-mixing would lower the local temperature gradient. The Brownian contribution was written as follows:

$$k_{Brownian} = 5*10^4 \theta \phi_s \rho_l c_l \sqrt{\frac{\kappa T}{\rho_s d_p}} f\left(T, \phi_s, etc..\right) \qquad \textbf{Eq 2.11}$$

where subscripts *l* and *s* represent the respective liquid and particle properties, θ is a variable that represents the liquid volume carried by a particle, and κ is the Boltzmann constant. This model closely correlated some data for aqueous Al_2O_3, CuO, TiO_2 nanofluids of small particle diameters (<100nm). The conceptual shallowness and the need to estimate or to experimentally determine the unknowns in equation 2.11 restricted the general usage of Koo and Kleinstreuer's model.

In a stepwise developing model Prasher and co-workers [89, 93, 97-100] considered more parameters than any other previous work. The influences of Brownian effect, liquid layering as well as nanoparticle aggregation were thoroughly examined. Brownian motion's contribution is by setting up the convection currents in the liquid body. They validated this claim through a dye experiment conducted in an aqueous Al_2O_3 suspension [100], where the occurrence of maximum mass transport (D_{eff}/D_L) and the occurrence of maximum thermal conductivity (k_{eff}/k_L) happened at two different particle concentrations.

This model captured the effect of liquid layering by using the interfacial thermal resistance explained by Nan et al. [101]. Accordingly there was a critical particle diameter, below which the nanofluid will conduct heat worse than the base liquid [98]. In fact there was no systematically obtained experimental data to support this claim. Their conduction-convection model is given in

equation 2.13. The overall enhancement was therefore given as a multiplication of enhancements due convection and conduction. The two constants *A* and *m* were to be empirically determined for a given particle-liquid combination.

$$k_{eff} = k_L\left(1 + A.\mathrm{Re}^m \Pr^{0.333} \phi_s\right)\left(\frac{k_s[1+2\alpha] + 2k_L + 2\phi_s[k_s(1-\alpha) - k_L]}{k_s[1+2\alpha] + 2k_L - \phi_s[k_s(1-\alpha) - k_L]}\right) \qquad \textbf{Eq 2.13}$$

The term α was called the nanoparticle Biot number calculated using the interfacial thermal resistance (R_b), liquid thermal conductivity and particle diameter, $\alpha = 2R_b k_L / d_p$.

The developing model then addresses the particle aggregation phenomena. It was postulated that the aggregation can influence thermal conductivity in two ways. Firstly the effective volume fraction of aggregates is larger than that of a non-aggregated powder. Secondly the speed of thermal transport through a solid aggregate is quicker than a liquid due to interconnectivity. Therefore the overall conductive contribution to the thermal conductivity of nanofluid can be derived by adding the aggregation component to Maxwell's model. The authors of the model achieved this by replacing the particle size by the aggregate size as follows.

$$k_{eff} = k_L\left[\frac{k_a + 2k_L + 2\phi_a(k_a - k_L)}{k_a + 2k_L - \phi_a(k_a - k_L)}\right] \qquad \textbf{Eq 2.14}$$

The final shape of the complete equation is therefore,

$$k_{eff} = k_L\left(1 + A.\mathrm{Re}^m \Pr^{0.333} \phi_s\right)\left[\frac{k_a + 2k_L + 2\phi_a(k_a - k_L)}{k_a + 2k_L - \phi_a(k_a - k_L)}\right] \qquad \textbf{Eq 2.15}$$

This model works like this; term k_a and ϕ_a, respectively the conductivity and volume fraction of aggregates, should first be calculated. Prasher et al. [93] explains how to determine these parameters using fractal dimensions and aggregation time constants. Those values should then be substituted in equation 2.15 to evaluate the conduction term on the right hand side. Meanwhile the convective term should be evaluated separately, taking into account the empirical constants. By applying to their own data, the authors had validated the model.

In summary, there has been commendable work done on developing analytical models to predict thermal conductivity. As the time passed, the prominence of particle aggregation emerged over other mechanisms. And the models that accounted for this factor has gained more recognition as

efficient prediction tools. However for these models to gain recognition, they need to be validated with independent experimental data collected from a broad cross section of researchers.

2.5 Convective heat transfer in nanofluids

Heat transfer involved with bulk motion of nanofluids comes under this classification. Study of nanofluid motion caused by external forces (forced convection) and without external forces (natural convection) has a history that is as long as the history of thermal conduction. Since more focus was on thermal conductivity, there are fewer publications dedicated to convective heat transfer of nanofluids. At least three review articles solely addressing this topic have been published [102-104] during this period. Following discussion is a brief revisit to the important milestones.

2.5.1 Forced convection

In flow heat transfer applications, forced convection plays the major role. The turbulent flow regime is further preferred as much as possible, due to fierce agitation of the liquid and the resulting high heat transfer rates. Nevertheless both turbulent and laminar flow conditions have been examined for nanofluids. Furnished in table 2.3 is a summary of literature. It can be noticed at a glance the reports of enhancement have vastly overweighed the reports of deterioration. The researchers attempted to reproduce their experimental data using classical correlations.

Table 2.3: A summary of experimental work on Forced convection

Nanofluid	Geometry*	Remarks
CuO-water[105] 0.3-2vol%	T (D=10, L=800)	Turbulent. Enhancement with concentration & Re. Pressure drop small.
Cu-water[106] 0.2-2.5vol%	T (D=6, L=1000)	Laminar. Heat transfer steadily increases with Peclet number and concentration
TiO_2-water [25] 0.24-1.1vol%	T(D=3.97, L=1834)	Laminar & Turb. Enhancement with concentration & Re. Pressure drops are close to base liquid.
Al_2O_3, TiO_2-water[107]	T	12% Deterioration at 0.3vol%, compared at constant average flow velocity.
Al_2O_3-water[28] 0.6-1.6vol%	T (D=4.5, L=970)	Laminar, Enhancement with concentrations & Re, higher at entrance

Al_2O_3, CuO-water[108]	Annular (D=6, L=1000)	Laminar. Enhancement. Al_2O_3 shows higher enhancement.
Graphite-water[109]	T (D=4.57, L=457)	Laminar. Enhancement but lower than *k* enhancement.
CNT-water[26] 0.1-0.5vol%	T (D=4.5, L=970)	Laminar. Enhancement in all concentrations. pH influence.
CNT-Water[110]	T (D=10.7, L=4000)	Laminar-increase & Turbulent – no change in pressure drop.
Au-water[111]	Disk-shaped heat pipe D=9, H=2	Reduction in thermal resistance
Au-water[112]	Heat pipe D=6, L=170	Reduction in thermal resistance

Legend: T – Tube, D-inner diameter, L-length, H-height, all dimensions in mm.

In view of building the correlation, Xuan and Li [105] recruited their own experimental data on turbulent forced convection with aqueous CuO nanofluids. Particle concentrations were in the interval of 0.3-2vol%. The experiments were conducted under constant wall heat flux conditions. The observed enhancement was attributed to the excess thermal conductivity and the nanoparticles accelerating the energy exchange in the liquid in flow. In a curve-fitting exercise, they obtained the equation 2.16.

$$\mathrm{Nu}_{NF} = c_1\left(1 + c_2\phi_p^{\ m_1}\ \mathrm{Pe}_d^{m_2}\right)\mathrm{Re}_{NF}^{m_3}\ \mathrm{Pr}_{NF}^{0.4} \qquad \textbf{Eq 2.16}$$

Where all fluid properties should be measured, the constants c_1, c_2, m_1, m_2, and m_3 are derived from experimental data, and the term (ρCp) to be computed as follows.

$$\left(\rho C_p\right)_{eff} = \phi\left(\rho C_p\right)_s + (1-\phi)\left(\rho C_p\right)_L \qquad \textbf{Eq 2.17}$$

This correlation was not bounded by the volume fraction. But the usefulness of equation 2.16 was severely hindered due to the requirement of five constants. Another important outcome of Xuan and Li [105]'s work was the demonstration of conventional correlations for pure liquids predicting the friction factor of nanofluids. This was the earlier showed by Pak and Cho [107] and later proved by several groups such as Boudouh et al. [113] and Liu and Yu [114].

A rigorous analysis of heat and mass transport mechanisms in nanofluids was performed by Buongiorno [115]. Seven slip mechanisms were considered for a nanoparticle in a flowing fluid. These were the Brownian diffusion, turbulent eddies, thermophoresis, diffusiophoresis, Magnus effect, fluid drainage, and gravity. After an order of magnitude analysis, the diffusiophoresis, Magnus effect, fluid drainage, and gravity were neglected as trivial. The author was of the view

that the particles travelling at high inertia would break the boundary layer and will thin the laminar sublayer. The temperature variation in the boundary layer meanwhile will alter the fluid properties. When these happen in the near-wall region of a flow, it was hypothesized the enhancement will occur. Appreciate that the thinning of boundary layer was a hypothesis earlier put forward by Wen and Ding [28] which has since been widely discussed.

Buongiorno's correlation is given in equation 2.18. This had to be solved by eleven-step method, with the knowledge of one empirical constant δ_v^+, which is the thickness of the laminar sublayer.

$$Nu_b = \frac{f(\mathrm{Re}_b - 1000)\mathrm{Pr}_b}{8\left[1+\delta_v^+\sqrt{\frac{f}{8}}(\mathrm{Pr}_v^{2/3}-1)\right]} \qquad \textit{Eq 2.18}$$

It was demonstrated that the aqueous CuO, TiO_2 and Al_2O_3 data of Xuan and Li [105] and Pak and Cho[107] were correlated by equation 2.18 to a high accuracy. However to validate the model to a greater extent, larger numbers of experimental data were needed.

Shear viscosity is an important property that determines the convective heat transfer. Nanofluids are often reported to have exhibited non-Newtonian behaviour. Few example are the aqueous TiO_2 [25], aqueous CNT [26], aqueous titanate nanotubes (TNT) [116], EG based TNT [117], polyalphaolefin based alumina [118], and water-EG based CNT [30] nanofluids. He et al. [119] recently conducted analytical study to examine the relationship between non-Newtonian behaviour and heat transfer enhancement. For this, they focused on water based CNT and TNT suspensions in laminar flow in a straight pipe. Their conclusion was that the non-Newtonian behaviour to certain degree helps to explain the enhancement of heat transfer.

2.5.2 Natural convection

There had been a small number of experimental and analytical studies conducted on natural convective behaviour of nanofluids. The investigated nanofluids were the water based alumina, titania, copper oxide, and the EG based copper. The test geometries were rectangular and cylindrical enclosures. The analytical studies on natural convection always predicted enhancement, whereas the experiments showing otherwise with the only exception of enhancement reported by Nanna et al. [120-121]. The trend of consistent deterioration appears to have sunk the enthusiasism on natural convection.

Aqueous alumina and copper oxide nanofluids were examined by Putra et al. [122] for natural convection in a horizontal cylinder which was heated from one end and cooled from the other. Data were reported as the plots of Nu vs. Ra. In doing so, they measured all properties but β, which was assumed as equal to water. The Nusselt number consistently deteriorated in all experiments, although the deterioration was decreasing with increasing Ra and aspect ratio for a given concentration. Putra et al. [122] attributed the deterioration to the slip between particles and the fluid. However this interpretation looks dubious as the particles were very small. Also the opaqueness of nanofluids prevented them from visualizing the interior of experiment.

Investigations by Wen and Ding [22, 58] supported the claim of heat transfer deterioration. They studied aqueous titania nanofluids in a short cylinder with vertically oriented main axis. The enclosure was heated from bottom while cooled from top. A systematic deterioration was observed, which worsened with increasing particle concentration. Subsequent to experiments, the possible influence of property variations, convection induced by particle movement, and particle-surface interactions were examined analytically. However the exact reason for deterioration could not be finalised.

Nnanna [121] et al. examined aqueous alumina suspensions in a small rectangular enclosure where the two opposite walls were maintained at two temperatures. When the particle concentration was in the interval of 0.2<vol%<2, they saw a slight enhancement. They postulated that the deterioration at high concentrations up to 8vol% was due to the increasing kinematic viscosity.

This author and coworkers conducted natural convection experiments with titania nanofluids based on water 75wt%-ethylene glycol 25wt% mixture [123]. Concentration of titania nanoparticles was varied between 0.4 to 8wt%. The experimental apparatus was similar to that previously used by Wen and Ding [22,58]. For constant heat flux condition of 221W/m^2 and titania concentrations of 0.4wt% and 2wt%, enhancement up to 12% was observed for both horizontal and vertical orientations of the apparatus. For larger concentrations and heat fluxes deterioration was recorded.

On analytical work, Kanafer et al. [124] modeled natural convection in two-dimensional horizontal cavity heated on the left wall. For simulations, they assumed the random motion of nanoparticles through the liquid. They found that the heat transfer increased with particle concentration at a

given Grashof number. This was attributed to the energy exchange as result of particle movements. Their work however was very likely to have used an incorrect viscosity model and hence the enhancement.

Kim et al. [125] conducted a study on convective instability and heat transfer characteristics of nanofluids. They assumed that the Hamilton-Crosser model and Bruggeman model accurately predict thermal conductivity, and the Brinkman model predicts viscosity of a nanofluid. Based on these assumptions and further simplifications of the problem, they demonstrated that the Rayleigh-Benard convection, shown on figure 2.22, was driven by the base fluid but not the nanoparticles. The model of Kim et al. [125] predicts enhancement for any nanofluid. Moreover the rod-like particles cause larger enhancement than spheres. Noticable this conclusion requires validation with experimental data.

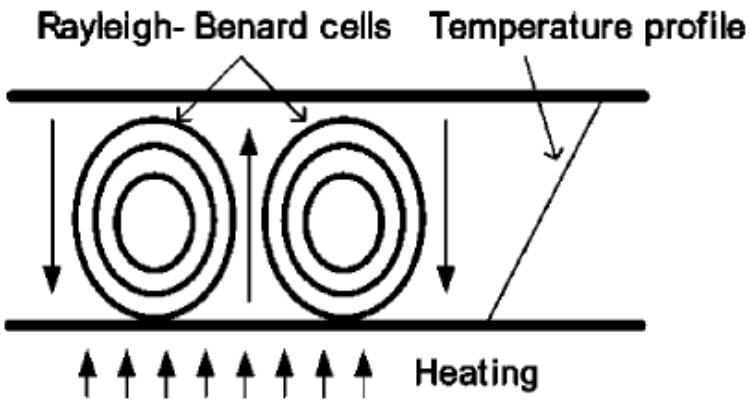

Figure 2.22: Rayleigh-Benard cells in natural convection [125]

Hwang et al. considered a rectangular cavity containing alumina-water nanofluid heated from below [126]. They worked under the assumption that the Jang and Choi's model [83] accurately predicted the thermal conductivity of nanofluid, and Pak and Cho's correlation [107] accurately predicted its viscosity. In addition to usual parameters, they also took into account the Kapitza resistance and particle Reynolds number. This model was successfully validated with Putra et al. [122]'s alumina-water data for heat transfer.

2.6 Boiling heat transfer

Boiling has historically been recognized as the most efficient mode of convective heat transfer. The classical boiling curve demonstrates that heat transfer rates exponentially increase with

excess temperature when the regimes change from free convection to boiling. There are a number of variables that influence boiling heat transfer. Rohsenow and Griffith [127] indentified them as surface parameters, fluid properties and surface-fluid interactions. As a consequence, understanding the boiling phenomena has been a very challenging task over the past few decades.

The concept of boiling a nanofluid immediately adds a third (solid) phase into an already existing two phase (liquid-vapour) system. Obviously now the challenge is bigger. Boiling of nanofluids has been a vastly explored research topic. There has been a rapid increase in the number of publications over the years, where the number of journal articles on boiling heat transfer only comes second to thermal conductivity [4]. Although it is hard to classify these articles under few specific subtopics, they have commonly addressed general boiling heat transfer [21, 128-153] and the critical heat flux [53, 133, 141-142, 153-166]. Table 2.4 presents a general summary of the published work on pool boiling of nanofluids.

The literature review given in the table reveals few quick observations at a glance. They are; all but six nanofluids were water-based, none of nanofluids were ethylene glycol (EG) based or water-ethylene glycol (WEG) based, CHF had enhanced in all experiments, and, the boiling heat transfer had exhibited selective behaviour dependent upon heater type, particle loading, and heat flux [138, 167-168].

Furthermore, it is encouraging to note that the CHF has increased in all experimental investigations on nanofluids, even in cases where the boiling heat transfer had degraded [161]. The enhancements in CHF were substantial, which was sometimes as high as 300% [136]. Boiling heat transfer however had been surrounded by controversies. The claims of enhancement were as large as 68%, while the claims of deterioration were in the order of 10-40% [169]. The following discussion builds around a few experimental cases which this author believes as representative of the general view on boiling of nanofluids.

Table 2.4: An overview of Pool boiling and CHF of nanofluids

Nanofluid	Boiling geometry	Remarks
Au-water[130] 0.0002, 0.0004 and 0.001 wt %	Horizontal Cu plate, D=100mm.	BHT enhanced and it increased with ϕ and heat flux
Al_2O_3-water[131] 0.1, 1, 2, 4vol%	Horizontal SS cylindrical cartridge heaters D=20mm.	BHT deteriorated, which increased with ϕ, boiling time, and surface roughness

Al_2O_3-water[132] 1, 2, 4vol%	Horizontal SS cylindrical cartridge heaters D=4, 6.5 and 20mm.	BHT deterioration, which decreased with decreasing D of the heater
Al_2O_3-water[170] 0-0.5g/l	Horizontal Cu flat square heater, 1cm x 1cm copper, polished.	No enhancement in BHT, but in CHF up to 200%
SiO_2-water[133] 0.5-0.67vol%	Horizontal NiCr wire D=0.4mm, L=75mm.	No enhancement in BHT, but CHF upto 60%.
Al_2O_3-water[129] 0.32, 0.71, 0.95, 1.25 wt %	Horizontal SS plate, D=150mm	BHT enhanced by 10-40%
SiO_2 – water[136] 0.5wt%	Horizontal NiCr wire D=0.32mm, L=46mm.	CHF enhanced up to 300%. CHF increased with ionic concentration of NF
Al_2O_3-water[161] 0.5, 1, 2, 4vol%	Horizontal & vertical Cu flat surface, 4x100mm^2.	BHT deteriorated, CHF enhanced and more on horizontal.
Al_2O_3-water, ZnO-water, Al_2O_3-water-EG[171] 0-0.5g/l	Horizontal Cu block 10x10x3mm.	CHF enhanced in all cases. BHT unchanged or deteriorated depending on heat flux.
TiO_2-water[21] 0.31, 0.44, 0.54, 0.72 vol %	Horizontal SS plate, D=150mm	BHT enhanced up to 50%.
Al_2O_3-water, TiO_2-water[154, 163]. 0-0.1vol%	Horizontal NiCr wire D=0.2mm, Ti wire D=0.2mm	CHF of Water on nano-fouled wire was same as nanofluid.
Al_2O_3-ethanol[172] 1-5 wt%	PTFE substrate	Nanoparticles promoted pinning of contact line.
Al_2O_3-water, ZrO_2-water, Silica-water[53, 173] 0.001, 0.01 and 0.1vol%	Horizontal SS plate, 5x45mm^2 Horizontal SS wire, D=0.381mm, L=12cm	Fouling reduced θ, which probably explains the increase in CHF
CNT-water, CNT-R22[174] 0-1vol%	Horizontal plain tube D=19mm, L=152mm	BHT enhanced depending on heat flux and ϕ. Higher HFs suppressed enhancement. No fouling.
Al_2O_3-DI water [128] 0.5, 1, 2wt%	Vertical tubular SS heaters of Ra=48, 98, 524nm	Only rough heaters enhanced BHT. Larger particles are more attractive to heater surface.
Al_2O_3-water, BiO_2 – water[166] 0-0.008g/Litre	Horizontal NiCr wire. D=0.64mm, L= 50mm.	CHF increased. Particle coating reduced θ. Increase in ϕ didn't increase θ
ZrO_2- water[138] 0.005, 0.01, 0.02, 0.05, 0.07, 0.15 vol%	Horizontal Cu plate of 60.5mm diameter	BHT increased with ϕ but deteriorates after a limit. Heater surface smoothens after boiling NF
CuO, SiO_2 in water and ethanol[139] 0.2-2wt%	Horizontal flat Cu surface, 20mm diameter	Layer formed on heater for aqueous NF. Roughness & θ decreased
Al_2O_3, CuO, Laponite in Water[140]	Vertical Cu heating block	BHT deteriorated for all NFs. Wettability increased by Al_2O_3 & Laponite NFs.

1wt%	120x50x50mm	Vaporization caused particle accumulation blocking cavities
SiO_2-water[141] 0.5vol%	Horizontal Ni wire. L=46mm, D=0.32mm	pH could control deposition CHF enhanced even without deposition
Al_2O_3-water, Al_2O_3-ethanol[160] 0.0001wt%-1wt%	Horizontal circular Cu surface 0.9cm^2	Oxidation changes contact angle. For oxidized Cu, CHF of W > CHF of aqueous NF. BHT no change or degrade.
CuO-water & CuO-SDBS-water[175] 0.1, 0.2,0.5 and 1 wt%, SDBS 1vol%	Inside SS tube, closed bottom. D=2-4.4mm, L=200-500mm	CHF increases with ϕ. But stabilizes after 1wt%. SDBS prevented deposition.
Al_2O_3-water 0.3-2wt%, SnO-water 0.5-3wt%[144]	Vertical SS cartridge heater. Cartridge D=25mm, L=76mm	Except for SnO 0.5wt%, HTC increased in all cases and with particle ϕ.
CuO-R134a[151] <1vol%	Horizontal Cu plate.	Enhancement in all cases, range 50-275%
Cu-water & Cu-SDS-water[152] Cu 0.25%, 0.5% and 1.0wt%, SDS 9wt%	Horizontal SS tube	CHF increased. BHT deteriorated. Roughness increased by a few hundred times
ZrO_2-water[176] 0-1vol%	Horizontal NiCr wire D=0.2mm	CHF increases with ϕ upto 0.02vol%, and from thereon it stabilizes
TiO_2, Al2O3, SiO2-water[157] 0.0001%-0.1vol%	Horizontal NiCr wire D=0.2 mm	CHF of all NFs increased but depends on kind of np & ϕ
TiO_2-R141b[143] 0.01, 0.03 and 0.05 vol%	Horizontal cylindrical Cu tube D=28.5mm, L =90mm	BHT deteriorates, which is larger with increasing ϕ, especially at high HFs
TiO_2-water[167] 0.00005-.01vol%	Horizontal circular plates – Cu & Al. Sizes unspecified Ra= 0.2-4um	On Cu plate, BHT always enhanced, depending on ϕ and roughness. On Al plate, BHT always deteriorated.
ZnO-water[168] 2.3vol%	Horizontal SS plates D=82.6mm, t=12.7 mm	BHT enhanced but it steadily declines upon repeated boiling. Ra increased from 0.06 to 0.44um in 8 tests.
Al_2O_3-water, Titania-water[177] 0.01vol%	Horizontal Cu or Ni plated Cu disk. D=20mm, t=7mm	BHT deteriorated. CHF enhanced by 30-40%. Deposition causes same CHF enhancement for NF & W
Cu-W & Cu-W-SDS[178] Cu 0.25%, 0.5% and 1.0wt%, SDS9wt%	Horizontal SS flat heater 30mm2, t=0.44	CHF increased but BHT deteriorated for all cases. Ra always decreased after boiling
Al_2O_3-water, CuO-water, Diamond-water[146] < 0.1wt%	Horizontal Cu block 1x1cm2	Critical coating thickness where max CHF enhancement occurs
Al_2O_3-water[179] 0.8, 1, 1.2, 1.4wt%, 0.5wt%CMC	Vertical SS cartridge heater. Cartridge D=25mm, L=76mm	BHT deteriorated. But addition of CMC enhanced BHT

Legend: NF – nanofluid, NP-nanoparticle, φ - vol%, D-diameter,W-water, CMC- Carboxy methyl cellulose, SS-stainless teel, HF-heat flux, BHT-boiling heat transfer

It is widely agreed among the research community that the boiling heat transfer and CHF behaviour of nanofluids are principally driven by the changes in heater surface. This may happen due to few reasons. Firstly and foremostly, it is likely to be the deposition of nanoparticles. However stable a nanofluid is in room temperature and slightly above it, it may still dissociate in boiling temperatures. There is ample evidence found in literature in terms of roughness measurements, contact angle measurements as well as SEM and AFM images. In fact in almost all these examinations, particle deposits were discovered on heaters. This is not surprising due to the higher temperature of the heater surface and consequent changes in solution chemistry.

Secondly any surfactant such as SDBS, SDS or Gum Arabic used to stabilize the nanofluid may fail at high temperatures. This can indeed be prevented by avoiding the use of surfactants as far as possible. Failing of a surfactant and deposition it on the heater is undesirable because the resulting change in the heater surface properties will directly influence the experimental data. This was earlier hypothesized by Wen and Ding [129], and later experimentally supported by Kathiravan et al. [178]. The CHF for water on stainless steel heater was 80% larger than CHF for water-9wt% SDS suspension. The data were then plotted along with You et al. [170], Vasallo et al. [133], Bang and Chang [161], Milanova and Kumar [136], Kim et al. [154] as shown in figure 2.23. Kathiravan at al [178] attributed the difference in CHF enhancement partly to the reduction in surface tension of water by the SDS surfactant. It is equally possible that the surfactant had scaled on the heater.

Yet there is unavoidable third reason, which is the surface oxidation. By way of measuring the contact angle on water-boiled copper surfaces, Coursey and Kim [160] demonstrated the strong effect of surface oxidation on surface tension.

The work of Kim et al. [53, 173] provides a good example for a sequence of occurrences that usually surrounds the boiling of nanofluids. In their study, nine samples of dilute nanofluids were boiled on two horizontal geometries, i.e., a flat stainless steel heater and a stainless steel wire. The surface topography and the static contact angles were measured before and after boiling experiments. Upon completion of the pool boiling tests, they found that the wettability and CHF had increased but also the heater was fouled with particles. Given in figure 2.24 are the images of wetting and surface roughness for water and water based alumina 0.01vol% nanofluid.

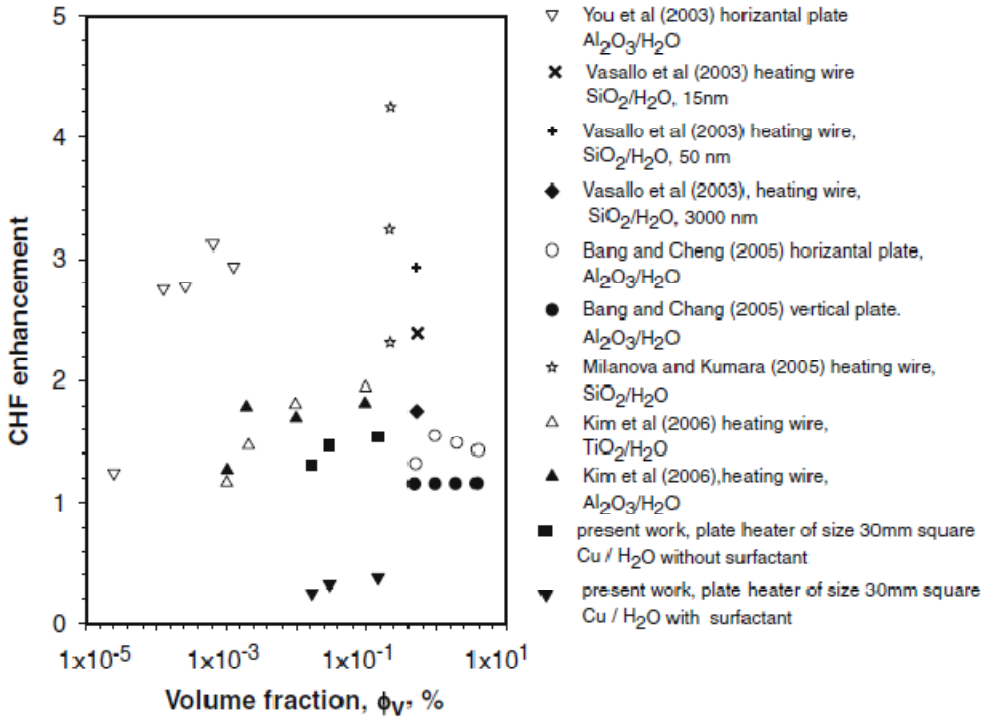

Figure 2.23: CHF data in literature. Modified from Kathiravan et al. [178]

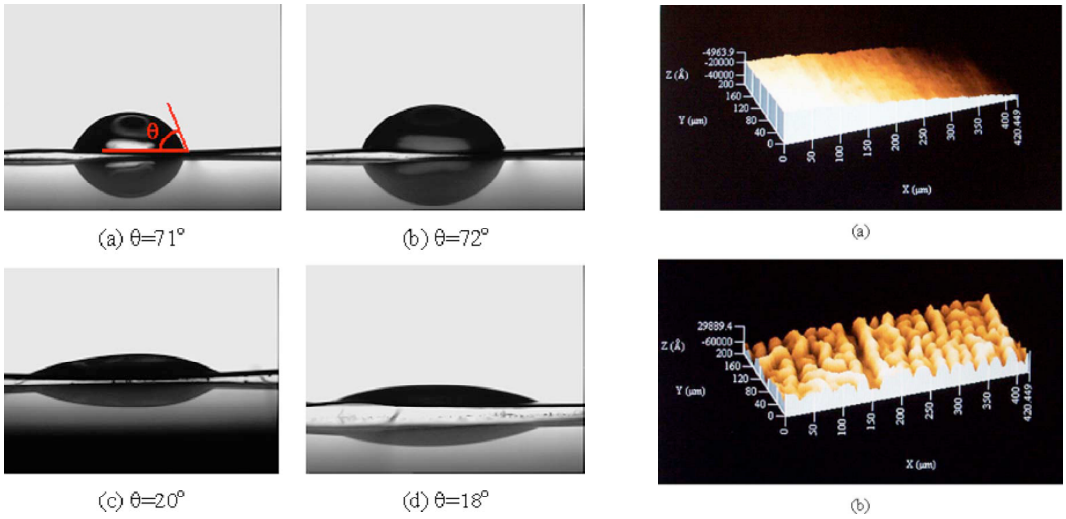

Figures 2.24: Droplets; (a) (b)-Water and aqueous Al_2O_3 on clean heater. (c)-(d) Water and aqueous Al_2O_3 on an aqueous Al_2O_3 boiled heater. Surfaces; (a)-(b)Heater after boiling water and aqueous Al_2O_3 [173]

Subsequent to experiments, the investigators [53] considered four of well established theories on boiling. Those were the hydrodynamic instability theory of Zuber [180], macrolayer dryout theory [181], hot/dry spot theory [182], and, bubble interaction theory [127]. They concluded that all but Zuber's theory sufficiently explained the nexus between experimentally obtained high CHF and the nanoparticle deposition.

In a separate study, Kim and Kim [165] boiled water on a nanoparticle-fouled NiCr wire. The CHF of water on a nanofouled heater was similar in magnitude to that for the nanofluid. They hypothesized that the key mechanism behind the CHF enhancement was capillary wicking. The porous layer produced by the deposition of nanoparticles on the heater increases the wicking action. Thus upon the departure of a vapour bubble, the liquid will easily be sucked into the dry spot, that will eventually delay dryout. This hypothesis is illustrated in figure 2.25. Furthermore it was observed that several CHFs were occurring around $\theta \sim 20°$. This led the authors to conclusion that the contact angle alone could not explain the CHF phenomenon.

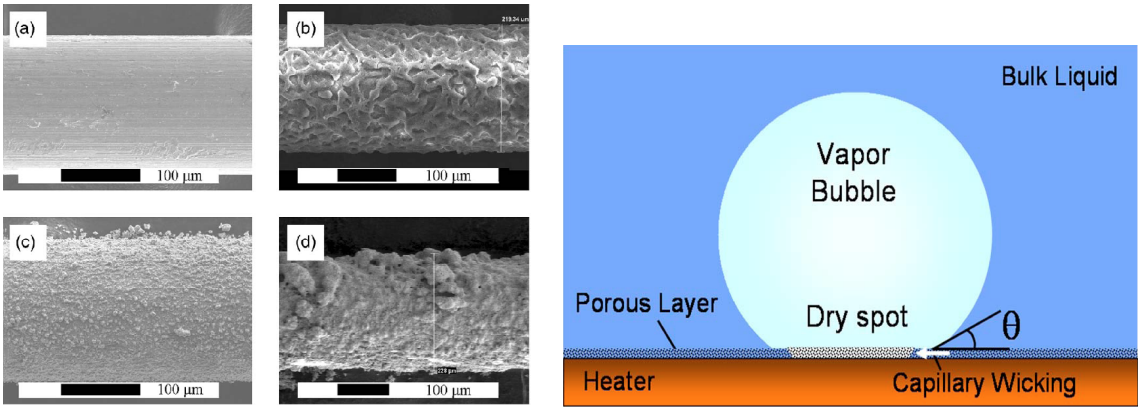

Figure 2.25: Left-(a) bare NiCr wire, (b)-(d) wire after boiling aqueous titania, silica and Ag 0.1vol%respectively. Right-Concept of capillary re-wetting during bubble growth [165]

The usefulness of zooming into the microlayer under the vapour bubble was underlined by several authors. Wasan and Nikolov [183], Sefiane [172], and Chon et al. [184] conducted studies on particle structuring under a bubble, and pinning and dryout scenarios of nanofluid droplets. More recently Kim et al. [177] revisited the microlayer and redefined its role in boiling. This time they suggested that the nanoparticle layer increases the stability of the evaporating microlayer underneath a bubble growing on a heated surface. This in turn inhibits the irreversible growth of a

dry spot even at a high wall superheat, resulting in the CHF enhancement observed when boiling nanofluids.

Kwark et al. [146] examined four mechanisms which they thought were driving the nanoparticle deposition. Their heater was a $1cm^2$ flat copper block and the nanofluid was 0.0025wt% alumina in water. The SEM imaging showed that boiling was by far the most efficient particle deposition mechanism, outweighing the settling due to gravity, natural convection and application of an electric field. Moreover the subsequent contact angle measurements yielded the smallest value for boil-deposited heaters. They extended this study to a single bubble experiment to demonstrate that the particle deposition is due to liquid microlayer evaporation underneath the bubble. A schematic view is given on figure 2.26.

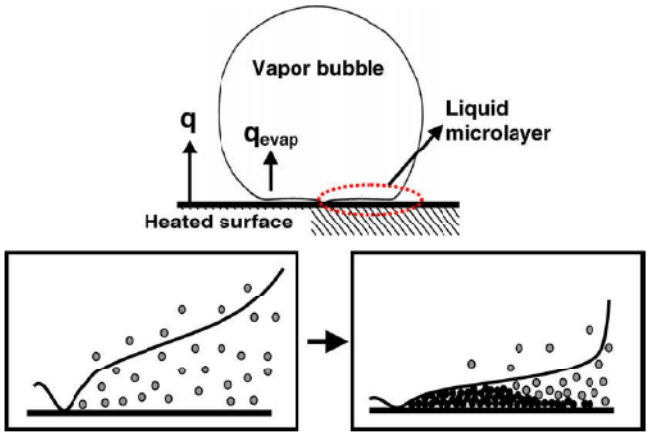

Figure 2.26: Nanoparticle deposition under a growing vapour bubble [146]

A simpler approach to explore the CHF phenomena was taken by Fokin et al. [176]. Having found their ZrO_2 nanoparticles deposited on the horizontal NiCr heater wire, they observed it under electron microscope. On SEM, they identified a layer of regularly deposited craters, each of around 20um in diameter. Zoomed in further, they found each crater was a porous matrix with characteristic macropore size and thickness of 2-5um. Investigators believed the cause for enhancement was the stable supply of liquid through this porous layer.

Oxidation of copper heaters due to boiling was explored by Coursey and Kim [160]. By boiling water on differently-oxidized heaters of four different roughnesses, they demonstrated that the level of oxidation influences the post-boiling contact angle. While recording degradation in boiling heat transfer in general, they saw that it was specifically dependent on both particle

concentration and surface-fluid wetting characteristics. Their evidence supported the claim that the wettability is a principal mechanism behind the CHF enhancement with nanofluids.

More evidence for particle-surface interaction emerged from the recent work of Suriyawong and Wongwises [167]. A 15% and 4% enhancement were respectively obtained on 0.2 µm and 4 µm rough *(Ra)* copper heaters by using 0.0001vol% aqueous titania nanofluid. But for larger concentrations up to 0.01vol%, they witnessed deterioration. With aluminum heaters of similar roughness case and nanofluids however the deterioration was always the case.

In search for the nexus between particle deposition and boiling performance, White et al. [168] boiled water and aqueous 2.3vol% ZnO nanofluid alternatively on a flat stainless steel heater. They repeated 8 cycles, as shown on figure 2.27. In the first nanofluid boil, 24.8% enhancement was recorded at 24 kW/m^2 heat flux. In subsequent runs however only the water continued to enhance, which recorded 62% enhancement at the end of 8th test. Meanwhile the AFM examinations confirmed the surface roughness was steadily increasing from 0.06 to 0.44 µm through 8 tests.

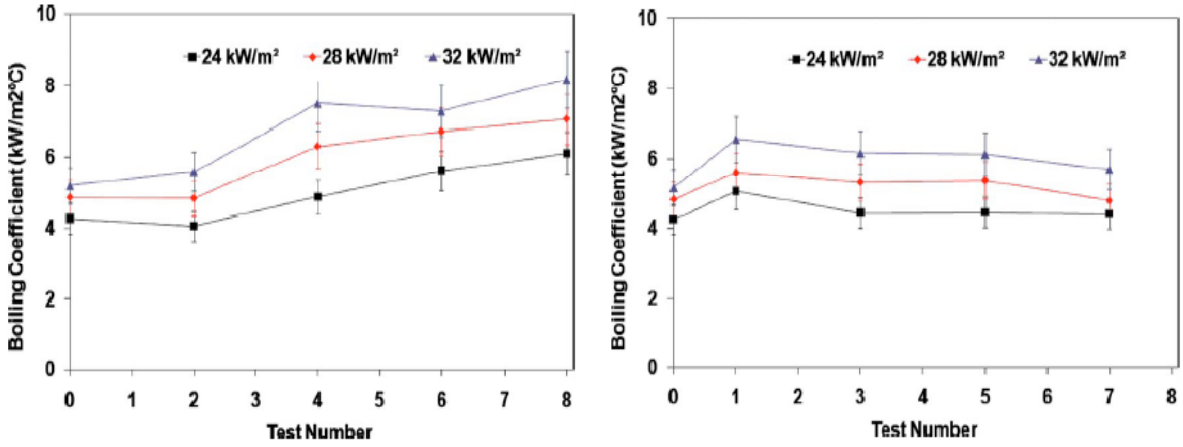

Figure 2.27: Left-alternative boiling of water, Right-aqueous ZnO nanofluid on same heater [168]

Initial enhancement shown by the nanofluid was credited to the increase in thermal properties and to the disruption of thermal boundary layer. White at al [168] speculated that the aforementioned pluses were counterbalanced in subsequent tests by the blocking of bubble transport and liquid stirring by the particles in suspension.

Heater geometry too had seemingly played an important role in decision-making on heat transfer. For example consider the experiments of Wen and Ding [129] and Das et al. [131]. Both groups boiled aqueous alumina suspensions of similar concentrations and primary particle sizes under atmospheric pressure. The heaters were stainless steel, of equal roughnesses and horizontally oriented. Ultimately the former group saw enhancement up to 10-40%, but the latter saw deterioration. Going by their reports, the only difference between the two groups was the heater geometry; which were a plate of 150mm in diameter and cylinder of 20mm diameter respectively. The question is however, was it the geometry alone or was it due to other unspecified parameters like cluster size and high temperature stability of nanofluids?

The ever changing nature of the interacting parameters and its strong influence on boiling is supported by several research articles. In one article, Kwark et al. [146] strongly suggest that the pool boiling of nanofluids can be a transient process influenced by both the duration of experiments and heat flux which in turn can affect BHT.

In spite of the fact that refrigeration is a massive industry, there have been a relatively fewer number of studies conducted on pool boiling of refrigerant based nanofluids. Kedzierski and Gong [151] examined CuO nanolubricant in R134a at saturation temperature 277.6 K. This nanolubricant was a blend of proprietary surfactant and RL68H compressor oil. A dramatic enhancement in heat transfer was recorded between 50-275% depending on the CuO concentration. Further the enhancement was found to be inversely proportional to concentration. The R141b based TiO_2 suspension was boiled on horizontal cylindrical copper heater by Trisaksri and Wongwises [143]. They reported a degradation of heat transfer for 0.05 and 0.03vol% TiO_2 concentrations. Park and Jung too had earlier reported heat transfer enhancement with water based and R22 based CNT 0.1vol% nanofluids [174]. To much of surprise, they did not observe CNT deposition on their stainless steel horizontal tubular heater. Furthermore, they claimed that they neither used a particular formulation mechanism nor added any stabilizers but “CNTs were merely added”. Few years ago, this author’s research group had observed CNTs sintered onto stainless steel heaters after boiling of water based CNT nanofluids. It was visibly different from a deposit.

Be it the role played by particle deposition with regard to nanofluids, the surface topography has its own significance in the history of boiling heat transfer. Artificial cavities, fins and structures fabricated on heaters have demonstrated varying degrees of enhancement, mainly depending on

their size, shape and number density among other parameters. This specialized branch in heat transfer engineering is popularly called enhanced surfaces [185-187]. With the introduction of MEMS technology, the length scales of these artificial structures were able to be reduced to micron and sub-micron sizes. Intuition would suggest that an artificial structure of sub-micron size would mimic a nanofluid-scaled surface to a good accuracy. Therefore it would be logical to attempt to understand the boiling phenomena of nanofluids through the investigation of carefully designed artificial cavity heater. Kim et al. [188] apparently had similar thoughts. To examine the influence of surface topography of CHF, they manufactured heaters consisting of micron and submicron-size fins. By boiling water on them, they confirmed that CHF and boiling heat transfer were superior to a plane heater.

Consider figure 2.28 which shows two CNT arrays produced in laboratory on a silicon chips of 1.27x1.27mm^2. This was work of Ujereh et al. [142]. On pool boiling with FC-72 liquid, they observed the heat transfer and CHF enhancements up to 450% and 45% respectively. They further claimed that the degree of enhancement was related to the roughness of bare surfaces.

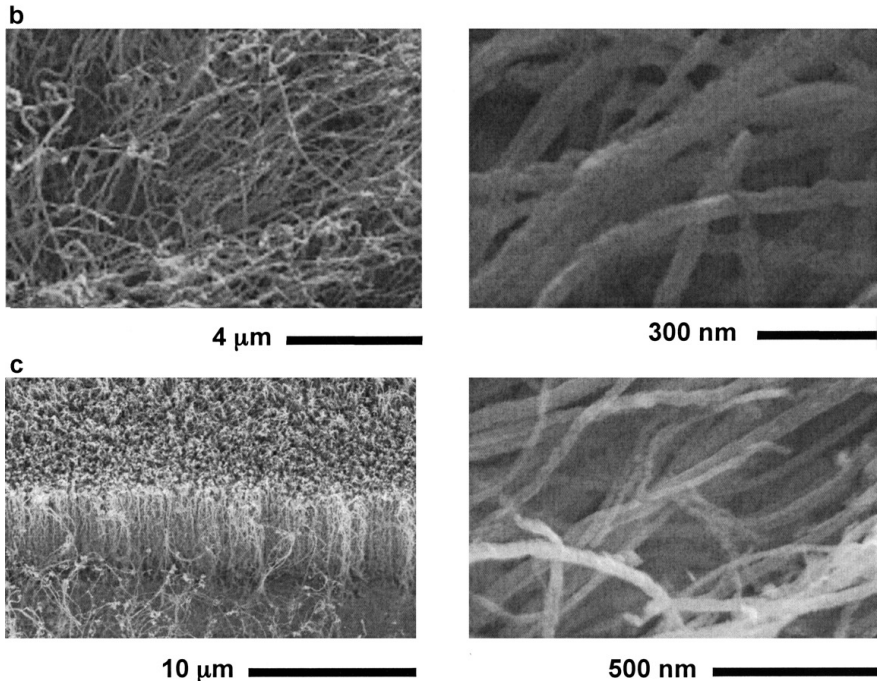

Figure 2.28: SEM images of Silicone surface coated with (b) light and (c) dense CNT array [142]

Controlled nanoparticle deposition on heaters is an evolving technology. Kwark et al. [189] used their experience in nanofluids boiling to produce controlled alumina nanocoatings on copper

heaters. In doing so, they manipulated boiling duration, heat flux, and nanoparticle concentration. The longer the boiling duration, they found the thicker the coating, and higher the surface wettability was.

In this sense, a remarkable contribution the boiling of nanofluids has made to the heat transfer science is the exposure of nexus between nanoscale particle deposition and enhancement. Thus far the smallest length scales of artificially enhanced surfaces were in the order of few microns. With the recent nanofluids experiences, the sizes have pulled it further down to sub-micron levels as illustrated by foregoing discussion.

Having reviewed the existing literature on this topic, the following discussion is an attempt to build a relationship between boiling of nanofluids and classical bubble nucleation theory.

For pool boiling of water on a vertical heater, Wang and Dhir [190] correlated the nucleation site density n'' to microcavity density N_c through wall superheat and contact angle as given in equation 2.19. Accordingly a reduction in contact angle would reduce n'' in turn.

$$n'' \propto N_c (1-\cos\theta)(T_w - T_{sat})^6 \qquad \textbf{Eq 2.19}$$

On the other hand, the classical boiling heat transfer correlation of Mikic and Rohsenow [191] given in equation 2.20 expresses a relationship between temperature, fluid and surface properties, and heater geometries and heat transfer.

$$q'' = 2\left[\pi (k\rho c)_l \, f\right]^{1/2} . A . d_b . n'' . (T_w - T_{sat}) \qquad \textbf{Eq 2.20}$$

The term $k\rho c$ of the base liquid does not significantly change for a nanofluid for small particle loadings. For a given wall superheat therefore, the heat flax q'' may then be expressed in terms of bubble frequency f, bubble departure diameter d_b and n'', for a given surface area A. Finally the boiling heat transfer coefficient correlates it all.

$$h = \frac{q''}{(T_w - T_{sat})} \sim F(f, d_b, n'') \qquad \textbf{Eq 2.21}$$

Experimental observations reported in the literature supports this hypothesis. There is evidence for particle deposition (which reflects n''), bubbles getting larger in departure (d_b) and the frequency decreasing (f) for nanofluids.

2.6.1. Summary of section 2.6

The forgoing discussion convincingly stands for the fact that the boiling behaviour of nanofluids is dictated by the particle loading, liquid properties and surface-liquid interactions. While a plausible amount of work has been done to advance the understanding of the boiling behaviour of nanofluids, still there are valid questions to be answered. What will be the scenario for common coolant like ethylene glycol? What will happen with non-circular nanoparticles? Will the particle dynamics change at elevated temperatures? Does the classical boiling theory hold at sub-micron cavities on nanofouled surface? Answers will be sought in this thesis.

2.7 Boiling on artificial cavities

A vapour bubble may initiate on a surface or in a liquid body itself. These events are respectively called heterogeneous nucleation and homogeneous nucleation. For either event to occur, the liquid should attain the bubble nucleation temperature. In heterogeneous nucleation, this temperature is characterised by the liquid microlayer temperature, which is related to the bubble radius. Classical Young-Laplace (Y-L) equation correlates the balance of forces that is necessary for a bubble to exist.

$$\Delta P = \frac{2\sigma}{r} \qquad \textbf{Eq 2.22}$$

The pressure difference between inner and outer sides of the bubble is denoted by ΔP, σ is liquid surface tension, and r is the radius of bubble in equilibrium.

It has historically been known that the surface cavities support heterogeneous nucleation by way of offering the vapour trapped in them. For the first time, Griffith and Wallis [192] developed a formula to calculate the superheat (ΔT) needed to maintain a stable bubble-producing cavity. They did it by combining the Y-L equation with Clausius-Clapyron equation.

$$\Delta T = \frac{2\sigma . T_{sat}}{h_{lv} . \rho_v . R} \qquad \textbf{Eq 2.23}$$

where R is the mouth radius of a conical cavity, h_{lv} and ρ_v are respectively the latent heat of vaporisation and vapour density.

For better understanding of the heterogeneous nucleation and to test the existing theories, numerous efforts had been made in the recent past. The work of Kant and Weber [193], Rule and Kim [194], Yin et al. [195], Demiray and Kim [196], Shoji and Takaji [197], Zhang and Shoji [198], Rammig and Weiss [199], Son et al. [200], Qi and Klausner [201-202], Siedel et al. [203], Wagner and Stephan [204], Moghaddam and Kiger [205], and Hutter [206] are a few to name. They fabricated artificial cavities of several sizes, typically below 100 µm, and shapes on metal and silicon surfaces. The smallest cavity that has been reported was 0.7 µm [205].

2.7.1 Cavity fabrication methods

Following is a brief overview of the cavity fabrication methods employed by experimentalists.

2.7.1.1 Lithography

This is a chemical process of removing selected areas from a substrate. Steps involved in the lithography are the surface preparation, application of the photoresist, alignment of the mask and substrate, and the exposure and developing. A schematic of the process is given in figure 2.29.

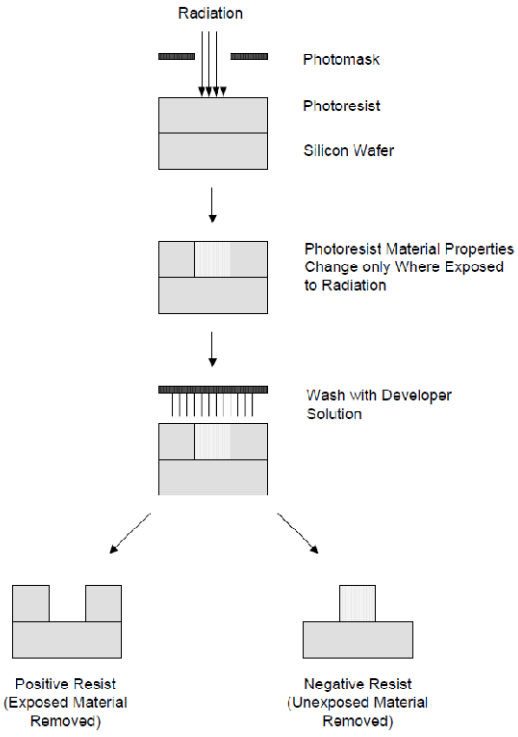

Figure 2.29: Lithography process

The fabric of structures that needs to be obtained on the photoresist has to be designed separately. The design will then be transferred onto a photo mask. By appropriate exposure of the photo mask to high energy radiation, the structure will be obtained.

2.7.1.2 Etching

There are two etching techniques, the wet etching and the dry etching. In the former the masked substrate is immersed in a chemical solution whereby the exposed material is dissolved. This dissolution happens along the crystallographic planes. The depth of cavity can be controlled by manipulating the etching duration. In the latter, the material is removed using reactive ions or vapour phase etchant. This is the preferred technique to obtain deeper and narrower cavities. Nevertheless the two methods have their own limitations for cavity sizes and shapes.

2.7.1.3 Micromachining

Lithography and etching are chemical methods of selectively removing the materials. The oldest method of metal removal is however the direct machining. The invention of focus ion beam device (FIB) has made it possible to fabricate tiny sub-micron cavities of desired sizes and shapes. FIB systems operate in a similar fashion to a scanning electron microscope (SEM). The difference is the FIB uses a beam of ions to etch the surface, in contrast to SEM using a beam of electrons to image the surface. The FIB often comes as a plug-in column to SEM. In a FIB operation, the SEM serves the purpose of visualizing the region which is being machined using FIB.

2.7.2 Boiling phenomena on small cavities

Nucleation and site interaction are two vital parameters in boiling. For example, Bhavani et al. [207] showed that bubble coagulation near the surface resulted low CHF and hence it should be avoided. To explore this further, let S and D to assume the cavity spacing and bubble departure diameter respectively. The ratio S/D has proved to be a crucial factor for boiling stability. Water boiling experiment by Chekanov [208] demonstrated that $S/D < 3$ or > 3 determines inhibition or promotion of nucleating the neighbouring cavity. Judd and co-workers [209-210] conducted series of experimental investigations to conclude that $1<S/D<3$ is inhibitive to the neighbour. Kenning and Yang [211] claimed that nucleation sites located within one bubble radius of each other $(S=D/2)$ interacted through fluctuations in wall temperature caused by bubble growth.

In contrast to the historical belief that bubbles would only originate from vapour trapping cavities, Qi and Klausner [202] and Theofenous [182] demonstrated that they are the preferred locations

for nucleation but not the exclusive. In a more recent study, Qi and Klausner [201] fabricated an array of cylindrical cavities on a silicon substrate. For boiling of water, they found that the wall superheat required to activate cavities was twice that predicted by Griffith and Wallis (Eq 2.23). They estimated the substrate temperature by one-dimensional extrapolation of data from a series of thermocouples fixed underneath. The accuracy of such extrapolation is however questionable as the highly thermal conductive silicon would rapidly spread the heat in a two-dimensional space making a nonlinear temperature distribution. Moghaddam and Kiger [205] moved closer to liquid microlayer by a novel design of temperature sensors. Their artificial cavities were 0.7, 1.3 and 2.4µm in diameter. By boiling FC-72, they convincingly reproduced the bubble cycle and hypothesised the heat transfer mechanisms in the neighbourhood. Unfortunately Moghaddam and Kiger's report falls short of pinpointing to a given cavity and its activity but rather gives a generalised view.

Kenning et al. [212] presented an update of recent advances in boiling investigations. As a part of it they reviewed the near-surface temperature measurement techniques of liquid crystals and IR thermography. It was pointed out that the measurement of temperature on the back side of the heater associates sizable errors. On one hand, there is a time delay between the event and the measurement. In addition, the lateral heat dissipation will occur along the heater. Thinner heaters would reduce the magnitude of the errors to some extent, although there are practical limitations to the minimum thickness. Figure 2.30 represents a typical image of a bubble activity produced by an IR camera. This image was produced by Wagner and Stephan [204] for pool boiling of FC-3284 liquid on a single nucleation site.

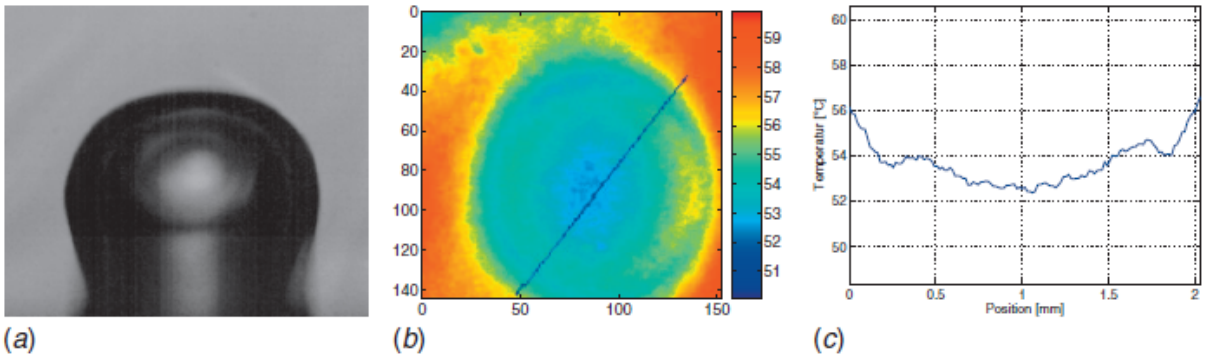

Figure 2.30: (a) a growing bubble, (b) IR image, (c) temperature profile across the bubble [204]

Furthermore on the use of IR thermometry, Golobic et al. [213] enhanced the strength of signals by providing a thin black layer of high emissivity between the IR camera and boiling surface. Geradi et al. [214] deposited a thin Indium-Tin-Oxide (ITO) layer on a 0.4mm thick sapphire substrate. They boiled water on it and used IR thermometry to record temperatures on the back side of sapphire. The IR transparency of sapphire and, thinness and IR opaqueness of ITO helped the investigators to accurately read the IR signals emitted by the ITO heater.

2.7.3 Summary of section 2.7

Knowledge of near-wall activities are of utmost importance in resolving the mechanism of heterogeneous bubble generation and growth. Until recent past the main challenge was to find means to reach this tiny and highly sensitive region and to do measurements without disturbing it. Then the Infrared (IR) thermometry was applied and considerable progress has been made. However all these efforts ended up at the back of the boiling surface at best but never crossed it though to the liquid side, where the microlayer exists. There is a need to fill this gap in research.

2.8 Small angle x-ray scattering (SAXS) for nanofluids

X-rays are electromagnetic radiation occupying the range of 0.01 to 100 Ă in wavelength. A lengthscale of around 1 Ă is of the same order of magnitude as the interatomic distances of most materials. This makes X-rays a perfect tool to study fine interior like the arrangement of atoms in matter. Therefore x-ray scattering falls within the range of technologies that are capable of visualizing nanoparticles and clusters. Recall the schematic view given in figure 2.10.

The principle of x-ray scattering works as follows; Imagine a sample irradiated with a carefully-collimated beam of x-rays. These x-rays will collide with the atoms and molecules in the sample and scatter as illustrated in figure 2.31. The resulting intensity as a function of scattering angle (2θ) on a detector contains the information on the structure of the solid objects in the sample.

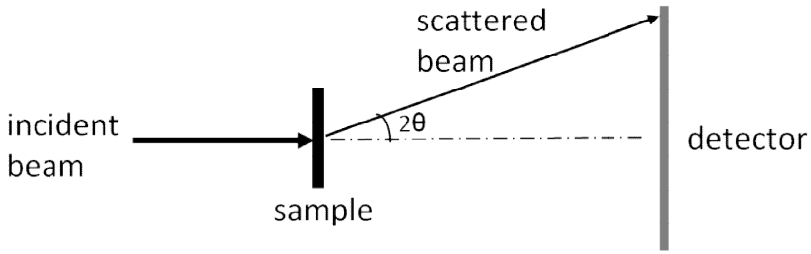

Figure 2.31: Scattering on a sample and detection

Bragg's law correlates the scattering angle, wavelength (*λ*) and the scattering lengthscale (*d*).

$$\lambda = 2d.\sin\theta \qquad \textit{Eq 2.24}$$

Typical to small angle scattering is 2θ< 2°. For an x-ray beam of λ=1 Ă, this setting will make it possible to see structural changes in lengthscales in the order of 2.9nm. Far smaller distances can be viewed by increasing the angle where the scattered beam is captured. That arrangement is called the wide angle scattering.

For scattering experiments, a scattering vector *q* is defined [35]. Assume two unit vectors for incident and scattered beams *S* and S_0 respectively. Then *q* becomes

$$q = \frac{2\pi}{\lambda}(S - S_0) \qquad \textit{Eq 2.25}$$

Recall that the angle between *S* and S_0 was 2θ. This leads to a very important scattering equation.

$$q = \frac{4\pi.\sin\theta}{\lambda} \qquad \textit{Eq 2.26}$$

Now the equations 2.24 and 2.26 yield the relationship between *d* and *q*.

$$d = \frac{2\pi}{q} \qquad \textit{Eq 2.27}$$

The main advantage in SAXS over electron microscopy is its ability to provide information on 3-D structures. In comparison to other light scattering techniques, the SAXS is a faster and more powerful tool. Once a sample is exposed to SAXS and data acquired, it is post-processed using standard data analysis algorithms to obtain fine details about interior of the sample. SAXS is therefore widely used to determine the shape and size distribution of particulate systems

[215-220]. An example is given in figure 2.32 where experimental SAXS data on titania powder is fitted with established models. The abscissa is marked with scattering vector q, and the ordinate represents the scattering intensity at the corresponding angle 2θ averaged over the chosen period of experiment. Information on particle size and shape are extracted from the nature of curve-fitting. For dense suspensions however, the interparticle interference comes into effect. The data analysis is more tedious and often needs to be solved using Monte Carlo methods [35].

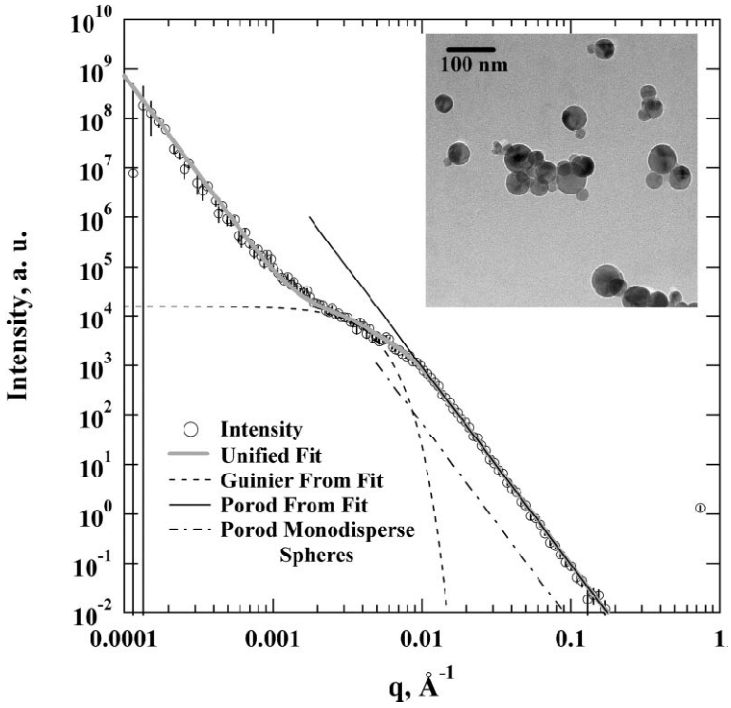

Figure 2.32: Curve-fitting on experimental SAXS data [217]

Figure 2.33 depicts another example for curve-fitting to SAXS data obtained for colloidal gold nanoparticles of 5-100nm in size. The investigators [220] then compared it with size measurements obtained from hundreds of TEM images. They claimed to have obtained the mean size of nanoparticles within 10% error by means of the slope of Guinier plot, when the particle size distribution was narrow.

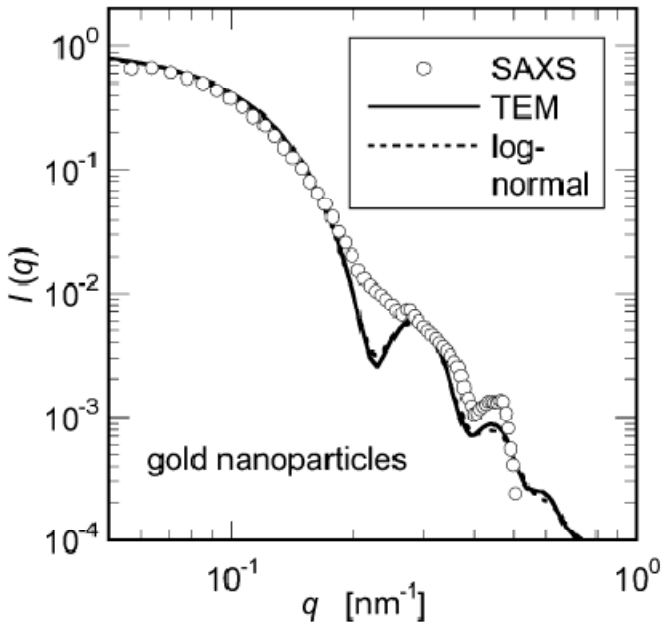

Figure 2.33: Curve-fitting on experimental SAXS data [220]

A direct application of SAXS in nanofluids was conducted by Chen et al. [80]. They used SAXS facility at Argonne National Laboratory to characterize SiO_2 nanoparticles suspended in water with the aim of finding the relationship between the particle size distribution and nanofluid's thermal conductivity. It was shown that the experimental data for 0.02vol% SiO_2 –water sample closely followed the maximum entropy algorithm for SAXS curve-fitting. The size data thus extracted were in good agreement with DLS data. Furthermore their work provided convincing evidence that the relative thermal conductivity of SiO_2 16vol%-water nanofluid increased with the particle size.

There has been an attempt by Lurio [221] to analyze Al_2O_3-ethylene glycol nanofluid using SAXS. The size of primary nanoparticles was 51nm. For a populated suspension of 5vol% Al_2O_3, they found a clear peak in the *I vs q* plot, which they interpreted as an indication of the presence of attractive forces between nanoparticles. Further details of the study were not given.

Analysis of SAXS data is often done by separation of the data plot into several regions such as Guinier, Debye or Porod, and 1/q regimes. One example was shown in figure 2.32. To elaborate

these regimes further, consider figure 2.34. It is important to note that the complete curve may not emerge from one single experimental setup and on one sample.

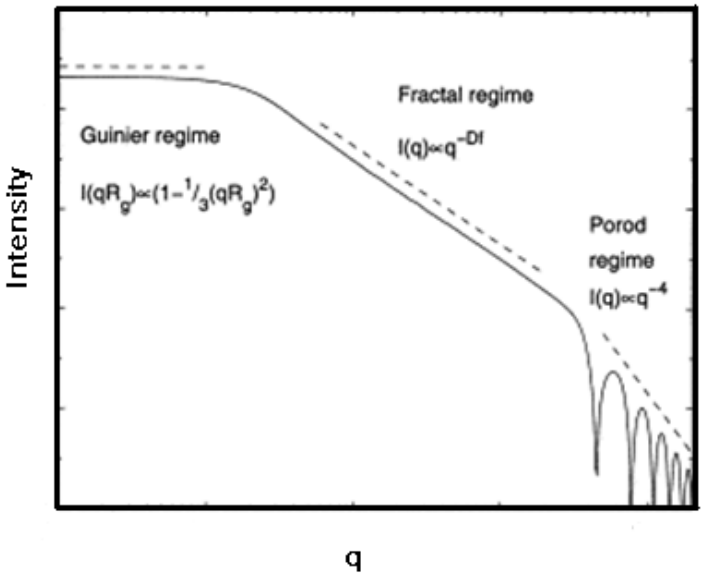

Figure 2.34: Regimes likely in a SAXS data plot

For example, if there are no primary particles present in the system, the right-most part (Porod regime) of the curve might miss out. The Guinier region gives the size information. Slope of the Guinier plot of *log (I) vs* q^2 is equal to one third of the radius of gyration of the objects. The shape information is contained in the Debye or Porod region [35, 215, 222]. Value of the slope of the curve of *log (I) vs log (q)* in this region indicates if the object is a surface or mass fractal, a branched aggregate or a cylindrical chain etc.

2.8.1 Summary of section 2.8

SAXS is a well established and powerful technique to analyze particle size and morphology. Its usage in exploring the heat transfer mechanisms of nanofluids has been very limited so far. The technological constraints associated with electron microscopy and light scattering underlines SAXS as a useful tool for nanofluids. Electron microscopy can handle dry samples. Light scattering can handle wet samples but the power of beam is limited and the measuring timescales are large in comparison with the dynamics of particles in liquids. It was stated in sections 2.4-2.6 that particle aggregation is likely to govern the thermal behaviour of nanofluids. The aggregation time constants are often small, although it is significantly influenced by the pH of suspension [93]. To

this end, the SAXS could be a versatile technique for in-situ investigations of particle structuring and morphological evolutions.

2.9 Summary of the chapter

From the foregoing review of literature, the following summary can be derived.

I. Thermal conductivity of nanofluids is likely to be mainly driven by nanoparticle aggregation in the liquid. There appears to be a nexus between the degree of enhancement and the extent of aggregation. The size, shape and the alignment of aggregates are thought to be key parameters in this regard, backed by evidence from computer-based modeling and limited experiments. Microscopy and light scattering were the popular experimental techniques. However their capabilities were insufficient to capture the aggregation kinetics of nanoparticles. Therefore there is a gap of knowledge, which needs to be filled by using a more powerful tool.
II. The boiling heat transfer behaviour of nanofluids is supposedly driven by particle deposition or sintering on the heater. As a consequence of deposition, microstructures develop on the heater which in return alters the bubble nucleation and wetting dynamics. Shapes and sizes of cavities in the microstructure and the thickness of deposition are likely to depend on the type of nanoparticle and also the boiling duration. All these parameters will have influence on the boiling heat transfer shown by a nanofluid. Water based nanofluids have been examined for boiling heat transfer in the past. Particle deposition had been widely reported and changes in surface roughness had been observed. The issue however is the inconsistencies in the enhancement/degradation pattern. Therefore a vacuum exists for a credible relationship between the boiling behaviour and changes in surface roughness of the heater.

The previous two paragraphs demonstrate that the thermal behaviour of nanofluids is more complicated than forecasted at the outset of nanofluids research. Instead of being dependent on one particular property, a nanofluid's thermal behaviour is a summation of several parameters such as the type and shape of nanoparticle, the type of base liquid and also the heater properties when it comes to boiling. As far as thermal conductivity and rheology are concerned, particle structuring in form of aggregates apparently plays a major role. It is worthwhile at this stage to recall from classical boiling theory that the thermal conductivity and rheology are key stakeholders in boiling heat transfer.

While acknowledging the possible challenges that one may face in filling the knowledge gap associated with thermal behaviour of nanofluids, the following methodologies are proposed to address the concerns outlined in I and II above as identified from the literature review.

- Series of systematic experiments on boiling heat transfer should be conducted with nanofluids at the laboratory scale. For these experiments the types of nanofluids and surfaces are to be carefully chosen to fill the gaps in knowledge highlighted above. Spherical nanoparticles, tubular nanoparticles and acicular nanoparticles are suggested. For the base liquid, water and water-ethylene glycol mixture are proposed. Despite the fact that the latter is widely used in the industrial cooling applications, it has not been examined for boiling as a nanofluid to the knowledge of this author. Vapour bubbles are to be recorded using high speed videography with the expectation of determining the bubble size which will later be related to surface parameters. Moreover the surface roughness and solid-liquid contact angle are to be measured before and after boiling the nanofluids.
- Rheological behaviour and thermal conductivity of the nanofluid samples prepared for boiling are to be measured respectively using the transient hot wire technique and rotational rheometer in the laboratory. This task is aimed at characterizing the samples.
- To move beyond microscopy and laboratory-scale light scattering techniques in order to visualize and calculate the aggregation kinetics of nanoparticles in suspended state, the small angle x-ray scattering techniques are proposed. These techniques are available on competitive basis at the synchrotron facilities of Daresbury Laboratory and the Diamond light source in United Kingdom.
- Pool boiling of liquids at micro and nano scales should be examined to mimic boiling on a nanoparticle-scaled heater. Moreover it will clear the doubts of the validity of classical boiling correlations on micro and nano scales. To face the challenge of accurate capturing of temperature of the liquid microlayer, infrared thermometry is suggested. Submicron cavities are to be manufactured on ultrasmooth substrate, followed by pool boiling at optimal cleanliness.

The literature review chapter winds up at this point.

CHAPTER 3 - Results & Discussion I

Materials and Methods

It was stated at the outset of this thesis that the boiling of nanofluids is a complex phenomenon that involves several parameters. In a subsequent literature review, the gaps in knowledge were identified. To shed sufficient light to further research, there is a need for a multi-dimensional approach. As much as close examination of nanofluid-boiled surfaces, it is important to conduct research on nanoscale boiling phenomena and the effect of particle aggregation and deposition in boiling. This identifies three research fronts, namely, surface examination of nanofluid-boiled heaters, in-situ study of nanoparticle aggregation in liquids using SAXS, and boiling of liquids on sub-micron size cavities. The research question was therefore established. The focus of this chapter is to present materials and methods employed in the forthcoming experimental work. The presentation is arranged as follows.

Formulation methods for stable nanofluids are discussed at the beginning. The samples are then characterized along the lines of thermal conductivity, rheology and viscosity, and wetting and spreading with descriptions of related techniques and instruments. To illuminate the discussion, newly acquired experimental data and analysis are brought forward. Presented lastly are the experimental facilities where these nanofluids are going to be used. These are the synchrotron radiation facility at Oxford, the pool boiling facility in Leeds, and the artificial cavity facility at MIT where this author was affiliated to as a visiting researcher on a boiling heat transfer collaboration program.

3.1 Formulation of Nanofluids

A nanofluid is by definition a stable suspension of nanoparticles. Being a two-phase system consisting of a dense and relatively less-dense media, there is a high probability for a nanofluid to break down to particle and liquid phases with time. The time could be shorter if the particle material and the host liquid react with each other to make compounds and hence change solution chemistry. A common example is alumina nanoparticles (Al_2O_3) reacting with water and creating aluminum hydroxide. What follows is the aluminum hydroxide changing the pH of the nanofluid. If the pH change is towards the iso-electric point (IEP), then the collapse of nanofluid is faster. The age of the sample is therefore a critical parameter when describing the stability of a nanofluid.

The formulation procedure broadly consists of a number of stages. They are the addition of nanoparticles to the base liquid, introduction of dispersant, mechanical actions such as milling, magnetic stirring, homogenization, ultrasonication, and lastly, the ionic strength and pH adjustment. The duration and the sequence of events may differ from one nanofluid to the other. As a result the formulation details are often unique for a given nanofluid.

3.1.1 Titania nanofluids

Anatase Titania (TiO_2) nanopowder was commercially purchased from Degussa Inc, Germany (currently known as Evonik Industries). The primary particle diameter and shape were described by the supplier as 25nm and spherical. The scanning electron microscopy (SEM) and Transmission electron microscopy (TEM) images of this nanopowder were taken using LEO 1530 FEGSEM and Philips CM200 FEGTEM devices. Featured in figure 3.1 (and also in Appendix A), the images demonstrate that the particles were in aggregates, slightly polydispersed and somewhat spherical in shape. Recall that the electron microscopy requires a nanopowder to be suspended in a liquid and dried at the time it goes to imaging. This is different from a dried droplet of a stable nanofluid.

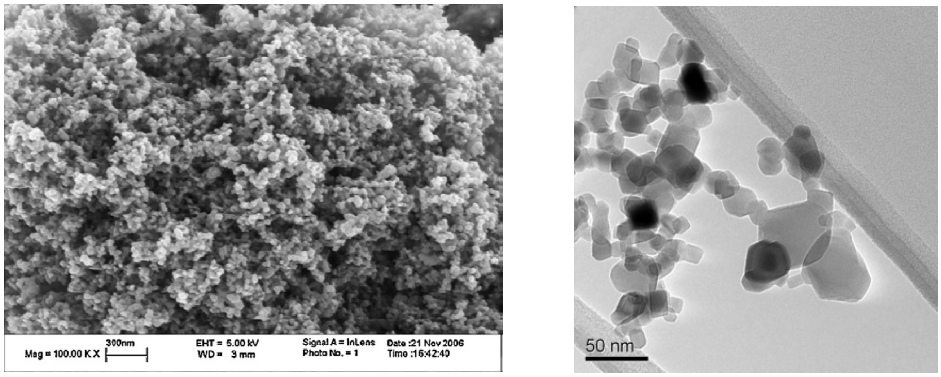

Figure 3.1: Titania nanoparticles

The aim was to prepare two samples of TiO_2 8wt% concentration in distilled water, and in distilled water 75wt%-ethylene glycol 25wt% (WEG25). A dense suspension can later be diluted as desired by addition of base liquid followed by quick processing. The ethylene glycol was purchased from Alfa Aesar with a guaranteed purity of >99%. Step one of the formulation process was to add the measured quantity of Titania nanopowder to liquid. Health and safety regulations require the nanopowder to be handled in a fumehood. The IEP plays the key role in electrostatic stability. A Malvern MPT-2 autotitrator was used to measure the IEP of TiO_2 particles. The titration curve given in figure 3.2 shows the IEP occurring near pH=5.9. This is in agreement with the literature,

for example [58, 223-224], where the IEP lies between pH=5.5 and 6.5 in the absence of an electrolyte.

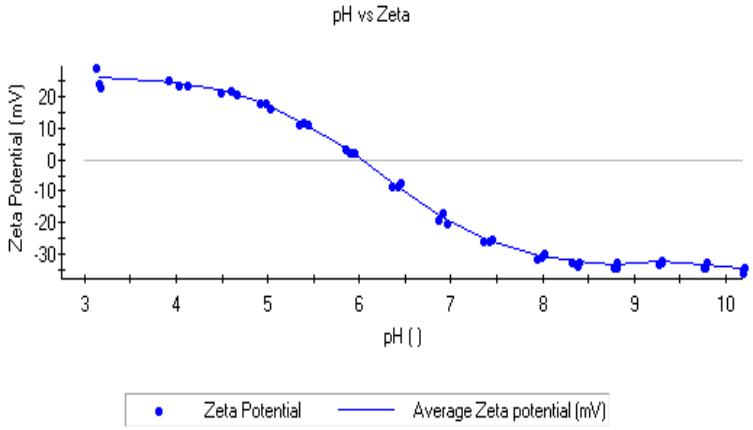

Figure 3.2: Zeta potential of Titania-water nanofluid

Titania particles as soon as added to the base liquids take the form of bulk granules. Magnetic stirring and homogenization are insufficient to break them apart. The proven technique to achieve smaller particles is the wet milling. The titania nanofluids were milled in the laboratory by a Dyno Multi-Lab Mill (*supplied by Willy A Bachofen, Switzerland*). Continuous milling of the 8wt% suspension was conducted while the particle size was measured at regular intervals. To prevent aggregation while milling, the pH of solution was maintained at 10.5 throughout.

The particle size measurements taken by Malvern Zetasizer-nano are given on figure 3.3. This device works on the light scattering principle. The nanofluid sample had to be very dilute for the measurements to be accurate. Particle size reduction by wet milling was fairly quick. SEM image of this nanofluid is presented in figure 3.4.

The stability of a sample is usually determined by the eye observation. Accordingly the titania nanofluids shown here were stable for a long time. Typically they did not show a visible separation for three months from the date of formulation. It should be noted that there was no surfactant or dispersant used in the formulation process.

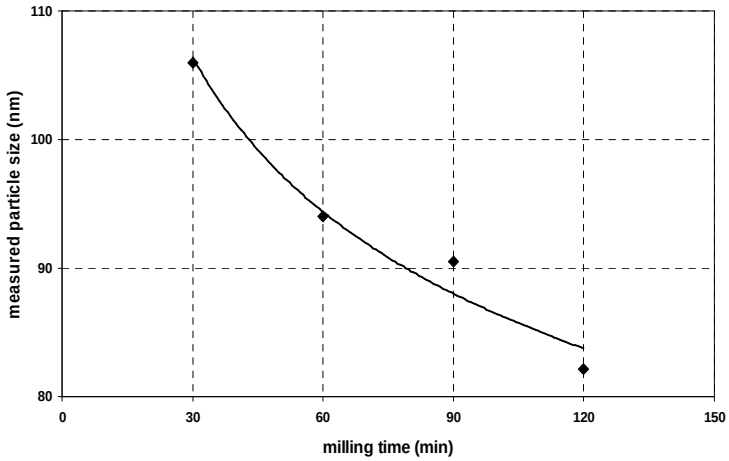

Figure 3.3: Wet milling of Titania-WEG25 nanofluid

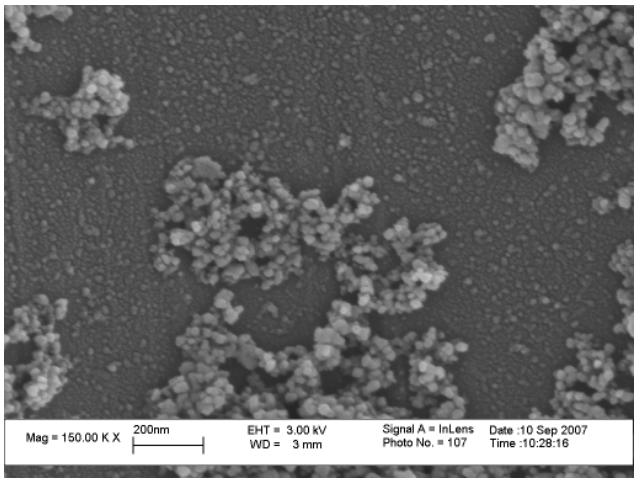

Figure 3.4: Titania-WEG25 nanofluid

3.1.2 Alumina nanofluids

Water-based, ethylene glycol (EG)-based and WEG-based alumina nanofluids were formulated for boiling experiments. Nanoparticles were of spherical and acicular shapes. The spherical particles were purchased from Nanophase Inc USA, as a dry powder of 45nm in size. Sasol Inc USA supplied acicular alumina particles (Dispal X-0, Lot V1326-23-1) having an aspect ratio (length:diameter) of approximately 10, as estimated from electron microscopy images. Corresponding TEM images are

given in figure 3.5 (see also Appendix A). The spherical particles were astonishingly polydispersed. The acicular particles were however in better agreement with the specified dimensions.

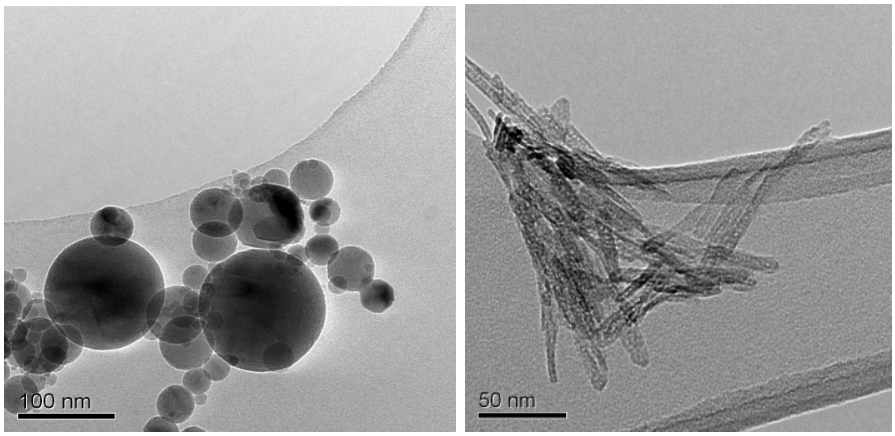

Figure 3.5: Alumina nanoparticles; Left-spherical, Right-acicular

Concentrated suspensions of alumina 8wt% in liquids were to be formulated. After adding the measured quantity of nanopowder to the base liquid, the mixture was magnetically stirred at room temperature for two hours. With reference to the titration curve in figure 3.6, the alumina suspensions should be stable on the acid side. This coincides with previous experience where alumina nanofluids were at pH7. In the present work therefore the samples were brought to pH7 while being stirred.

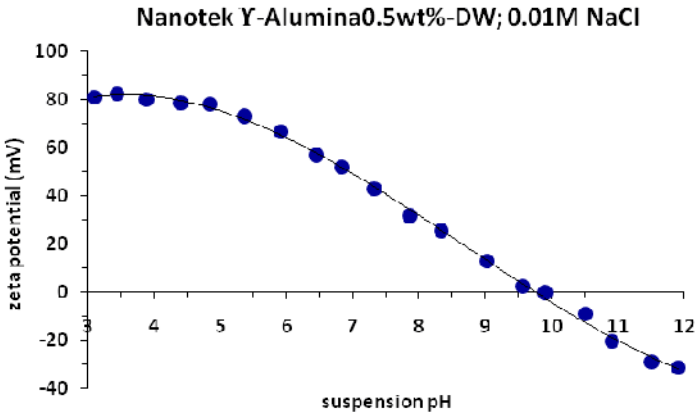

Figure 3.6: Zeta potential of Alumina nanoparticles

The samples were then transferred to an ultrasonic bath and sonicated continuously for 24 hours. For spherical particles, the size measurement was conducted using a Malvern Zetasizer-nano. An example of size distribution is given in figure 3.7. On four measuring cycles on this sample, there

is one repeating peak around 134.1nm. The intensity-averaged particle size was 147nm. Comparison of this size data with the TEM image in figure 3.5 suggests that the nanoparticles were in clusters in the suspension.

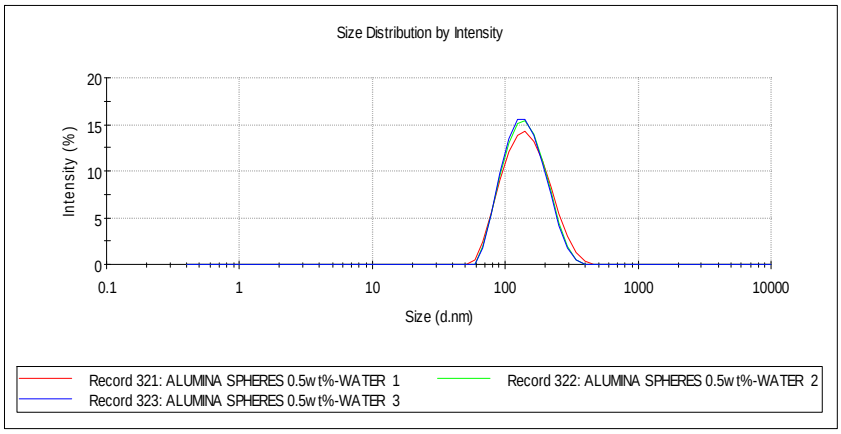

Figure 3.7: Size distribution of spherical Alumina-water nanofluid

These alumina nanofluids were stable for a few months. However alumina is known for its reactivity with water. A separate investigation of this aspect demonstrated that the suspension pH was gradually changing over the time.

3.1.3 Carbon nanotube (CNT) nanofluids

The formulation method for water and ethylene glycol based carbon nanotube nanofluids is disclosed. Multi-walled carbon nanotubes (MWCNT) were supplied by Nanocyl Inc Belgium as a dry powder. The aspect ratio was stated as 150. TEM images shown in figure 3.8 indicated the diameter of nanotubes was in the order of 10-15nm. However the lengths are not clearly measurable on these images.

The formulation procedure for CNT nanofluids was significantly different from titania and alumina nanofluids. It had a pre-processing stage where the nanopowder was ultrasonicated overnight and rinsed subsequently with acid. The ultrasonication was aimed at breaking dry agglomerates, which were expected to be considerable due to the length of tubes. Rinsing helps to remove amorphous carbon in the powder and to clean the tube surface by removing loosely bonded impurities.

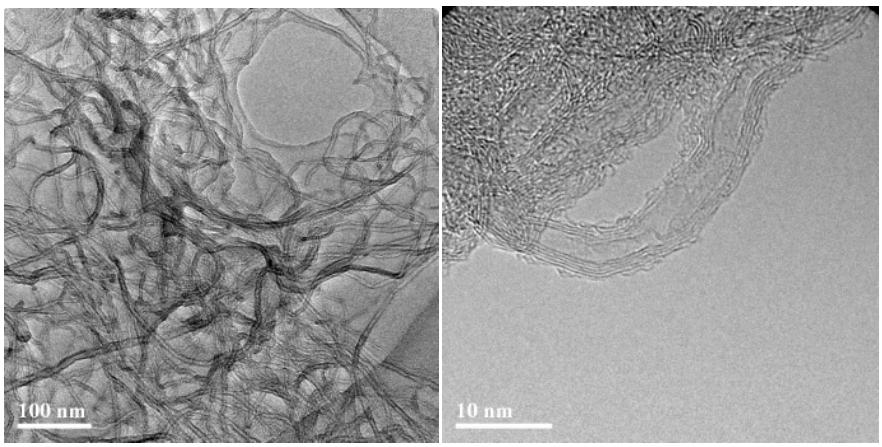

Figure 3.8: Multi-walled Carbon nanotubes

The sonicated dry nanopowder was measured into a beaker and was submerged in acid by adding 0.1M HNO_3. The impurities were soon emerging from the powder and reached the liquid surface. After a few minutes the solution was gently stirred to enhance the cleaning of tubes. The acid was carefully poured away along with the suspended impurities. In this process a dilute acid was chosen to prevent acid damage to the nanotubes. The SEM image on figure 3.9 confirms that the nanotubes appeared to be mostaly intact even after the acid treatment.

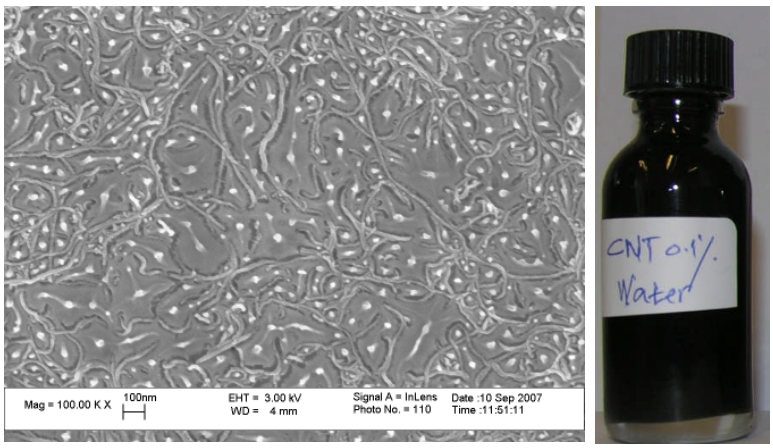

Figure 3.9: Aqueous MWCNT nanofluid

After ultrasonication and rinsing of nanotubes, they were added to the base liquid along with the surfactant Gum Arabic. CNTs are known for agglomeration due to their shape and length. Hence a surfactant was necessary to keep the nanofluid stable. However to minimize the surfactant's impact on boiling experiments, the added amount had to be kept at a minimum. Experience has shown that 0.25wt% of gum Arabic was sufficient to stabilize CNT nanofluids. The mixture was

then transferred to a vessel fitted with an IKA Turrax T25 device for mechanical stirring, also called high shear homogenizing. Recall that the suspension was still slightly acidic. An acidic atmosphere was desired to facilitate the surfactant to coat the nanotubes while being mechanically dispersed. It was understood that 20minutes of homogenization at 14500rpm was sufficient to disperse the nanotubes. Adjustment was made to the pH of the sample to 7 and sent to storage. A picture of the nanofluid is given in figure 3.9. These MWCNT nanofluids were stable for at least 6 months. A formulation sequence for CNT nanofluids was not available in the open literature.

3.1.4 Silica nanofluids

The Ludox TM-50 aqueous colloidal silica 49.8wt% suspension was purchased from W.R. Grace & Co, USA. Nanoparticles had been stabilized by making the system alkaline, and the dispersion contained also 500ppm of a proprietary biocide. The SiO_2 particles were spherical in shape, 22nm in diameter, and the suspension pH was 8.9. These parameters were verified in the laboratory. For the present work the Ludox TM-50 suspension was further diluted in distilled water followed by stirring.

3.2 Equipment and Instrumentation

Classical correlations presented under the literature review indicated a number of fluid properties that shapes up the boiling heat transfer of that fluid. For common liquids these properties are well researched and therefore often found in literature. Nanofluids being relatively new and debated, either their properties are not available to be referred or doubtful to trust. A salient feature of a critical study on nanofluids should be the establishment of fluid properties. This section of thesis firstly discusses the characterization of nanofluids for thermal conductivity, rheology, viscosity, and wetting and spreading. It will be followed by introduction of experimental facilities for boiling, x-ray scattering and artificial cavity investigations.

3.2.1 Thermal conductivity characterization of nanofluids

Three measuring devices were used occasionally to conduct measurements of the thermal conductivity of nanofluids. They were the KD2 probe, 3-Omega meter, and the Lambda meter. Since the transient hot wire (THW) technique is the principle of operation for these instruments, it would be timely to give a brief introduction to it.

In THW technique a small diameter wire is immersed in a fluid and used simultaneously as electrical resistance heater and as resistance thermometer to measure the resulting temperature rise due to the resistance heating. The hot-wire cells are designed to resemble a 1-dimensional transient line-source of heat in an infinite medium as closely as possible to minimize corrections for the actual geometry.

Healy et al. [225] explains the theory of transient hot wire technique in this manner. Consider an infinite line source of constant flux *q"* per unit length is applied step-wise at time *t=0*. The line source loses heat radially through conduction alone into an infinite incompressible medium of constant density ρ, thermal conductivity λ, and specific heat C_P shown in figure 3.10.

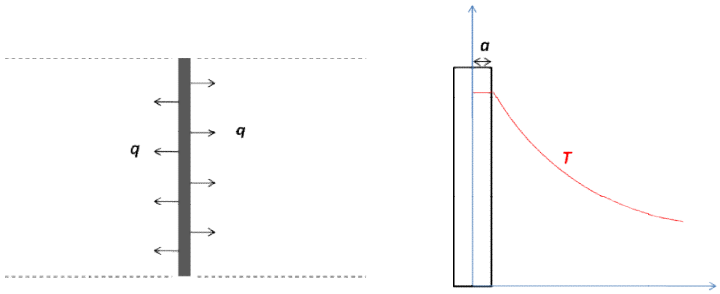

Figure 3.10: An illustration of THW technique

The thermal diffusivity of the medium is given by:

$$\alpha = \lambda / \rho C_p$$

For sufficiently long times of $t>>a^2/4\alpha$ where *a* is wire radius, the temperature history of the wire can be expressed as

$$\Delta T(a,t) = T(a,t) - T_0 = \left(q'' / 4\pi\lambda\right).\ln\left(4\alpha t / a^2 C\right) \qquad \textit{Eq 3.1}$$

Here *C* is a constant that takes the value of 1.781.

For a fixed radial distance in two instances in equation 3.1, the temperature change can be represented in much simpler form;

$$\Delta T_2 - \Delta T_1 = \frac{q''}{4\pi\lambda}\ln\left(\frac{t_2}{t_1}\right) \qquad \textit{Eq 3.2}$$

Finally the slope of a plot of *ΔT vs ln(t)* diagram will give λ .

$$\lambda = \frac{q''}{4\pi}\frac{d\ln(t)}{d\Delta T} \qquad \textit{Eq 3.3}$$

It is important however to note that the complete solution to equation 3.1 should incorporate corrections for wire properties, finite outer cell diameter, compressible work, viscous dissipation, radiation, Knudsen effects, and variable fluid properties. It is also to be noted that natural convection could come into play for very low viscosity fluids, which could be a likely reason for data scattering reported in Chapter 2.

Setting up of convection currents in the fluid body can introduce significant errors into measurements. For instance, Poltz [226] estimates very small vertical fluid velocity of the order of 0.01mm/min may cause an error of 1% of the measured thermal conductivity value. In this aspect the THW is considered as superior to parallel plates technique [227]. A review of literature shows that the THW is the widest used method to determine the thermal conductivity of nanofluids [71].

3.2.1.1 The KD2 probe

Pictured in figure 3.11, the handy KD2 device operates on the THW principle. This follows the assumption that the medium is both homogeneous and isotropic, and at uniform initial temperature. The sensor is a needle of 60mm in length and 0.9mm in diameter. The stated range of measurement and the measuring accuracy are 0.02-2W/mK, 5-40°C, and 5% respectively. From the start of a measurement it waits first 90 seconds to achieve temperature stability with the surrounding fluid. Then it heats the probe with 40mA current for next 30seconds, while reading its temperature at each second. At the end the device calculates the thermal conductivity of fluid from the temperature vs. time data.

The operational guidelines requires the fluid sample to be in thermal equilibrium with the surroundings, the probe held vertical, and a time lapse of approximately 5 minutes be allowed between two consecutive readings. The KD2 device has the advantages of the small size, easy operation, quick measurement, inexpensive and the adequacy of smaller fluid volumes.

Figure 3.11: KD2 probe and a measurement being conducted

Calibration of the KD2 probe was done by using base liquids such as water and ethylene glycol. In practice the fluid samples were placed in a temperature-controlled water bath. Once the measuring temperature was achieved, the KD2 device was switched on. Seven consecutive data points were acquired for a given temperature. The first two data point were usually out of range, possibly due to start-up transients of the probe. Data collected at room or moderate temperatures as well as data obtained with high viscous fluids such as ethylene glycol were in better agreement with literature data.

To demonstrate the KD2 measurements, two nanofluids of CNT and TiO_2 will be presented. CNT nanofluid was ethylene glycol based. EG and its derivatives are popular coolants and a secondary refrigerant for its favorable boiling and freezing point temperatures. Also there were claims that CNT-EG nanofluids exhibited substantial enhancement in thermal conductivity [228-229]. Besides in the present work, the boiling heat transfer experiments are scheduled for water-ethylene glycol (WEG) based nanofluids.

Figure 3.12 presents thermal conductivities of WEG based CNT nanofluids. Plotted by the side of it are the literature data for the particular mixture [230]. The concentration of CNT was kept low at 0.1wt% (0.028vol%) presuming practical applications. It had been learnt from experience that CNT causes enormous increase in fluid viscosity. But the EG concentration in base liquid was varied between 0 to 100%. There is no appreciable enhancement in thermal conductivity. Moreover the difference between the literature data and experimental data fluctuated between 0 to 7.3%. However the nearly invisible error bars on data points on figure 3.12 display the high degree of precision of KD2 device for these type of fluids.

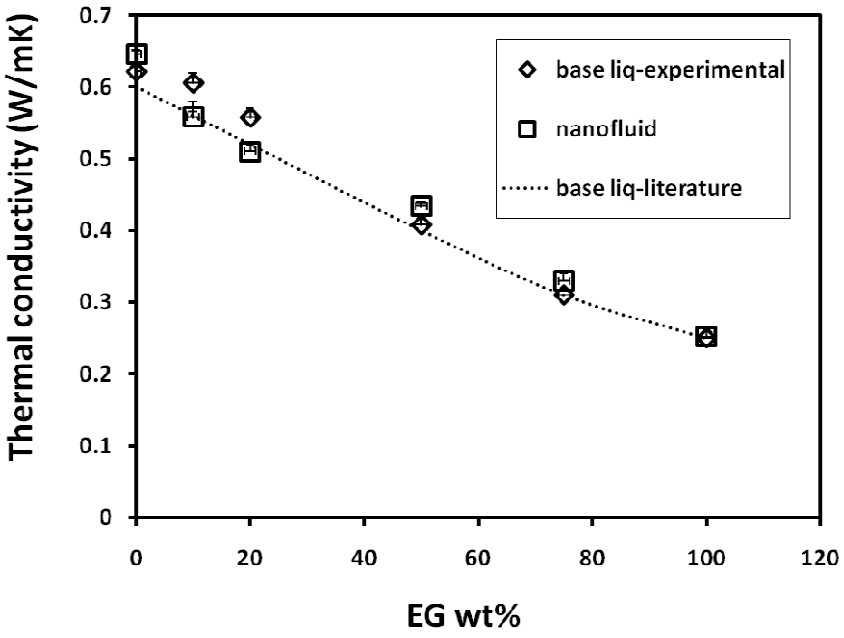

Figure 3.12: KD2 measurement for CNT 0.1wt%-EG nanofluids at 20°C

Measurements for TiO_2-WEG25 nanofluid is given in figure 3.13. The nanoparticle concentration was raised from 0 to 5wt% (0-1.25vol%). The %enhancement was calculated from measured values of base liquid (k_L) and nanofluid (k_{nf}) in the conventional method as follows;

$$\%enhancement = \frac{k_L - k_{nf}}{k_L} * 100 \qquad \textit{Eq 3.4}$$

Each data point on the two figures was the average of five consecutive measurements. The repeatability of measurements was in agreement with the instrument specifications. With reference to CNT nanofluids, the introduction of 0.1wt% of nanoparticles did not cause noticeable change in the thermal conductivity of base liquid. The TiO_2-WEG25 nanofluid however showed an average enhancement of 5.5% at the highest particle loading of 5wt%.

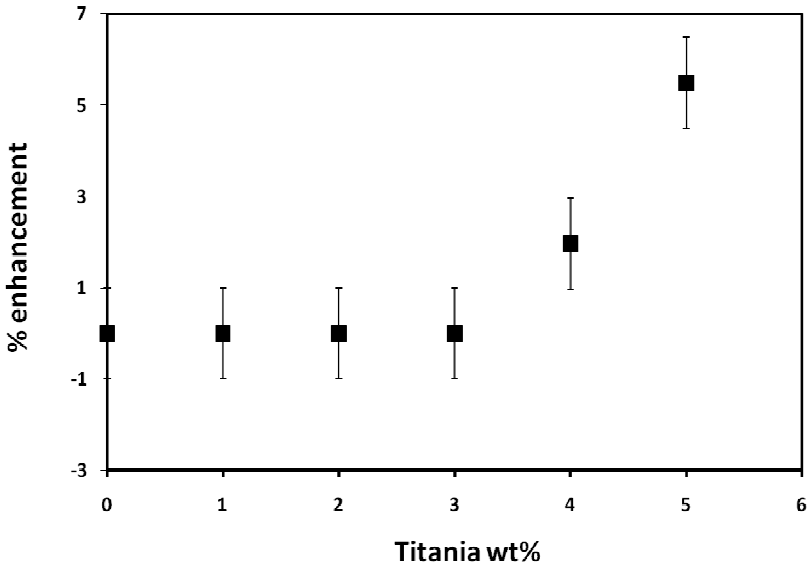

Figure 3.13: KD2 measurement for Titania-WEG25 nanofluids at 20°C

Zero or low enhancement may not be very attractive from a commercial viewpoint, but it is encouraging to note their agreement with more recent literature.

3.2.1.2 The 3-Omega meter

Figure 3.14 features the 3-Omega instrument. Its principle of operation is to utilize an AC heating current and a lock-in amplifier to directly measure thermal conductivity of a substrate, typically a dielectric material. A short thin wire that is similar to the needle in KD2 device acts as both heater and the thermometer. When a current of frequency Ω is supplied to the wire, the voltage at the third harmonic (3Ω) contains useful information about the thermal properties of the system.

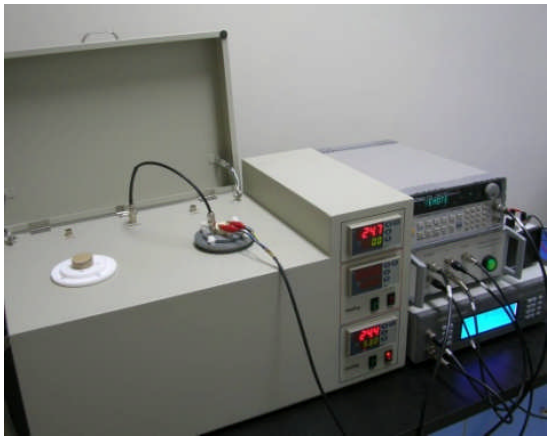

Figure 3.14: 3-Omega meter

Once the fluid is loaded and the measuring temperatures are set, the instrument slowly approaches the set point. At the set point it stays for a sufficient time, which is followed by a quick step of data collection. The measurement probe is a thin platinum wire, which is also the most delicate component of hardware. Each time it breaks, fresh replacement and re-calibration is needed. Volume of the measuring chamber is 100ml. This instrument takes approximately 45min to climb 10°C in temperature and complete the data acquisition.

Since the instrument was new to handle nanofluids, there was a need to establish its accuracy by taking measurements on a known liquid. Subsequently the distilled water was measured and compared with literature, as shown in figure 3.15. The measured data lie approximately within ±5% of literature data for water [230].

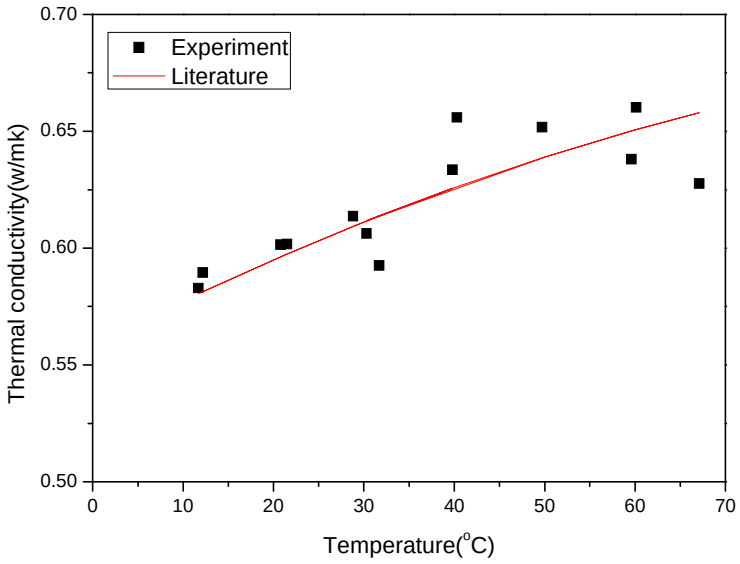

Figure 3.15: 3-Omega measurement for water

The calibration procedure was followed by the measurements on dilute TiO_2-WEG25 nanofluids presented on figure 3.16. The error bars on each data point reflect the high precision of measurement. As far as the thermal performance is concerned, the nanofluid is slightly inferior to the base liquid. The deterioration was however less than 2%.

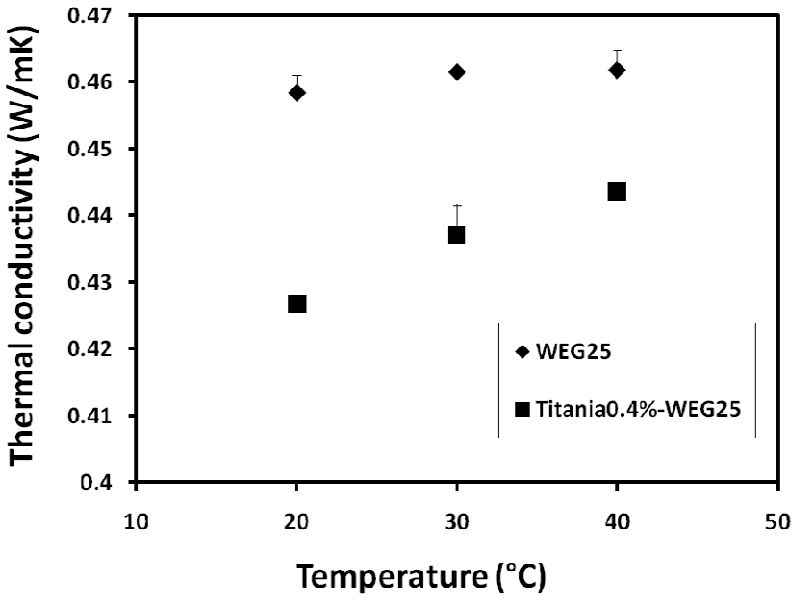

Figure 3.16: 3-Omega measurement for titania-WEG25 nanofluid

The 3-Omega device can work over a broad temperature range of -25^{o}C to 220^{o}C. In comparison to the KD2 meter this instrument is high in precision and also maintains precision at high temperatures. However the error in the order of 5% is significant in terms of dilute nanofluids where the expected enhancement is low.

3.2.1.3 The Lambda meter

The Lambda meter is the state-of-the art device developed on ASTM D2717 test method to measure thermal conductivity of nanofluids. It operates on THW principle. The unit shown on figure 3.17 was supplied by PSL Measurement Systems GMBH Germany. The measurement probe is a thin platinum wire of diameter and length 100µm and 40mm respectively. Operating temperature and thermal conductivity ranges are given as -30 to +190°C and 10-1000 mW/mK. It can reproduce data to ±1%. The required size of liquid sample is 50 ml.

Figure 3.17: Left-Lambda meter, Right-measurement probe and fluid container

In order to calibrate the instrument, two known liquids were measured. Shown in figure 3.18, each data point is an average of five consecutive readings. Two series of measurements are in good agreement with the literature values. Water data had a maximum error of 0.4%, while for ethylene glycol it was below 2.3%.

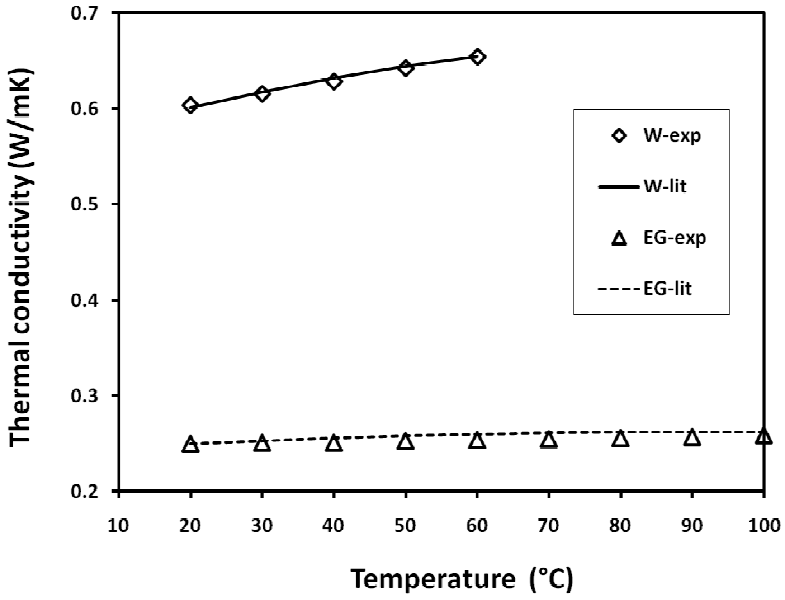

Figure 3.18: Lambda meter measurements for water and ethylene glycol

Calibration was followed by characterization of alumina nanofluids. First to be presented here are the data for ethylene glycol based acicular alumina nanofluids. Figure 3.19 displays a significant enhancement for all concentrations. A temperature effect is seen for 8wt% loading which needs to be explored further. Dotted lines indicate average values.

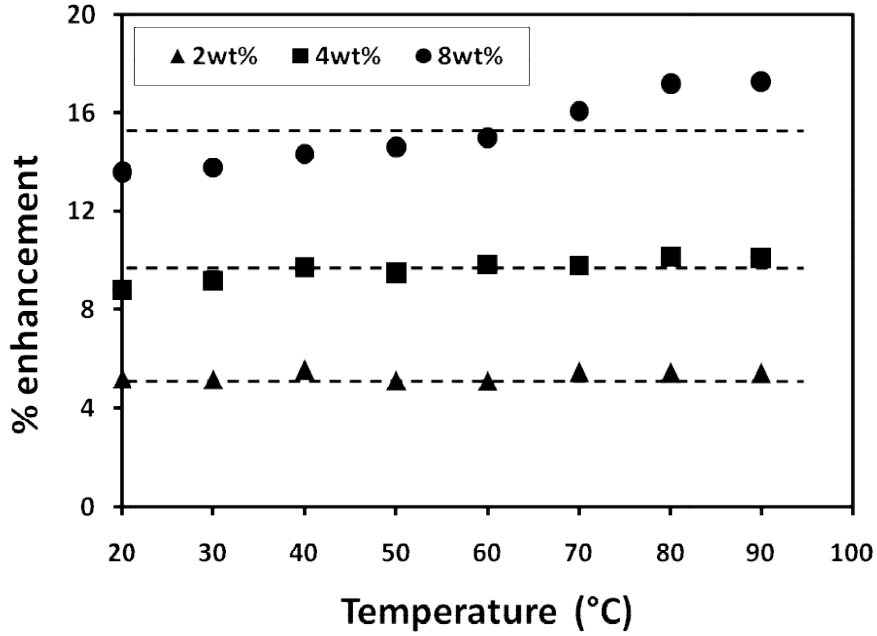

Figure 3.19: Acicular alumina-EG nanofluid

Data for spherical alumina nanofluids obtained using the Lambda meter are plotted on figure 3.20. The percentage enhancement has increased with particle concentration while remained unchanged with sample temperature. This trend is in agreement with recent literature [231].

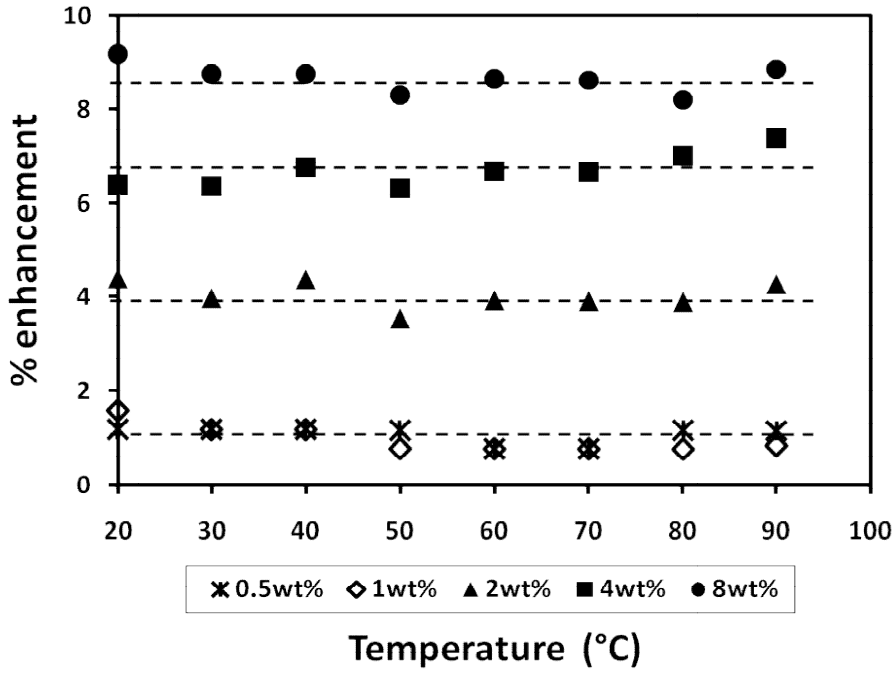

Figure 3.20: Spherical alumina-EG nanofluid

Characterization of alumina nanofluids was followed by titania nanofluids. The concentration and temperature dependencies of enhancement were found to be similar to spherical alumina nanofluids. Subsequent data analysis was conducted to examine the agreement with classical theories. The Hamilton-Crosser correlation [43] largely underpredicted the experimental data but its modified version which accounts for aggregate size [232] very closely forecasted it. The illustrations are given in figure 3.21.

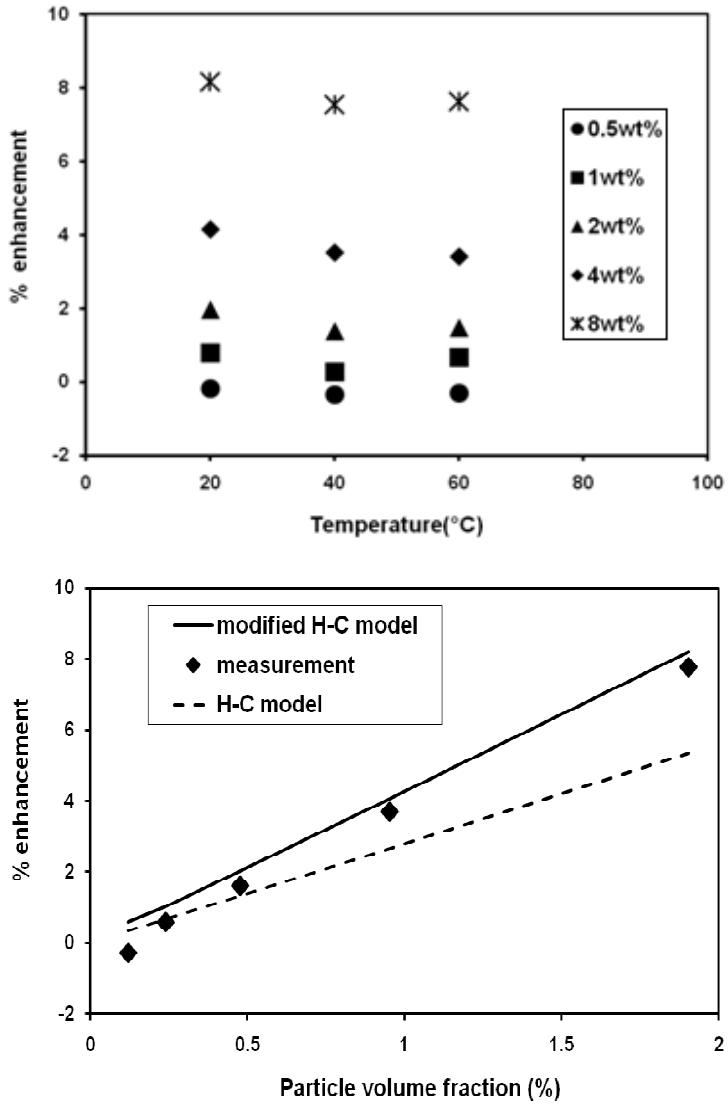

Figure 3.21: TiO_2-EG nanofluids, above-experimental, below-predictions

In summary for thermal conductivity characterization, it could be said that the dilute nanofluids irrespective of particle material, shape or base liquid, failed to demonstrate noticeable

enhancement. This observation agrees with both recent literature and classical theories. Higher particle concentrations beyond 2wt% caused enhancement, which increased with concentration, but is generally insensitive to temperature. The temperature insensitivity supports the hypothesis that Brownian motion is not a key mechanism behind enhancement. Moreover the modified H-C equation (eq 2.14) was capable of predicting the thermal conductivity of ethylene glycol based nanofluids made of spherical nanoparticles.

3.2.2 Rheological characterization of nanofluids

This section discusses the rheology and viscosity measurements conducted using a rotational rheometer and U-tube capillary viscometer.

3.2.2.1 Viscosity measurements

The U-tube capillary viscometer depicted in figure 3.22 is a classical instrument used to measure the kinematic viscosity (v) of pure liquids. This equipment was calibrated at 25°C and certified by the supplier (Technica Corp., Great Britain).

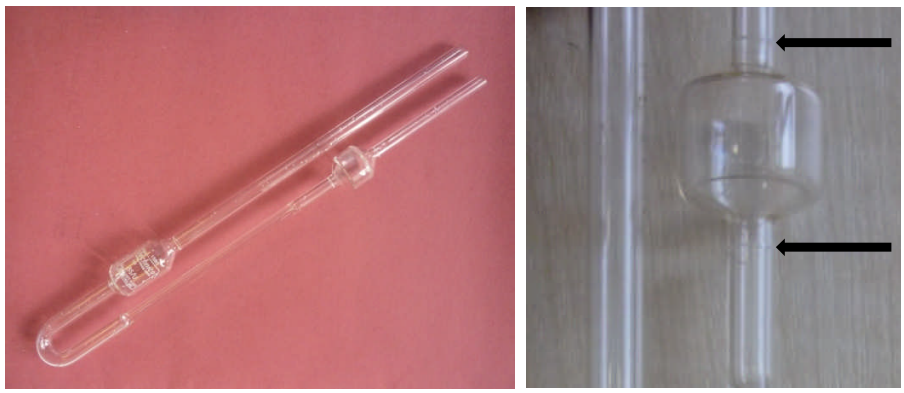

Figure 3.22: U-tube capillary viscometer and graduation marks

Viscosity is to be determined as follows. If *t* is the time taken by the fluid to travel between two graduation marks, then the viscosity of measured liquid is given by;

$$\upsilon = C.t \qquad \textit{Eq 3.5}$$

where *C* is called the viscometer constant, a viscometer-specific value assigned at the calibration stage. A given viscometer is recommended to be used at a given temperature and *t*. This information is provided on the calibration sheet.

Nanofluids described here are to be characterized for an interval of temperatures. The viscometer model was *O1959VHB-320-030R* where *C=0.0008519 mm^2/s^2* and *t* was recommended to be greater than 1500 s. Prior to nanofluids it was essential to calibrate the device for the base liquid to record its accuracy in the desired temperature range. In view of that, the viscometer was filled with a WEG25 sample and placed in a large thermal bath. Once the sample reached thermal equilibrium with the surrounding bath temperature, the liquid column was released letting it a free fall through the viscometer arm (figure 3.22). Travel time (*t*) for the liquid between two arrowheads was recorded. At each temperature the experiment was repeated five times and the respective readings were recorded. Table 3.1 presents the viscosity calculated using equation 3.5.

It was encouraging to see that the viscometer could operate in the temperature interval of 25°C to 40°C within a modest deviation in comparison to literature data. Moreover these measurements were repeatable to a precision of more than 99.3%.

Table 3.1: Viscosity of WEG25 base liquid

T(°C)	ν_Experiment (mm^2/s)	ν_Literature (mm^2/s)	% Deviation
25	1.5860	1.6054	1.21
30	1.4340	1.4183	-1.11
35	1.2600	1.2618	0.14
40	1.1195	1.1311	1.03
45	1.0841	1.0194	-6.35

The *O1959VHB-320-030R* U-tube viscometer was then used to conduct measurements on TiO_2-WEG25 dilute nanofluids. Figure 3.23 presents the data for the base liquid and the nanofluid. Obviously the addition of a small amount of nanoparticles was sufficient to enhance the viscosity of the base liquid steadily from 2% to 7% in this temperature interval. Hence this demonstrates a temperature effect on the viscosity of nanofluids.

In deed the challenge in viscosity measurement was to select the appropriate U-tube viscometer for a given fluid. Often the travel time (*t*) did not meet the recommended value. Selecting a viscometer then becomes a trial-and-error task.

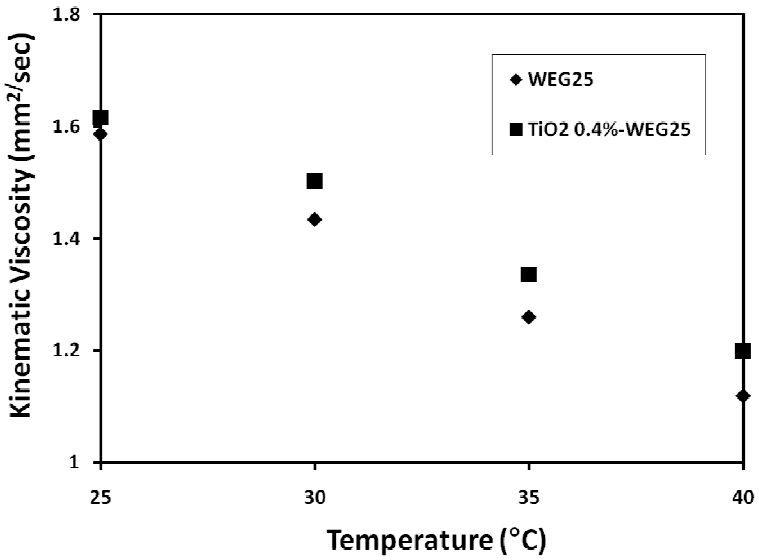

Figure 3.23: U-tube viscometer measurement

With reference to nanofluids, there are three more aspects to fulfill. Firstly the nanofluids should not clog the capillary tube, secondly they should be stable at the measuring temperature, and lastly the capillary should not cause appreciable separation of particles from the fluid due to chromatographic effect. It was found to be difficult to measure dense TiO_2 samples or any CNT nanofluid due to the issue of clogging.

3.2.2.2 Rheology measurements

Dynamic viscosity of a fluid has a significant impact on heat transfer and fluid flow. For a Newtonian fluid the dynamic viscosity is independent of shear rate whereas a non-Newtonian fluid could exhibit shear dependent behaviour such as shear thickening or shear thinning with shear. Newtonian and non-Newtonian phenomena are respectively characterized by linear and non-linear relationships between shear stress and shear rate. Those who attempted to resolve the convective heat transfer of nanofluids treated dynamic viscosity as a key parameter [115]. Recently the knowledge of shear viscosity made it possible to predict the thermal conductivity of nanofluids [231]. Arguably this is a very important property in thermal transport of nanofluids.

The Bohlin CVO rheometer which was used in this work is featured in figure 3.24. This instrument falls under the category of rotational rheometers and was capable of handling a range of fluids from thin liquids to thick slurries. A thermal bath connected to the rheometer made it possible to conduct measurements at elevated temperatures. For the experiments described here the

cylindrical *'mooney'* cell and a 70µm gap size were used. Moreover a pre-shear was applied to all samples before subjecting to shear.

Figure 3.24: Bohlin CVO Rotational rheometer

In par with the general experimental procedure, the rheometer had to be calibrated with a known liquid. Ethylene glycol was chosen for this purpose. At 20°C measuring temperature, the dynamic viscosity of EG was independent of shear rates. Its maximum deviation of 4.5% from literature values [230] was thought to be satisfactory to proceed to nanofluids measurements.

Figure 3.25 plots viscosity vs. shear rate data for water-ethylene glycol (WEG) based CNT nanofluids. Ethylene glycol concentration was varied while that of the CNT was kept constant.

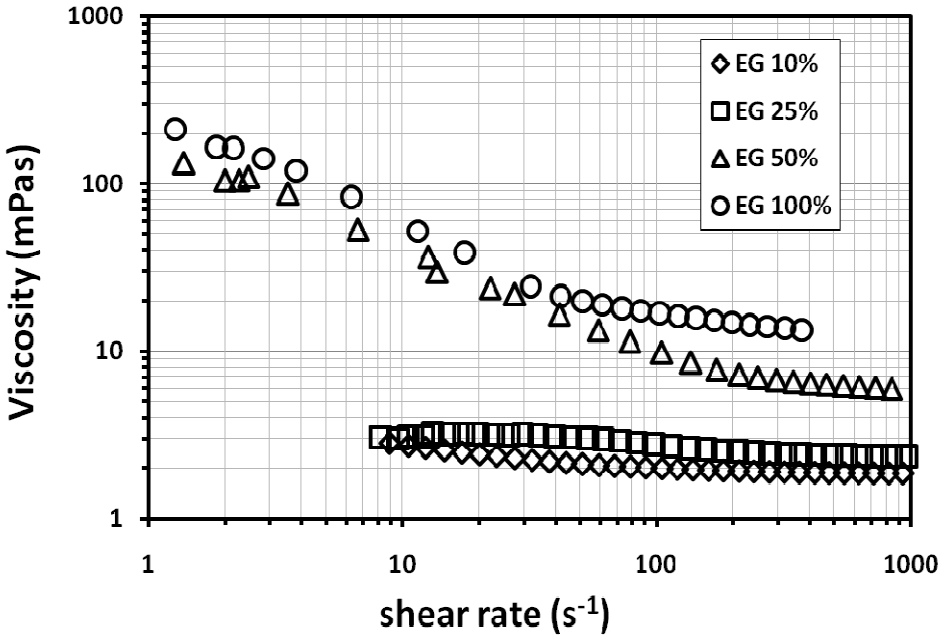

Figure 3.25: CNT0.1wt%-WEG nanofluids at 20°C

It can be noticed that the addition of nanotubes has introduced a shear thinning effect to the Newtonian base liquids. This effect is more pronounced with increasing EG concentration. A possible explanation could be found from a viscosity dimension. 50% and 100% EG samples are substantially viscous. If the nanotubes are entangled in these samples though to a lesser degree than dry CNTs, the first few minutes of shearing would basically be doing the dispersion of nanotubes, which is reflected by shear thinning. Raw data sheets are provided in the Appendix A.

Spherical alumina-EG nanofluids which were earlier characterized for thermal conductivity are now examined for rheology. Data were collected at 20°C, 40°C, and 60°C fluid temperatures. Figure 3.26 is for the 8wt% particle concentration. The sample shows Newtonian behaviour and the relative increase in viscosity is steady at 11%-12% in this temperature interval.

Rheological behaviour of 4%, 2% and 1% spherical alumina nanofluids followed similar trends to figure 3.26. The conclusion therefore should be that the shear viscosity of spherical alumina-EG nanofluids is shear rate independent but concentration and temperature dependent.

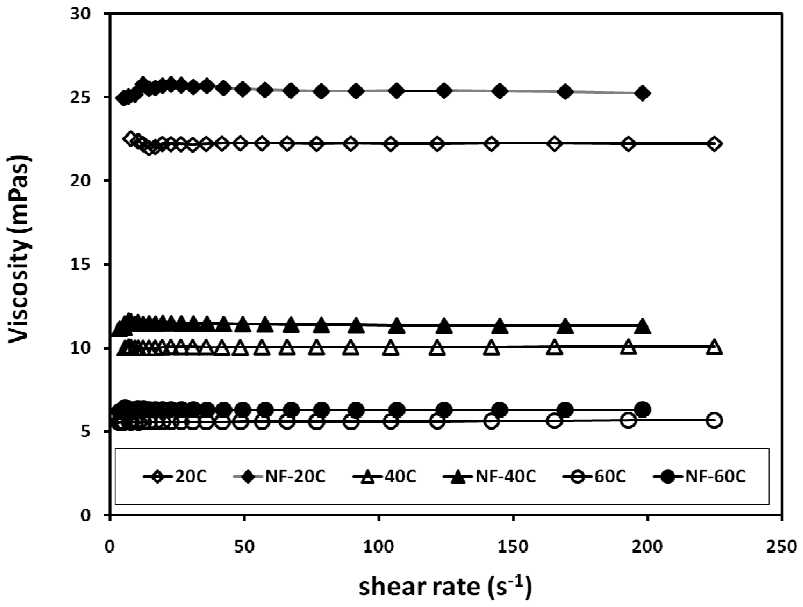

Figure 3.26: Spherical alumina8wt%-EG nanofluid and base liquid

However the shear behaviour of acicular alumina-EG nanofluids was remarkably different. Shown on figure 3.27, they were shear thinning at a rate comparable in three temperatures. Furthermore, the relative increase in viscosity was more than 50%. In comparison to spherical particles, the acicular particles seem to have a larger influential on the base liquid viscosity.

There was a clear influence of particle concentration on shear thinning. Illustrated on figure 3.28, the acicular nanofluids have gradually recovered as the particle concentration decreased. Though not presented here, the trends were similar at 20°C and 60°C temperatures.

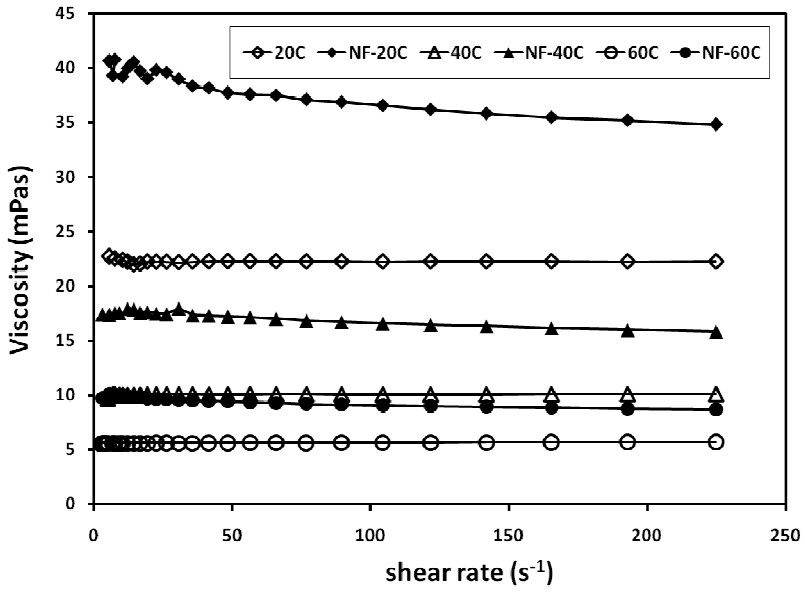

Figure 3.27: Acicular Alumina8wt%-EG nanofluid

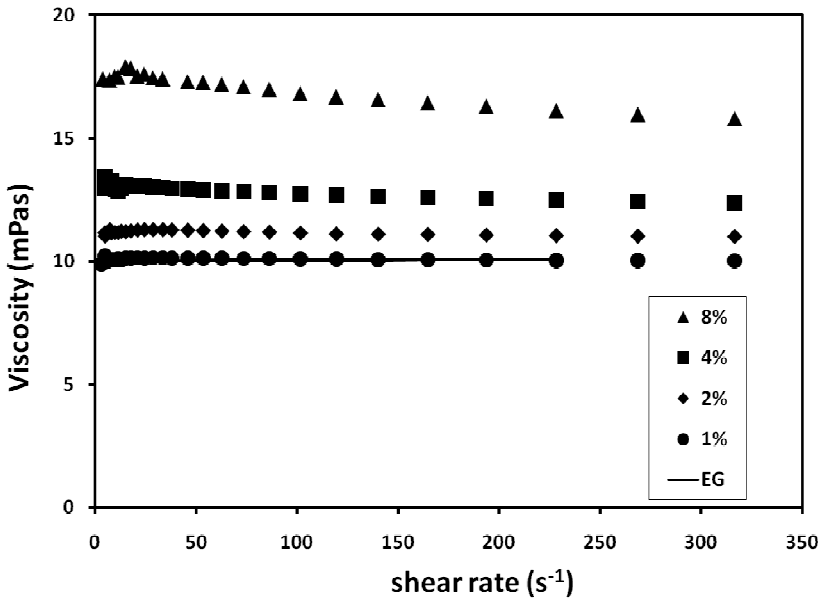

Figure 3.28: Acicular Alumina8wt%-EG nanofluid at 40°C

From the foregoing presentation of the shear viscosity of tubular (CNT), spherical (alumina) and acicular (alumina) nanofluids, it could be seen that the tubular and acicular particles have

introduced shear thinning to base liquid. Recall that CNTs are hollow and flexible tubes whereas acicular particles are solid and brittle. In order to acquire a broader view of shear viscosity, a comparison was made with similar data in the literature. Available experimental data on EG based nanofluids of tubular titanate [117], multi-walled CNT, acicular alumina, spherical titania [233] and spherical alumina were recruited for a comparative analysis. These datasets are plotted on figure 3.29.

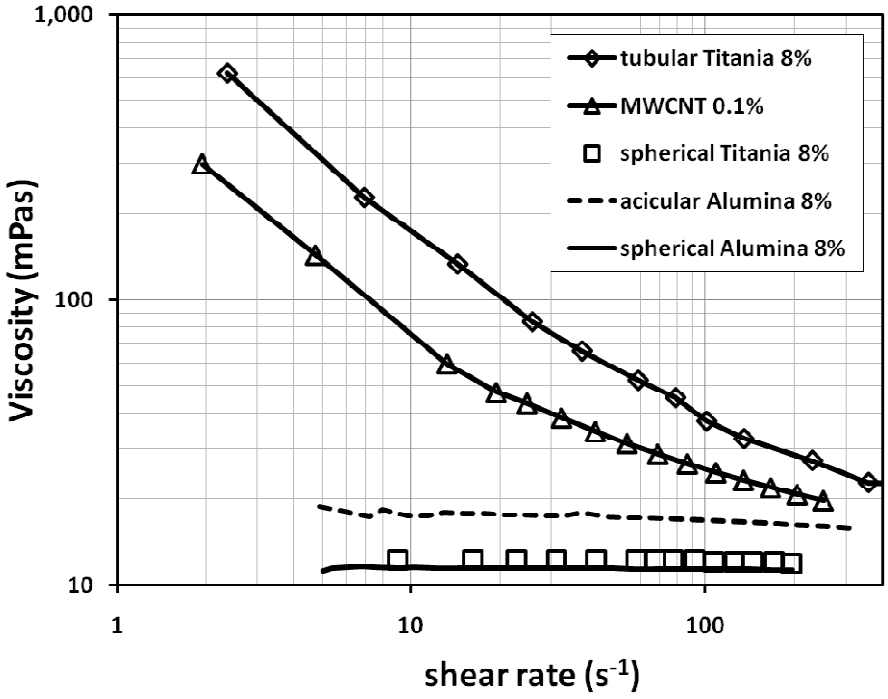

Figure 3.29: Rheology of EG-based nanofluids at 40°C

Shear dependent behaviour of titanate nanofluids follows that of CNT nanofluids while alumina acicular nanofluids, alumina spherical nanofluids and titania spherical nanofluids behave alike. Their respective primary particle sizes are as follows: titanate particles D~10nm, L~100nm; MWCNT D~15nm, L=1500nm; acicular alumina D~15nm, L~150nm; spherical alumina D=45nm; spherical titania D=25nm. Particle sizes in suspended state are significantly different. Zetasizer measurement for spherical alumina and titania were 140nm and 100nm respectively. Chen et al. [117] estimated the average effective particle diameter for titanate as 260nm. For acicular alumina the suspended size can be estimated from SEM image given in figure 3.30.

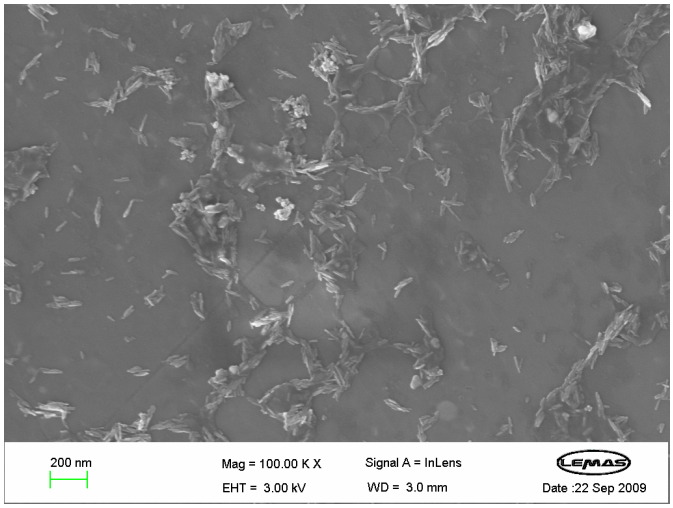

Figure 3.30: Acicular Alumina-EG nanofluid

According to the SEM image the particles are well-dispersed, and the individual particles were close to the dimensions of primary particles. However they are in aggregates, and their shapes resemble more of a circular than acicular or tubular in contrast to titanate and CNT. It can therefore be hypothesized that the size, shape and the particle distribution can be possible explanations for the spherical-like rheological behaviour of acicular alumina-EG nanofluids.

3.2.3 Wettability characterization of nanofluids

Wetting and spreading characteristics of nanofluids is treated with high priority for their influence on boiling heat transfer and critical heat flux. The contact angle between a liquid and a substrate is the parameter that helps to understand wetting and spreading behaviour. Figure 3.31 features the concept of contact angle (θ), interfacial tension (γ and σ) and the measuring device KRUSS goniometer. This device works in two stages, firstly the camera acquires the droplet image and then it analyzes the droplet using image analysis software called DSA1. Basically the software does curve-fitting to the acquired drop shape. It determines the contact angle θ at the intersection of the drop contour line with the solid surface line (baseline) graphically illustrated on figure 3.31. To describe this further, the software calculates the root of the secondary derivative of the brightness levels to receive the point of greatest change of brightness. This becomes the baseline. The found drop shape is adapted to fit a mathematical model which is then used to calculate the contact angle. The various methods of calculating the contact angle therefore differ in the mathematical model used for analyzing the drop shape.

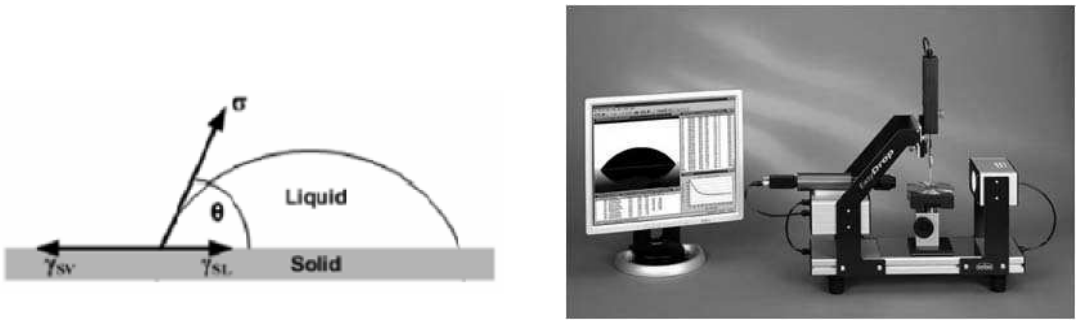

Figure 3.31: Concept of contact angle and the KRUSS DSA100 measuring device

As a part of the work presented in this thesis, a series of contact angle measurements were performed using the KRUSS DSA100 goniometer. The fluids included base liquids and nanofluids, and the substrates were glass, copper and silicon wafers. Substrates were either clean or purposely nanoparticle-fouled. All measurements were conducted at room temperature.

A liquid droplet deposited on a solid substrate is commonly known as a sessile drop, which distinguished itself from a hanging 'pendant' drop. There are three methods offered by the device to evaluate the drop shape. They are namely Polynomial method, Circle fitting method, and Young-Laplace (sessile drop fitting) method [234]. These methods differ from each other in terms of the curve fitting technique used to resemble the actual drop contour. Sessile drop fitting method fits the Young-Laplace equation on to the drop contour assuming a symmetric drop shape and taking into account the weight of droplet. In comparison to other methods available with the KRUSS device, this method is high in accuracy. Therefore in the context of present work, the sessile drop fitting method was chosen to analyze droplets.

The contact angle is known to be very sensitive to substrate roughness and contamination. This characteristic becomes very useful when it comes to compare clean and nanoparticle-fouled surfaces. A technically clean substrate such as a silicon wafer would be the most suitable to demonstrate the influence of cleanliness. A wafer in a sealed pack delivered by the supplier is considered as theoretically clean and optically smooth. This assumption is derived after considering the clean atmosphere these wafers are manufactured and packaged. As verification, its roughness was determined using non-invasive Wyko optical surface profiler (Dymek Company Ltd.), which is capable of conducting measurements from 0.1nm to 8millimeters. The roughness (R_a) of the silicon wafer was found to be 0.5nm.

Two pieces were diced out from this wafer using a diamond cutter and subsequently cleaned by following a standard procedure. Surface cleaning is a highly specialized area in surface science. For instance, the RCA method [235] is the most practiced three-step sequence for silicon wafer cleaning. However it demands finer facilities to handle the chemicals and procedures involved. In this cleaning exercise the first step was to flush the pieces with de-ionised (DI) water. Secondly the pieces were immersed in acetone and ultrasonicated for 3-4 minutes. Subsequently they were fetched out and rinsed with DI water, followed by drying in a vacuum oven.

Shown on figure 3.32 are the static contact angles for 5 µl sessile droplets of water deposited three substrates. The solid line represents fresh wafer, and the open symbols represent diced pieces. Evidently the data on diced wafer-1 were fairly close to fresh wafer while diced wafer-2 deviated by up to 10°. Given the consistency of the cleaning procedure and the conduct of experiments, the likely cause for the observed deviation could be the attachment of dust particles on to the diced wafer-2 in between cleaning and the experiment. Nevertheless the experimental data are in good agreement with the literature for water on silicon, which is 45±2% [236].

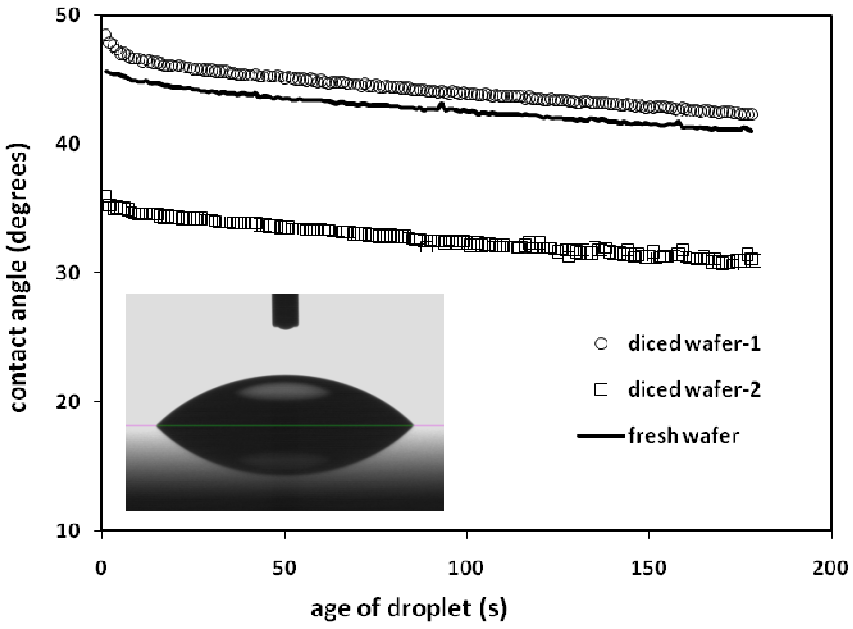

Figure 3.32: Contact angle of distilled water on silicon wafer

An important lesson was learnt from this exercise. A modest change in contact angle may not necessarily have caused by an applied process such as nanoparticle fouling. It could probably be

an artifact created by the operating conditions in the laboratory. Kim et al. [154] also considered it that way when interpreting surface wettability data.

It is customary to measure contact angle of water on a glass substrate. In this work the glass substrates were the standard microscopy slides. They were cleaned firstly by liquid detergent, then by acetone, before drying them in a vacuum oven. Later a 5 µl droplet of distilled water was deposited on one of these slides and measurements were taken using the KRUSS device. Three consecutive tests were conducted from which the data are plotted on figure 3.33. Repeatability falls within an interval of ±1.5°. In comparison with literature, the average value of θ at the time of droplet deposition is approximately 10° smaller. The reason could be the contamination or the difference in hydrophobicity of glass substrate.

Figure 3.33: Distilled water on glass substrate in three consecutive runs

In summary it can be stated that the contact angle is extremely sensitive to cleanliness and hydrophobicity of a surface. The measuring device KRUSS DSA100 is capable of reproducing data to a good accuracy. However upon the evidence presented on figures 3.32 and 3.33, it would be safe to assume that a substantial change in contact angle is needed to indicate a sizable alteration in surface roughness. The main objective of contact angle measurement is to relate it to the boiling of nanofluids. In view of that, it is worthwhile to remember the possible repercussions of above uncertainties.

That brings the discussion on nanofluid characterization techniques to a closure.

3.2.4 SAXS studies for Nanoparticle structuring

It was shown by way of SEM images and light scattering data that nanoparticles are in the form of aggregates in liquids. Arrangement of particles in aggregates and aggregation itself has profound influence on thermal and rheological properties of nanofluids. Speed of aggregation is characterized by aggregation time constant (t_p) which can be expressed in terms of mass of particle (m_p) and mass of aggregate (m_a) after a time interval t.

$$t_p = \frac{t}{m_a / m_p - 1} \qquad \textit{Eq 3.6}$$

According to Prasher et al. [93], t_p depends on the size and concentration of nanoparticles, and the temperature and pH of suspension. Despite the knowledge of t_p is very useful for nanofluids, this information is yet to be documented in the literature. Although plenty of attempts have been made by colloidal scientists, the measurement of t_p has remained a challenging task that requires tools to capture particle dynamics occurring in the order of milliseconds. A powerful beam of synchrotron radiation should be a way to do.

There is clear difference between the heat transport in a spherical aggregate and a non-spherical one. Although the shape of nanoparticle aggregates is vital information, this is yet to be discovered experimentally. Electron microscopy is limited to handle dried droplets. X-ray scattering is a powerful technique to face the challenge.

With the objectives of studying the in-situ particle structuring and aggregation kinetics using small angle x-ray scattering (SAXS), an experimental procedure and apparatus were developed. The following discussion describes them.

3.2.4.1 The synchrotron light and beamline

The synchrotron light is a portion of electromagnetic spectrum that spans in wavelengths from infrared to x-rays. The Diamond Light Source, Oxford and Darsbury National Laboratory are synchrotron radiation facilities that provide high energy synchrotron light. The experiments reported here were conducted at Diamond. Nevertheless both facilities operate on the same technological principle and the apparatus and experimental procedure were very similar.

Figure 3.34 illustrates the synchrotron machine in the Diamond Light Source. It consists of three particle accelerators; a linear accelerator (Linac), booster synchrotron and a storage ring.

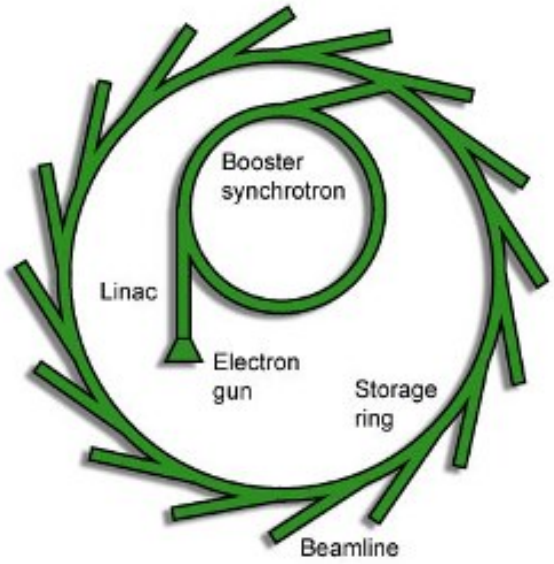

Figure 3.34: Synchrotron machine at Diamond Light Source

Billions of electrons generated in the electron gun are injected in bundles to a 30m-long Linac. Subsequently they enter into the booster, which is 158m in circumference, where they are accelerated to very high speeds under vacuum conditions. At the booster the electrons are energized until they gain nearly the speed of light. Electrons are then diverted into the storage ring. In travelling through strong electromagnetic fields in the 562m-circumference storage ring at nearly the speed of light, the electrons begin to emit electromagnetic rays known as synchrotron light. This light is then directed to a number of experimental stations called beamlines. Each beamline provides filtered light for the needs of a specific category of experiments viz. diffraction and scattering, spectroscopy, and imaging.

A photographic view of Diamond I22 beamline's experimental hutch is presented in figure 3.35. This was one of three areas in the experimental station. The control cabin is pictured in figure 3.36. Not shown on pictures is the optics hutch.

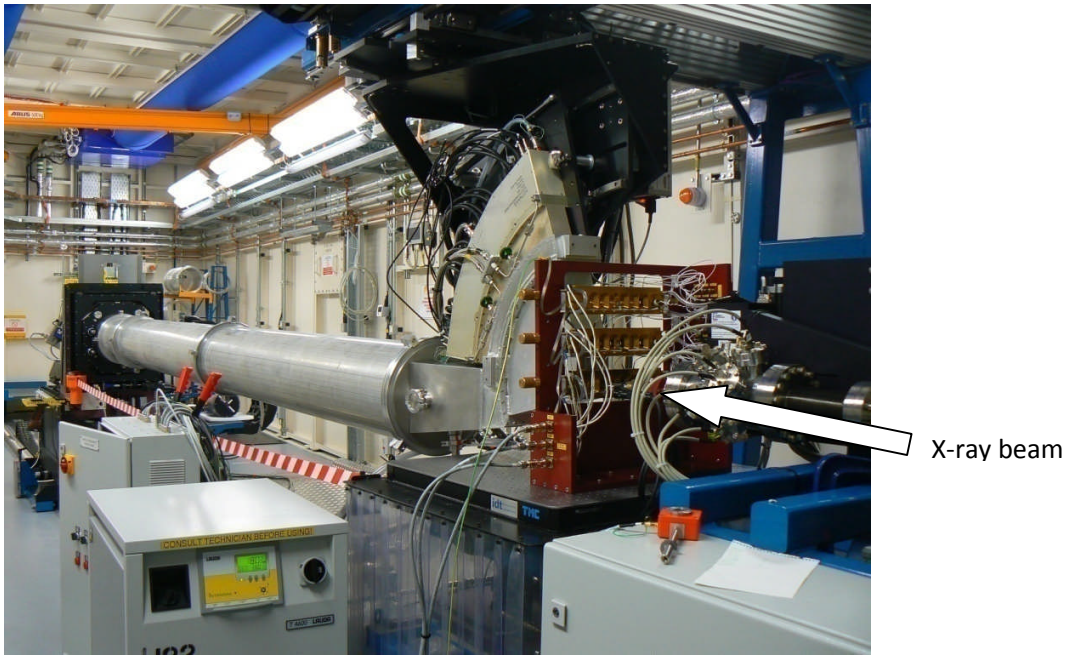

Figure 3.35: Diamond I22 experimental hutch

The x-ray beam enters as shown by the arrow and penetrates the samples mounted on the rack. Solid particles in the sample cause the x-rays to scatter upon collision. The scattered light is directed through a tube to a detector at the far end. The distance between the sample and the detector is called the camera length, which is important parameter in data reduction. Before and during an experiment, controlling and a real-time monitoring were possible from the control cabin. Facilities for data analysis were also there.

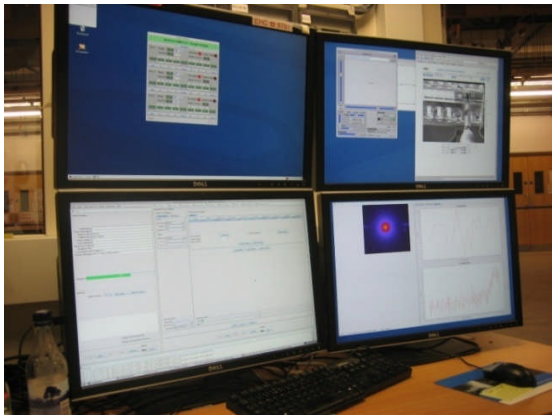

Figure 3.36: Control cabin

SAXS experiments at Diamond demanded strict safety regulations. Furthermore in spite of the provision of limited laboratory access on site to users, there was a considerable amount of preparatory work needed to be done before arriving in Diamond.

3.2.4.2 Experimental set up

For stationary fluid experiments, the sample cells provided in-house were used. For convective experiments, a flow cell was designed and fabricated at University of Leeds. The flow cell was an annular heat exchanger made of brass pictured in figure 3.37. It had two fluid loops; one for the heating water and the other for nanofluid.

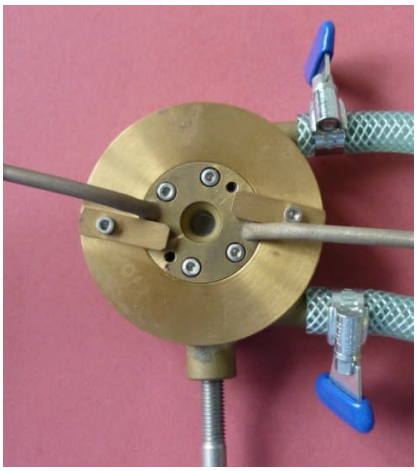

Figure 3.37: Flow cell for SAXS experiments

Nanofluid circulation for convective experiments was obtained by using a gear pump where the circulation speed (rpm) was set according to the experimental requirement. A continuously-stirred glass vessel placed on a hot plate was used as the nanofluid reservoir. Temperature lift given by the hot plate helped to reduce the heating demand from hot water produced and circulated by a Lauda thermal bath. Photographic views of the flow cell and rack of static cells mounted on beamline, and the nanofluid heater are given on figure 3.38. Samples mounted on static cells were heated by resistive heating.

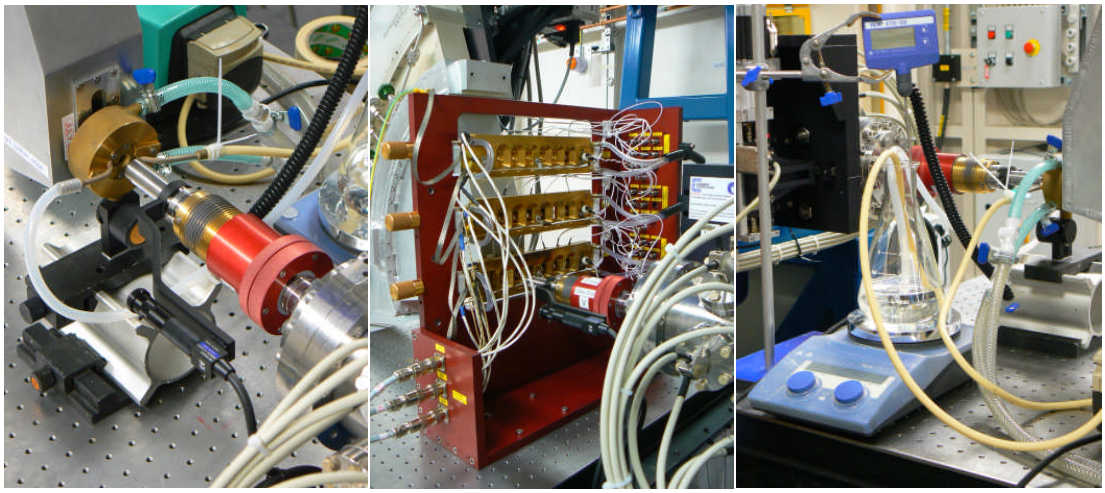

Figure 3.38: from Left to Right - Flow cell, static cells in rack, hot plate

The liquid samples were exposed to the x-ray beam through a tiny circular transparent window of 10mm diameter in the flow cell and static cells. Figure 3.39 shows the interior of a static cell.

Figure 3.39: Interior of a static cell

The sample is held in the cell by two transparent mica windows separated by the PTFE spacer ring. Mica is a material that possesses the advantages of ordered crystal structure, atomic smoothness, and total transparency to x-ray light. Mica is a standard for x-ray scattering experiments. The mica windows used in present experiments were 25µm in thickness.

3.2.5 Pool boiling of Nanofluids

A considerable part of this thesis covers the boiling heat transfer of nanofluids. In order to conduct boiling experiments in the laboratory a test rig had to be designed and constructed. Main design criteria were;

- To boil dilute nanofluids under atmospheric pressure
- To boil these fluids on selected surfaces (samples) and change them periodically
- To visualize boiling activity using a high speed video camera
- To measure and record the boiling temperatures and applied heat fluxes
- To comply with safety guidelines of the laboratory

There should be two heaters in the test rig; one to maintain the pool of liquid at saturation temperature, the other to supply excess heat to the sample. Thus the latter generated data points for surface heat flux. A condenser is needed to condense the vapour efficiently and retain in the boiler. If vapour escapes in large quantities requiring refilling quite often, it will disturb the system's thermal equilibrium. With respect to nanofluids, a drastic reduction of liquid volume will cause increase in particle concentration. Even though boiling occurred under atmospheric pressure, the condenser is an integral part of the system.

Regarding the pool temperature measurements, the most important for heat transfer calculations is the liquid temperature near the sample surface. In fluid dynamics point of view however it is essential to hold the pool at saturation temperature. Hence it was thought to place three thermocouples along a vertical line in the pool; one located just above the sample surface (~10mm), and others in 20mm spacing from the first thermocouple and vertically upwards.

Insulation was required to minimize the heat loss. Scenarios will be that for boiling of water based nanofluids, a temperature difference between the inside and outside of the boiler of around 80-85°C is anticipated. For EG based nanofluids this will be even larger. Thermocouples were placed on the insulation to help heat loss calculations. There was an observation window on the insulation layer to see the liquid inside.

Automatics and controls play a useful role in regulation and data acquisition. The top heater and the bottom heater needed independent power and temperature control. When the fluid reached the saturation temperature the former should cut-off. Hence it should be a temperature-

controlled power supply. Heat input to the sample will be through the bottom heater, which will therefore need a manned DC power supply. It further needed a high-temperature cut-off to safeguard from overheating damage. After incorporating above mentioned considerations, the test rig shown in figure 3.40 was designed. A list of accessories is provided in tables 3.2 and 3.3.Manufacturing of the test rig took place in the Mechanical Engineering workshop of Leeds University.

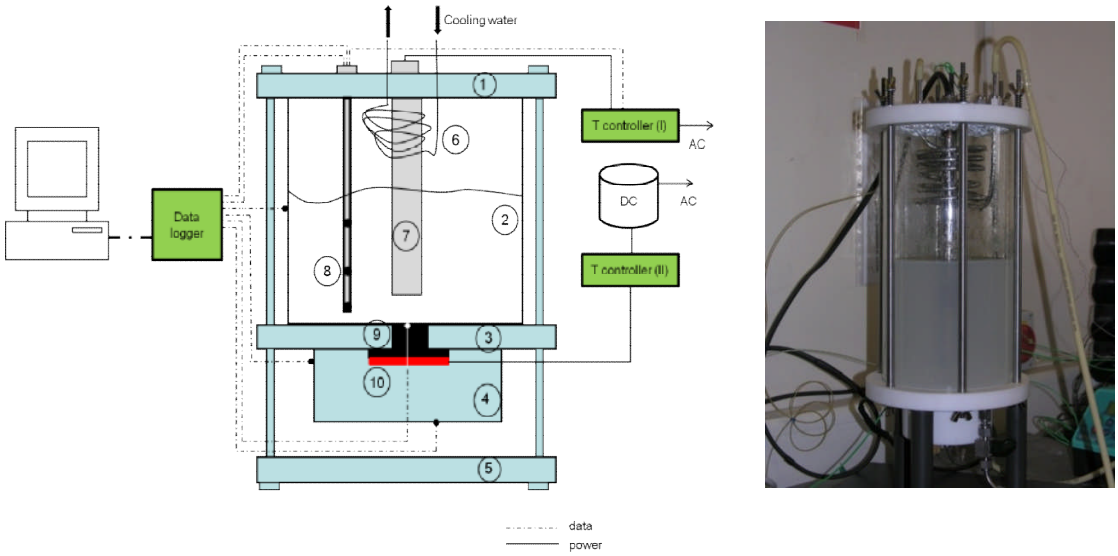

Figure 3.40: The pool boiling test facility. See also tables 3.2 and 3.3

The boiler was a commercially-available cylindrical vessel made of borosilicate glass supplied by YorLab Co., UK. It can withstand high temperature and high pressure. To allow for glass expansion, springs were used between the vessel and the tightening bolts. Liquid filling and drainage were provided from top and bottom of boiler respectively. This configuration was easy to dismantle and clean.

Top and bottom plates, and the bottom heater holder which are part no. 1, 3 and 4 respectively in Table 3.2, were fabricated of PTFE. This is a material that has low thermal conductivity (0.25W/mK), high temperature resistance, light weight and easy machinability. Base of the test rig was made of Acrylic. A stainless steel tube was purchased from Swagelok to make the condenser. The tube in part no. 6 of table 3.2 was of 1.4mx4mmx6mm in length, inner and outer diameters respectively. This tube was bent to make a coil of diameter 80mm. Two ends of the coil were subsequently connected to a rubber tube which runs through a circulation pump into a cooling water bath.

Table 3.2: List of materials for pool boiling test facility

Part no.	Description	Material	Dimension (mm)
1 & 3	Top, bottom of boiler	PTFE	Φ160xH20
2	Boiler	Borosilicate glass	Φ140xH30
4	Heater holder	PTFE	Φ60xH40
5	Base	Acrylic	Φ160xH20
6	Condenser	Stainless steel tube	Φ4xL1400

Ref: Φ – diameter, H-height, L-length

The measurement and controls devices are given in table 3.3. One part of these items was custom-made while the other parts were commercially purchased according to the requirement.

Table 3.3: List of accessories

Part no.	Description	Make	Accuracy
7	Top heater	Elmatic Ltd, UK	N/A
8	K-type Temperature probe	Southern Temp, UK	0.1°C
10	Bottom heater	Elmatic Ltd, UK	N/A
	K-type Thermocouples	TC Direct, UK	0.1°C
	Temperature controller (I)	Fluke 9000	0.01°C
	Temperature controller (I)	Fluke 6600	0.01°C
	DC power supply	Carroll & Meynell Ltd, UK	
	Data logger	NI SCXI 1000	
	Computer	Dell	

The top heater is of cartridge-type with a stainless steel sheath and 1kW capacity. Shown on figure 3.40, this has a 5cm heated length, which is designed to be submerged in liquid. Stainless steel is safe with nanofluids too. A thermocouple embedded in the heater prevents the unit from getting overheated. The top heater is connected to *temperature controller (I)*, see figure 3.41, along with a thermocouple immersed in the liquid. This arrangement raises the liquid to saturation temperature and maintains there.

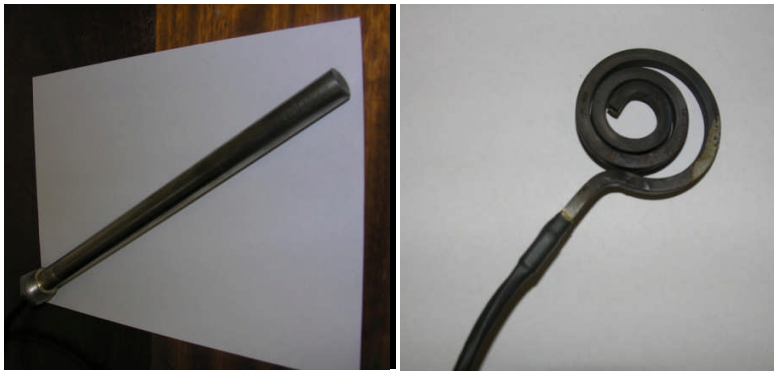

Figure 3.41: Left-top heater, Right-bottom heater

The bottom heater was a coil-shape, where a nickel-chromium core was wrapped in a stainless steel strip. Figure 3.41 provides a photograph. There is an embedded thermocouple as a high temperature cutout. The power cable and the thermocouple cable connect to the *temperature controller (II)*, which in turn connects to a DC power supply. The resistivity of the heater material varies nonlinearly with temperature. Hence heater calibration was needed. Calibration procedure will be described in results section.

Part no. 8 on table 3.3 is a K-type temperature probe, which is a stainless steel rod embedded with three thermocouple tips. This arrangement will measure temperatures of the liquid at three vertical points as indicated on figure 3.40. There are three lead wires coming out of the probe, where one goes to the *temperature controller (I)* and observes the saturation temperature. Other two lead wires go to the NI SCXI 1000 datalogger. The temperature signals acquired by the datalogger are fed to a PC where the signals are subsequently interpreted into numbers by the Labview software on the PC.

In addition to those stated above, there are several thermocouples at various locations on test rig. One goes into the sample from underneath and stays 2mm below the surface and reports temperatures. The surface temperature is deduced from this information. Other thermocouples are placed on glass wool insulation, bottom and sides of heater holder, as well as in the cooling water tank. Temperature data from these locations help to calculate heat losses and also to verify the steady state operation of the system. All thermocouples were calibrated by following the standard procedure of dipping them once in ice slurry and once in boiling water and were verified for conformity with the expected accuracy.

There were major difficulties encountered at the testing stages of the pool boiling test facility. The biggest of them was the vapour bubble formation on the edges of copper coupon. It was found that the bubbles were appearing from the tiny air gap between the circular coupon edge and the surrounding PTFE *(part numbers 9 and 3 respectively)*. Given the press-fit between two components, a clearance has to be expected, however small it is. As they heat up, the expansion will occur. Due to the difference in expansion coefficients of copper and PTFE, it was initially thought the clearance will diminish. In practice however the gap was still sufficient for bubble formation. There were several attempts made to close the gap. Firstly silicon fillers were used. They soon failed due to high temperature. Moreover it seemingly contaminated the nanofluid. Thereafter few kinds of glues were tried on the gap. They too could not withstand prolonged heat in boiling. Despite extensive literature survey and market search, it was impossible to find a lasting and economical solution. The massive effort proved to be futile and problem of edge bubbles persisted. These edge bubbles hindered the view of bubble activities on the copper surface to the high speed video camera. But the search for a solution continued. Few months later during a visit to MIT, this author came across a shrink moisture seal tubing. It melts with heat and perfectly seals the gap.

3.2.6 Boiling on Artificial cavities

An experimental facility was designed and manufactured to examine the boiling heat transfer characteristics on sub-micron size artificial cavities. This equipment was to be operated together with an infra red camera and a spot heater. IR thermometry is the key feature of the present approach. A conventional thermocouple in contrast would need physical attachment, which demands space while introducing a contact resistance.

Since non-invasion of the surface and liquid microlayer should be the most critical features of the test rig, a distant heating arrangement had to be found. A high wattage halogen lamp was chosen. Moreover it offers the added benefits of portability of test rig while eliminating the risk of electricity leakage.

3.2.6.1 The boiling chamber

Recall the aim of this exercise is to examine bubbles originating from artificial cavities on smooth and clean surfaces. Contaminants of all sizes can also act as natural bubble nucleation sites. Cleanliness therefore becomes of paramount importance. As much as contaminants, another

source for unwanted bubbling is the edges of heater. Edges usually are trapped with gases which produce bubbles at low superheats. The chamber should therefore be sealed to prevent contamination and sufficiently wide to avoid the edge effects.

Initial plan was to produce cavities on silicon wafers in Leeds University. They will subsequently be taken to the MIT boiling facility to be tested for bubble nucleation, in conjunction with IR thermometry. Cavity fabrication at Leeds was done using an FIB device with the expert assistance from Dr. Li Chen of Electronic Engineering department. The FIB device in Leeds University is of FEI make. The largest sample it can accommodate for machining is 4x4cm^2. Silicon wafers were diced to this size and cleaned as explained under section 3.2.3. Then the cavities of desired geometries were machined on the FIB. When carried to MIT, it was realized that their boiling facility can easily introduce contaminants to the experiments. As a result, the need arose to develop a suitable test rig. This author and Dr. HD Kim of MIT Nuclear Science & Engineering Department began the designing and manufacturing of the brad new unit. First few designs were tailored for Leeds samples. While conducting test runs, the edge nucleation was experienced. As it was gradually overcome through improved design, the contamination issue was still prevailing. After the learning cycle, the designers understood the need for a paradigm shift in thinking. It ended up designing for a larger substrate and a sealed boiling chamber. Fresh cavities were to be micromachined at the Centre for Nanoscale Systems at Harvard University.

The largest silicon wafer that can be accommodated in Harvard University's FIB device was 100mm in diameter. This information determined the maximum width of the chamber. Centering mechanism for wafers and provisions for wafer interchangeability in-between experiments were essential features to be addressed. Height of the chamber was not bounded but preferably be low for halogen heat to reach the wafer in full strength. The liquid pool will be kept shallow for it to reach the boiling temperature soon.

As far as the raw material selection is concerned, firstly they will have to withstand temperatures above 100°C. They should be compatible with potential boiling liquids of water, ethanol, methanol, and refrigerants. The bottom of chamber should be IR-visible, top should be transparent to halogen light. Side walls should preferably be transparent or semi-transparent to eye vision to observe the interior activities of boiling.

To meet the above criteria a test rig was designed at the MIT by this author and Dr HD Kim with the occasional help from the laboratory staff under the supervision of Professor J. Buongiorno. The unit was manufactured at one of MIT's workshops. Schematic and pictorial views are given in figure 3.42 (and also in Appendix A). It was modest in size and portable. Table 3.4 lists the raw materials.

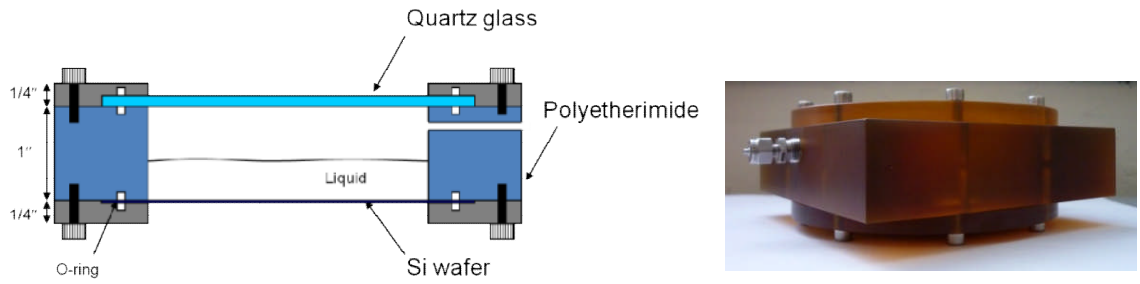

Figure 3.42: The boiling chamber; Left-schematic, and Right-pictorial

The inner diameter of polyetherimide chamber was 78mm. It holds the liquid that is supported in the bottom by the silicon wafer. This gives ample room for the IR camera to capture activities on the other side. Quartz glass on the top is transparent for visible light but opaque to IR. The glass and the wafer at either side of the polyetherimide chamber were clamped using bolts. There were narrow grooves on opposite sidewalls for the purposes of vapour escape and liquid refilling.

Table 3.4: List of materials for the test rig

Part no.	Description	Material	Dimension
1	Top cover	Quartz glass	Φ 100mm, t=5mm
2	Bottom cover	Silicon wafer	Φ 100mm, t=0.28mm
3	Boiling chamber	polyetherimide	Φ75mm
4	O-rings	Rubber	Φ 90mm
5	Vent holes fittings	Stainless steel	N/A

Ref: Φ -diameter, t-thickness

As seen from figure 3.42, the test rig was handy and portable. Length, width and height after assembling were 125mmx125mmx25mm respectively. It could contain 60ml of liquid before reaching the spill level. Presence of only two removable parts i.e. the top and bottom covers underline its versatility as a dust-proof, semi-sealed apparatus.

3.2.6.2 The IR camera

Infrared thermometry is a means of measuring the temperature of an object. In contrast to visible light, any object at lower temperatures above absolute zero emits IR light. This exiting characteristic of IR is an advantage to determine the temperatures of low-temperature objects. A brief presentation of IR vision is given in figure 3.43. The picture is colour-coded such that the red colour represents the warmest regions while the blue colour the coldest. It should be noted that there are black and white images and grayscale images as well.

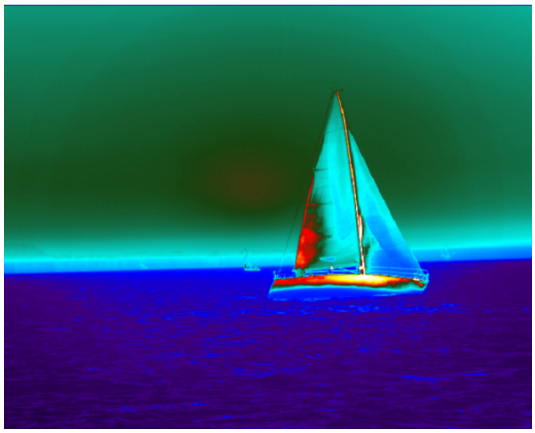

Figure 3.43: IR image of a yacht [*courtesy: FLIR Systems Inc.*]

The FLIR ThermoVision SC6000 IR camera used in this project is capable of receiving infrared light in the spectral range of 3-5 micrometers. Camera and the operation curve are shown as figure 3.44. Electromagnetic signals of other wavelengths will hence be filtered out. This camera is fitted with a Janos Technology Inc ASIO 50mm lens for zooming.

The signals received by the camera are fed in real-time to a PC and converted into readable images and videos. These raw images, produced by ThermoVision ExaminIR software are in gray scale. By using the ThermaCAM software, a colour code can be assigned to raw images. Often it is necessary to post-process the still IR images or image sequences (aka videos) to obtain finer details of events. An example is to estimate the temperature on a particular site and its immediate surroundings on the image. Software called ImageJ is often used for the post-processing of ThermoVision ExaminIR images.

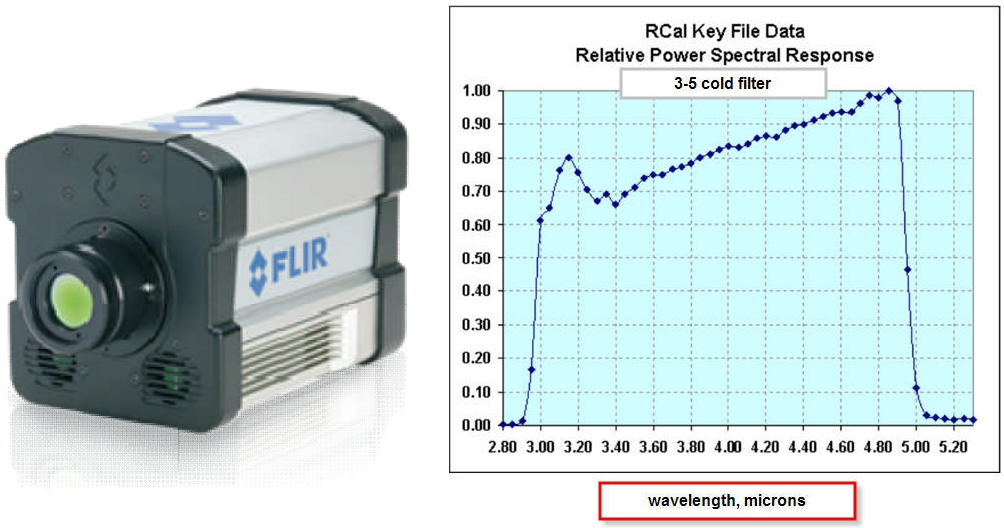

Figure 3.44: FLIR ThermoVision SC6000 camera and its operation curve

The wave theory states that the radiation received by the camera is a summation of signals those are emitted by, transmitted through and reflected on the object under investigation. If each of these components are respectively identified by I_E, I_T and I_R, then equation 3.7 gives a mathematical expression for total radiation *(I)* received by the camera.

$$I = I_E + I_T + I_R \qquad \textbf{Eq 3.7}$$

Here I_R only adds errors to measurements hence are undesired. To minimize it, the surroundings have to be adjusted such that its view factor with the object is very small. The reflective contribution can further be reduced by keeping the surrounding temperatures as low as possible.

3.2.6.3 The heat source

A halogen spot heater pictured in figure 3.45 was imported from Fintech Co Ltd, Japan. The selection was based on the wattage, the focal length and the size of exit aperture. This lamp was rated 36V and 450W, and focal length and the size of aperture were 30mm and 50mm respectively. Then the maximum output heat flux turned out to be 209kW/m^2. By connecting to the DC power supply traded by Electronics Measurements Inc., the heat output was regulated. Applied power at each stage of experiment was calculated by multiplying the respective voltage and ampere readings.

Figure 3.45: Halogen spot heater

To wind up this section, a schematic view of the test rig is presented in figure 3.46. Noticeably this is an assembly of components shown in figures 3.42, 3.44, 3.45 and some peripheral devices. Operation is rather simple where the halogen light heats up the liquid from the top and the IR camera captures the IR intensity from underneath and directs to the PC. The gold-plated mirror turns the IR beam by 90° to feed the camera.

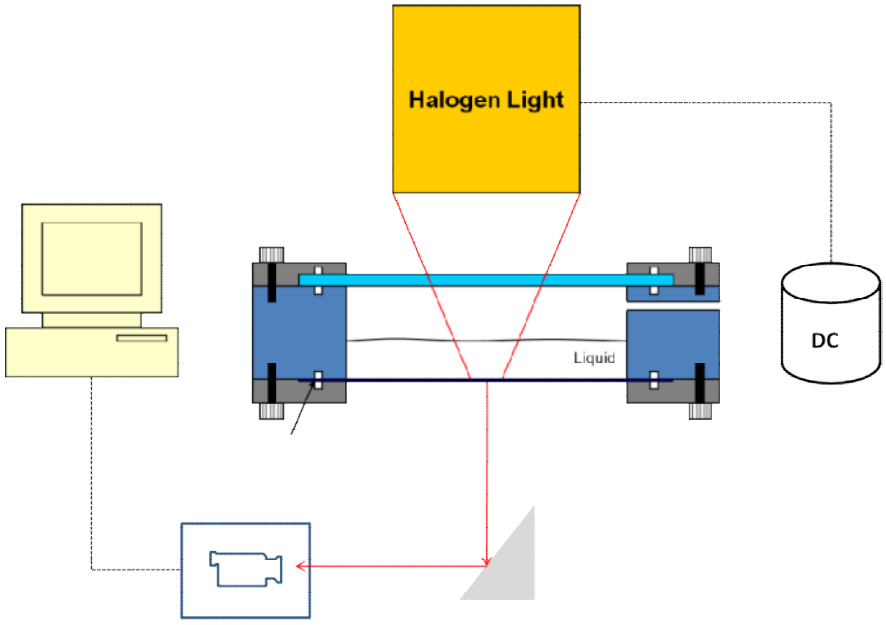

Figure 3.46: Test rig for Boiling on artificial cavities

For the best of the knowledge of this author this was the first time a boiling test rig was successfully developed and tested for zero contamination.

3.3 Summary of the chapter

This chapter generated a discussion on material and methods employed in this research project. It opened up with a description on formulation procedures and went on to present the instrumentation and experimental results on thermal conductivity, rheology and viscosity of nanofluids. Some of these were novel findings and set preamble to further research. One such instance was illustrated by figure 3.21 where the dependence of thermal conductivity on the size of aggregate was featured. The classical theories developed for solid composites could closely predict the thermal conductivity of a nanofluid when the aggregation was embedded into the equations. This underlines the importance of studying the particle aggregation kinetics. Next chapter is dealing with this aspect.

Second half of this chapter was dedicated to present experimental facilities for nanofluids boiling, SAXS, and boiling on artificial cavities. Forthcoming three chapters will discuss the experimental procedures and data acquisition using the materials and methods outlined here.

CHAPTER 4 - Results & Discussion II

Small Angle X-ray Scattering for nanofluids

This chapter describes the small angle x-ray scattering experiments conducted at the Diamond synchrotron light source in Oxford UK with the hope of studying particle structuring and aggregation kinetics of nanofluids. It was earlier shown that the need for SAXS arose because of the deficiencies in light scattering and electron microscopy techniques to meet the demands for high speed data acquisition and wet state sample analysis simultaneously.

Securing bematime at Diamond was a competitive process. Typical timeline between submission of a research proposal and securing a bematime is approximately one year. Being the beamtime is precious as such, the preparation and prior knowledge of operations are the keys for a successful SAXS session. It will be seen from the forthcoming discussion that data analysis and interpretation are the crucial parts of post-experimental work.

4.1 Calibration and the hardware

The detector angle and the camera length were selected to suit the particular experiment. However the upper limit of the camera length of Diamond I22 beamline was 6meters. Beamline scientists calculated the corresponding *q range* as 0.0055-0.1Å^{-1}. Now from eq 2.27 the interval of observable lengthscales *(d)* becomes 114.2-6.28nm. Also with the knowledge of the wavelength of x-ray beam *(λ)*, the detector angle *(2θ)* can be calculated. For beam energy of 12.4keV, the *λ* would be *1 Å.* Then the *2θ* happens to be 0.92°. After setting these geometries for hardware, the standard procedure was that the beamline scientist calibrates the *q-axis*. The user does not interfere with the calibration procedure.

A material with well defined diffraction peaks is used to calibrate the *q-axis*. Customarily it is either Silver Behenate [237] or Rat tail collagen [238]. When they are exposed to x-ray beam a periodic profile of peaks can be visualized similar to those shown on figure 4.1. As a result of calibration, a useful correlation appears as follows.

$$q = 4.02529 \times Channel\# - 2.58858 \times 10^{-5}\ \mathring{A} \qquad \textbf{\textit{Eq 4.1}}$$

Channels are the locations where diffraction intensities are recorded on the detector. It is clear from this description that the *q-axis* calibration is specific to a given camera and beam setting.

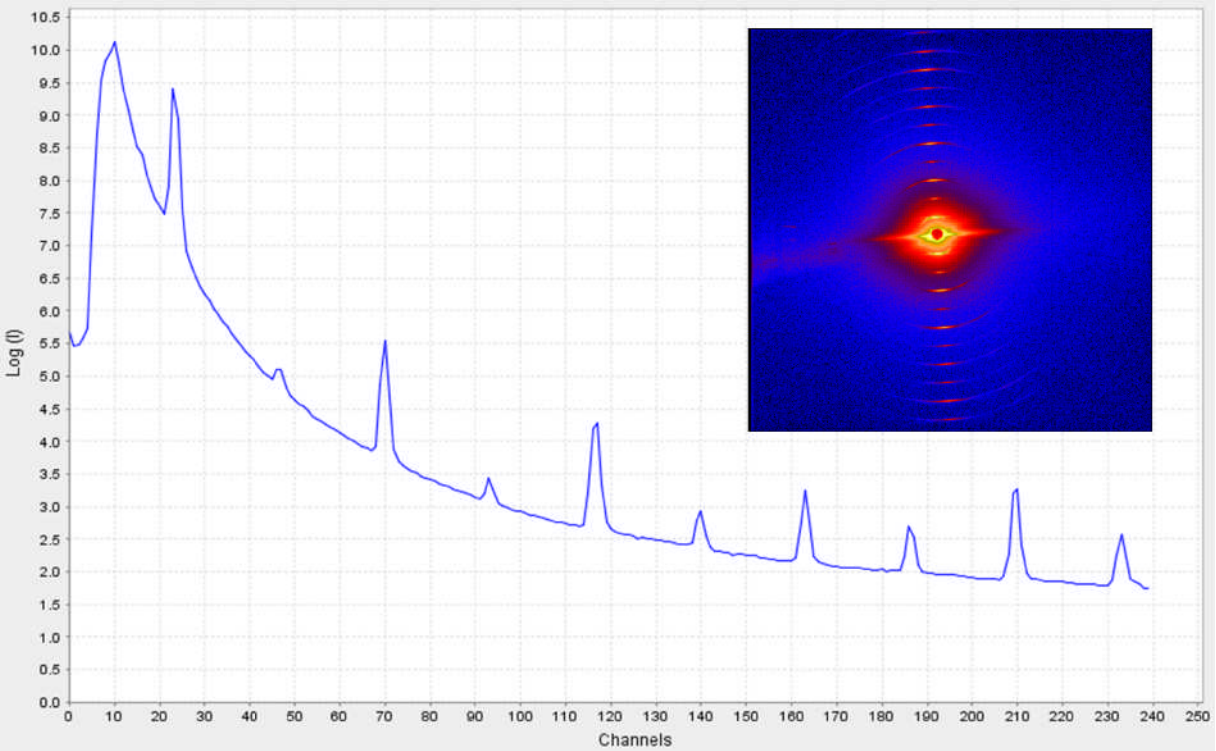

Figure 4.1: Calibration with Rat tail collagen

Beam slit of I22 is shown on figure 4.2. It was rectangular in shape and 340x300µm in size. The x-ray beam exits through the beam slit and shines on the sample.

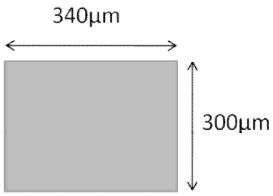

Figure 4.2: Diamond I22 beam slit

The sample should be aligned with the beam slit for proper scanning. By movement of the sample table in horizontal and vertical directions the alignment was obtained. For the case of several samples mounted on one sample rack, the alignment position for each cell was noted down as x, y and z coordinates prior to experiment. Appreciate that the present work is time-intensive. The samples have to be scanned as soon as possible before the particles cease restructuring. Hence the table movement coordinates were taken at the calibration stage, so that when it came to operation the sample table can quickly be moved to align the particular cell with the beam slit.

Beam stop is another important part of the synchrotron beamline. Shown in figure 4.3, the beam stop is placed between the sample and the detector. The purpose is to absorb the straight-through (unscattered) beam, preventing it from hitting the detector and damaging it. For present experiments the beam stop was placed in the middle of the detector.

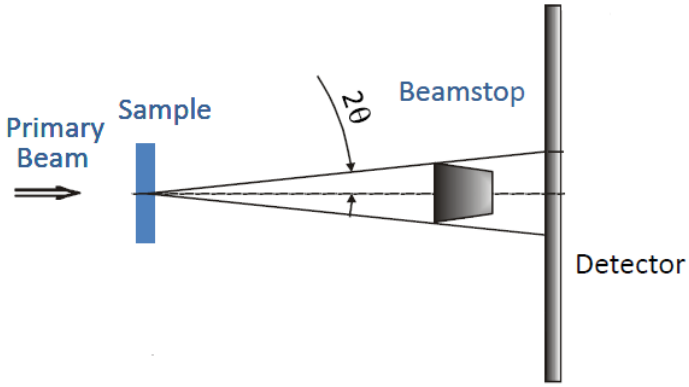

Figure 4.3: The beam stop

To obtain reliable scattering data, a steady x-ray beam is of paramount importance. This is known as beam intensity. In practice an x-ray beam would decay with time and this is why the re-injection of electrons is provided periodically. However the beam intensity should not change over the duration of experiment, which is a problem known as the beam decay. VDUs at I22 beamline show the status of beam in real time. It confirmed that the beam was in excellent stability and did not demonstrate decay during experiments. As a standard procedure however, a new bunch of electrons are injected into the storage ring of synchrotron machine in every 24hour interval.

4.2 Experiments

Samples listed on Table 4.1 were to be analyzed. They were formulated in the Leeds University laboratory. Only three nanofluids were chosen to examine during the visit to Diamond, considering the possible challenges and delays associated with this novel work.

Table 4.1: Nanofluids

Material	Primary particles		Wet state		Base liquid
	Shape	Ave size (nm)	Shape	Ave size (nm)	
TiO_2	Spherical	25nm	Aggregates	130nm	Water
Al_2O_3	Spherical	45nm		145nm	
	Acicular	10x150nm		n/a	

Nanoparticle aggregation is sensitive to solution pH and the temperature, which is more pronounced near the iso-electric point (IEP). The unknown was how fast they would aggregate, characterized by the aggregation time constant, which was yet to be experimentally determined. To get a start and test the procedure, it was decided to conduct first few experiments around the IEP. The IEP values for these nanofluids had been measured prior to the experiments. Moreover the particle concentration was kept low at 0.5wt% (5000ppm) to obtain neat scattering data by avoiding multiple scattering. The samples were tuned to suit the objectives in the I22 users' laboratory. Details are given on Table 4.2. Note that measured amounts of NaCl salt was added to some TiO_2 samples aiming to speed up aggregation.

Table 4.2: samples for SAXS experiments

Nanoparticle	Base liquid	Wt%	pH
Spherical TiO_2	Water Water+ 10mM NaCl Water+ 20mM NaCl	0.5	5.9, 6.0, 6.3, 6.7 7.0 6.5, 7.0
Spherical Al_2O_3	Water	0.5	6.3, 7.2, 7.5, 7.8, 8, 8.7, 9.2
Acicular Al_2O_3			7.6, 8.5, 9.4

Since the aggregation is rapid around the IEP, there was the challenge of quick setting up of the sample in the Beamline and immediate exposure to x-ray beam. The set up and the personnel had to be ready to kick-start the experiment, while the pH-monitored samples were on the magnetic stirrer waiting to be loaded onto SAXS cells.

4.2.1 Data collection

The experimental procedure was as follows. A sample in Table 4.2 was on magnetic stirrer while being monitored for the targeted pH. A few milliliters from the sample were fetched using a syringe fitted with a needle. The sample was then injected into a SAXS cell (figure 3.39). After ensuring it was leak proof, the cell was hurried to the beamline (figure 3.35) and fitted on the

sample rack. After a quick glance to confirm that the sample cell was aligned with the beam slit, the safety sequence was followed. Popularly known as 'search' among beamline users, the safety procedure confirms there are no people left inside the experimental hutch at this time. While being manually searched, a noisy siren warns anyone inside the hutch to vacate it. The interlock system requires three buttons to be pressed in sequence within two minutes. Upon the completion of search, the doors are locked, x-ray beam is on and warning signs and lights are on. A photographic view from outside is given in figure 4.4. From then onwards all controls, observations and manipulations have to be executed from the control cabin.

Figure 4.4: Experimental hutch ready for x-ray beam

The x-ray beam scans the sample. Diffracted x-rays are captured by the SAXS detector at the far end of beamline. The duration of scan is adjustable to suit the user but usually in the order of few seconds. The duration is important to ensure that the detector does not get saturated. Too short durations on the other hand may miss out important structural changes occurring in the sample. After the period of scanning, a frame is produced on the monitor. The frame gives information about the sample, the precious moment a researcher is waiting for. Two such frames would reveal time-dependent information. Beam pause between two frames, known as dead time, can be decided by the user. For all experiments but one conducted under this study the dead time was fixed to 1milisecond. Tables 4.3 and 4.4 give summaries.

Table 4.3: Experimental details for 20°C tests

Sample	pH	Sample age (min)*	No of frames	Test duration (s)
TiO_2-W	5.9	0	90	900
		60	10	100
		180	10	100
	6.0	0	60	600
		30	15	1050[#]
		60	10	10
	6.3	0	60	600
		60	60	600
		90	10	10
Spherical Al_2O_3-W	6.3	0	90	900
		60	10	100
		120	10	100
	7.5	0	90	900
		60	10	100
		300	10	100
	7.8	0	90	900
		30	90	900
	8	0	10	100
		120	10	100
	8.7	0	90	900
	9.2	0	60	600
		15	10	100
		90	10	600
Acicular Al_2O_3-W	7.6	0	60	600
		60	60	600
		105	10	100
		225	10	100
	8.5	0	60	600
		60	60	600
		120	10	100
		240	30	2100[#]
	9.4	0	90	900

*Ref: *since setting up on beamline. [#] one minute dead time*

All experiments stated on Table 4.3 were conducted under static conditions and at 20°C. Only a few experiments were conducted at 60°C. These are outlined on Table 4.4.

Table 4.4: Experimental details for 60°C tests

Sample	pH	Sample age (min)*	No of frames	Test duration (s)
TiO_2-W	6.7	0	60	4200[#]
Spherical Al_2O_3-W	7.2	0	90	900
		30	60	600
		60	60	600
Acicular Al_2O_3-W	8.5	0	90	900
		30	60	600
		45	60	600

Background subtraction is a very important step in data processing exercise. Respective backgrounds for the samples used in this study were water at 20°C and 60°C, water+ 10mM NaCl at 20°C and water+ 20mM NaCl at 20°C. These backgrounds were scanned in a similar style to that of nanofluids samples.

4.2.2 Data processing

While the samples were being scanned by x-rays, a contour of scattering appeared on the monitor in control cabin such as the picture in figure 4.5. In the background of these images, SAXS data files were being automatically generated on a UNIX platform in BSL and OTOKO formats.

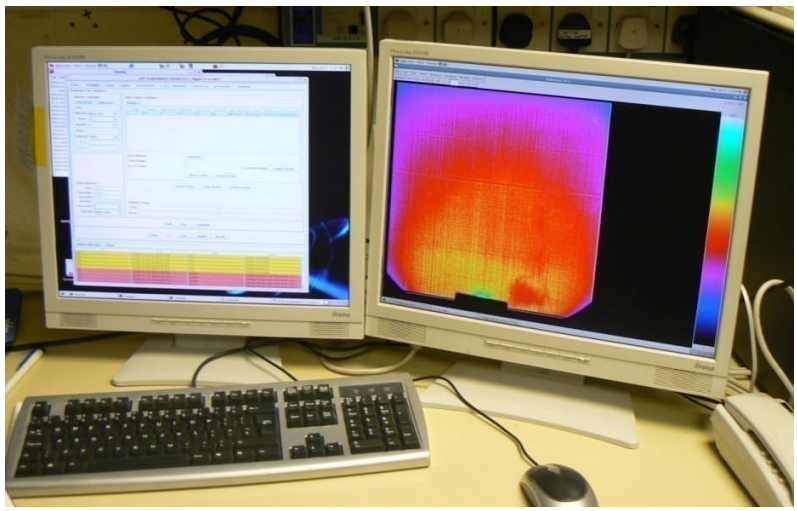

Figure 4.5: SAXS experiment in progress

The in-house program called DREAM (Data Reduction Automatically Made) was used to convert UNIX files into ASCII files. These ASCII files were then imported to SAXSutilities software for frame averaging and background subtraction. SAXSutilities also offers the facility of fitting the SAXS data

to several standard models found in literature. Now the tedious data reduction task is over and the data are ready to be exported to common graphics software such as Origin or Excel.

4.3 Data analysis

It is customary to analyze SAXS data by plotting them in the form of intensity *(I)* vs. scattering vector (*q)*. The *q* was described in Literature Review chapter. However the raw data does not contain *q* as such but the channel number. Conversion had to be obtained using the equation 4.1.

In *I vs. q* plot, the information of size and morphology are contained in the shape of the curve. A time dependent change in size will be symbolized by a shift of knee (the *q* value that corresponds to the highest intensity, I_{max}) in respective curves. To extract this information from SAXS data, several data files stated on Tables 4.3 and 4.4 were plotted. But all of them did not sufficiently exhibit information on time-resolved change of size. These are furnished in Appendix A. In view of giving an overall picture at this stage, figures 4.6 to 4.7 are presented. Only the experiments that indicated significant change in profiles were deemed worthwhile and will be explored to a greater depth.

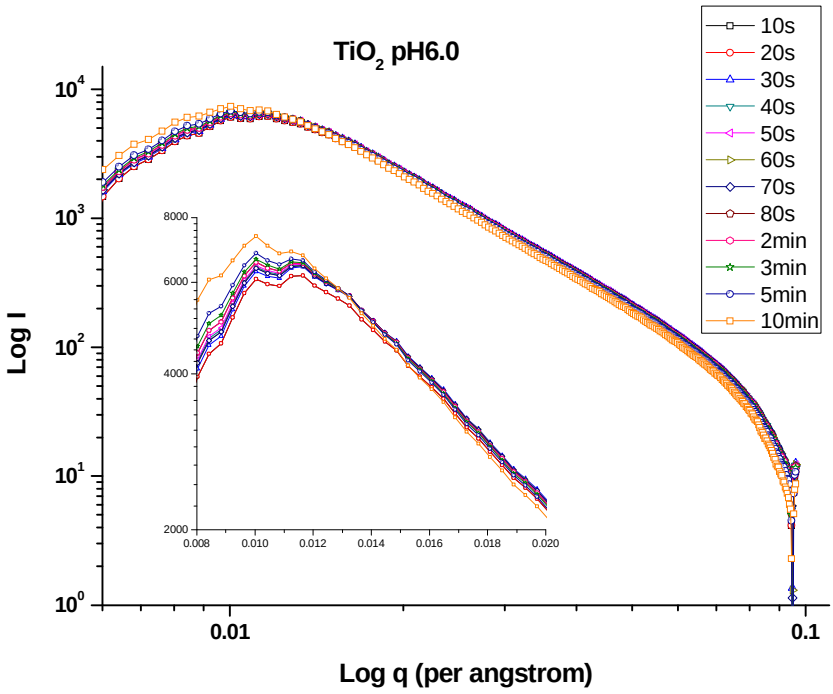

Figure 4.6: SAXS patterns of TiO_2-water nanofluid. pH6.0, 20°C

One would expect TiO_2 nanofluid to change its size and shape significantly around the IEP of 6. But the SAXS patterns on figure 4.6 shows very little change with time. Within the experimental duration of 15 minutes, the knee *(I_{max})* had only slightly shifted in 7th frame that corresponds to 70 seconds from the start of scanning. Again from 8th frame onwards there was no further change of knee. Inset shows finer details of the knee shift. With help of the correlation between *q* and lengthscale *(d)*, the corresponding change in *d* between 7th and 8th frames can be calculated. It turns out to be 8.6nm. This could mean movement of a particle or aggregate (i.e. the change of interparticle distance), or reorientation of particles within an aggregate (intra-aggregate spacing). However the exact interpretation of the lengthscale needs further analysis and is discussed further on in this chapter.

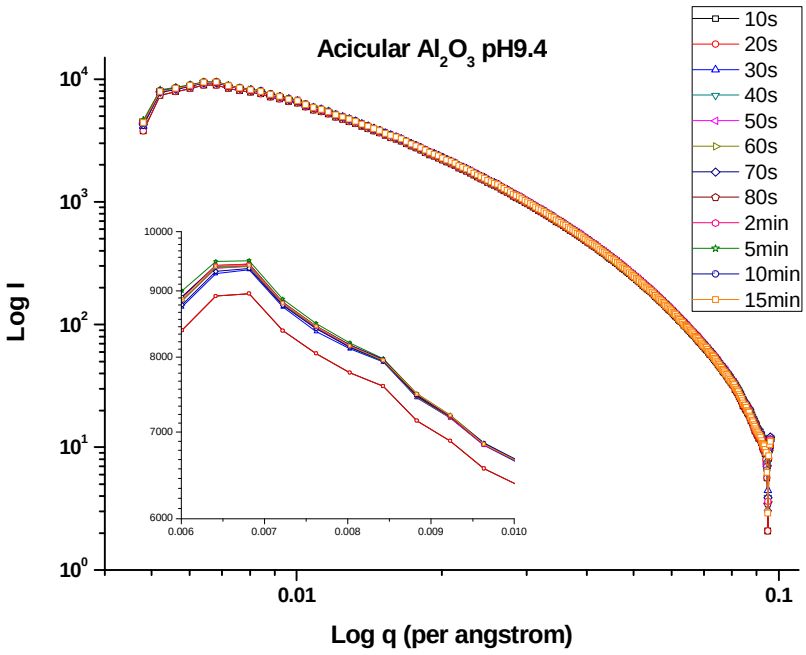

Figure 4.7: SAXS patterns of acicular Al_2O_3-water nanofluid. pH9.4, 20°C

Near its IEP of 9.4, acicular Al_2O_3 nanofluids did not exhibit a noticeable change. There was no horizontal movement of the knee in a course of 15 minutes as elaborated on the inset of figure 4.7. With reference to all TiO_2 and acicular Al_2O_3 nanofluids, the observation was always similar to what shown above; either the change was very small or unnoticeable. A possible explanation is that the nanoparticles had completed their aggregation process during the pre-scanning preparations (note that it was approximately 5 minutes between the filling to the cell and first

SAXS frame being captured). It can also be argued that the duration of experiment was insufficient for lengthscales to change. The second argument disqualifies due to the fact that some of these samples were scanned throughout 4hours with breaks in-between. It is common knowledge that around IEP, the particles aggregate and settle rapidly.

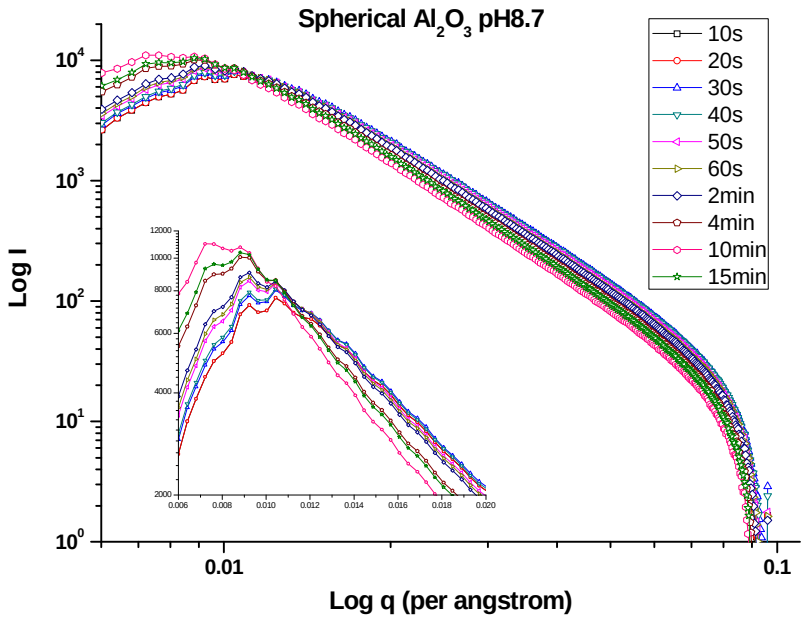

Figure 4.8: SAXS patterns of spherical Al2O3-water nanofluid. pH8.7, 20°C

The example given on figure 4.8 is for spherical Al_2O_3 nanofluids. Within experimental duration of 15 minutes, value of *d* had changed from 60.2 to 71.2nm. Furthermore in a 60°C experiment, there was a similar magnitude of change in *d* in 5minutes. Arguably the spherical Al_2O_3 nanofluids have behaved encouragingly different from its acicular counterpart as well as TiO_2. Therefore it would be fair for the rest of this chapter to focus exclusively on spherical Al_2O_3 nanofluids.

4.3.1 SAXS data

Consider figure 4.9. It presents data extracted from a 15minutes long SAXS experiment of spherical Al_2O_3-water nanofluids. There is a horizontal shift of knee with time. Change in *q* (hence *d*) has taken place at 60s, 560s and 580s. Calculations show the *d* had increased from 62.6nm to 92.1nm. This is a significant increase in lengthscale of 30% in magnitude. This size information is plotted on figure 4.10.

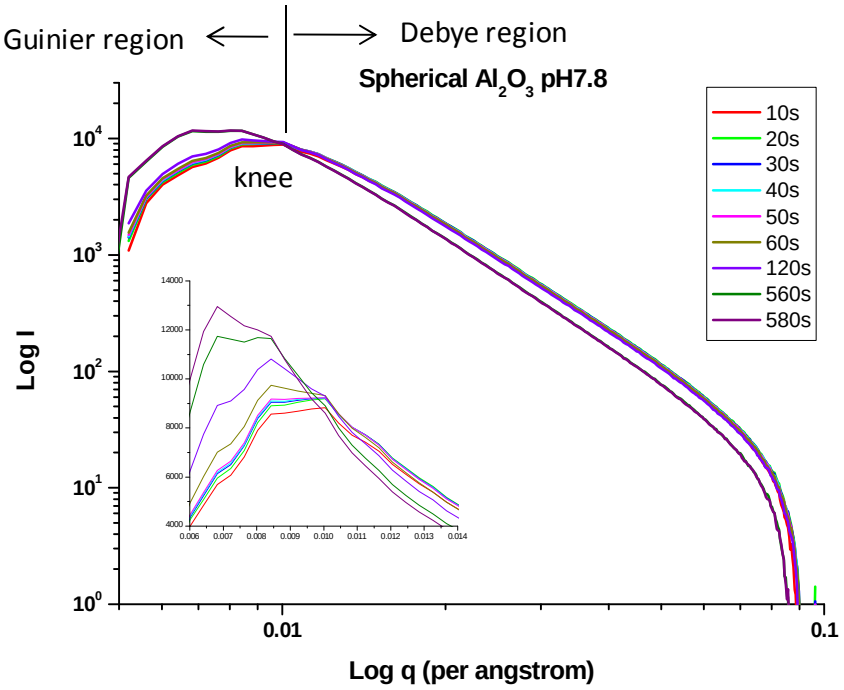

Figure 4.9: Knee shift for spherical Al_2O_3-water nanofluid, 20°C

Also marked on figure 4.9 are the knee position (which in deed has shifted with time), and the Guinier and Debye regions. In principle these two regions are located respectively to the left and right hand side of the knee. Slopes of SAXS data plots give important information about the sample [35], which was previously elaborated under the literature review. The slope of a Guinier plot is equal to one third of the radius of gyration *($R_g/3$)*. In turn the radius of a solid spherical particle *(R)* is related to R_g such that *R=Rg/0.77*. In the Debye region the shape of the SAXS curve gives information about particle morphology [215, 217]. In view of extracting such details, figure 4.11 was constructed.

Now consider figure 4.10 to discuss the change in lengthscale. Three step-changes occurred at 60s, 560s and 580s respectively since the nanofluid sample was exposed to the beam. Another way to look at this is, the location on detector where the maximum scattering intensity was recorded has moved at these time spots. It can be speculated that the increase in *d* could be due to a change of interparticle or inter-aggregate distance, or intra-aggregate distance. What follows is an attempt to interpret this observation in a meaningful way.

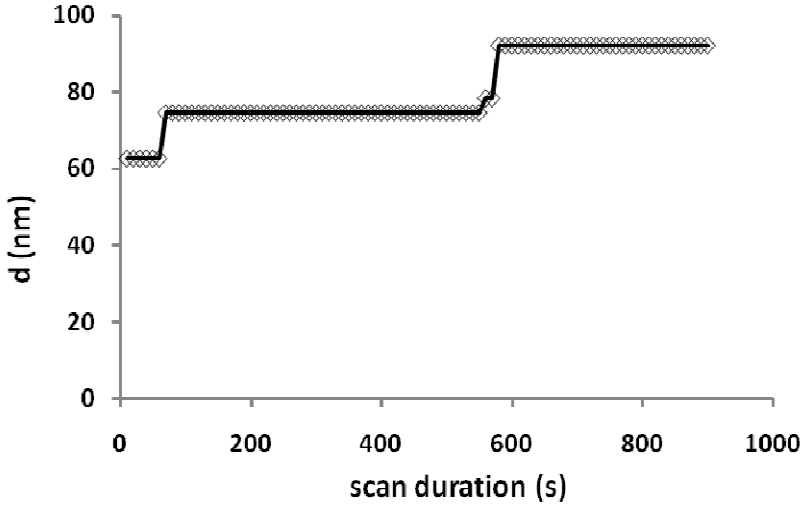

Figure 4.10: Time dependent change in size

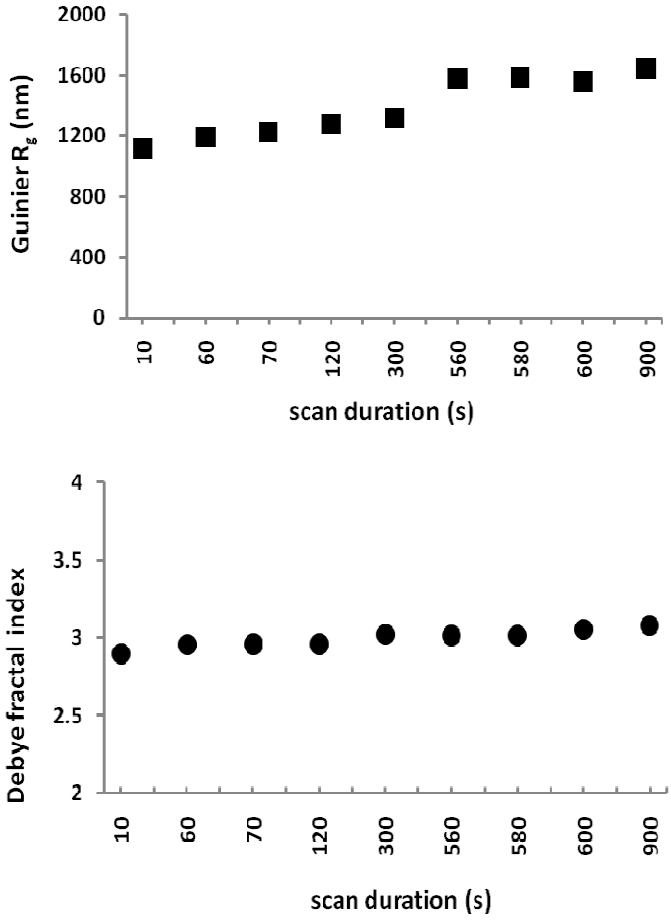

Figure 4.11: Shape analysis of SAXS curves

The *Guinier R_g vs Scan duration* plot demonstrates that the radius of gyration in the first few seconds of the experiment was close to 1100nm. Then it gradually increases and stabilizes near 1650nm. It is worthwhile to note that the Guinier's law requires fulfilling three conditions for it to be accurate for data interpretation. Firstly it needs $q<<1/R_g$, secondly the sample should be dilute for particles to scatter independently, and thirdly the sample should be isotropic so that the particles take random orientations.

Figure 4.11 also plots the Debye fractal index *(D_f)*. There is a gradual increase in D_f from 2.9 to 3.1, during the course of this experiment. According to literature [239-240], $D_f<3$ signifies mass fractals of rough surface and less dense core. $D_f>3$ is for surface fractals of rough surface and solid core. In the present context of Al_2O_3 nanoparticles, D_f ranging between 2.9 and 3.1 may symbolize the existence of aggregates. Lee et al. [219] describes aggregates as mass fractals.

On the other hand a change in *d* is a change in lengthscale. In principal this can have several meanings. This could either be interparticle, inter-aggregate or intra-aggregate scattering. Does this represent particle aggregation or settling in this instance? Although 62.6nm to 92.1nm increase is substantial for nanoparticles, given the polydispersity of Al_2O_3 (shown in figure 4.12), more evidence is needed to explain the nature of lengthscale in question.

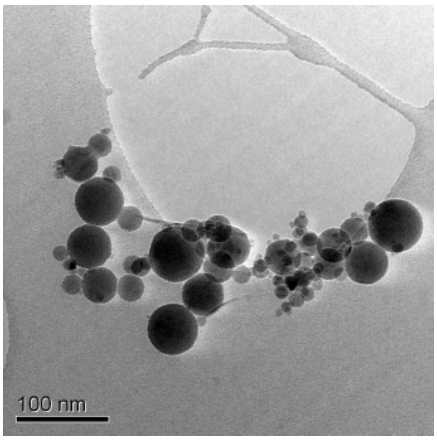

Figure 4.12: Polydisperse Al_2O_3 nanopowder

It would be helpful if few more experiments were conducted on the SAXS beamline. However access to synchrotron facilities is limited and long waited. Due to this reason further SAXS investigations had to be spared as future work. Instead it was decided to use photography and microscopy methods for further data gathering.

4.3.2 Settling studies

The experimental plan was as follows. Two samples of Al_2O_3–water nanofluids were reproduced mimicking the SAXS samples. The samples were at pH 7.8 and pH 6.5. The Al_2O_3 nanoparticles were spherical in shape and taken from the same batch that was used to formulate SAXS nanofluids. For the photographic study, the particle settling in these samples were periodically photographed at room temperature using Nikon Coolpix8800 digital camera. For the SEM study, a droplet was fetched from each sample and deposited on SEM stub simultaneously. In a similar style, droplets were deposited on glass substrates for drying and observation under Nikon Eclipse TE2000 optical microscope.

4.3.2.1 Photographic study

Featured in figures 4.13 and 4.14 are the photographs of two samples. Duration of each test was 60 minutes. The heights of particle column were estimated from post-processing of photographs.

Figure 4.13: settling in Al_2O_3–water nanofluids pH7.8 at room temperature

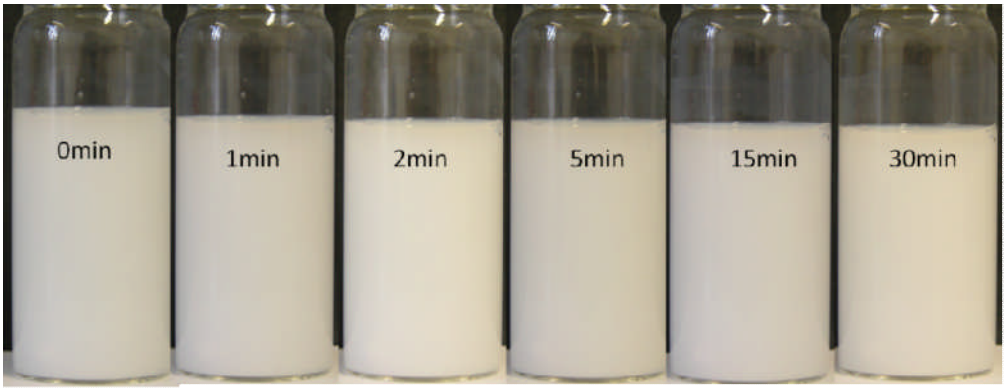

Figure 4.14: Al_2O_3–water nanofluids pH6.5 at room temperature

As seen from the picture, there was rapid settling occurring in the first two minutes in the pH7.8 sample. From 4 minutes onwards, the settling rate became slow and steady. As expected from the stable pH6.5 sample, no settling was visible. Settling rate was determined from the gradient of the plot of *height of interface vs. age of sample* shown in figure 4.15. The reading error was determined by taking three eye-readings of the interface height. However the error bars are too small to be shown on the plot.

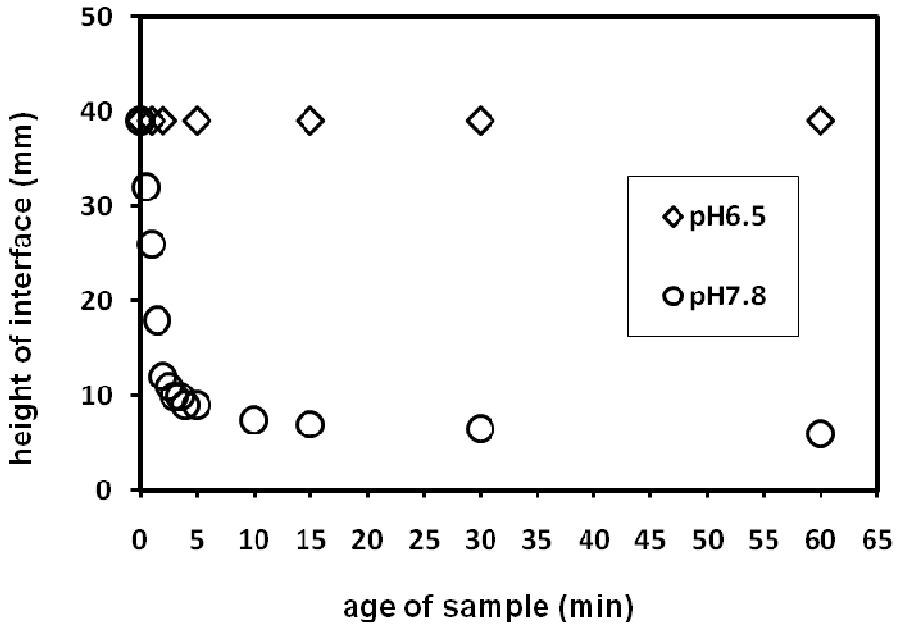

Figure 4.15: Settling rates for Al_2O_3–water nanofluids

Life in the first 20 minutes of the unstable sample is of interest for this study. Had this been mounted on SAXS beamline, it would be 10 minutes before acquiring the first frame. From then onwards the scanning will progress and the data is expected to look reproduce figure 4.8. In the time interval of 10 to 20 minutes the settling rate calculated from figure 4.15 is in the order of 0.3 to 0.2mm/min.

For low Reynolds number and low concentration suspensions of spherical solid particles, the Stokes settling equation expresses the settling rate U_t in terms of particle diameter d, density difference between solid and liquid $(\rho_s - \rho)$ and viscosity of liquid μ as follows.

$$U_t = \frac{d^2(\rho_s - \rho)g}{18 * \mu} \qquad \textit{Eq 4.2}$$

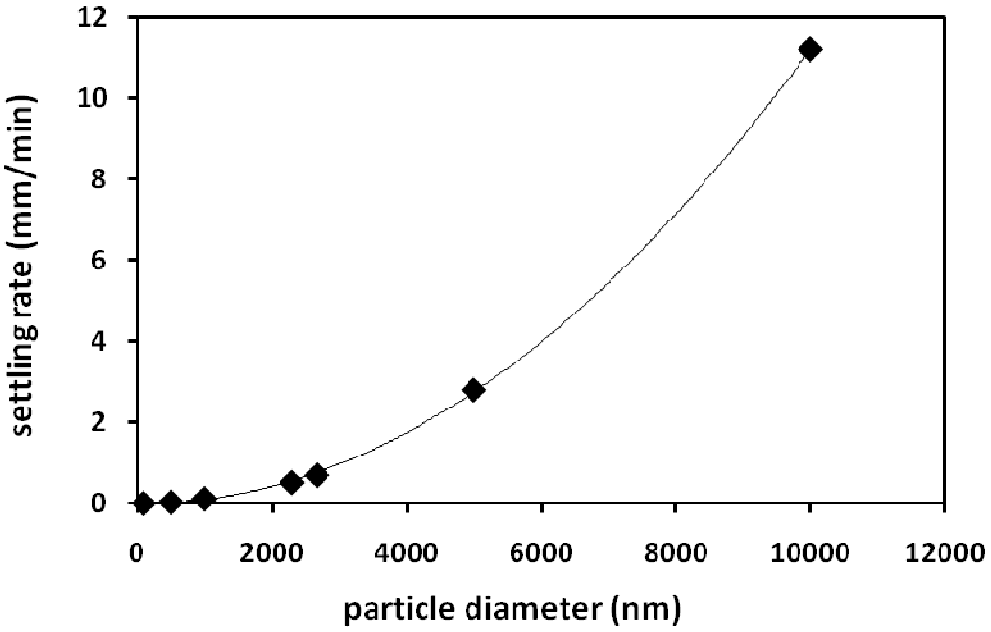

Figure 4.16: Predictions from Stokes law

If Stokes equation is applied to an Al_2O_3 sphere suspended in water, a 0.3 to 0.2mm/min settling rate will correspond to a particle diameter of 1.5µm. However if a certain porosity is assumed for the spherical object, then due to ρ_s becoming smaller the particle diameter will increase. It is well known fact that a nanoparticle aggregate usually has high degree of porosity.

4.3.2.2 SEM study

The objective of acquiring SEM images was to estimate aggregate size distribution and their shapes. Recall that the droplets were carefully fetched each time from the middle of liquid body. SEM was zoomed in to view particle assemblies from micron to nano sizes. The images on figure 4.17 cover the first 3 minutes of settling experiment of unstable nanofluid. Given in figure 4.18 are the stable samples.

Seemingly the droplets from the unstable sample have dried up in a systematic style. Further explanation can be given in conjunction with figure 4.13. The SEM image at time zero (0s) is corresponding to the sample before starting the separation. Apparently it is the image on figure 4.17 that consists of a continuous solid phase. As the time passes from 0s to 30s to 60s etc., this bright solid ring gradually breaks into pieces. The longer the elapsed time, the smaller the sizes of fractals those appeared on the SEM images. Possibly this indicates the larger objects getting

settled in the early stages. In later stages the droplets fetched from the sample bottles had very few big objects. As a result, when these droplets were dried and observed under the SEM, majority of the fractals were small. Figure 4.17 therefore clearly establishes as a fact the variation of size of fractals with the age of suspension.

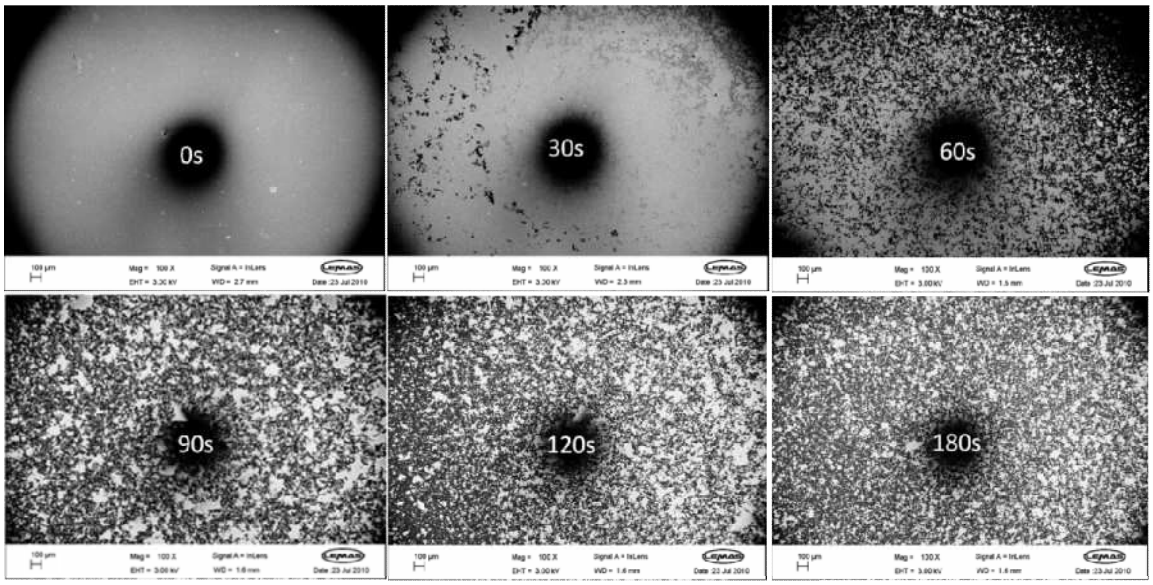

Figure 4.17: SEM images of unstable Al_2O_3–water samples. Mag=100x

A systematic study that uses electron microscopy to visualize an aging particle suspension has not been found in literature. Hence this can be regarded as a fresh approach to examine nanofluids. Since this is the introduction of a new methodology, it can be expected that there will be finer usage of this principle.

The 180s sample was further zoomed-in to see the details of aggregates. These images are given on figure 4.19. Note the scale bars in clockwise direction; 10 µm, 1 µm, 1 µm and 100 nm respectively. Also note that the fractals were of many sizes. They were having a large porosity.

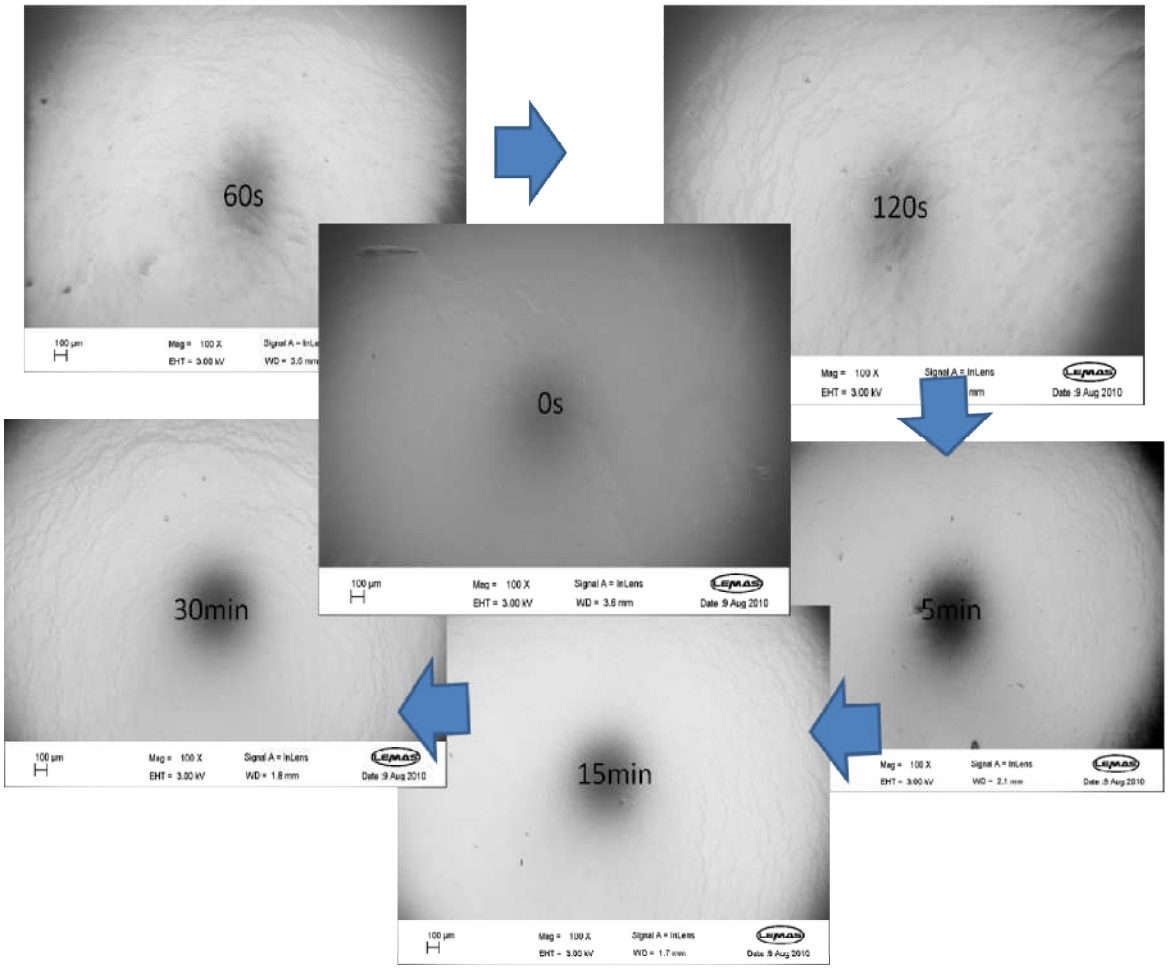

Figure 4.18: SEM images of stable Al_2O_3–water samples. Mag=100x

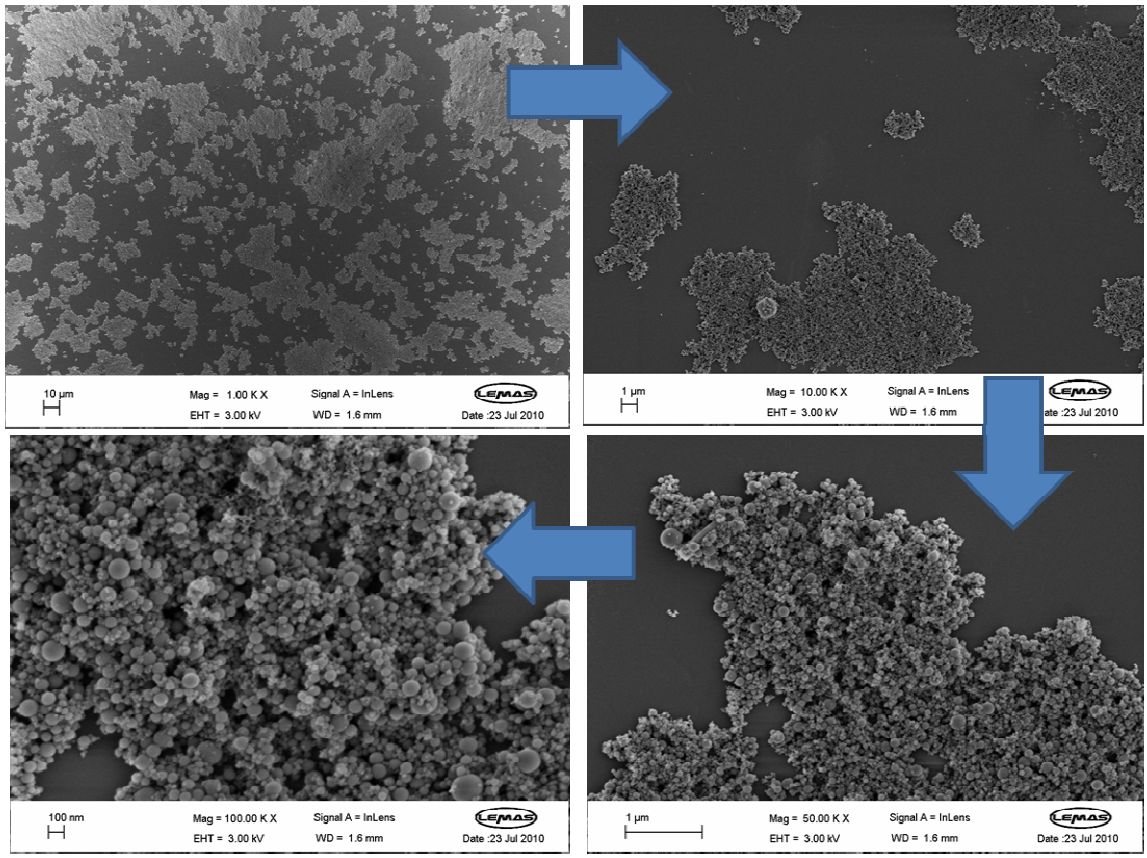

Figure 4.19: Magnified views of 180s sample

More evidence for the aggregate (fractal) size emerged from optical microscopy. Although it is low in resolution, the optical microscope (OM) offers the advantages of a large field of view and ease of handling. Unlike SEM, it can image drying droplets too. In order to represent a big collection of systematic OM images, three are featured in figure 4.20.

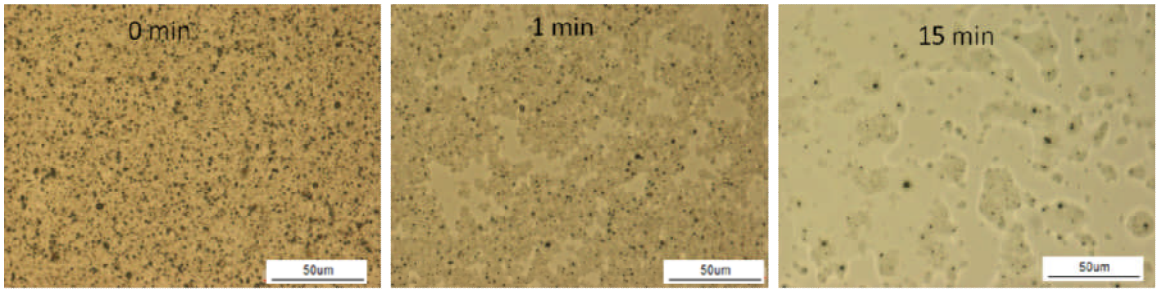

Figure 4.20: Dried droplets of unstable sample. Scale bar is 50 µm

The picture portrayed by OM images synchronize with that of SEM images in terms of the fractal population decreasing with time. They are diverse in size, although the vast majority are visible to naked eye, which suggests they are of micrometers.

4.3.3 Particle aggregation

Aggregation kinetics is characterized by the Brownian diffusion. The average Brownian velocity of a particle *(v)* can be estimated using the Boltzmann constant *(κ)*, solution temperature *(T)*, and diameter *(d)* and density *(ρ)* of the particle.

$$v = \sqrt{\frac{18\kappa T}{\pi \rho d^3}} \qquad \textit{Eq 4.3}$$

If the knee changes seen in SAXS data were caused by aggregation then the Brownian velocities should support that claim. Given in Table 4.5 are values of *v* calculated from equation 4.3 for some arbitrarily chosen particle sizes of Al_2O_3. Temperature *T* was assumed as 293K.

Table 4.5: Brownian velocity

d(nm)	v(ms^{-1})
10	2.42
100	7.64E-02
1000	2.42E-03
5000	2.16E-04
10000	7.64E-05

From TEM images it was confirmed that the largest Al_2O_3 particle was in the proximity of 100nm. It corresponds to 0.0764ms^{-1} in Table 4.5. In fact the size of SAXS beam slit was 340x300µm. A particle travels in the aforementioned speed would cross the beam slit in a fraction of a second. Thus the Brownian velocities become irrelevant in the present context.

4.4 Summary of the chapter

SAXS investigations were conducted using water based titania and alumina nanofluids. The titania nanoparticles were spherical in shape whereas alumina nanoparticles were spherical and acicular in shape. When plotted on *I vs q* axis, the shape of curves was nearly identical. Moreover the curves produced by the Al_2O_3-water samples closely resemble the plots of Lurio [221] obtained for

their Al_2O_3-EG nanofluid. However the SAXS data patterns for certain samples appeared to be changing during the course of exposure to x-ray beam, demonstrating a time-dependent phenomena. One set of data was separated from others for deeper analysis. This was the dataset for water based spherical alumina nanofluid. pH of this sample was at 7.8. After the data analysis, it emerged as a fact that the SAXS data on their own could not convincingly explain the events in the nanofluid sample. Especially it should be appreciated the difficulties to interpret SAXS data of a highly polydispersed system like those studied here. Although there are methods and tools to analyze such systems [241-243], they need specialized expertise which is beyond the timeline of this work and hence saved for future.

As a result further explorations were needed to fill the gaps in the interpretation of present data. Considering the limited access to SAXS experimental facilities, it was decided to conduct supplementary experiments in the university laboratories. These were the classical settling experiments, with the help of microscopy and camerography. Lastly the data and observations from all techniques, viz., SAXS, SEM, Optical microscopy, photography and theoretical analysis were compared and contrasted. It can be stated that the SAXS data were more of reflecting settling phenomena of particles rather than aggregation. Explanation goes as follows.

Firstly consider the Guinier R_g in figure 4.11. It was between 1116nm and 1642nm throughout experiment. Now keep it aside for a while. Secondly consider the settling experiments. The settling rates of the unstable nanofluid sample shown in figure 4.13 were in the order of 0.2-0.3mm/min. With help of equation 6.2, it was shown that these settling rates will correspond to particles of radius 1116nm and 1642nm with porosities of 35-45%. Thirdly consider the sequence of SEM images of the unstable nanofluid featured in figure 4.18. By eye observation of these images it would be reasonable to assume the Al_2O_3 aggregates to have porosities in the order of 35-45%. Therefore it would be safe to state that the SAXS experiments have very closely predicted the settling phenomena of nanoparticle aggregates.

This author is confident that this is the first time the small angle x-ray scattering technique has been used to estimate the particle settling rates. Yet the significance of this approach is appealing. The SAXS is a fast, powerful and accurate tool on its own. Being a technique that scans the sample continuously, the scanning does not have a lead time. As a result, even the tiniest change occurred in the particle suspension can be captured in principle, which is a feature lacking in the Dynamic Light Scattering and Laser Diffraction techniques.

CHAPTER 5 - Results & Discussion III

Pool Boiling of Nanofluids

This chapter presents the details of a systematic experimental investigation into pool boiling of nanofluids. The experimental plan involved several types and sizes of heaters, base liquids, and shapes, materials and concentrations of nanoparticles. Heater roughnesses and contact angles were measured before and after boiling, and SEM imaging was conducted on the same when needed. Experimental data on pool boiling were analyzed alongside with heater topography data.

At the time this study was designed, there had been a large controversy surrounding the underlying mechanisms that triggered the boiling behaviour of nanofluids. At that time it was mostly attributed to the change in surface roughness that occurred due to particle deposition on heater. In the following two years the number of publications emerged under this theme rose tremendously. It is now possible to see that some of the concerns have now been resolved.

5.1 Preparation and characterization of test surfaces

The test surfaces were the heaters which supplied excess heat into the boiling liquid. Their location in the boiling test rig was shown on figure 3.40. The heat to the surface was provided by the electric heater beneath it. By thermal conduction the heat is then transported through the material onto the fluid. The surfaces were of T-shape as illustrated on figure 5.1. The smaller (25mm) side was in touch with the fluid.

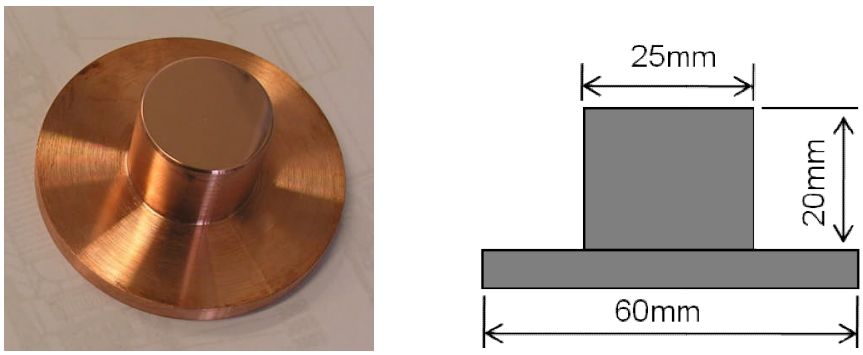

Figure 5.1: A test surface

The decision on the shape, size and material of the test surface was based on technical and rational justifications. A circular shape is favored for pool boiling experiments as it discourages possible edge effects. Especially when it comes to bubble visualization, edge interferences would distort the vision. Moreover this component will assemble to the main body of the test rig in a

press fit. When two mating surfaces are of circular shape, the press fit is easier to achieve. Also the circular metal bars were available in abundance.

The top and bottom diameters were a choice between the size of the bottom heater and the heat flux required to be delivered to the fluid. At this point the heater manufacturers' catalogues were taken into consideration. As the power of heater (wattage) increases, its temperature too follows. The holder for the heater is PTFE (Table 3.2), which had melting a point of 350°C. This melting point set the limit for the heater. Manufacturers were able to fabricate a mica-plate heater of 300W capacity. It had a coil diameter of 60mm. Having set the bottom diameter of the test surface to 60mm, the top was to be reduced to obtain the maximum possible heat flux. Mathematically the smaller the cross section, larger will be the heat flux. It was logical to expect the circular edge would not be as smooth as the centre, and the possibility of bubble nucleation at edges (in fact later this became an operational problem as described in section 3.2.5 of this thesis). For such eventuality, it would be wise to leave a neat and spacious area in the middle for nucleation to occur. As a compromise the top diameter was made to 25mm.

Heat conduction was the transport means for heat from bottom to the top. Apart from the loss to the surroundings, the thermal conductivity of material is the most critical parameter that governs the quantity of heat that reaches the other end. Thermal conductivity of copper is as high as 400W/mK which is nearly 30 times superior to stainless steel. Also copper has been a popular material for numerous heat transfer investigations in the past. Due to its softness, copper surfaces can be polished to mirror finish, and regenerated after each use. Copper was therefore favored as the material for the test surfaces. In addition to these a few stainless steel surfaces were fabricated out of curiosity.

Change in surface roughness and texture due to boiling was a major parameter in this study. Knowledge of a test surface's original roughness was therefore most important. All surfaces were originally sectioned from a cylindrical copper bar and turned into specified dimensions on a lathe machine. Thus their surface textures were of a machine finish. The roughness parameter *(R_a)* was nearly 1µm. This original roughness was kept as the ceiling and was decided to smoothen the surfaces as much as the polishing machines permitted. Consequently a series of surfaces were created belonging to three levels of roughnesses stated in table 5.1. The tolerances (in terms of standard deviation) were derived from measurements on several samples.

Table 5.1: Classification of test surfaces

Class	Method	Roughness (Ra), µm	Tolerance
Rough	Lathe machine	1.0	±10%
Intermediate	P400, P1200 grinding paper with water 2mins each	0.2	±10%
Smooth	6 µm cloth with Diamond lubricant for 3mins	0.035	±10%

The roughness measurements stated above were conducted using the Wyko apparatus, which was a non-invasive technique. An example for a Wyko output is given on figure 5.2. More graphs are presented later in this chapter.

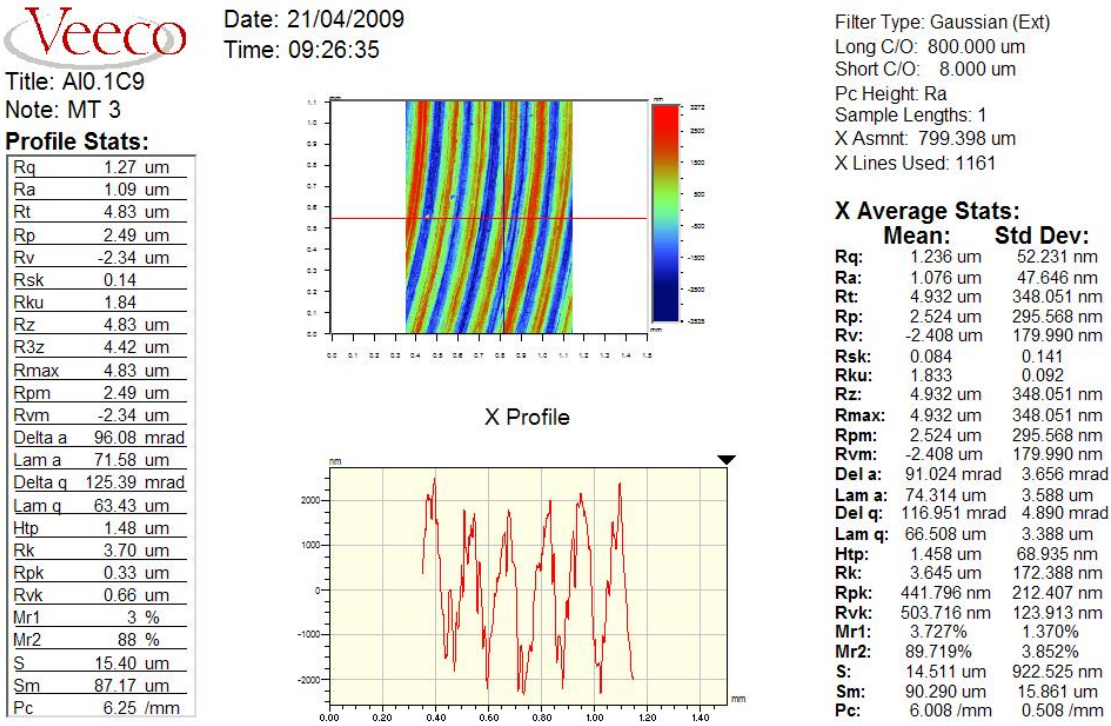

Figure 5.2: A surface profile along the horizontal direction

It is widely known that copper polishing is a highly skilled job. Given the softness and ductility of the material, polishing is extremely sensitive to pressure [244]. Details like the orientation of sample and its duration of contact with the wheel, the relative motion between the two, and the type and amount of lubrication etc. are crucial factors on repeatability.

In the present work polishing was realized in steps with help of Buehler grinding machines. A rough coupon was ground on P400 and P1200 wheels respectively 2 minutes each. Washing of the surface with water followed by drying in hot air and the eye observation were customary while grinding.

Those which were needed to polish down to 'smooth' class were separated out from the lot. They were taken to a grinding wheel that had a delicate 6µm polishing cloth instead of sandpaper. The polishing duration was 3 minutes. While the surface being polished the cloth was occasionally lubricated with diamond suspension. That the diamond suspension was viscous, the surface had to be cleaned more often with ethanol and blow-dried for eye inspection. At the end of the process, the surfaces had achieved nearly a mirror-like finish. After the grinding and polishing, the samples were sent to Wyko to measure the surface roughness.

5.2 Calibration of test rig

As a custom-built device, it was essential the test rig be calibrated. It included the calibration of thermocouples, the bottom heater and the circulation pump.

5.2.1 Thermocouple calibration

There were seven K-type and thermocouples attached onto the test rig and one in the condenser cooling water bath. Each of these had been calibrated and certified by the supplier at the time of purchase. However for conformity a standard calibration procedure was followed in the laboratory. Practice is to record the readings of known and stable temperatures, which are the melting ice and boiling water. Firstly the thermocouple cables were connected to the NI SCXI 1000 data acquisition system and the PC. The thermocouples were then dipped in ice slurry to establish the melting point. The slurry was being stirred to ensure fair temperature distribution. Subsequently they were immersed in boiling water to establish the boiling point. In each of these exercises, the temperature readings were continuously recorded for two minutes. The ambient pressure was also recorded. It was confirmed that the deviation of measured temperature from the calculated values was within a ±0.1°C band. It agreed with the manufacturer's claims.

5.2.2 Heater calibration

The heat generated by the heater *(W)* is the ratio between the square of input voltage *(V^2)* and the heater resistance *(R)*.

$$W = V^2 / R \qquad \textit{Eq 5.1}$$

In this calibration exercise, *W* was determined using three avenues;

(a) *R* measured at room temperature

A Fluke multimeter was used to measure the resistance of the heater at room temperature, and the corresponding values for *W* were calculated as above.

(b) *R* determined at various operating temperatures

This is the method recommended by the heater manufacturer. The Resistance at a given temperature *(R)* can be correlated to resistance at room temperature *(R_r)* in the form; $R=FR_r$. The correlation factor *F* is material dependent. For this heater, *F* varies from 1.006 to 1.015 in the temperature range of 100°C to 200°. Now, if a linear distribution is assumed, *F* becomes 0.00009°C^{-1}. Consequently *R* becomes a function of operating temperature, and so does *W* on equation 5.1

(c) *W* measured using a power meter

A digital power meter was connected in-between the DC power supply (variac) and the heater, such that the power input to the heater passes through the power meter. This enabled reading *W* values directly from the display at any applied voltage.

The heater wattage determined using three methods described above is presented in calibration curves on figure 5.3. Shown in the legend are the three methods (a,b,c) described above.

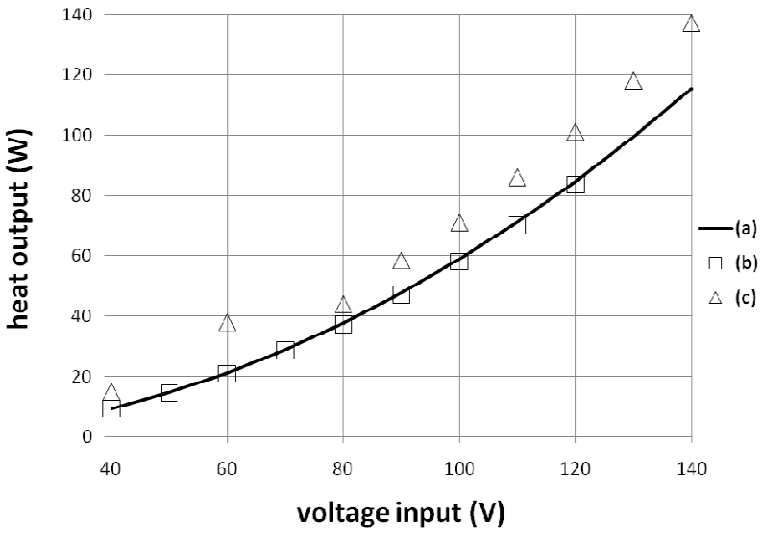

Figure 5.3: Calibration curves for bottom heater

The measured values for heat output, which are shown by dataset (c) on figure 5.3, are larger and the gap is widening with the voltage. This presumably indicates true variation of the heater resistance with the temperature. Dataset (c) having obtained from on-site measurements and therefore regarded as the most reliable, will be used for the purpose of calculating the surface heat flux. Then, the heat flux on the boiling surface at a given voltage will be equal to the corresponding *W* value on (c) divided by the heater surface area. On top of this, the heat losses were accounted for which will be described later in this text.

5.2.3 Circulation pump calibration

It was a Marlow-Watson gear pump that circulated the condenser cooling water. Objective of calibration was to record the flow rate against the pump speed. The water temperature was set around 35°C, and the pump was set to run at a particular rpm. Selection of 35°C operating temperature for condenser coolant was to simulate a boiling experiment. The circulating water was collected into a measuring cylinder over a period of 3minutes. This procedure was repeated until the pump covered a full range of speeds. The pump calibration curve was hence developed as shown in figure 5.4.

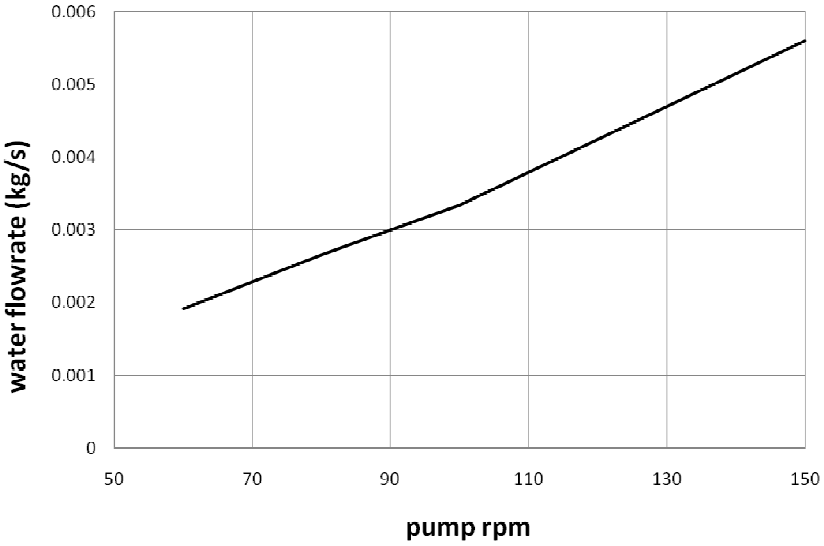

Figure 5.4: Calibration curve for pump

Knowledge of the cooling flow rate is useful to calculate the heat balance of the boiler at steady state operation.

5.3 Experiments and results

Pool boiling experiments were conducted with aqueous nanofluids and water-ethylene glycol based nanofluids. They were formulated as described in chapter 3. Test surfaces (copper coupons) were described on Table 5.1.

The experiments were conducted in the Multiphase and Reacting systems laboratory at University of Leeds. A typical boiling experiment can be described as follows. At the outset, the boiler was dismantled and the interior was thoroughly cleaned with water and acetone. Cleanliness is a mandatory requirement when working in the nanoscale. Next step was the visual inspection of hardware viz. heaters, thermocouples, joints, tubing and insulations. Then the test surface was fitted followed by filling of the boiler with test liquid. Water level of the cooling water tank was checked and the circulation pump was started. The top heater was switched on, with the power cutoff point set to the normal boiling point of the test liquid. When the liquid bulk temperature approached the boiling point, the bottom heater was switched on and its power level was gradually raised to the test point. The system was allowed to reach the thermal equilibrium with the surroundings. Attainment of thermal equilibrium was verified by the temperature profiles on the Labview program being plotted realtime on the PC. Temperature readings at equilibrium were recorded in an Excel spreadsheet. Power level was read from the digital power meter and recorded manually on a paper. Having done so, the heat was raised to the next test point by turning the dial of the variac. When it came to a change of experiment, a safe the shut down procedure was followed. The electrical devices were shut down, followed by the circulation pump. Then the system was first left to cool down before draining the incumbent liquid. Subsequently the test surface was carefully removed without touching its top which is yet to be examined.

5.3.1 Heat loss estimation

Recall there were several thermocouples attached to the test rig. Several of them were placed on the PTFE insulation aimed at estimating the heat loss. Temperature readings obtained from them were plotted in MATLAB (with the assistance from Eric Forrest of MIT) in order to visualize the actual heat distribution in the bottom half of the test rig. Presented in figure 5.5 is the MATLAB output where the top surface is in contact with the boiling liquid (a dark boundary has been added to demarcate the heater). As the thermocouples were not present on the top surface of heater, the respective temperatures were taken with the help of a handheld Fluke IR thermometer.

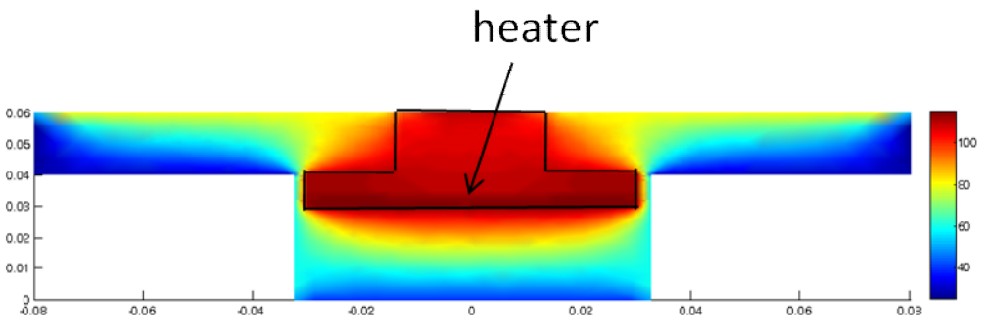

Figure 5.5: Heat distribution from copper substrate

Heat loss calculations were subsequently performed with reference to the scheme given in figure 5.6. Shown in black colour is the bottom heater, of which the temperature *(T)* could be read using the embedded thermocouple. With the knowledge of *T, T1, T2* and *T3*, the radial and axial heat loss due to steady state conduction can be estimated using the well known equations 5.2 and 5.3.

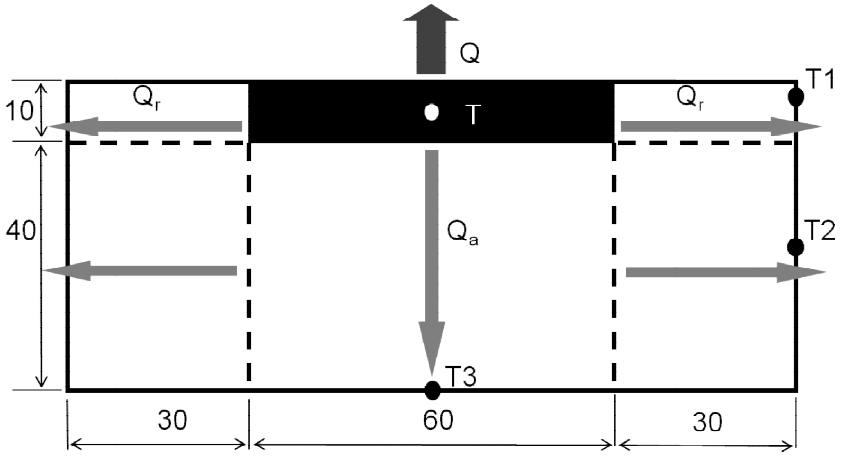

Figure 5.6: Heat loss through PTFE insulation

$$Q_r = \frac{2\pi L k (T_i - T_o)}{\ln\left(r_o / r_i\right)} \qquad \textit{Eq 5.2}$$

$$Q_a = \frac{kA(T_i - T_o)}{L} \qquad \textit{Eq 5.3}$$

Here T_i and T_o are the temperatures of inner and outer walls under consideration, L is the thickness of wall, r_i and r_o are inner and outer radii of walls, k is thermal conductivity of wall, and

A is the cross-sectional area perpendicular to heat conduction. All these parameters are either known or measured. Due to the fact that the heat input to the bottom heater is a set value for any given experiment, it is fair to assume that its temperature *(T)* is constant for a given heat flux. The bottom heater is further considered as a uniform heat generator, which supports the condition of *T* being uniform throughout.

A model calculation performed using the experimental data showed that the heat loss to the surroundings was less than 5% of the total heat input from the heater at any level of heat input. Appendix A presents the calculation.

5.3.2 Results

Experimental results for water-ethylene glycol based nanofluids will be discussed first, followed by water based nanofluids.

5.3.2.1 Water-ethylene glycol based nanofluids

Figure 5.7 presents data for boiling of water. Each experiment was repeated three times. Therefore each data point is an average of three readings.

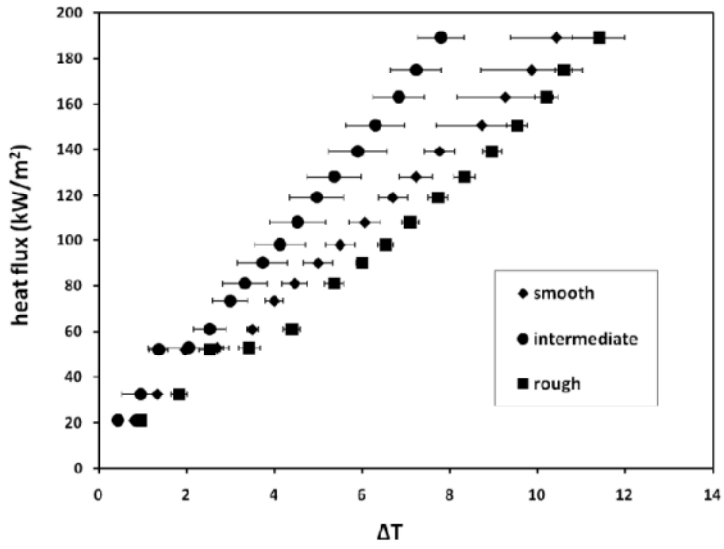

Figure 5.7: Water boiling on copper coupons

With increasing heat input to water, the temperature difference between the heater surface and the surrounding saturated liquid *(ΔT)* has increased as expected. However this does not provide convincing evidence on a clear correlation between the surface roughness and *ΔT*. Recall that

copper is known to be a highly oxidizing material. Coursey and Kim [160] had previously noticed the change in surface roughness after boiling on copper. The error bars on each data point on figure 5.7 may suggest, although not conclusively, an effect of oxidation due to boiling. If that is the case, still the degree of oxidation appears to be insignificant.

Next to be examined were the water-ethylene glycol (WEG) based nanofluids. Plotted on figure 5.8 are the data for boiling on intermediate coupons. The featured nanofluid is TiO_2 0.1wt% in Water75%-EG25% (WEG25).

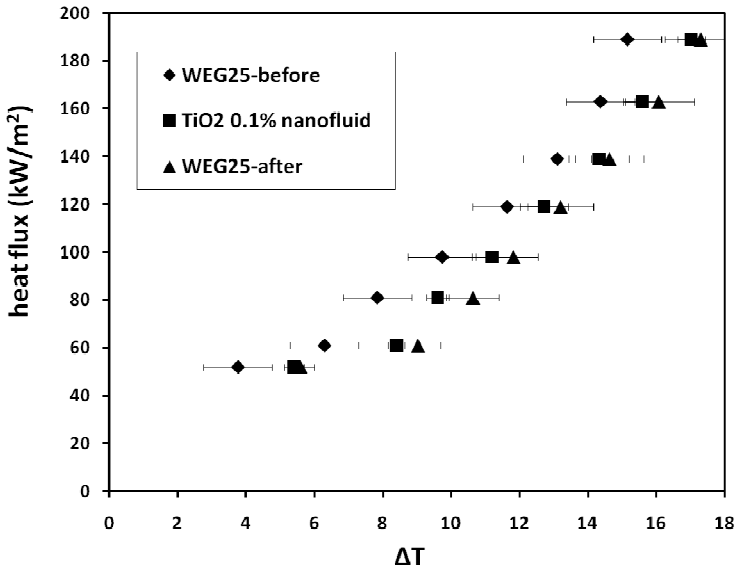

Figure 5.8: Boiling of TiO_2 0.1wt%-WEG25 nanofluid on copper heater

Witnessed from the plot is that the addition of TiO_2 nanoparticles to the base liquid has caused deterioration in boiling heat transfer. When WEG25 was reboiled, indicated by ▲ symbols in figure 5.8, the data points nearly coincided with the nanofluid. Moreover the post-boiling SEM images showed particle deposition on heater. Taking it into account, it can be hypothesized that the difference between the initial WEG25 boiling and the nanofluid boiling was due to particle scaling. This new structure built on the heater was not enhancing but impeding the heat transfer.

Nanofluid with a low TiO_2 concentration was boiled on a heater of similar grade. Data are plotted on figure 5.9. In contrast to what was seen with 0.1wt% nanofluid, now the data from first two experiments lie close to each other while the third experiment stays distant.

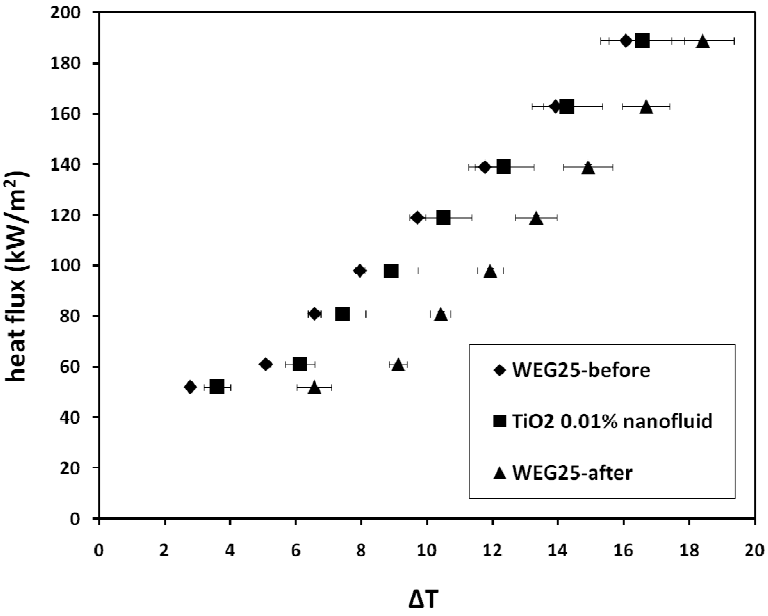

Figure 5.9: Boiling of TiO_2 0.01wt%-WEG25 nanofluid on copper heater

In order to explore the influence of nanoparticle concentration on boiling, the nanofluid data were extracted from figures 5.8 and 5.9 and plotted on figure 5.10. This was possible because both plots were constructed on one platform, i.e. the intermediate grade heater. The degree of deterioration has increased with the concentration. Given the fact that both nanofluids were stable formulations, it can only be expected the denser nanofluid to settle in a relatively large quantity. When figure 5.10 is examined in that point of view, the particle scaling from TiO_2 0.1wt% nanofluid has worsened the heat transfer. Arguably the amount of deposition at this instance had caused a reduction in the active nucleation site density, which in turn deteriorated the heat transfer. The phenomena of particle deposition smoothening the heaters was witnessed by several investigators such as Chopkar et al. [138].

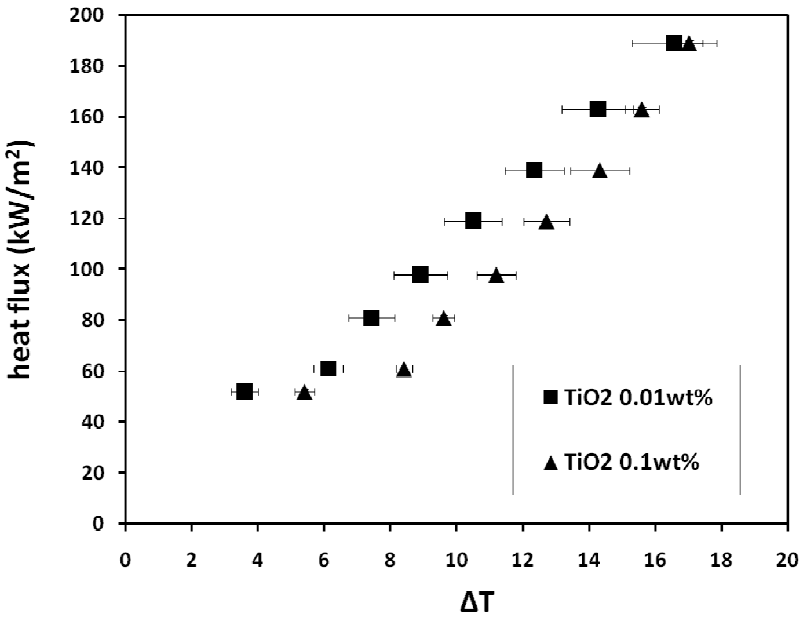

Figure 5.10: Effect of TiO_2 concentration in WEG25-based nanofluid in boiling

Having established the effect of particle concentration, then the experiments were directed to examine the influence of EG concentration in the base liquid. This is an important aspect to document given the fact that the EG percentage is a variable in commercial usage such as in secondary cooling.

The deterioration trend has extended to the WEG10 based TiO_2 0.1wt% nanofluids illustrated in figure 5.11. Moreover quite similar with the figure 5.8, the re-boiling data for WEG10 base liquid was coinciding with the nanofluid dataset. This suggests that in WEG-based nanofluids boiling, the influence of the ethylene glycol percentage in the base liquid is fairly insignificant in deciding the boiling heat transfer. Rather it is the particle dynamics that has likely caused the difference.

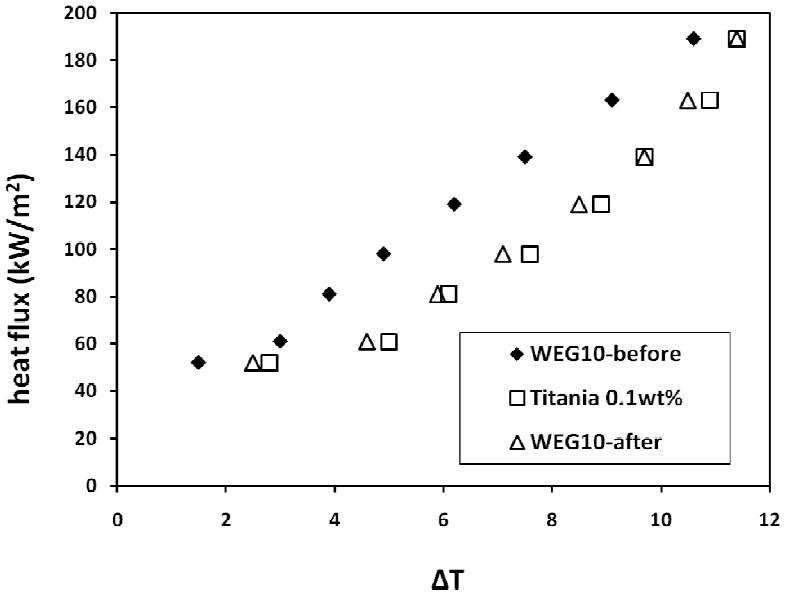

Figure 5.11: Boiling of TiO_2 0.1wt%-WEG10 nanofluid on copper heater

Lastly the relationship between the boiling duration and amount of deposition for TiO_2–WEG nanofluids was investigated. Data gathered for three consecutive boiling tests are plotted on figure 5.12.

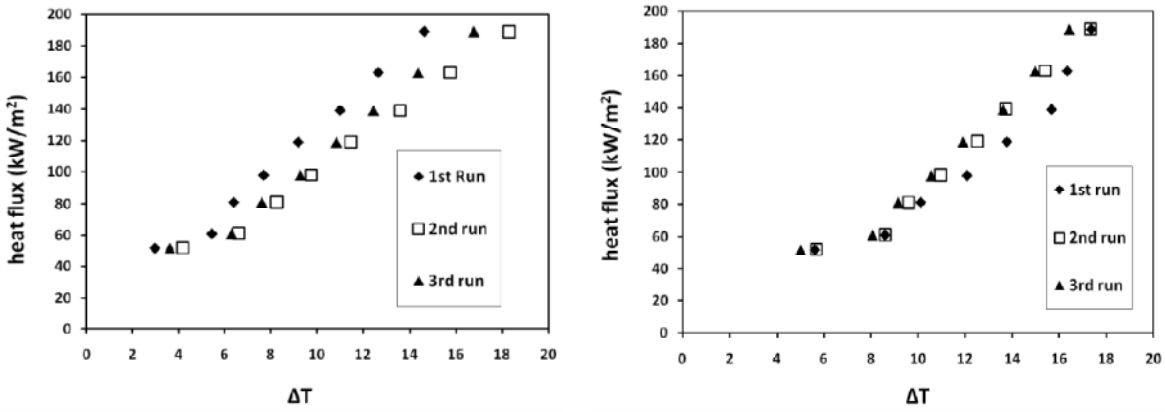

Figure 5.12: Repeated boiling of TiO_2-WEG25 nanofluid. Left-0.01wt%, Right-0.1wt%

For the more dilute suspension shown on left hand side of figure 5.12, repeated boiling has yielded negative impact on heat transfer. Meanwhile for the sample on the right hand side where the particle concentration was an order-of-magnitude larger, it was an increase in heat transfer. In common to two samples was the overlapping of 2nd and 3rd datasets. This could be thought as an indication of ceasing the deposition after the 2nd run.

Several experiments were conducted with the spherical Al_2O_3-WEG nanofluids. The observations were similar to that of TiO_2-WEG samples. Hence the Al_2O_3-WEG nanofluids boiling data will not be presented here.

5.3.2.2 Water based nanofluids

This discussion now moves towards the water based nanofluids. To keep up with literature the ordinate is plotted with the enhancement ratio which is the ratio of heat transfer coefficients of nanofluid to water. Boiling heat transfer coefficient *(h)* is determined from experimental data in the classical style. It is written as the ratio of surface heat flux to excess temperature as follows.

$$h = {q''}/{\Delta T} \qquad \textit{Eq 5.4}$$

Figure 5.13 features data for spherical Al_2O_3 and carbon nanotube (CNT) nanofluids. These were boiled on a smooth coupon. In general the two Al_2O_3–water samples have exhibited deterioration that has worsened with heat flux. Apparently there has been a marginal difference between 0.1wt% and 0.01wt% samples. Meanwhile the CNT nanofluids have behaved remarkably differently. It has demonstrated a steady increase in heat transfer enhancement from 60kW/m^2 heat flux which is presumably the onset of nucleate boiling. Clearly more experiments are needed to verify these observations.

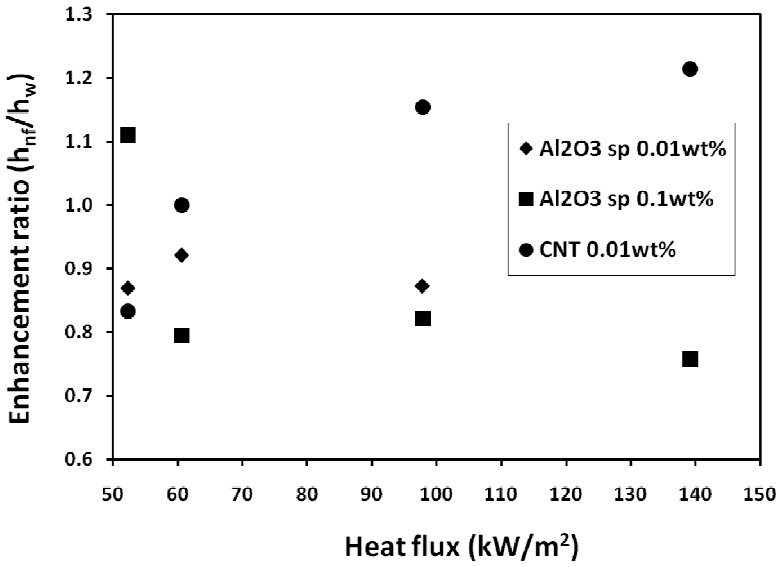

Figure 5.13: Boiling of aqueous-based nanofluids on smooth heater

Water based spherical and acicular Al_2O_3 nanofluids were boiled on rough heaters. A representation is given on figure 5.14. Once again the dependence of enhancement on heat flux has been highlighted. The acicular-shape Al_2O_3 particles had behaved superior to their spherical counterparts. A comparison of figures 5.13 and 5.14 creates a view of the dependence of heater roughness for spherical Al_2O_3-water nanofluids. In the nucleate boiling regime, i.e. from 60kW/m^2 onwards, the heater roughness has not significantly influenced the boiling behaviour of Al_2O_3 0.1wt% nanofluid.

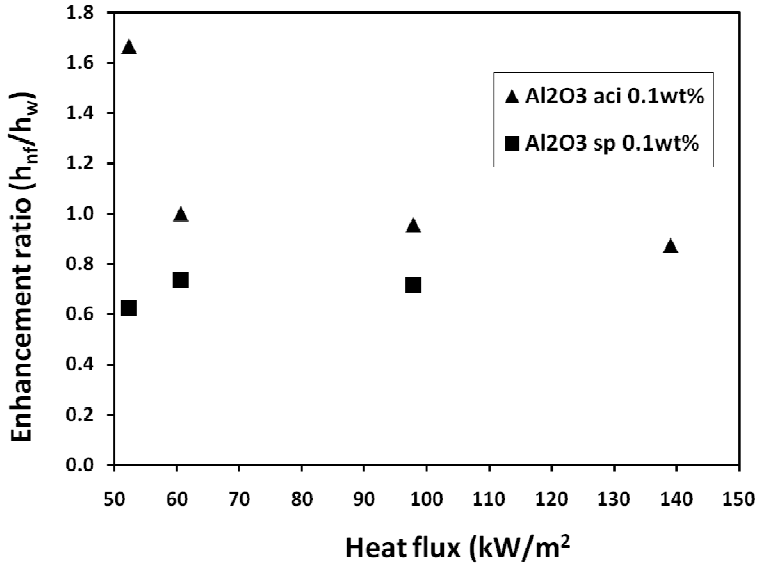

Figure 5.14: Boiling of aqueous-based Al_2O_3 nanofluids on rough heater

Finally in figure 5.15, present data are plotted along with the datasets recruited from Wen and Ding [129], Das et al. [131], and Bang and Chang [161]. All these reports were for Al_2O_3–water nanofluids with either stated or implied primary particle diameter of nearly 40nm. The *S* and *R* in the legend respectively indicate boiling on smooth and rough heaters.

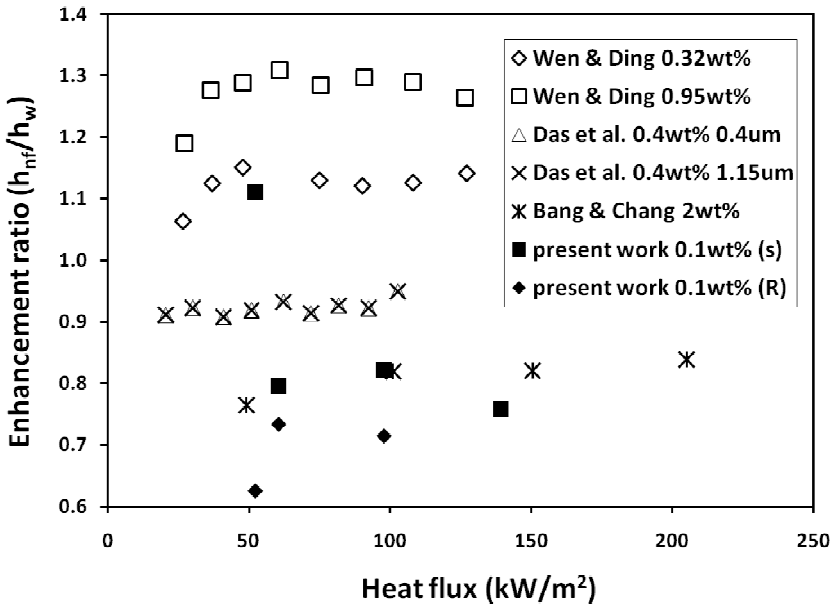

Figure 5.15: Pool boiling data for Al_2O_3-water nanofluids

The data gathered from present experiments appear to be in reasonable agreement with the literature. Firstly the boiling heat transfer deterioration with nanofluid has been reestablished. Secondly the near independence of enhancement ratio on heat flux has reappeared. Das et al. [131]'s datasets were tagged with roughness parameter. In the present work, the rough heater was approximately same as theirs but the smooth heater was smoother than theirs. Either from their work or present work it is not possible to build a nexus between the heater roughness and boiling performance.

5.3.2.3 Boiled surfaces

A closer examination of the boiled surfaces will be conducted in this section. The boiled heaters were carefully removed from the test rig and taken to the SEM without disturbing the top surface. Consider the images given on figure 5.16. In both cases the surface structure has altered after boiling the nanofluids while the deposit on the smooth surface appears to be more solid. A vast number of cavities of varying sizes and depths are formed as a result.

Formation of pits and cracks may either enhance or deteriorate boiling heat transfer depending on several associated parameters. They might act as bubble nucleation sites or the grooves therein may function as liquid supplying routes to bubble sites. However in order to see a change, either enhancement or deterioration, the net effect of deposition should surpass the original surface topography by a significant magnitude. One way to evaluate it is by measuring the

difference in surface roughness. Hence it would be logical to discuss the roughness profiles of the surfaces shown on figure 5.16 (a) and (b).

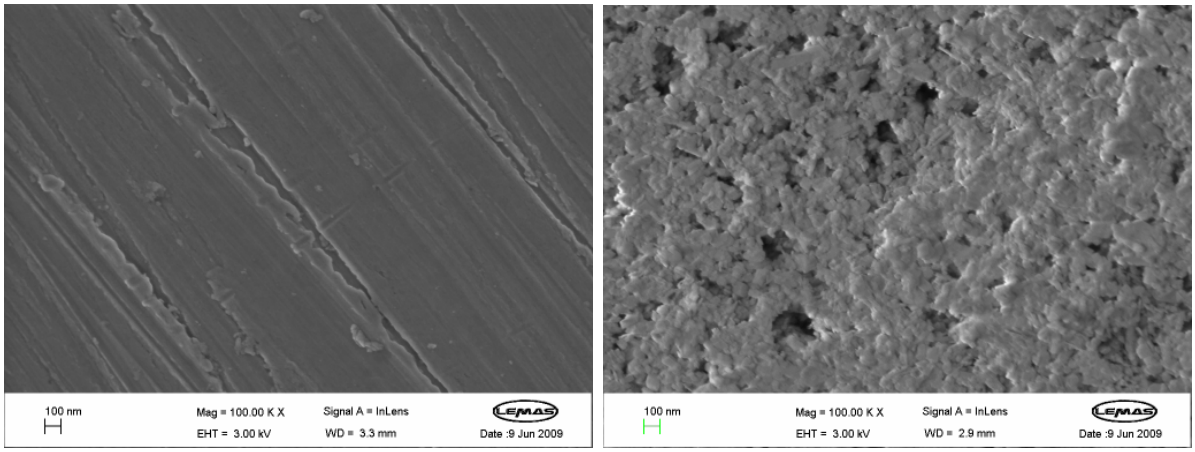

(a) a smooth surface

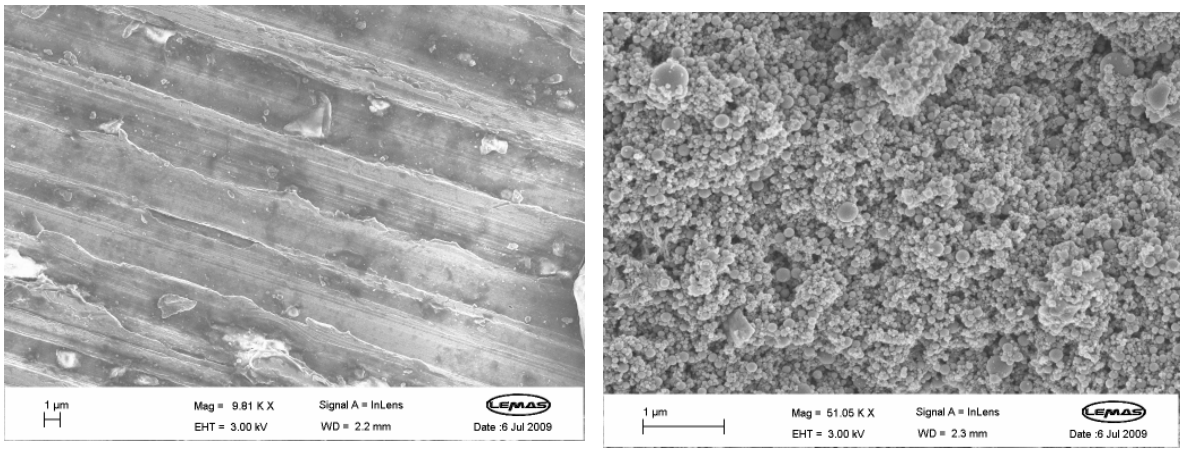

(b) a rough surface

Figure 5.16: Surfaces before and after boiling Al_2O_3-water nanofluids

Figure 5.17 features two images produced by the Wyko surface profiler. One is a smooth heater before boiling and the other image is after boiling alumina nanofluid. Note that the roughness parameters were determined by the Wyko by tracing along a diameter. Due to boiling the R_a value has nearly doubled to 49.8±8.9nm. Deposition of nanoparticles has therefore increased the surface roughness.

Veeco

Title: C#4
Note: MT 5

Date: 25/02/2009
Time: 15:14:18

Profile Stats:

Rq	36.42	nm
Ra	26.50	nm
Rt	317.01	nm
Rp	119.13	nm
Rv	-197.87	nm
Rsk	-0.80	
Rku	6.91	
Rz	317.01	nm
R3z	179.24	nm
Rmax	317.01	nm
Rpm	119.13	nm
Rvm	-197.87	nm
Delta a	9.72	mrad
Lam a	17126.61	nm
Delta q	13.50	mrad
Lam q	16947.05	nm
Htp	31.03	nm
Rk	77.58	nm
Rpk	40.96	nm
Rvk	51.98	nm
Mr1	11	%
Mr2	87	%
S	10.81	um
Sm	16.78	um
Pc	27.52	/mm

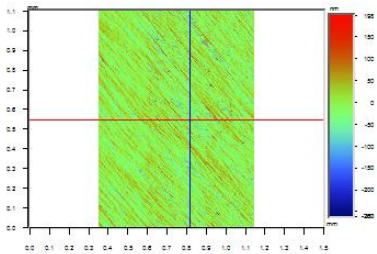

X Profile

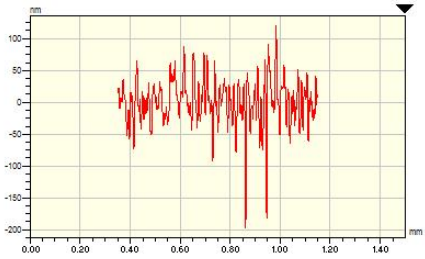

Filter Type: Gaussian (Ext)
Long C/O: 800.000 um
Short C/O: 8.000 um
Pc Height: Ra
Sample Lengths: 1
X Asmnt: 799.398 um
X Lines Used: 1164

X Average Stats:

	Mean:	Std Dev:
Rq:	29.816 nm	2.968 nm
Ra:	23.235 nm	2.151 nm
Rt:	199.086 nm	40.197 nm
Rp:	88.257 nm	19.674 nm
Rv:	-110.830 nm	28.385 nm
Rsk:	-0.288	0.277
Rku:	3.759	1.173
Rz:	199.086 nm	40.197 nm
Rmax:	199.086 nm	40.197 nm
Rpm:	88.257 nm	19.674 nm
Rvm:	-110.830 nm	28.385 nm
Del a:	7.644 mrad	1.006 mrad
Lam a:	19.250 um	1.518 um
Del q:	10.015 mrad	1.417 mrad
Lam q:	18.862 um	1.413 um
Htp:	28.604 nm	3.076 nm
Rk:	71.510 nm	7.690 nm
Rpk:	27.835 nm	6.775 nm
Rvk:	37.056 nm	8.316 nm
Mr1:	9.593%	1.984%
Mr2:	87.631%	2.026%
S:	11.731 um	650.994 nm
Sm:	19.548 um	2.031 um
Pc:	22.386 /mm	3.547 /mm

7

(a)

Veeco

Title: C#4_after
Note: MT 0.1

Date: 04/03/2009
Time: 12:27:40

Profile Stats:

Rq	57.77	nm
Ra	45.33	nm
Rt	321.19	nm
Rp	151.12	nm
Rv	-170.07	nm
Rsk	-0.59	
Rku	3.29	
Rz	321.19	nm
R3z	291.61	nm
Rmax	321.19	nm
Rpm	151.12	nm
Rvm	-170.07	nm
Delta a	13.91	mrad
Lam a	20479.59	nm
Delta q	17.76	mrad
Lam q	20444.29	nm
Htp	56.30	nm
Rk	140.76	nm
Rpk	46.60	nm
Rvk	80.16	nm
Mr1	7	%
Mr2	86	%
S	11.20	um
Sm	20.72	um
Pc	16.26	/mm

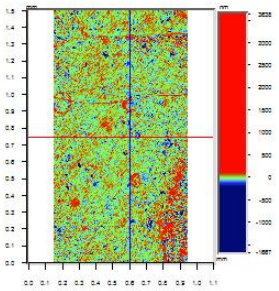

X Profile

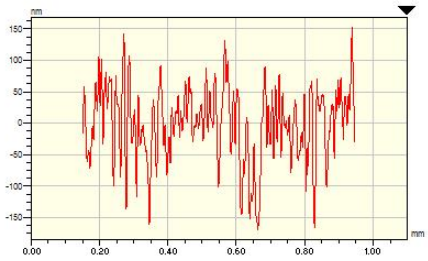

Filter Type: Gaussian (Ext)
Long C/O: 800.000 um
Short C/O: 8.000 um
Pc Height: Ra
Sample Lengths: 1
X Asmnt: 799.398 um
X Lines Used: 1587

X Average Stats:

	Mean:	Std Dev:
Rq:	69.513 nm	23.256 nm
Ra:	49.765 nm	8.937 nm
Rt:	549.529 nm	332.913 nm
Rp:	257.970 nm	283.051 nm
Rv:	-291.559 nm	158.282 nm
Rsk:	-0.276	1.432
Rku:	7.396	10.779
Rz:	549.529 nm	332.913 nm
Rmax:	549.529 nm	332.913 nm
Rpm:	257.970 nm	283.051 nm
Rvm:	-291.559 nm	158.282 nm
Del a:	15.092 mrad	2.246 mrad
Lam a:	20.725 um	2.114 um
Del q:	20.849 mrad	5.575 mrad
Lam q:	20.903 um	2.516 um
Htp:	56.352 nm	8.791 nm
Rk:	140.880 nm	21.978 nm
Rpk:	82.147 nm	58.262 nm
Rvk:	98.047 nm	43.573 nm
Mr1:	10.609%	2.193%
Mr2:	87.011%	2.211%
S:	11.046 um	537.990 nm
Sm:	20.466 um	2.513 um
Pc:	16.398 /mm	3.928 /mm

(b)

Figure 5.17: Smooth heater (a) before and (b) after boiling

Now consider figure 5.18 which is for boiling of alumina nanofluid on a rough heater. Obviously when the nanofluid was boiled on the rough heater the R_a had decreased by approximately 20% to 1076±47.6nm.

A relationship between the surface roughness and boiling heat transfer performance can be drawn by comparison of boiling data on figure 5.15 with figures 5.16 through 5.18. Apart from the nucleation incipience which occurred around 50kW/m^2, there was only a marginal difference in the boiling heat transfer coefficients. On the other hand when the respective post-boiling heaters were compared, i.e. figures 5.17 and 5.18, there was a massive difference in roughness, 49.8±8.9nm vs 1076±47.6nm. Respective surface topographies shown on figure 5.16 too can be taken into consideration. After taking all these facts into account, it would be logical to suggest that the highly polarized surface roughnesses of the two heaters were not sufficient to trigger enhancement in heat transfer. Both of them acted in one direction to deteriorate the boiling performance.

Performance of acicular alumina particles were earlier shown on figure 5.14. The relevant surface profiles are presented in figure 5.19. Recall that this heater was similar in roughness to the one which was shown on figure 5.18 before they were used to boil nanoparticles of two shapes.

Veeco

Title: C9
Note: MT 3

Date: 07/04/2009
Time: 15:16:02

Profile Stats:

Rq	1.45 um
Ra	1.21 um
Rt	5.46 um
Rp	2.73 um
Rv	-2.73 um
Rsk	0.06
Rku	2.00
Rz	5.46 um
R3z	5.15 um
Rmax	5.46 um
Rpm	2.73 um
Rvm	-2.73 um
Delta a	100.79 mrad
Lam a	75.34 um
Delta q	130.83 mrad
Lam q	69.46 um
Htp	1.69 um
Rk	4.22 um
Rpk	0.44 um
Rvk	0.75 um
Mr1	7 %
Mr2	90 %
S	15.70 um
Sm	64.55 um
Pc	6.25 /mm

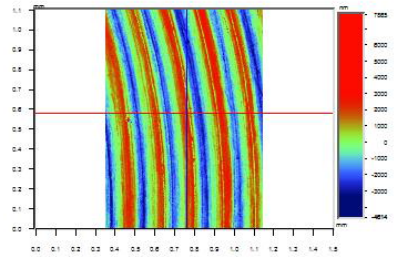

X Profile

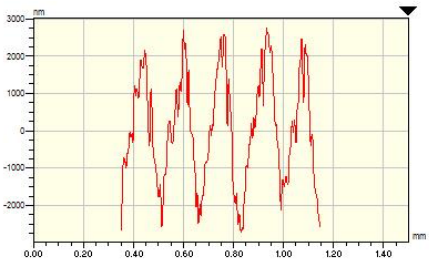

Filter Type: Gaussian (Ext)
Long C/O: 800.000 um
Short C/O: 8.000 um
Pc Height: Ra
Sample Lengths: 1
X Asmnt: 799.398 um
X Lines Used: 1164

X Average Stats:

	Mean:	Std Dev:
Rq:	1.503 um	36.939 nm
Ra:	1.278 um	33.773 nm
Rt:	6.057 um	479.259 nm
Rp:	2.868 um	403.515 nm
Rv:	-3.190 um	265.473 nm
Rsk:	-0.002	0.072
Rku:	1.967	0.142
Rz:	6.057 um	479.259 nm
Rmax:	6.057 um	479.259 nm
Rpm:	2.868 um	403.515 nm
Rvm:	-3.190 um	265.473 nm
Del a:	102.541 mrad	5.682 mrad
Lam a:	78.523 um	4.583 um
Del q:	133.871 mrad	8.796 mrad
Lam q:	70.805 um	4.464 um
Htp:	1.842 um	74.430 nm
Rk:	4.604 um	186.123 nm
Rpk:	439.391 nm	199.428 nm
Rvk:	680.914 nm	174.289 nm
Mr1:	5.597%	3.057%
Mr2:	93.006%	1.516%
S:	15.742 um	1.126 um
Sm:	91.814 um	19.399 um
Pc:	5.409 /mm	0.601 /mm

(a)

Veeco

Title: Al0.1C9
Note: MT 3

Date: 21/04/2009
Time: 09:26:35

Profile Stats:

Rq	1.27 um
Ra	1.09 um
Rt	4.83 um
Rp	2.49 um
Rv	-2.34 um
Rsk	0.14
Rku	1.84
Rz	4.83 um
R3z	4.42 um
Rmax	4.83 um
Rpm	2.49 um
Rvm	-2.34 um
Delta a	96.08 mrad
Lam a	71.58 um
Delta q	125.39 mrad
Lam q	63.43 um
Htp	1.48 um
Rk	3.70 um
Rpk	0.33 um
Rvk	0.66 um
Mr1	3 %
Mr2	88 %
S	15.40 um
Sm	87.17 um
Pc	6.25 /mm

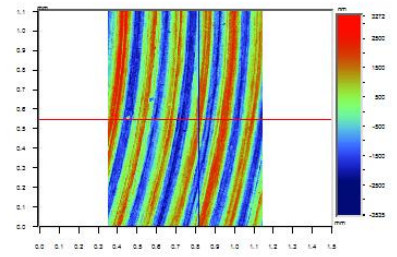

X Profile

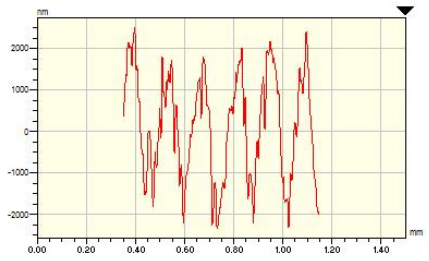

Filter Type: Gaussian (Ext)
Long C/O: 800.000 um
Short C/O: 8.000 um
Pc Height: Ra
Sample Lengths: 1
X Asmnt: 799.398 um
X Lines Used: 1161

X Average Stats:

	Mean:	Std Dev:
Rq:	1.236 um	52.231 nm
Ra:	1.076 um	47.646 nm
Rt:	4.932 um	348.051 nm
Rp:	2.524 um	295.568 nm
Rv:	-2.408 um	179.990 nm
Rsk:	0.084	0.141
Rku:	1.833	0.092
Rz:	4.932 um	348.051 nm
Rmax:	4.932 um	348.051 nm
Rpm:	2.524 um	295.568 nm
Rvm:	-2.408 um	179.990 nm
Del a:	91.024 mrad	3.656 mrad
Lam a:	74.314 um	3.588 um
Del q:	116.951 mrad	4.890 mrad
Lam q:	66.508 um	3.388 um
Htp:	1.458 um	68.935 nm
Rk:	3.645 um	172.388 nm
Rpk:	441.796 nm	212.407 nm
Rvk:	503.716 nm	123.913 nm
Mr1:	3.727%	1.370%
Mr2:	89.719%	3.852%
S:	14.511 um	922.525 nm
Sm:	90.290 um	15.861 um
Pc:	6.008 /mm	0.508 /mm

(b)

Figure 5.18: Rough heater (a) before and (b) after boiling

Date: 13/01/2009
Time: 10:47:34

Title: Original
Note: MT 2

Profile Stats:

Rq	1.63 um
Ra	1.05 um
Rt	8.76 um
Rp	2.37 um
Rv	-6.39 um
Rsk	-2.28
Rku	8.53
Rz	8.76 um
R3z	6.77 um
Rmax	8.76 um
Rpm	2.37 um
Rvm	-6.39 um
Delta a	114.61 mrad
Lam a	57.77 um
Delta q	170.57 mrad
Lam q	60.19 um
Htp	0.92 um
Rk	2.31 um
Rpk	0.81 um
Rvk	4.67 um
Mr1	7 %
Mr2	84 %
S	19.44 um
Sm	55.69 um
Pc	3.76 /mm

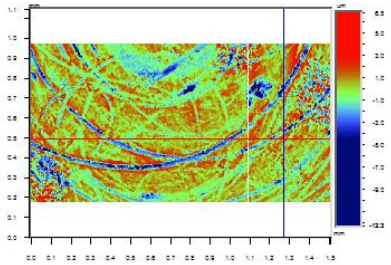

Y Profile

Filter Type: Gaussian (Ext)
Long C/O: 800.000 um
Short C/O: 8.000 um
Pc Height: Ra
Sample Lengths: 1
X Asmnt: 798.863 um
Y Lines Used: 734

Y Average Stats:

	Mean:	Std Dev:
Rq:	1.385 um	264.393 nm
Ra:	1.060 um	193.726 nm
Rt:	7.979 um	1.927 um
Rp:	3.191 um	1.181 um
Rv:	-4.788 um	1.450 um
Rsk:	-0.784	0.620
Rku:	4.419	1.686
Rz:	7.979 um	1.927 um
Rmax:	7.979 um	1.927 um
Rpm:	3.191 um	1.181 um
Rvm:	-4.788 um	1.450 um
Del a:	125.964 mrad	24.238 mrad
Lam a:	53.385 um	7.044 um
Del q:	184.505 mrad	36.690 mrad
Lam q:	47.647 um	6.691 um
Htp:	1.136 um	237.291 nm
Rk:	2.840 um	593.216 nm
Rpk:	1.104 um	690.742 nm
Rvk:	2.103 um	685.643 nm
Mr1:	7.941%	2.846%
Mr2:	82.672%	4.415%
S:	21.793 um	1.709 um
Sm:	52.241 um	11.314 um
Pc:	6.735 /mm	2.007 /mm

(a)

Veeco

Date: 27/01/2009
Time: 09:54:51

Title: C1-after boilingAlne
Note: after boiling Alneedles

Profile Stats:

Rq	0.70 um
Ra	0.57 um
Rt	3.34 um
Rp	1.62 um
Rv	-1.72 um
Rsk	-0.49
Rku	2.48
Rz	3.34 um
R3z	2.88 um
Rmax	3.34 um
Rpm	1.62 um
Rvm	-1.72 um
Delta a	99.99 mrad
Lam a	35.61 um
Delta q	141.20 mrad
Lam q	31.01 um
Htp	0.66 um
Rk	1.65 um
Rpk	0.40 um
Rvk	0.89 um
Mr1	3 %
Mr2	80 %
S	10.28 um
Sm	36.54 um
Pc	11.26 /mm

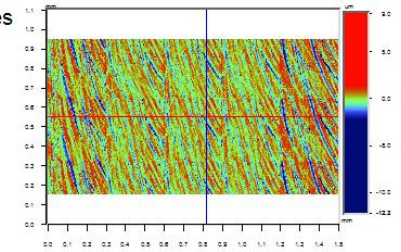

Y Profile

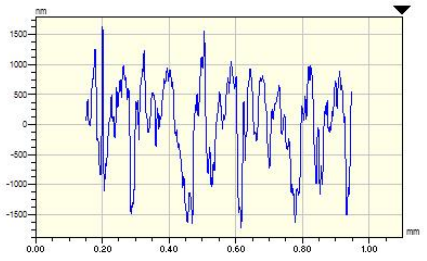

Filter Type: Gaussian (Ext)
Long C/O: 800.000 um
Short C/O: 8.000 um
Pc Height: Ra
Sample Lengths: 1
X Asmnt: 799.398 um
Y Lines Used: 1852

Y Average Stats:

	Mean:	Std Dev:
Rq:	729.586 nm	187.628 nm
Ra:	583.516 nm	152.135 nm
Rt:	4.608 um	1.621 um
Rp:	1.732 um	712.207 nm
Rv:	-2.877 um	1.334 um
Rsk:	-0.659	0.557
Rku:	4.136	3.508
Rz:	4.608 um	1.621 um
Rmax:	4.608 um	1.621 um
Rpm:	1.732 um	712.207 nm
Rvm:	-2.877 um	1.334 um
Del a:	100.838 mrad	17.208 mrad
Lam a:	36.253 um	6.634 um
Del q:	144.246 mrad	27.901 mrad
Lam q:	31.808 um	5.650 um
Htp:	650.326 nm	161.210 nm
Rk:	1.626 um	403.024 nm
Rpk:	403.147 nm	219.255 nm
Rvk:	1.021 um	451.818 nm
Mr1:	6.323%	3.662%
Mr2:	82.667%	6.209%
S:	10.209 um	813.143 nm
Sm:	40.419 um	11.449 um
Pc:	7.970 /mm	2.838 /mm

(b)

Figure 5.19: Rough heater (a) before and (b) after boiling acicular particles

Despite the fact that two nanofluids were same in all aspects but particle shape, the degree of deposition has been very different. Figures 5.18 and 5.19 give evidence. While the spherical particle reduced the R_a by 20%, the reduction with acicular particles was about 45%. Boiling heat transfer too was larger with acicular particles and the deterioration was at insignificant magnitude.

Having previously seen the very smooth and very rough heaters behave alike when boiling spherical particles, the observation for acicular particles points to a new direction. It suggests that the optimum surface enhancement may lie between smooth and rough heaters.

5.4 Summary of the Chapter

Pool boiling of dilute nanofluids was experimentally examined in this chapter. These nanofluids comprised of water based and water-ethylene glycol based Al_2O_3, TiO_2, CNT nanoparticles. According to the literature review this is the first time the boiling of water-ethylene glycol based nanofluids is reported. All experiments were conducted under the atmospheric pressure and the heat fluxes up to 189kW/m^2 on flat copper heaters. Heating to these heaters was provided by using a resistive coil heater which was placed immediately underneath. Temperature measurements were taken at several locations that will help to determine boiling heat transfer rates as well as heat losses to ambience. Through data analysis it was found that the general trend was the nanofluids deteriorating the boiling heat transfer in all instances came under investigation. This agrees with a vast amount of literature [131-132, 140, 143, 152, 160-161, 170, 172, 177, 179]. The degree of deterioration indicated dependence on the type and shape of nanoparticle and the base liquid. Since this was the first time the influence of particle shape was studied, it is not possible to make a comparison with the prior art. Also found common to all of the present experiments was the deposition of nanoparticles on heater surfaces. Upon surface roughness measurements, it was found that these deposits altered the surface roughness of heaters. Further analysis suggested that possibly there is an interval of roughnesses that may yield optimum boiling heat transfer. Two extremes of this interval appears to be approximately R_a=*50nm* and R_a=*1μm*. This is indeed a broad interval which needs to be finetuned by conducting further experiments. In recent literature, similar statements can be found regarding the repeated boiling and surface roughness. White et al. [168] for instance saw the deposition of ZnO nanoparticles increasing the heater roughness from 0.06μm to 0.44μm through eight rounds of pool boiling tests. In the 1st test the boiling heat transfer increased, but in subsequent tests it

steady decreased. Narayan et al. [128] too saw the rough heaters in the order or Ra~524nm had larger tendency to enhance the boiling performance than the smoother ones.

SEM imaging of the nanofouled surfaces clearly indicated the presence of a porous structure on them. When these SEM images are compared with the respective surface roughness measurements, it is possible to visualize a qualitative relationship. For example, some deposits look smooth on SEM images. Their measured surface roughness is lower than the bear heaters.

A valuable disclosure emerged from SEM images was the characteristics of the pores, pits and cracks on the nanoparticle deposits. They were in large numbers, with the mouth sizes in the order of few hundreds of nanometers, and circular or conical in shape. These porous structures were often appeared to have sub-surface connectivity. In conventional heat transfer the surfaces with artificial irregularities are often referred to as enhanced surfaces [186]. They are supposed be more efficient in boiling [185, 187, 245]. In the present work however the results were somewhat contradictory to the above statement. On the other hand, the surface cavities studied in the conventional heat transfer were either in micron or millimeter sizes. Now the question is whether an unknown phenomenon governs the boiling heat transfer at sub-micron scales. This underlines the need to investigate the boiling mechanisms in tiny structures.

Young-Laplace theory puts forward the fundamental mechanisms of bubble nucleation on cavities. It is widely accepted for its accuracy in predicting the bubble nucleation superheat. It has been shown that the Young-Laplace theory sufficiently agrees with the experimental data for boiling on micron or millimeter sizes [246-248]. However it’s standing for sub-micron size cavities is yet to be proven. In the backdrop of the findings appeared from nanofluids boiling data analysis, along with the revelation of tiny cavities on nanofouled surfaces, it seems logical to explore the Young-Laplace theory for sub-micron length scales by experimentation.

CHAPTER 6 - Results & Discussion III

Boiling on Artificial Cavities

The aim of the present experiments was to investigate boiling phenomena on sub-micron size artificial cavities of known geometry. A sizable amount of work has readily been documented on boiling on small cavities. But the sizes of these cavities were often in the order of micrometers or larger. Another novelty in the present work is the heating method. A distantly placed halogen lamp that heats up the cavities is a non-invasive technique that does not physically interfere with the liquid or the substrate. Assisted by the Infra Red thermometry, present work will contribute to broaden the existing knowledge on the fundamental physics of boiling. This study was conducted at the Nuclear Science and Engineering Department, Massachusetts Institute of Technology.

6.1 Selection of substrate material

Artificial cavities were to be microfabricated on a suitable substrate which should ideally be smooth, thin, electrically and thermally conductive, micro-machinable, and IR transparent. Electrical conductivity is for resistive heating, while thermal conductivity and IR transparency are for temperature measurement. With the decision to introduce halogen light as heat source, the electrical conductivity became no more significant. Mica as a material meets several of these criteria but it is too brittle to be machined on FIB. Silicon on the other hand has long been established in Microfabrication industry. They are smooth *(Ra~0.6nm)*, highly thermally conductive (~150W/mK for undoped silicon) and fairly IR-transparent.

Silicon wafers are available in double-side polished or one side polished and one side etched. Pure silicon transmits a good part of electromagnetic spectrum. By deposition of a thin layer of silicon dioxide (SiO_2) on the wafer, usually by atomic layer deposition method, introduces a great deal of IR opaqueness. After careful consideration of above facts, silicon wafer was chosen as the most favourable substrate for this work.

6.2 Cavity parameters and boiling liquids

In historical viewpoint, conical cavities were seldom examined in literature. They are likely to demand large nucleation superheat, and also less likely to sustain bubble production in comparison to cylindrical and re-entrant cavity shapes [246]. In machining perspective too, cylinders are easier to obtain than well-defined miniature cones. However conical shapes are more often found in nature. For example, a crack on a surface is most likely to be v-shape (conical). The decision to select conical shape cavities was based on these facts.

Then the mouth diameter too was chosen to fill gaps in existing knowledge. While sub-micron cones have not been examined elsewhere, the reported smallest cylinder was in the order of 0.75microns [205]. Moreover, smaller the cavity diameter becomes, closer it resembles a smooth surface. Hence a systematic selection of tiny mouths would eventually converge to a smooth surface, shedding light on hitherto possibly unknown physics of boiling. On the other hand in nanofluids point of view, small lengthscales resemble particle aggregates as seen from SEM images of nanoparticle fouling shown in chapter 5. The present study therefore will be instrumental to explain boiling phenomena of nanofluids.

It was stated in section 3.2.6 that the artificial cavities were first microfabricated in Leeds University, then at the Centre for Nanoscale Systems of Harvard University. Leeds cavities were used to develop and test an experimental facility for pool boiling. For the real boiling experiments, the cavities were fabricated afresh in Harvard. This discussion is therefore focusing on Harvard cavities for that reason. The tool used to fabricate the artificial conical cavities on silicon substrates was the Zeiss NVision 40 Crossbeam device. This device works on the principle of Focused Ion Beam. It can accommodate a 100mm diameter wafer in its machining chamber.

There were three important steps in the FIB operations; calibration of beams, patternmaking, and surface fabrication. The instrument manufacturer has laid down a sequence of steps to calibrate the beams for precision machining that includes the determination of eucentric axis and coincidence point. Creation of a pattern of a desired cavity could either be done on the instrument's software itself or imported from a more sophisticated platform such as AutoCAD. However for the conical shapes in this work, in-house patternmaking was found to be sufficient. After choosing the standard annular shape, the beam current and dwell time were adjusted until the cone was obtained. Verification of the cavity depth and angle were done by cavity cross sectioning. Table 6.1 outlines the cavities to be machined on FIB.

Table 6.1: Plan for artificial cavities on silicon wafer

Mouth diameter (D), µm	Included angle(^{o})	Depth (H), µm
0.5	20	1.42
1.0		2.84
1.5		4.29
2.0		5.68
4.0		11.36

The Young-Laplace (Y-L) equation was applied to estimate the cavity nucleation superheats. Y-L predictions for water are plotted in figure 6.1 along with Griffith-Wallis (G-W) for comparison. These two equations were earlier introduced under the literature review chapter as eq 2.22 and eq 2.23 respectively. The plot shows an order of magnitude difference for 0.5µm cavity size. But the two predictions rapidly converge with the increasing cavity sizes. Similar trends were observed for methanol and ethanol.

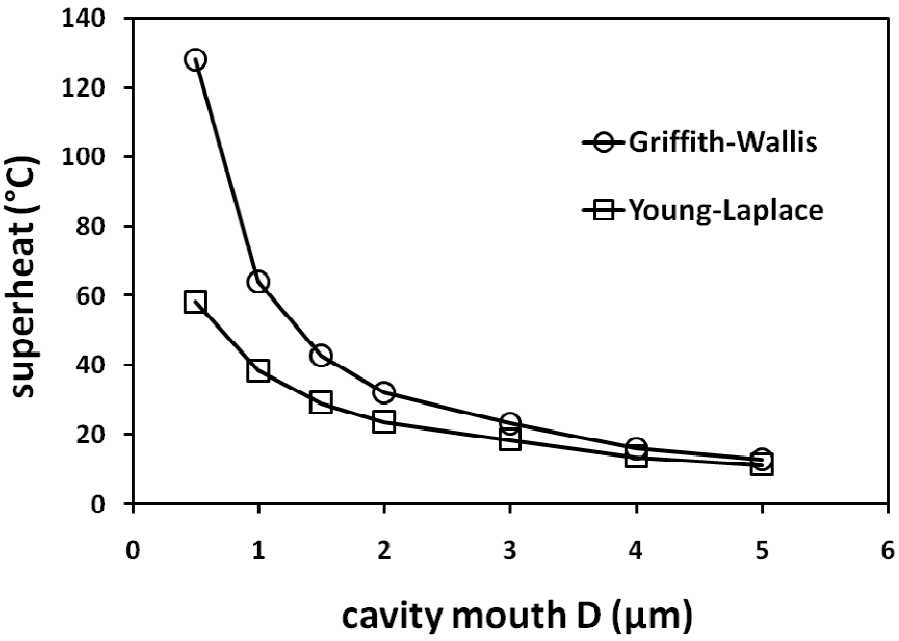

Figure 6.1: Predicted cavity nucleation superheats for water

Young-Laplace equation is regarded as superior in accuracy for it is derived from first principles. Also it is the superheat needed form a vapour embryo on a cavity. In the meantime the G-W prediction is for the minimum superheat required for the bubble to grow beyond the mouth of cavity. That is, basically G-W discusses the bubbles after a cavity nucleates. Hence it is felt that the Y-L is more appropriate for the cause of this study. On that basis, appreciate from figure 6.1 that the heat source that is going to heat the liquid should have the capacity to raise its temperature above the Y-L predicted temperature. For water and the 0.5µm cavity, the predicted temperature is 158.2°C.

6.3 Characterization of Microfabricated surfaces

Mouth diameters of cavities were verified by SEM imaging. The interior shape was confirmed by transverse cross-sectioning. Two representative images are given on figure 6.2. Since the cross-sectioning is destructive, it was only practiced at the fine-tuning stage of fabrication process.

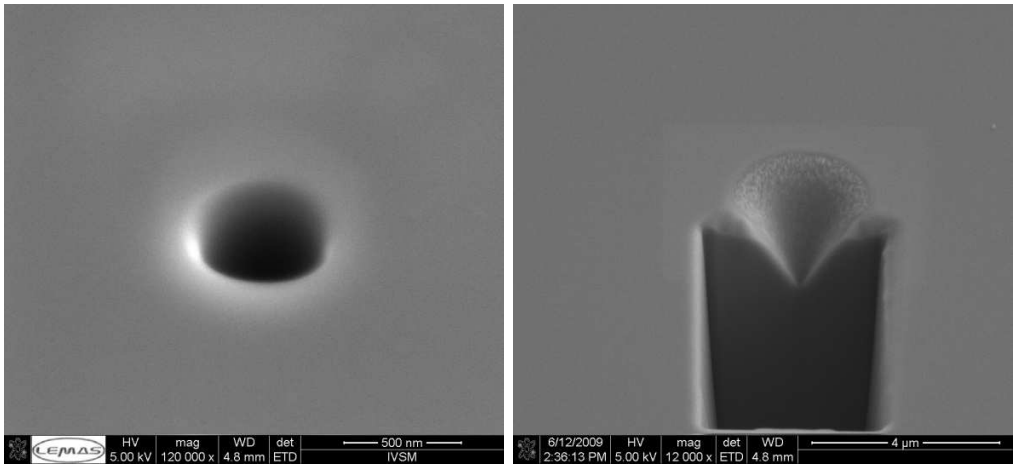

Figure 6.2: A cavity and its cross section generated using FIB

Obtaining the expected cavity diameter was fairly easy and straight forward. Producing the conical shape however was a challenging task. The shape is very sensitive to the speed of material removal. After the conical shape (pattern) was fed into the FIB, several hours of test runs had to be conducted to fine tune the shape. Hence the cavity manufacturing consumed substantial amount of machine time while needing high level of machining skills.

6.4 Calibration of equipment

Test rig described in Section 3.2.6 was aimed at recording the temperature footprint of bubbles using an IR camera placed underneath the substrate. The camera would collect the IR intensities which will later be converted to respective temperatures by software. Hence the precision of capturing IR intensities will increase the accuracy of temperature data, which involves careful calibration of the equipment. To elaborate this further, consider the scenario given in figure 6.3.

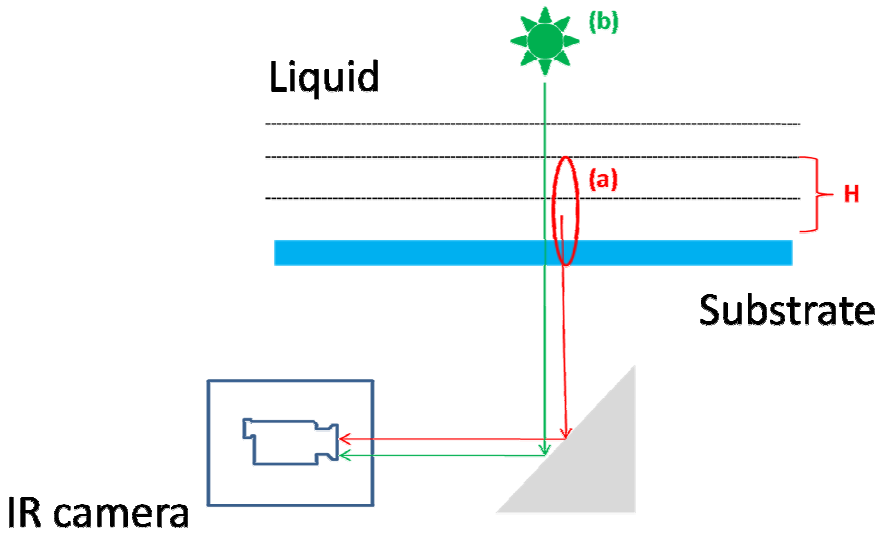

Figure 6.3: Temperature signal integration by IR camera

The halogen lamp heats up the liquid that rests on the substrate. Depending on the IR transmittance of the liquid and the substrate, the camera underneath may receive IR signals emitted by a liquid depth of H denoted by *(a)*, heat source *(b)* and the substrate. The effect of *(b)* can easily be eliminated by placing an inexpensive IR barrier such as a piece of glass. However other two components will prevail. In order to separate them from each other, some sort of filtering should be applied. Or else the contribution from either part has to be estimated. Calibration of the equipment is geared to serve this purpose. It involves the determination of the IR transparencies of substrate and liquid, and conversion of IR signals to temperature data through a calibration curve.

6.4.1 IR transparency of substrate

Two kinds of silicon wafers were subjected to IR transparency tests. There were two types of tests where one was using IR camera and the other using FTIR device (Fourier Transform Infrared Spectrometer). In the former, a hot object of 200°C was held against pieces of the two wafers. The IR camera was subsequently used to photograph them from the other side of wafers. Figure 6.4 illustrate the hot object on its own, through a double polished wafer, and a SiO_2 coated wafer respectively. A double polished wafer was purchased from Silicon Valley Microelectronics Inc, USA. The wafer with 100nm SiO_2 coating was supplied by Si-Mat GMBH, Germany. Both substrates were 380micron in thickness and had been doped with boron to introduce a resistivity range of 5-30 Ohm-cm. At the calculation stages, it was found that this degree of resistivity was needed in

order to heat the wafers by resistive heating. Later however the heating method was shifted to halogen light.

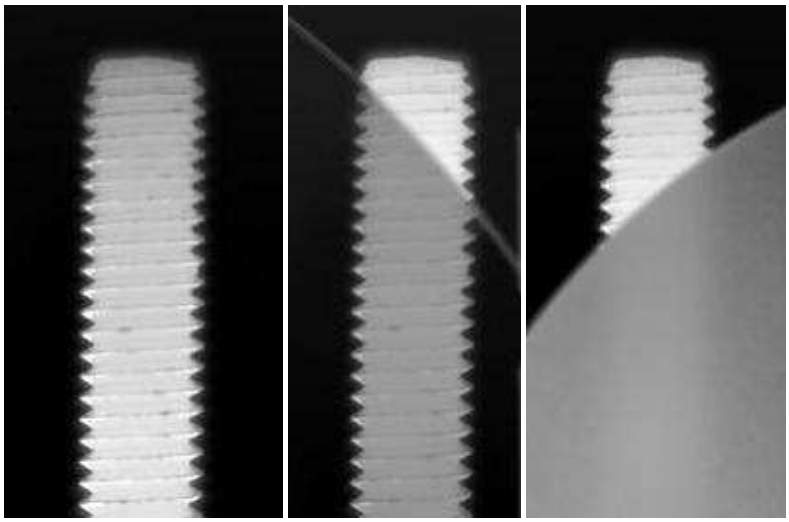

Figure 6.4: A qualitative test for IR transmittance of silicon wafers

For the second experiment, the Thermoscientific Nicolet 6700FT-IR device was hired from the Centre for Material Science at MIT to measure the transmittance of silicon wafers. In this technique a beam of light of known wavelength is shined on the substrate and measures difference between the incident intensity and departing intensity. Presented in figure 6.5 is the output obtained output from FTIR device. Upper and lower curves respectively stand for coated and uncoated wafers. The wavelengths were selected to cover the range of the IR camera.

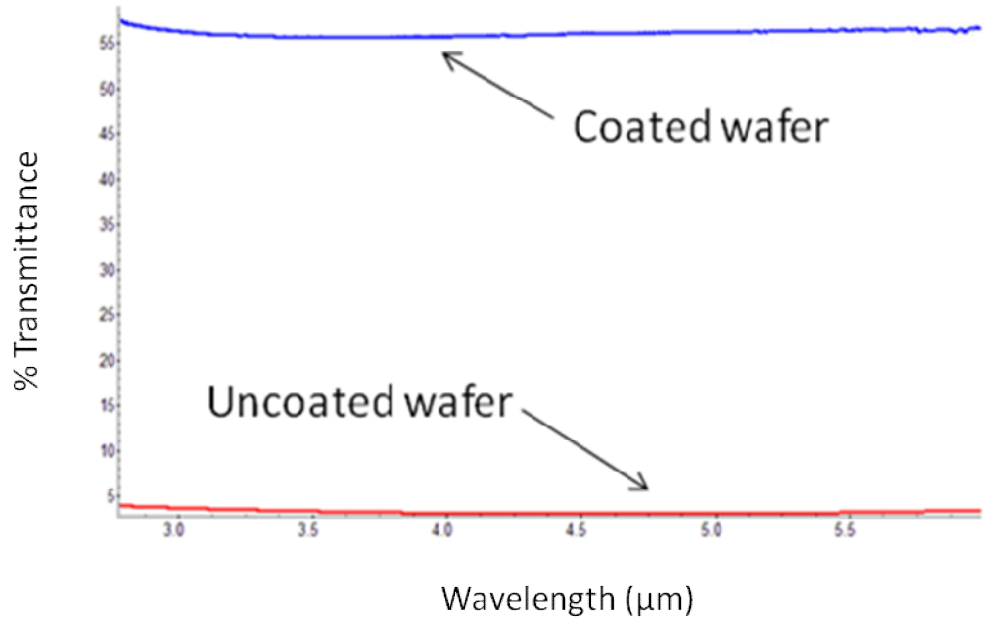

Figure 6.5: FTIR measurement of IR properties of Silicon wafers

Apparently the reason behind the remarkable difference in transmittance was the thin SiO_2 layer. The IR transparency of SiO_2 is very low in comparison to Si. Also in passing compare figures 6.4 and 6.5 to appreciate that the bench top test is a good first approximation for IR visibility of silicon substrates.

6.4.2 IR transparency of liquids

Recall that the temperature of the liquid microlayer in bubble nucleation is the focus of this investigation. Microlayer thickness in deed is very small in the order of few tens of micrometers. To capture it by way of IR thermometry, it has to be ensured that the IR signals emitted by elsewhere are barred from entering the camera. The boiling liquid on top of the substrate emits IR signals, a part of which is absorbed by the liquid itself on its way downwards. Unless the substrate is fully opaque, the unabsorbed part may reach the substrate and subsequently pass through to the camera. On figure 6.3 this was the scenario *(a)* where height *H* is far larger than microlayer thickness. A means of preventing this is to select high IR-absorptive liquids. Following discussion expedites the IR transmittance of liquids.

For monochromatic light passing through a medium, the intensity *I* at a distance *x* is given by Beer-Lambert Law;

$$I = I_0.10^{-\alpha x} \qquad \textit{Eq 6.1}$$

Where I_0 is the initial intensity of light and α is the absorption coefficient of the medium. Quantity αx together is often referred to as the absorbance. When α is known, the liquid depth necessary to absorb a percentage radiation can be found. A sample calculation for water is given below.

Assume it is needed to determine the water depth that can filter our 99% $(I/I_0=0.001)$ of the incoming IR light. The equation 6.1 can now be rearranged as;

$$x = -\log\left(\frac{I}{I_0}\right).\frac{1}{\alpha} \qquad \textit{Eq 6.2}$$

The respective x values are given in Table 6.2. Values for absorption coefficient α of water were recruited from Irvine and Pollack [249] .

Table 6.2: IR absorption in water

λ (μm)	α (1/cm)	x (um)
3	10860	2.76
3.1	7430	4.04
3.2	3700	8.11
3.3	1650	18.18
3.4	698	42.98
3.5	334	89.82
3.6	198	151.52
3.75	119	252.10
3.83	111	270.27
4	151	198.68
4.5	411	72.99
4.66	468	64.10
4.8	431	69.61
5	308	97.40

The maximum water depth to fulfill the condition of $I/I_0=0.001$ will be found as 270.27μm, which in turn corresponds to the wavelength of 3.83μm on the table.

There are several thermodynamically attractive liquids in addition to water, such as Novec649, FC72, Methanol, and Ethanol. They are widely applied, have low normal boiling points (49°C, 56.7°C, 64.5°C and 78.5°C respectively), and predicts smaller Y-L nsuperheats for bubble

nucleation on tiny cavities. Unfortunately the IR spectra obtained from the vendors lacked the vital information of path length which made it impossible to accurately determine parameter *x*. The IR spectra therefore had to be generated in the laboratory. The approach taken here was similar to that described in section 6.4.1.

For bench-top IR transparency tests, a small test cell was designed. A piece of transparent silicon wafer was glued to one end of a polycarbonate tube. The IR camera was placed under the cell to capture the transmission. A solder iron tip was firmly held 3cm above the bottom of the cell with the tip temperature being set to 200°C. Figure 6.6 illustrates the arrangement.

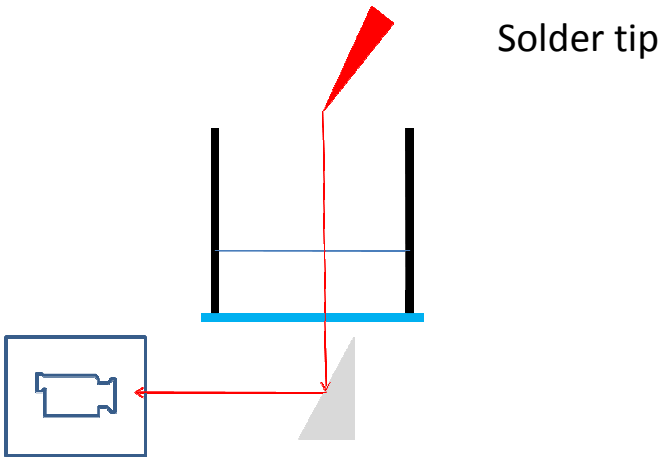

Figure 6.6: Apparatus for IR transmission test of liquids

The IR camera was subsequently tuned on to acquire the sharpest image of the tip and the corresponding IR count was taken. IR image without liquid is brighter as seen from figure 6.7. This procedure was repeated for a series of liquid depths.

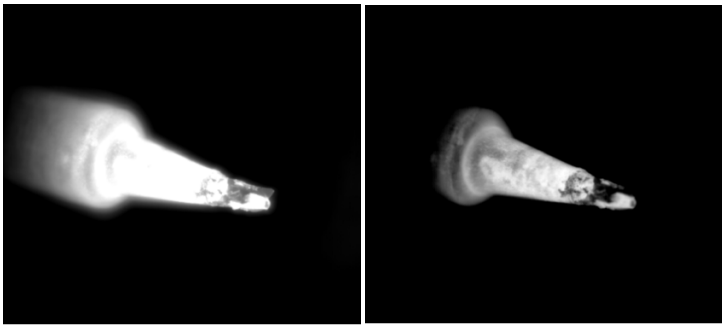

Figure 6.7: IR transmission of FC72. Left-no liquid, Right-liquid depth 5mm

Given on Table 6.3 are the IR count obtained this way. For comparison purposes, the IR count of a point in the surroundings is also presented. Water was examined as a benchmark.

Table 6.3: IR transparency of liquids

Fluid	NBP (°C)	Liquid height (mm)	IR Count	
			Tip	Surround
FC-72	56.7	1 2 5	2400 2200 2000	1800 1800 1800
Novec649	49	5	2000	1800
Methanol	64.5	1	1800	1800
Ethanol	78.5	1 2	2200 1800	1800 1800
Water	100	1	1800	1800

Two right-most columns on the Table 6.3 offer a qualitative picture of each fluid's IR transmittance. FC-72 and Novec649, despite being thermodynamically attractive, are highly transparent to IR light. However Ethanol and Methanol have shown some promise by way of barring IR with only a thin liquid layer of 1-2mm. This attracted interest for further investigation of their IR spectra.

6.4.2.1 Determination of IR spectra of liquids

An in-depth investigation was conducted to establish the IR spectrum of ethanol, methanol and water using the Thermoscientific Nicolet 6700FT-IR device. There were three standard methods to measure optical properties of liquids, viz., the liquid cell method, the ATR (Attenuated Total Reflection Spectroscopy) method and the GATR (Grazing angle ATR) method.

In the first method, the liquid cell shown in figure 6.8 was loaded with the liquid sample. Inside the cell were two Zinc Selenide (ZnSe) windows separated by a thin spacer. Thickness of the spacer was critical as it sets the thickness of liquid sample, known as path length or penetration

depth for the beam. The interior and liquid filling mechanism of the cell resembled a SAXS cell described in Section 3.2.4.

Figure 6.8: The infrared absorption cell

Firstly the cell was flushed with acetone, dried with Helium gas and sent to the plasma cleaner. Secondly the background scanning was conducted, where the empty cell was mounted on the FTIR device and IR beam was sent through. These background signals were to be deducted from the signals gathered from the sample. Also the background scanning provides an opportunity to calibrate the path length. Ideally the path length should be equal to the spacer thickness, but in practice these are different. The theory states that the path length *(L)* can be expressed in terms of starting and ending wave numbers (W_1 and W_2) and the number of fringes *(n)* in between W_1 and W_2.

$$L = \frac{n(10)}{2(W_1 - W_2)} \qquad \textit{Eq 6.3}$$

The background scanning was followed by the sample scanning to obtain the IR absorbance spectra of water, ethanol and methanol. These data were then used to calculate the absorption coefficient, which is the ratio of absorbance to path length. Figure 6.9 gives a graphical representation of absorption coefficients obtained from liquid cell method.

In ATR and GATR methods, the liquid is loaded onto horizontal plates respectively made of ZnSe and Ge. This plate is then mounted on the FTIR device to collect the absorbance data. Unlike in liquid cell method, there was not a pre-defined penetration depth. It has instead to be computed as a function of the wavelength and angle of incidence of light on to the sample and the refractive indices of liquid and the cell material. The angle of incidence for ATR and GATR were 45° and 65° respectively.

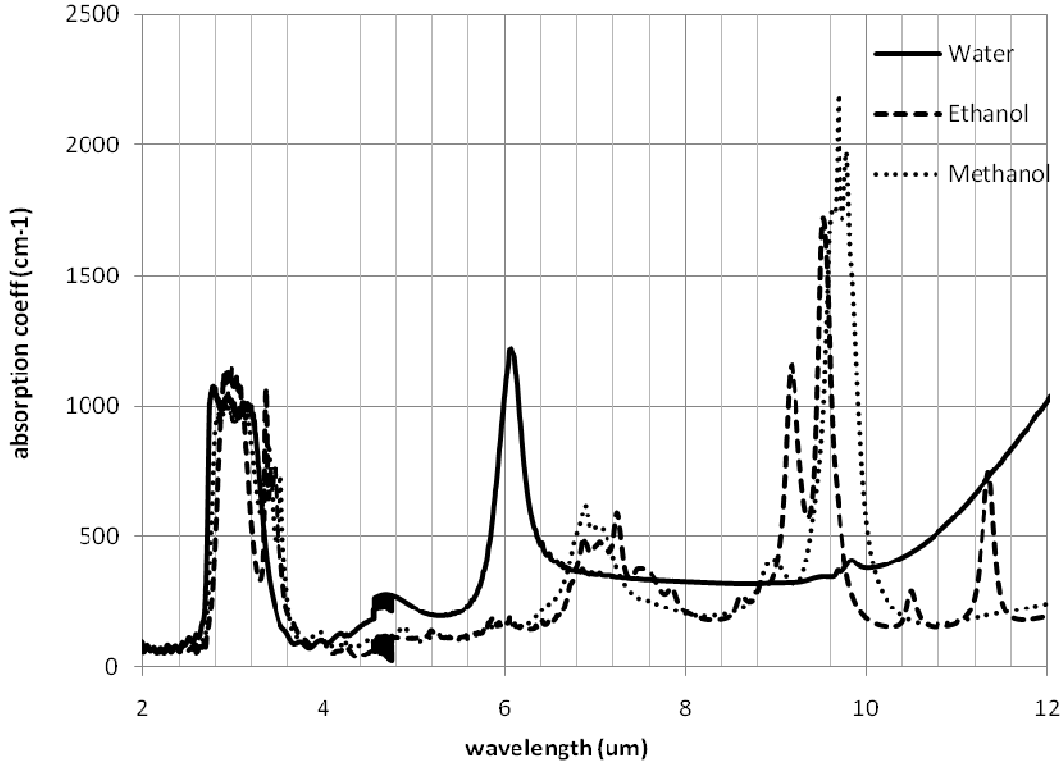

Figure 6.9: Absorption spectra for Water, Ethanol and Methanol

Above-mentioned instruments generated the absorbance data. These had to be divided by the pathlength to obtain the absorption coefficient. Table 6.4 presents the pathlengths calculated using the CrisCalc computer program supplied by Harrick Scientific Inc. The respective spectra are given in Appendix A.

Table 6.4: Pathlengths for ATR and GATR techniques

λ(μm)	1	2	3	4	5	6	7
ATR	0.1478	0.2956	0.4434	0.5912	0.739	0.8864	1.0347
GATR	0.0471	0.0943	0.1415	0.1887	0.2359	0.2831	0.3303

Due to the unavailability of absorption coefficients for ethanol and methanol in open literature, it was only possible to compare water data to verify the accuracy of experiments. This is presented in Table 6.5. *H* is the maximum depth needed to absorb 99.9% of incident IR, and *λ* is the wavelength where this occurs. Note that the absence of GATR data is due to its large disagreement with the other datasets.

Table 6.5: Required water depth for 99.9% absorption

	H(μm)	λ(μm)
Literature	270.3	3.83
Liquid cell	397	3.84
ATR	40	3.80

To be on safe side, it would be advisable to pick the largest value of H, which in this case corresponds to liquid cell method. In that case, then the depths needed to meet the 99.9% absorption criteria are given in Table 6.6.

Table 6.6: Depth to meet 99.9% absorption

	H(μm)	λ(μm)
Water	397	3.84
Ethanol	1430.6	4.76
Methanol	405.8	4.33

In the spectral range of 3-5μm presented on Table 6.6, values for *H* for water and methanol are in close agreement while ethanol seems to be more transparent to IR light. These values determined from optical measurements are in reasonable agreement with bench-top experiments previously presented in Table 6.3.

6.4.3 IR filter

Use of an IR filter on the camera is a way of filtering out selected wavelengths from the spectrum that are bound to the camera. Its advantage in the present context can be understood by revisiting Table 6.2, where the highest absorption was demonstrated when the wavelength was 3μm. At this point, a 2.76μm depth of water will absorb 99.9% of waves of 3μm IR light incident on it. By choosing a filter that blocks all wavelengths but 3μm will ensure that the IR intensities recorded by the camera are coming from a liquid layer of 2.76μm in thickness.

However there is a penalty associated with the filter. Since the IR bandwidth is very narrow the signals will be weaker and images blurred. To cope with this the IR camera has to be manually calibrated. Without a filter the camera functions well with factory calibration alone.

6.4.4 Conversion of IR intensity signals to temperature data

There is a relationship between the IR intensity recorded by the camera and the actual temperature of the particular location. To plot a curve to obtain this relationship, a calibration vessel was designed which is shown in figure 6.10. Further details are provided in Appendix A.

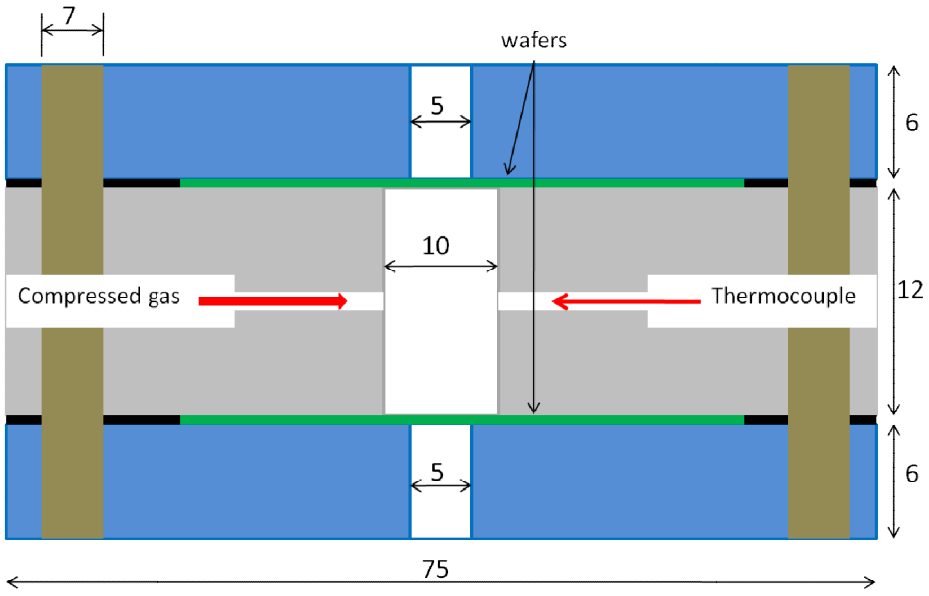

Figure 6.10: Intensity-Temperature calibration vessel. All dimensions are in mm

The cavity in the middle is 10mm in diameter that holds the liquid. The silicon wafers are sandwiched between the middle part made of polycarbonate and the two cover plates made of aluminum. The vessel was pressure tested up to 5bar using helium gas. At elevated pressures the boiling point of liquid is high which is beneficial for high temperature calibration. The setup for calibration exercise is illustrated on figure 6.11.

In the calibration facility there are two heater blocks on top and the bottom of calibration vessel. These are to heat up the liquid inside. Three thermocouples *(T)* sense the liquid and heater temperatures. Agilent Technologies 34980A BenchLink Datalogger system acquires and displays the realtime temperature values. Central holes in the heater blocks coincide with that in the vessel. Signals coming through the hole of the bottom block are received by the IR camera and transmitted to computer. The tests were conducted in descending temperatures.

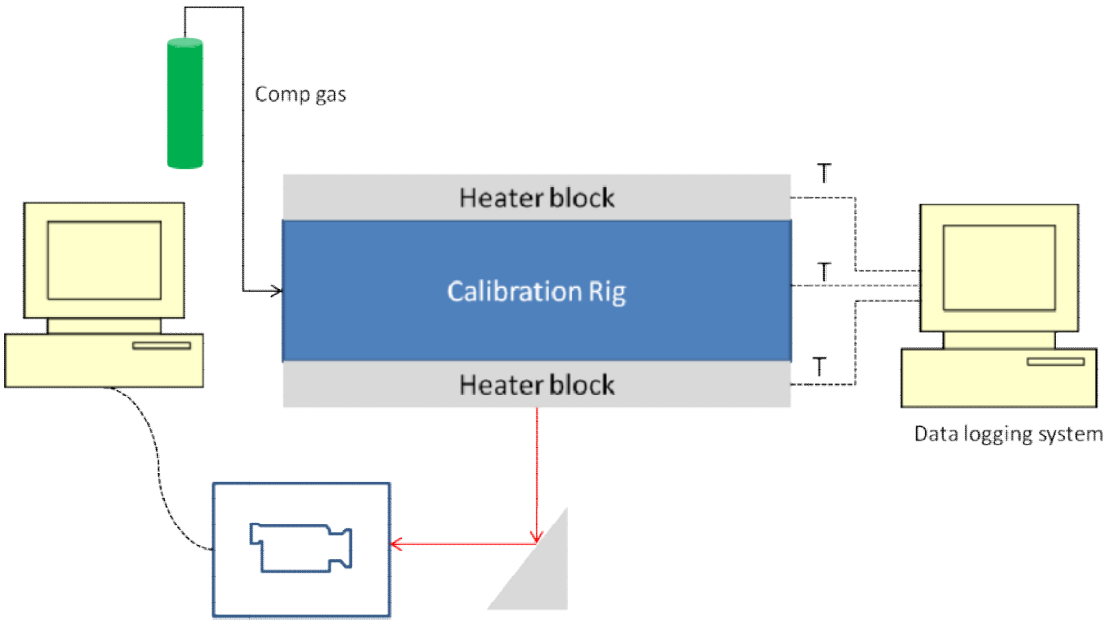

Figure 6.11: Calibration facility

A typical test sequence began with the heater blocks being switched on through the variac and liquid temperature being brought to the highest value. After the system achieved the steady state, temperatures were recorded and an IR image was taken. Subsequently the power input was reduced to bring the system to the next level of temperature and so on. At each step an IR image was taken. Later when the data analysis was conducted, the IR intensity corresponding to a given temperature was extracted from these IR images. The temperature-intensity relationships was thus obtained and plotted. Figure 6.12 presents the calibration curves for *(a)* dry transparent wafer *(b)* transparent wafer with water *(c)* dry semi-transparent wafer *(d)* semi-transparent wafer with water. Similar calibration curves were obtained for ethanol and methanol although not shown here.

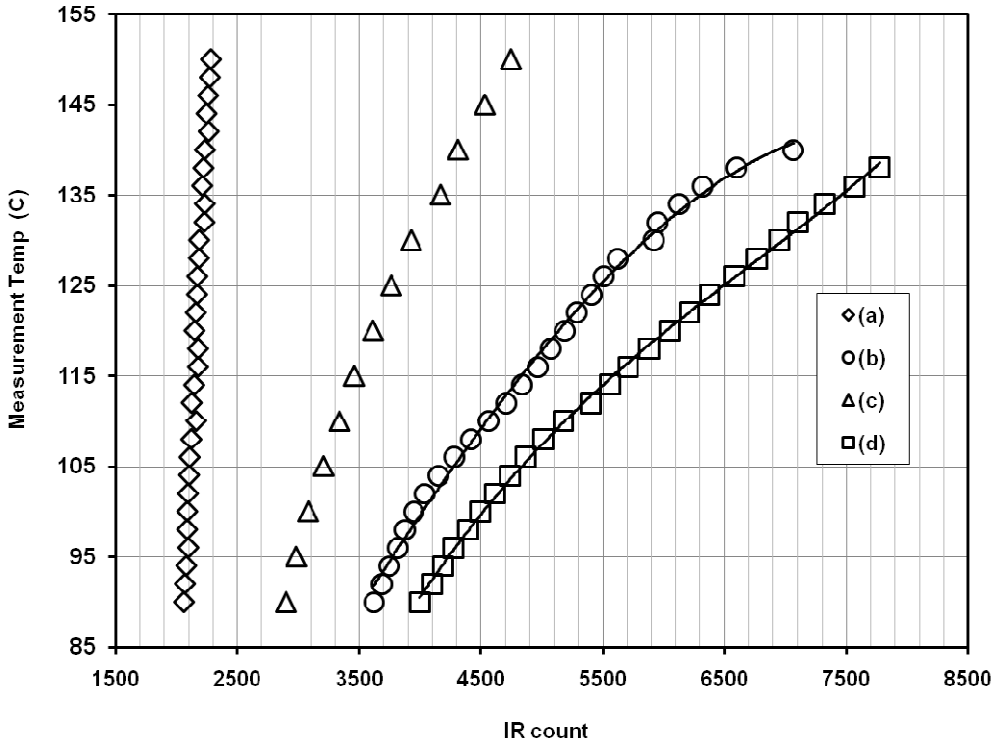

Figure 6.12: Temperature-IR calibration curves for water

This brings the description on calibration of equipment to an end. Now that the equipments are ready, the forthcoming discussion will present experimental results.

6.5 Experiments

Table 6.1 stated the expected cavity sizes. However when they were fabricated on FIB, the real sizes had become slightly different. Given on Table 6.7 are the actual sizes of cavities (D) those used for boiling experiments. Size tolerances are also mentioned. Each wafer is assigned with a number for reference purposes. Note that wafer numbers 10 to 12 were plain wafers.

Table 6.7: Artificial cavities for boiling experiments

Wafer	Actual cavity D(μm)	Liquid
1	4.55±0.45	water
2	4.40±0.40	water
3	2.35±0.45	water/ nf
4	2.15±0.35	water/ nf
5	1.85±0.15	water/ nf
6	1.45±0.25	water/nf
7	1.40±0.40	nf
8	0.65±0.05	nf
9	0.60±0.05	water/ nf
10	0	water
11	0	nf
12	0	nf

Boiling experiments were conducted with water, ethanol and methanol liquids. The experimental procedure was as follows.

Preparation of water was the first step towards experiments. It was Millipore water used for these experiments. However any dust and dissolved air may act as nucleation sites and contaminate the real picture. Hence purity and cleanliness are two critical parameters in boiling at small scale. A method to remove dissolved gases from water was taken from literature [250]. Accordingly the Helium gas was purged for 20mins while the water being stirred at temperature of 37°C. To clean this water further it was filtered using a 100nm filter. In nanofluids experiments, degassed Millipore water was used to prepare nanofluids and subsequently filtered through 100nm filter.

To fill the liquid the boiling chamber was taken to clean room. It was opened and cleaned using acetone and water followed by drying. To the bottom slot in the chamber the silicon wafer was fitted and the test liquid was filled. Two side holes in the chamber were sealed before it was packed in airtight bag.

In the test laboratory the boiling chamber was placed on a rigid holder, and the camera and accessories were arranged as shown on figure 6.13. The halogen light was subsequently shone on the liquid pool. Simultaneously the realtime bubble videoing was started. Power input to the halogen lamp was slowly increased by turning the variac. When a bubble activity was about to occur, which could be forecasted by closely watching the fluid motion patterns, the video was

turned to recording mode. Due to the massive memory the videos consume on the PC, the recordings had to be selective. The halogen light was a spot heater and it shines on a selected region. When finely focused, it would be possible to do selective heating of a region on a wafer to nucleate at a given time.

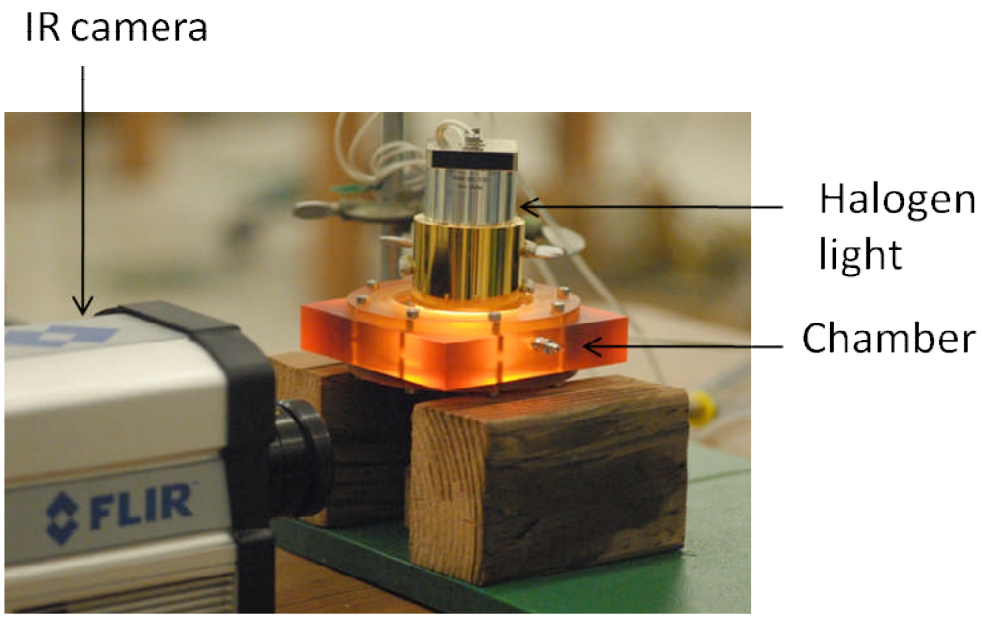

Figure 6.13: A boiling experiment

Few bubble cycles were recorded this way. If the liquid was all evaporated, then the boiling chamber was carefully refilled. After the boiling experiment the videos were retrieved, analyzed and temperature data were extracted.

6.5.1 Data analysis

Figure 6.14 illustrates an example for a still image and the color code of a vapour bubble on an artificial cavity acquired by FLIR IR camera. A continuous video film produced large numbers of such images which were later exported to ImageJ software. It had the capacity to convert the IR images into IR intensity data. Later these IR intensity data were converted to temperature profiles with the aid of calibration curves shown on figure 6.12. Also shown on figure 6.14 is the evolution of the temperature profiles of the bubble obtained that way. This profile maps the temperature of the bubble along the chord shown on the neighboring bubble image.

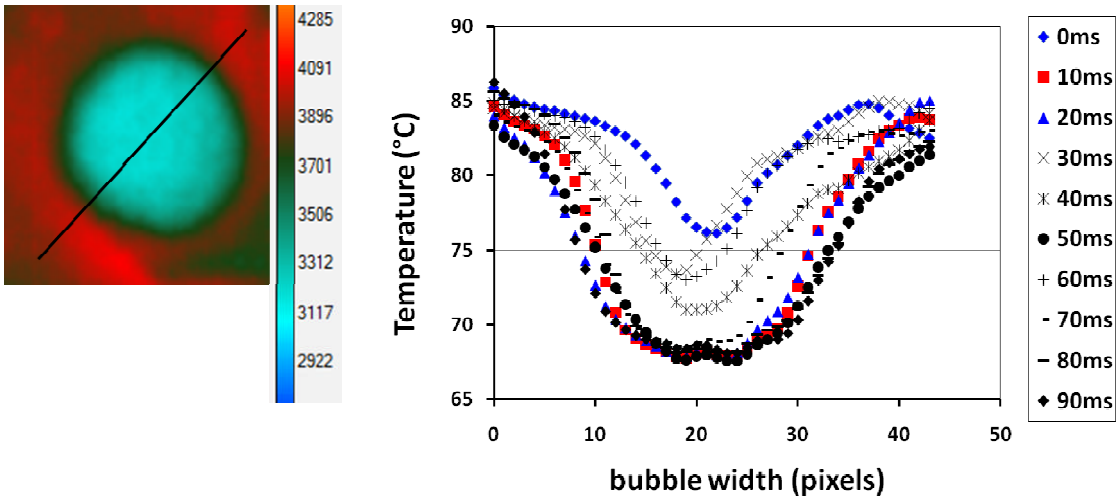

Figure 6.14: IR image and temperature profile for a methanol bubble

This bubble was videoed at a frame rate of 100fps. Thus the time gap between two consecutive temperature profiles on the graph was 10miliseconds. Also eye observation showed that this cavity was fast producing bubbles. Hence the 100fps frame rate was inadequate to capture all activities on the site. This is reflected from the graph in figure 6.14, where some lines had missed out such as the top most line. Nevertheless the important information of the shape of bubble temperature profile is contained in this graph. In the periphery of the bubble is the superheated liquid layer. The temperature of this layer does not vary considerably throughout the cycle. A complete description of the meaning of temperature profile of a bubble cycle is presented later in this chapter, with the aid of still images.

6.5.1.1 Boiling on plane wafers

Plain silicon wafers did not contain artificial cavities. They were as smooth as the *Ra=0.5nm*. Since the wafers container was opened in the cleanroom, they are presumably ultra clean. Such a wafer would make the ideal conditions to reproduce homogeneous nucleation on a smooth surface.

Heat transfer literature, for example Carey [246] among others, expresses the liquid temperature *(T_l)* at the time of homogeneous bubble nucleation as follows.

$$J = N_l \left(\frac{3\sigma}{\pi m} \right)^{1/2} \exp\left\{ \frac{-16\pi\sigma^3}{3\kappa T_l [\eta P_{sat} - P_l]^2} \right\} \qquad \textbf{Eq 6.4}$$

where

$$\eta = \exp\left[\frac{P_l - P_{sat}}{\rho_l R T_l} \right] \qquad \textbf{Eq 6.5}$$

Here J is the rate of vapour embryo formation per unit volume of liquid, N_l is the number density of liquid molecules per unit volume, and ρ_l, σ and m are respectively the density, surface tension and mass of one molecule. Moreover P_l and P_{sat} are liquid and saturation pressures and T_l is liquid temperature corresponding to P_l. J is customarily assigned the value of 10^{12} [246]. Lienhard and Karimi [251] estimated the homogeneous nucleation temperature $(T_l=T_{SL})$ was approximately 0.8 of the critical temperature (T_{crit}), i.e., $T_{SL}\sim 0.8 \times T_{crit}$. Blander and Katz [252] and Eberhart [253] stated that $T_{SL}\sim 0.88$ to 0.9 of T_{crit}.

Heterogeneous nucleation on a smooth surface is influenced by the liquid-solid contact angle (Θ). Accordingly the equation 6.4 needs to be modified as follows in order to account for Θ [246].

$$J = \frac{N_l^{2/3}(1+\cos\theta)}{2F} \left(\frac{3F\sigma_{lv}}{\pi m} \right)^{1/2} \exp\left\{ \frac{-16\pi F\sigma_{lv}^3}{3\kappa T_l [\eta P_{sat} - P_l]^2} \right\} \qquad \textbf{Eq 6.6}$$

where

$$F = \frac{2 + 3\cos\theta - \cos^3\theta}{4} \qquad \textbf{Eq 6.7}$$

By measurements it was found that Θ for water on silicon wafer was close to 50°. For methanol Θ was immeasurably small. For water the figure 6.15 was obtained from MATLAB programming of equation 6.6, with help from Bren Philips of MIT. The MATLAB graph for methanol is provided in Appendix A.

For water on silicon, the T_{SL} taken from figure 6.15 at J=10^{12} is about 310°C. Meanwhile Blander and Katz [252]approximation for homogeneous nucleation predicts an interval of 296.6°C to 309.6°C. Hence they are in good agreement. Lienhard and Karimi [251] estimate is ~ 245°C.

For methanol T_{crit} is known to be 240.15°C. If Lienhard and Karimi's limit is taken as the lower limit and Blander and Katz's as the upper limit, then the homogeneous nucleation should occur in the temperature range of 137.5°C to 188.8°C. For very small θ (<10°) of methanol on silicon, homogeneous nucleation should occur ~ 198°C.

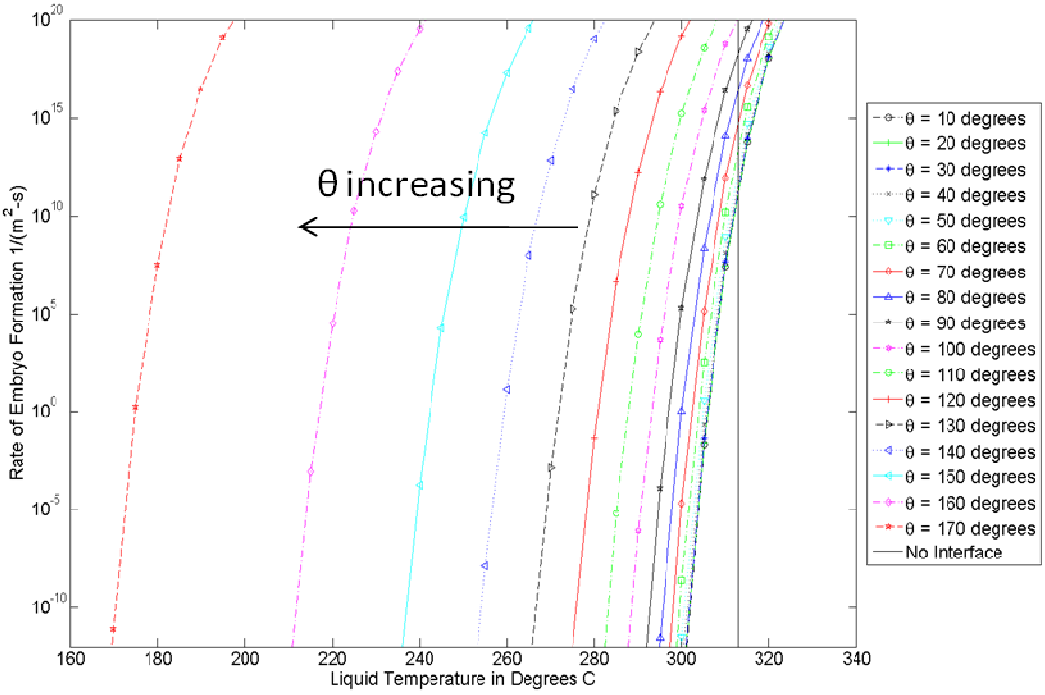

Figure 6.15: Heterogeneous nucleation of water vapour on a smooth surface

Filtered water, water based SiO_2 0.01wt% nanofluid, filtered water based SiO_2 0.01wt% nanofluids, and methanol were boiled on four individual fresh plain wafers. The IR images were taken on the first bubble appearance. Thereafter the temperatures corresponding to the first bubble were plotted as shown on figure 6.16.

All four samples had exhibited large bubble nucleation temperatures on plain wafers. For water it was 173°C. This is considerably below the predicted T_{SL} but plausibly above generally reachable limit. Appreciate that the theoretical superheat needed to nucleate a 0.5µm cavity was 58.2°C. In turn this is a confirmation of the suitability of the experimental apparatus and procedure for current experiments.

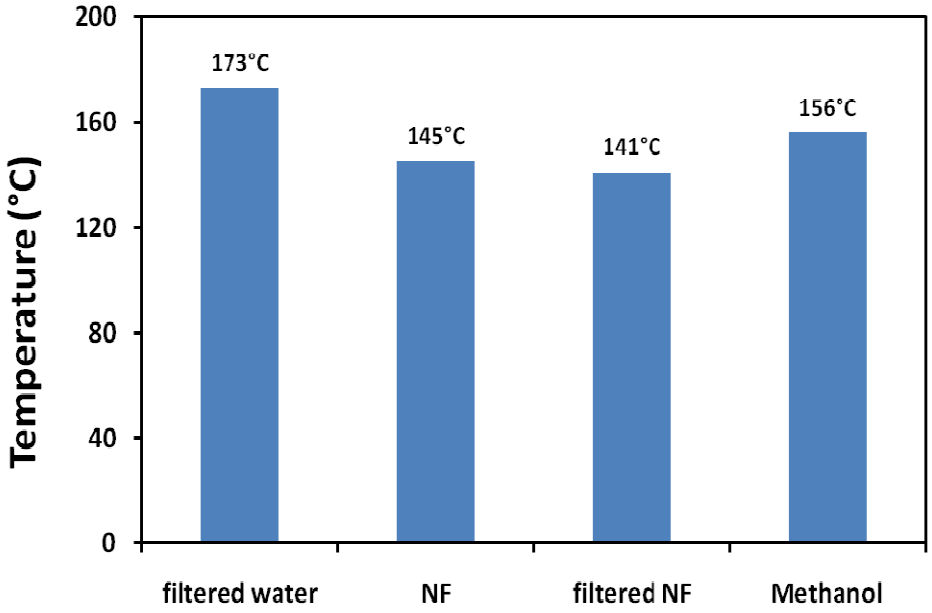

Figure 6.16: Appearance of first bubble on plain wafers

Nanofluids (NF on figure 6.16) have however nucleated the vapour bubbles at relatively low temperatures than water. As will be seen from the forthcoming discussion, the values shown on figure 6.16 are larger than the largest obtained cavity nucleation superheat for nanofluids. Lower nucleation temperatures for nanofluids than water raise the speculation that the nanoparticles may have formed nanosize nucleation sites on the wafer. In deed particle deposits were found on the wafer which will be shown later on figure 6.20.

Finally consider methanol on figure 6.16. Its nucleation at 156°C falls within the upper and lower limits for T_{SL} described before. Thus it can be declared with confidence that the present experiment was able to witness the homogeneous nucleation of methanol.

6.5.1.2 Boiling of water on cavities

Filtered degassed water was boiled on the array of cavity sizes stated in Table 6.7 with the aim of capturing the bubble nucleation temperature. Figure 6.17 illustrates a typical bubble cycle for nucleation on an artificial cavity.

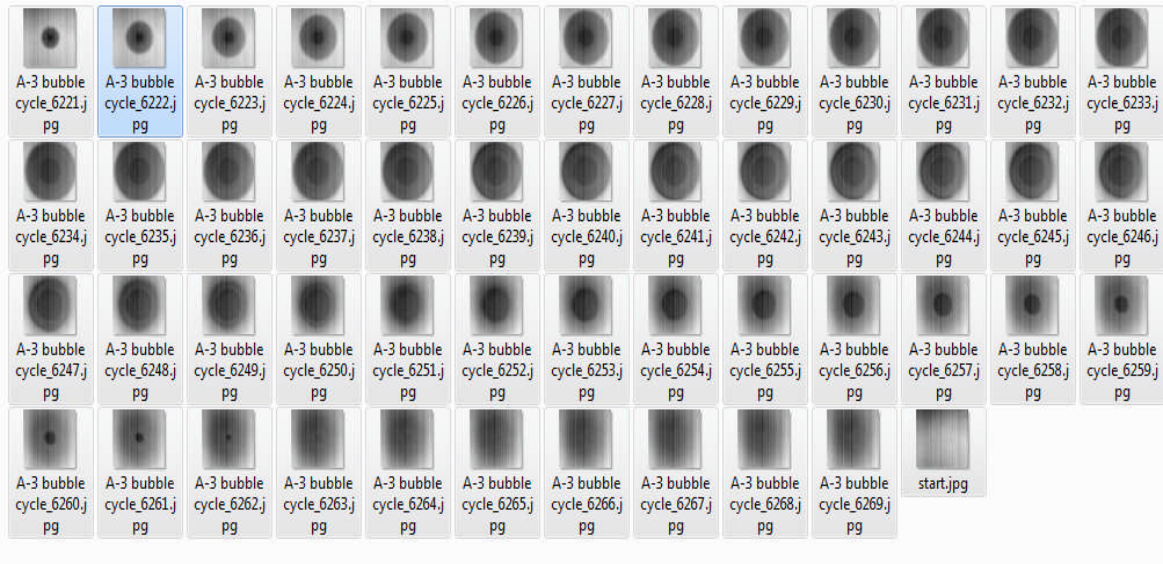

Figure 6.17: A bubble cycle on a cavity

Moment before a bubble cracks out from a cavity, the picture is as bright as the last frame on figure 6.17 (“start.jpg”). This can be considered as the superheated liquid layer that would facilitate a bubble to nucleate on the particular cavity. Then the bubble appears with a dark spot in its middle, surrounded by a white rim. This dark area is low in IR intensity which is accurately reflected by the dip in temperature profile on figure 6.18. As the time passes, the dark spot as well as the white rim grows in size. At a certain stage the white rim ceases to grow further. The dark spot would continue to grow for a while. From this point onwards the dark spot begins to shrink.

With reference to Gerardi et al. [214] who used this IR camera previously, a physical interpretation follows like this. The dark centre is the vapour-filled cavity. As the bubble grows out of the cavity, a microlayer is formed. Temperature of the microlayer as seen by the IR camera is something between the temperatures of vapour and superheated liquid. This intermediate temperature of the microlayer is characterized by its pale color that falls between dark centre and bright outskirts. Microlayer evaporates and the bubble grows. When it is ready to depart, the contact line receded toward the cavity as reflected by the shrinking dark area. Subsequently the bubble departs and superheated liquid in neighborhood rushes towards the cavity.

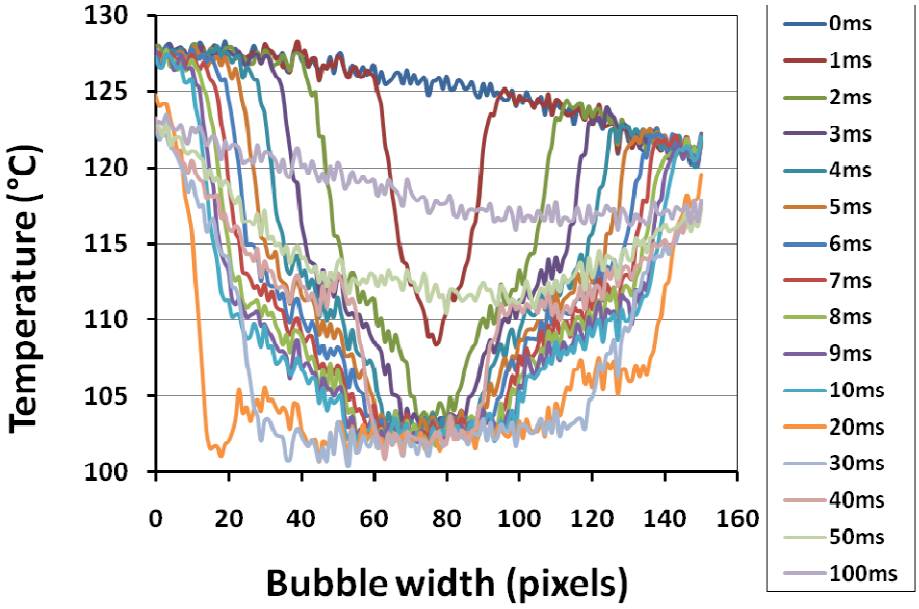

Figure 6.18: Temperature profile on 2.15µm cavity in water

The bubble temperature profiles shown in figure 6.18 was recorded at a speed of 1000Hz, enabling the temperature profile of the cavity to be mapped every millisecond. The topmost line (0ms) can be considered as the status of the superheated liquid layer. The slope is due to the temperature slide across the bubble. Such behaviour has previously been reported in IR studies [204, 212-213].

In the context of this investigation, most important is the temperature of superheated liquid layer. In figure 6.18, this will be the average value of the topmost line. It turns out to be 125.2°C.

Plots similar in shape were obtained for other cavity sizes. Analyses similar to the aforementioned were conducted to find the temperature of superheated liquid layer. A summary of findings are given on Table 6.8. The cavity diameters *(D)* are stated with the respective machining tolerances caused by the FIB. The liquid superheat is derived as the average value of the topmost line of the bubble temperature profile as describe earlier. While deriving it, averaging was done for the top most line of several bubble cycles. Out of them, the 'Highest' and 'Lowest' in the table 6.8 for a particular cavity size refer to the largest and smallest values obtained from averaging the top most line for the respective cavity. Hence it represents the largest and smallest superheats exhibited by that cavity.

Table 6.8: Liquid superheat for water

Cavity D(µm)	Liquid superheat (°C)	
	Highest	Lowest
4.55±0.45	13.3	11.8
4.40±0.40	16.7	12.8
2.35±0.45	26.2	21.8
2.15±0.35	28	20.9
1.85±0.15	25.6	20.8
1.45±0.25	33.3	27.1
0.60±0.05	56.1	48.7

6.5.1.3 Boiling of nanofluid on cavities

Ludox silica 0.01wt%-water nanofluids were boiled on wafer nos. 3-9 and 11-12. Wafers 7, 8, 11, 12 were fresh at the time of boiling the nanofluid, whereas other wafers were earlier boiled in water. An example for cavity temperature profiles is given on figure 6.19. This cavity was earlier shown on figure 6.18 for boiling of water. But in here the frame rate is 800Hz. Shapes of temperature profiles were similar for all cavities.

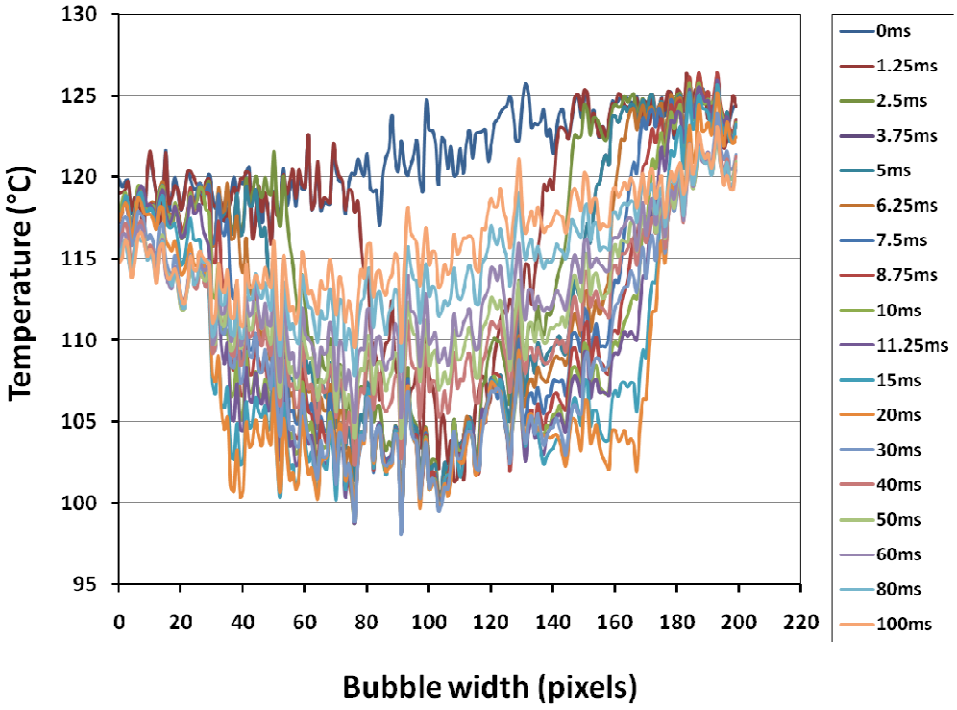

Figure 6.19: Temperature profile on 2.15µm cavity in nanofluid

For nanofluids the superheat temperatures were found to be smaller but the fluctuations appeared to be considerably larger than water. Cavity temperature profiles were presumably influenced by nanoparticle movements or even their deposition. Table 6.9 gives a summary for boiling of nanofluid. The method of determination of liquid superheat was precisely as described for Table 6.8.

Table 6.9: Liquid superheat for nanofluid

Cavity D(μm)	Liquid superheat (°C)	
	Highest	Lowest
2.35±0.45	16.6	15.9
2.15±0.35	20.7	17.1
1.85±0.15	12.7	12.5
1.45±0.25	18.1	16.7
1.4±0.40	39.5	39.1
0.65±0.05*	35.4	33
0.60±0.05*	35.4	32.4

Note: denotes fresh cavities*

SEM image of a silicon wafer after boiling the nanofluid shown in figure 6.20 portrays a homogeneously spreaded deposit of silica nanoparticles. In between the deposited nanoparticles are the nano-size pores and channels. Presence of these pores and channels resembles the shape of heater surfaces after boiling of nanofluids presented in Chapter 5. These particles however are monodisperse.

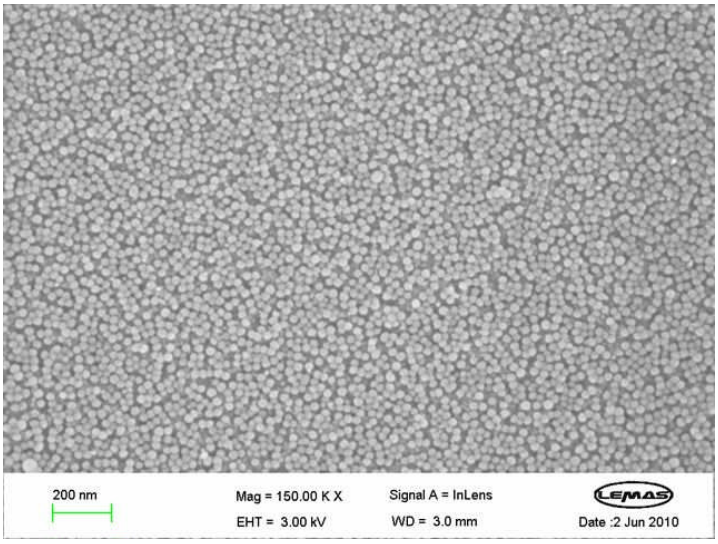

Figure 6.20: Ludox silica nanoparticles deposited due to boiling

Particle deposition is a phenomenon that would therefore happen anyway in nanofluids boiling, irrespective of the particle or the heater material. Particle deposition seen on silicon wafer contradicts Kwark et al. [146]'s claim. They thought the nanoparticle deposition was due to liquid microlayer evaporation underneath the bubble. But here on figure 6.20, deposit was evenly distributed, not only in the cavity neighborhoods. Furthermore the nanoparticle deposition has produced a novel structure on the silicon substrate that might have in turn altered the bubble dynamics. This could possibly have paved the way for SiO_2-water nanofluids to enhance the boiling heat transfer.

Lastly the most important discovery from this investigation will be presented. The data gathered from pool boiling experiments were compared with the predictions from the classical Young-Laplace equation and plotted on figure 6.21. Each data point has error bars. For Y-L predictions the error bars are based on the fact that the actual cavity diameter had a tolerance. The upper and lower end values for the diameters had respective Y-L prediction of superheat.

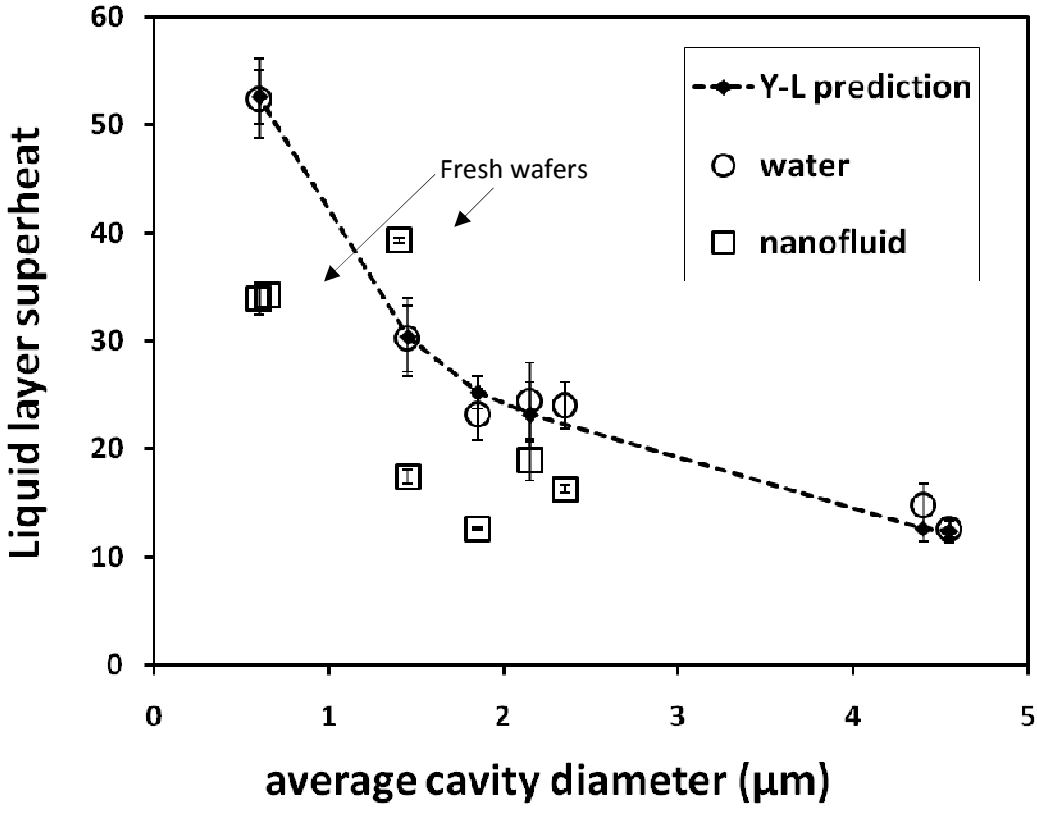

Figure 6.21: Experimental data and Young-Laplace predictions

Now it is very clear that the experimental data for water were in excellent agreement with the classical Young-Laplace predictions. Also observed is that the liquid layer superheat for nanofluid was far below the water in all but one cavity, where the data point lies above the Y-L prediction line on figure 6.21. This is a very encouraging occurrence. In the extreme case that occurred with the 1.85μm cavity, the nanofluid was 45% lower in liquid layer superheat. It is worth recalling that water was always boiled on fresh wafers. However the nanofluid was boiled on water boiled wafers except for two occasions. One may expect cavities to have oxidized after boiling the water. Such oxidation can happen given the high temperature of cavities and the long exposure to the high temperature under an aqueous environment.

6.6 Summary of the chapter

Boiling was conducted on artificial cavities of predetermined sizes and shape manufactured on silicon wafers using the FIB device. The smallest cavity considered in this study was smaller than the one reported in literature [205]. Transparent silicon wafers were chosen as substrate. Noninvasive halogen heat source and infrared thermometry were respectively employed to heat the cavities and measure temperatures. By careful selection of IR filters, it was possible to measure the temperature of a liquid layer of 2.76μm in thickness. This degree of delicacy in measuring the microlayer hitherto has not been reported elsewhere.

Test rig and the procedure were phenomenally clean. This was proved by boiling methanol and reaching the theoretical heterogeneous nucleation temperature on a smooth substrate as shown in figure 6.16. Had there been any contaminant in the rarest possibility, it should have been far smaller than cavities and may become irrelevant in the context of this study.

By boiling water on artificial cavities, it was proved for the first time that the classical Young-Laplace equation stands for sub-micron size cavities. The agreement between the prediction and the experimental data was splendid. Boiling data for silica-water nanofluids demonstrated that there exists a window of opportunity to enhance the boiling heat transfer at sub-micron scale.

Finally this exercise became an example for utilizing the modern technology and critical thinking to prove an established scientific theory.

CHAPTER 7

Conclusions and Recommendations

7.1 Conclusions drawn from present work

This thesis addressed the research question of thermal transport in nanofluids with special emphasis on boiling heat transfer. At the outset in the Introduction chapter it was underlined the importance of nanofluids in heat transfer context. Nanoparticles themselves were highly reactive and nanofluids were a means of extracting some of the goodness in nanoparticle properties for the benefit of energy conservation. Through a comprehensive literature review it was shown that the prior art could broadly be classified into three categories. They were the conductive, convective and boiling heat transfer. Out of these three areas, thermal conduction was the highest addressed and most widely researched. The reason was that the conduction is not only important on its own but also influences convection and boiling. Classical correlations those developed for solid-solid composites such as Maxwell's theory were unable to predict the experimental data for nanofluids conduction. This discrepancy pointed to a knowledge gap and triggered a whole new stream of research.

As a consequence, eight years ago when the nanofluids research was still very young, Pawel Keblinski and coworkers [84] put forward four hypotheses to explain heat conduction mechanism in nanofluids. They showcased the Brownian motion of, liquid layering around, mode of heat transport in, and clustering of nanoparticles as possible contributors. First and the last hypotheses earned wide recognition and further research. As at today, clustering of nanoparticles is speculated to be the major mechanism of thermal conduction in nanofluids. Research has developed to a stage where the accurate knowledge of cluster size and their fractal and chemical dimensions will lead to the accurate prediction of thermal conductivity. Nevertheless there are groups who still believe Brownian motion is the major player.

With reference to boiling heat transfer, there has been a surge of publications during past 2-3 years. Coincidently that was about the time when this research study was begun. They had identified nanoparticle deposits on boiled heaters and thought that it triggered the observed difference in boiling heat transfer. Drawing a nexus to the classical bubble nucleation theories, they speculated that such deposits altered the boiling dynamics on the heater. If that was true, then there should be a correlation between the surface roughness and heat transfer. Although there were references to the bubble nucleation theories, there was no proof in prior art that those theories would stand at sub-micron scale.

Forgoing discussion pronounced two important areas to explore in order to supplement the existing knowledge on thermal transport in nanofluids. On one hand it was the nanoparticle aggregation kinetics. On the other hand it was the boiling at nanoscale. This thesis was written in this background. Following are the conclusions drawn from this work.

Dry nanopowders commercialized by vendors were often polydisperse. Sometimes their polydispersity index was fairly high. As soon as dispersed in a liquid, these nanoparticles flock together to form aggregates. These aggregates are several times larger than the primary nanoparticles. By following appropriate procedures, these aggregates were broken down to smaller units. Thermal conductivity measurements were taken with help of the sophisticated Lambda device over a range of temperatures and particle mass concentrations. For aluminum oxide (alumina) and titanium dioxide (titania) nanofluids, the thermal conductivities were dependent on particle mass concentration but nearly independent of the measuring temperature. Influence of the nanoparticle shape was indicated by the slight difference in data for spherical shape and acicular shape alumina nanofluids. Measured data were then compared with the Hamilton-Crosser (H-C) correlation, which is essentially the Maxwell's correlation modified to account for the particle shape. Taking ethylene glycol based titania nanofluid as an example, it was demonstrated that the H-C correlation could closely predict the measured data. The key point here was the replacement of particle size and particle volume fraction with the aggregate size and their volume fraction. Two important conclusions surfaced at this point. Firstly the temperature independence of thermal conductivity nullified the claims of Brownian motion being a key governing mechanism for the nanofluid's thermal conductivity. Predictability of test data using the H-C correlation further supports this argument. Secondly, the great importance of knowing the size and shape of aggregates. In passing it is worth to note that moderate concentrations of nanoparticles did not trigger anomalous enhancement of thermal conductivity which contradicts one school of thought while supporting the other.

Dynamic viscosity ratio of the nanofluids to base liquid was independent of shear rate and temperature, but dependent on particle concentration. The nanofluids with acicular particles would be expected to exhibit strong non-Newtonian behaviour in line with carbon nanotubes and titania nanotubes, but they did not. This was explained using SEM images, where the acicular particles were found to be broken during the formulation stage. Due to this reason, arguably the acicular particles did not pose initial high resistance to shearing like tubular particles.

Despite the utter usefulness of the aggregation information to predict the thermal conductivity, there was no record of such data in the open literature. Understandably the experiments are hindered by rapid rate of aggregation. Only a tool like the small angle x-ray scattering (SAXS) may cope with it. As a part of this thesis the SAXS technique was evaluated as a method to capture nanoparticle aggregation kinetics. The aim was to determine the size and shape of nanoparticle aggregates by taking in-situ measurements. Experiments were subsequently conducted at I22 beamline at Diamond Light Source in Oxford. Firstly the stable nanofluid samples were studied. Successive data processing demonstrated little or no change in scattering patterns suggesting that the experiment timescales did not match with the aggregation timescales. Possibly the aggregation had happened already or was yet to occur. If the latter was the case, a way to address the situation would be to study unstable nanofluids. Near-IEP samples were therefore studied using SAXS. While all samples showed changes under this condition, alumina-water sample was more significant. Hence alumina was taken as a showcase and analyzed further. Undoubtedly the data were genuine and looked promising. However to interpret them to fit the objective of this study was a challenge. The large polydispersity of the alumina nanoparticles made the analysis far more complicated. Also due to the originality of this work it was unable to find prior art that address similar systems.

The ambiguity surrounding SAXS data was whether they represented particle aggregation or particle settling. To find the answer a three-fold approach was followed. On one front was the classical gravity settling experiments conducted in the laboratory with use of photography. On the other were SEM and optical microscopy imaging of dried and drying nanofluids droplets. In addition the theoretical calculations were performed to consider the Brownian motion induced aggregation. Finally the observations from all explorations were synthesized. Finally it was established that the SAXS data represented the settling of particles. Accordingly this thesis has proved beyond doubt that SAXS is a hitherto unused tool that is powerful enough to capture settling dynamics of highly polydisperse nanoparticle aggregates. This revelation will hopefully open up a new stream of research along these lines.

Saturated pool boiling experiments were systematically conducted under atmospheric pressure with water and water-ethylene glycol based nanofluids on a custom made test rig. The primary aim was to observe the boiling behaviour and heater alterations. Dilute nanofluids were boiled to minimize the number of interfering parameters. The test matrix had copper heaters of known

roughnesses, several types and shapes of nanoparticles, and a series of heat fluxes. Boiling test data were found unique to a given surface and liquid. In some cases there was heat transfer enhancement while in most instances it was deterioration. Repeated consecutive boiling of nanofluid on the same heater was an important aspect of this test plan. It should reveal how far the particle deposition occurs and to what degree it would influence heat transfer. Data for each run different from the other, which suggested possible effect of repeated boiling. Repeated boiling of titania 0.1wt% nanofluid systematically increased the heat transfer coefficient. However for titania 0.01wt% nanofluid the result was otherwise. Hence there was an effect of particle concentration. As far as the particle shape is concerned, it can be stated that the acicular particles were slightly better than spherical particles.

Eye observations and SEM imaging clearly demonstrated particle deposition on heaters in all cases. These deposits were either highly porous or very dense layers of particles. In either case there were pores of vivid sizes. As a result the surface roughness *(R_a)* had considerably changed. Confirming the customary relationship between the surface roughness and the liquid spreading, the solid-liquid contact angle had changed between before and after boiling.

In conclusion on the pool boiling of nanofluids, it can be stated that the boiling heat transfer can either enhance or deteriorate heat transfer. Particle deposition on heaters was found but a direct relationship between the surface roughness and the boiling performance is yet to be established.

Last of the experimental chapters of this thesis addressed the fundamental scientific question of the bubble nucleation on sub-micron size cavities. In the context of this thesis it was aimed at resolving the issue of boiling on nanoparticle scaled heaters. On a larger perspective, it is addressing a basic scientific question. It is the Young-Laplace equation which is the universally accepted theory to predict liquid superheat temperatures at bubble nucleation on cavities. This equation had been experimentally proven true over the decades. However the gap in knowledge was its unproven applicability to very small cavity sizes. The present experiments were conducted on artificial cavities fabricated on ultra smooth silicon wafers. Cavity sizes and shapes were predetermined. The toughest challenge however was to ensure the cleanliness of experiments and neatness of temperature measurement. When boiling on a cavity of 500nm size, there should not be any object in the liquid pool that is larger than the cavity. If it did, then the nucleation would occur on it instead of the cavity. A test rig was carefully developed that comprised a distant heat source and noninvasive temperature measuring techniques. Respectively these were a

halogen light and infrared camera. Incidentally these two objects interfere with each other to the extent that the halogen light emits IR waves and the IR camera captures them. Therefore the liquid in-between, which happens to be the boiling pool, had to be a good IR absorber. This issue was resolved by measuring the IR absorbance of favoured liquids. Next challenge was to filter out the IR signals emitted by the silicon substrate. Only then the camera will receive IR signals emitted by the superheated liquid layer. At this point, the IR properties of silicon wafers were measured. Cavities were fabricated on silicon wafers at Leeds University and the Harvard Centre for Nanoscale Systems. Experiments were conducted at the Nuclear Science and Engineering Department of the MIT.

Assembly of the wafers to the boiling chamber was done in a cleanroom. Hence the cleanliness was at its level best. This was further verified by boiling pure liquid on plain wafers. The liquids reached the theoretically predicted homogeneous bubble nucleation temperature near a smooth surface. Subsequently the boiling experiments were conducted with water on artificial cavities. Experimental data were in excellent agreement with Young-Laplace predictions. Boiling experiments were repeated on fresh cavities of similar sizes. Again the agreement between the experiments and prediction was outstanding. In the history of two-century old Young-Laplace theory, this was the first time its validity was experimentally proven for sub-micron cavity sizes. Water tests were followed by silica-water nanofluid boiling tests. In all but one experiment the nanofluids exhibited lower values for liquid superheat. In turn this indicates the bubble nucleation with nanofluids was easier and the heat transfer was better than water. However prolonged tests with nanofluids were not possible due to particle deposition on the wafers. These wafers when observed after boiling were found to be consisting of homogeneous deposition of silica nanoparticles with pores and channels in-between them.

As the last few words in concluding remarks, it should be said that the research that led to this thesis produced groundbreaking revelations in particular in the fields of usage of x-ray scattering and vapour bubble nucleation at tiny scales.

7.2 Recommendations for future work

As a result of the work done for this thesis, the following have emerged as work for the future.

7.2.1 X-ray scattering

This thesis pioneered SAXS as a tool to capture particle aggregation kinetics and settling. By comparison with commonly available light scattering and electron microscopy techniques, it was proved that SAXS will be the only means that offers a combination of facilities such as short time scales, wet state, size and shape of particulate objects, wide range of temperatures in in-situ measurements. Having done preparatory work, tools finetuned, preliminary experiments conducted, and data successfully analyzed, the foundation for successful SAXS experiments has been laid. Therefore it would be logical to strongly suggest the SAXS branch of this thesis be taken forward. Firstly the readily existing data can be analyzed further into great depths to squeeze out further details of the in-situ particle dynamics. Secondly, having settling being already experimented, the upcoming work should focus more on the aggregation aspects in stable suspensions. As lessons learnt from the concluded work, a few points need attention in future experiments. Firstly, consider the polydispersity. Although this is a reality with commercial applications, it created lots of problems when interpreting the scattering data. To sort this out, it is suggested to run a few preliminary tests with a known monodisperse sample such as Ludox silica colloidal suspension. Secondly consider the effect of multiple scattering. The concluded work was performed with 0.5wt% (5000ppm) concentration. For neater scattering profiles, 50-500ppm concentrations are recommended. Thirdly consider the aggregation timescales. Although this was the research question itself, it was felt that the tested timescales missed out the crucial information. Although it would be a very time consuming, it is immensely worth to conduct a more thorough literature review and computer-based modeling on possible aggregation timescales in preparation for the next round of small x-ray scattering experiments.

7.2.2 Boiling on artificial cavities

Experimental determination of the superheated liquid later temperature in bubble nucleation was another pioneering contribution made by this thesis. It was entirely new experimental approach assisted by modern equipment. At last the cleanest boiling test rig was built and operated. As a result a two-century old theory was proven for nanoscale. In experiments the nanofluids were also boiled although the main focus was on water. This essentially left the room for further research. Having a splendid experimental approach and facilities in place, it is hereby suggested to

proceed with the expedition. As the immediate successor to this project, water can be boiled on non-conical cavities. It is claimed that the nucleation superheats are different with other cavities. Now there is opportunity to test that hypothesis right away. Moreover by simply following the present footsteps, the heterogeneous nucleation temperatures on smooth interfaces can be established for other liquids.

A survey of literature on enhanced surfaces points to the fact that cavities are only one way of enhancing heat transfer. An equally pronounced technique was to produce fins on the heater. The experience gained from present work sheds light onto that side of research. Liquid can be boiled on micro-finned surfaces, with IR and high speed video cameras synchronized side by side. Nucleation of a bubble on the top of a fin can be recorded. Now the nucleation, growth and departure of bubble on a fin can be evaluated against the same on a microcavity.

In the long run, the bubble nucleation behaviour of highly wetting and commercialized liquids is proposed to be examined. Methanol, ethanol and common refrigerants like R134a and propane are good candidates, although some of them will need a pressurized boiling vessel. Findings from such a study will help design enhanced boiling surfaces for those specialty liquids.

7.2.3 Pool boiling of nanofluids

General pool boiling of nanofluids once more highlighted the need of studying nanofluidic systems in greater detail. While the present work confirmed the particle deposition followed by change in wetting and boiling heat transfer coefficients, it fell short of establishing a correlation between the effecting parameters. However the lessons learnt were of enormous value for future work. The bubble nucleation along the edges of heater is regarded as a common problem in boiling experimentation. Despite the prior understanding of this issue and remedies being implemented, the problem still persisted. These stray bubbles disturbed the bubble visualization to an extent that the high speed camera became inoperable. Before further experiments, this issue should be addressed with high priority, preferably by designing a large surface similar to artificial cavity test rig, or by using a more appealing method of sealing such as shrink moisture seal tubing or liquid viton etc. Secondly the boiling chamber can be made cleaner and smaller in size. Since the initial roughness of the smooth heaters did not change significantly after boiling the nanofluids, smoother surfaces such as silicon are suggested for further experiments.

These suggestions will hopefully help expand the research outlook in nanofluids.

References

[1] M. P. Beck, Y. Yuan, P. Warrier, and A. S. Teja; "The effect of particle size on the thermal conductivity of alumina nanofluids," *Journal of Nanoparticle research,* vol. 11, pp. 1129-1136, 2009.

[2] M. P. Beck, Y. Yuan, P. Warrier, and A. S. Teja; "The thermal conductivity of alumina nanofluids in water, ethylene glycol, and ethylene glycol + water mixtures," *Journal of Nanoparticle research,* vol. 12, pp. 1469-1477, 2010.

[3] J. A. Eastman, U. S. Choi, S. Li, L. J. Thompson, and S. Lee; "Enhanced thermal conductivity through the development of nanofluids," in *Proceedings of Materials Research Society symposium,* , Boston, MA, USA, 1997, pp. 3-11.

[4] *SciFinder Scholar*. Available: https://scifinder.cas.org.

[5] S. U. S. Choi, Z. G. Zhang, W. Yu, F. E. Lockwood, and E. A. Grulke; "Anomolous thermal conductivity enhancement in Nanotube suspensions," *Applied physics letters,* vol. 79, pp. 2252-2254, 2001.

[6] T. K. Hong, H. S. Yang, and C. J. Choi; "Study of the enhanced thermal conductivity of Fe nanofluids," *Journal of Applied Physics,* vol. 97, Mar 2005.

[7] Z. H. Han, B. Yang, S. H. Kim, and M. R. Zachariah; "Application of hybrid sphere/carbon nanotube particles in nanofluids," *Nanotechnology,* vol. 18, Mar 2007.

[8] C. G. Granqvist and R. A. Buhrman; "Ultrafine metal particles " *Journal of Applied Physics,* vol. 47, pp. 2200-2219, 1976.

[9] S. Lee, S. U. S. Choi, S. Li, and J. A. Eastman; "Measuring thermal conductivity of fluids containing oxide nanoparticles," *Journal of Heat Transfer-Transactions of the Asme,* vol. 121, pp. 280-289, May 1999.

[10] Y. Xuan and Q. Li; "Heat transfer enhancement of nanofluids," *International Journal of Heat and Fluid flow,* vol. 21, pp. 58-64, 2000.

[11] J. A. Eastman, S. U. S. Choi, S. Li, W. Yu, and L. J. Thompson; "Anomalously increased effective thermal conductivities of ethylene glycol-based nanofluids containing copper nanoparticles," *Applied Physics Letters,* vol. 78, pp. 718-720, Feb 2001.

[12] X. L. Dong, Z. D. Zhang, S. R. Jin, and B. K. Kim; "Carbon-coated Fe–Co (C) nanocapsules prepared by arc discharge in methane," *Journal of Applied Physics,* vol. 86, 1999.

[13] M. Brust, M. Walker, D. Bethel, D. J. Schiffrin, and R. Whyman; "Synthesis of Theol derivatised Gold nanoparticles in a two-phase liquid/liquid system," *Journal of Chemistry Society, Chemistry communication,* pp. 801-802, 1994.

[14] H. E. Patel, S. K. Das, T. Sundararajan, A. Sreekumaran Nair, B. George, and T. Pradeep; "Thermal conductivities of naked and monolayer protected metal nanoparticle based nanofluids: Manifestation of anomalous enhancement and chemical effects," *Applied Physics Letters,* vol. 83, pp. 2931-2933, Oct 2003.

[15] H. T. Zhu, Y. S. Lin, and Y. S. Yin; "A novel one-step chemical method for preparation of Copper nanofluids," *Journal of Colloid and Interface scienec,* vol. 277, pp. 100-103, 2004.

[16] C. H. Lo, T. T. Tsung, and L. C. Chen; "Shape-controlled synthesis of Cu-based nanofluid using submerged arc nanoparticle synthesis system (SANSS)," *Journal of Crystal Growth,* vol. 277, pp. 636-642, Apr 2005.

[17] C. S. Jwo, T. P. Teng, and H. Chang; "A simple model to estimate thermal conductivity of fluid with acicular nanoparticles," *Journal of Alloys and Compounds,* vol. 434, pp. 569-571, May 2007.

[18] R. Chein and J. Chuang; "Experimental microchannel heat sink performance studies using nanofluids," *International Journal of Thermal Sciences,* vol. 46, pp. 57-66, Jan 2007.
[19] H. Zhu, C. Zhang, S. Liu, Y. Tang, and Y. Yin; "Effects of nanoparticle clustering and alignment on thermal conductivities of Fe3O4 aqueous nanofluids," *Applied Physics Letters,* vol. 89, p. 023123, 2006.
[20] J. N. Israelachvili; *Intermolecular and Surface Forces* vol. 3: Academic Press, 2010.
[21] D. S. Wen, Y. L. Ding, and R. A. Williams; "Pool boiling heat transfer of aqueous TiO2-based nanofluids," *Journal of Enhanced Heat Transfer,* vol. 13, pp. 231-244, Jul-Sep 2006.
[22] D. S. Wen and Y. L. Ding; "Formulation of nanofluids for natural convective heat transfer applications," *International Journal of Heat and Fluid Flow,* vol. 26, pp. 855-864, Dec 2005.
[23] J. J. Gulicovski, L. S. Čerović, and S. K. Milonjić; "Point of Zero Charge and Isoelectric Point of Alumina," *Materials and Manufacturing Processes,* vol. 23, pp. 615–619, 2008.
[24] G. A. Parks; "The Isoelectric Points of solid oxides, solid hydroxides, and aqueous hydroxo complex systems," *Chemical Reviews* vol. 65 pp. 177–198, 1965.
[25] Y. R. He, Y. Jin, H. S. Chen, Y. L. Ding, D. Q. Cang, and H. L. Lu; "Heat transfer and flow behaviour of aqueous suspensions of TiO2 nanoparticles (nanofluids) flowing upward through a vertical pipe," *International Journal of Heat and Mass Transfer,* vol. 50, pp. 2272-2281, Jun 2007.
[26] Y. Ding, H. Alias, D. Wen, and R. A. Williams; "Heat transfer of aqueous suspensions of carbon nanotubes (CNT nanofluids)," *International Journal of Heat and Mass Transfer,* vol. 49, pp. 240-250, Jan 2006.
[27] T. Sato and R. Ruch; *Stabilization of colloidal dispersion by polymer adsorption*: Marcel Dekker Inc., New York, 1980.
[28] D. S. Wen and Y. L. Ding; "Experimental investigation into convective heat transfer of nanofluids at the entrance region under laminar flow conditions," *International Journal of Heat and Mass Transfer,* vol. 47, pp. 5181-5188, Nov 2004.
[29] M. A. Worsley, J. H. Satcher Jr, and T. F. Baumann; "Influence of sodium dodecylbenzene sulfonate on the structure and properties of carbon aerogels," *Journal of Non-Crystalline Solids,* vol. 356, pp. 172-174, 2010.
[30] S. Witharana, H. Chen, and Y. Ding; "Enhanced natural convective heat transfer of CNT-Water-Ethylene Glycol suspensions," *http://dx.doi.org/10.1115/MNHT2008-52372* 2008.
[31] J. H. Lee, P. E. Gharagozloo, B. Kolade, J. K. Eaton, and K. E. Goodson; "Nanofluid Convection in Microtubes," *Journal of Heat Transfer,* vol. 132, 2010.
[32] O. Glatter, J. Sieberer, and H. Schnablegger; "A Comparative Study on Different Scattering Techniques and Data Evaluation Methods for Sizing of Colloidal Systems Using Light Scattering," *Particle & Particle systems characterization,* vol. 8, pp. 274-281, 1991.
[33] S. E. Harding and K. Jumel; "Light Scattering," *Current Protocols in Protein Science* vol. 7.8, pp. 1-4, 1998.
[34] ISO13320-1 (1999); *Particle Size Analysis—Laser Diffraction Methods, Part 1:General Principles*. Available: http://www.iso.ch
[35] R.-J. Roe; *Methods of X-ray and Nutron scattering in Polymer science*: Oxford University Press, 2000.

[36] P. Debye; "Light Scattering in Solutions," *Journal of Applied Physics,* vol. 15, pp. 338-342, 1944.
[37] B. H. Zimm; "Molecular Theory of the Scattering of Light in Fluids," *The Journal of Chemical Physics,* vol. 13, 1945.
[38] J. P. Robinson; (2009, *The Principles of Microscopy* Available: http://www.cyto.purdue.edu/flowcyt/educate/pptslide.htm
[39] *Electron Microscopy*. Available: http://www.unl.edu/CMRAcfem/semoptic.htm
[40] X. Wang, X. Xu, and S. U. S. Choi; "Thermal conductivity of nanoparticle-fluid mixture," *Journal of Thermophysics and Heat transfer,* vol. 13, pp. 474-480, 1999.
[41] J. C. Maxwell; *A treatise on Electricity and Magnetism*, 2 ed. vol. 1: Clarendon Press, Oxford, UK, 1881.
[42] D. A. G. Bruggeman; "Calculation of various physics constants in heterogenous substances I Dielectricity constants and conductivity of mixed bodies from isotropic substances," *Annalen der Physik* vol. 24, pp. 636-664, 1935.
[43] R. L. Hamilton and O. K. Crosser; "Thermal conductivity of hetrogeneous two-component systems," *Industrial & Engineering chemistry fundamentals,* vol. 1, pp. 187-191, 1962.
[44] D. P. H. Hasselman and L. F. Johnson; "Effective thermal conductivity of composites with Interfacial thermal barrier resistance," *Journal of Comopsite materials* vol. 21, pp. 508-515, 1987.
[45] P. Keblinski, R. Prasher, and J. Eapen; "Thermal conductance of nanofluids: is the controversy over?," *Journal of Nanoparticle research,* vol. 10, pp. 1089-1097, 2008.
[46] Z. Hashin and S. Shtrikman; "A variational approach to the theory of the effective magnetic permeability of multiphase materials," *Journal of Applied Physics,* vol. 33, p. 3125, 1962.
[47] A. G. Every, Y. Tzou, D. P. H. Hasselman, and R. Raj; "The effect of particle size on the Thermal conductivity of ZnS/Diamond Composites," *Acta metall. mater.,* vol. 40, pp. 123-129, 1992.
[48] S. K. Das, N. Putra, P. Thiesen, and W. Roetzel; "Temperature dependence of thermal conductivity enhancement for nanofluids," *Journal of Heat Transfer-Transactions of the Asme,* vol. 125, pp. 567-574, Aug 2003.
[49] H. Q. Xie, J. C. Wang, T. G. Xi, Y. Liu, F. Ai, and Q. R. Wu; "Thermal conductivity enhancement of suspensions containing nanosized alumina particles," *Journal of Applied Physics,* vol. 91, pp. 4568-4572, Apr 2002.
[50] C. H. Li and G. P. Peterson; "Experimental investigation of temperature and volume fraction variations on the effective thermal conductivity of nanoparticle suspensions (nanofluids)," *Journal of Applied Physics,* vol. 99, Apr 2006.
[51] D.-H. Yoo, K. S. Hong, and H.-S. Yang; "Study of thermal conductivity of nanofluids for the application of heat transfer fluids," *Thermochimica Acta,* vol. 455, pp. 66-69, 2007.
[52] X. Zhang, H. Gu, and M. Fujii; "Experimental study on the effective thermal conductivity and thermal diffusivity of nanofluids," *International Journal of Thermophysics,* vol. 27, pp. 569-580, Mar 2006.
[53] S. J. Kim, I. C. Bang, J. Buongiorno, and L. W. Hu; "Surface wettability change during pool boiling of nanofluids and its effect on critical heat flux," *International Journal of Heat and Mass Transfer,* vol. 50, pp. 4105-4116, Sep 2007.

[54] C. H. Li and G. P. Peterson; "The effect of particle size on the effective thermal conductivity of Al2O3-water nanofluids," *Journal of Applied Physics,* vol. 101, p. 044312, 2007.

[55] H. A. Mintsa, G. Roy, C. T. Nguyen, and D. Doucet; "New temperature dependent thermal conductivity data for water-based nanofluids," *International Journal of Thermal Sciences,* vol. 48, pp. 363-371, 2009.

[56] Y. Hwang, J. K. Lee, C. H. Lee, Y. M. Jung, S. I. Cheong, C. G. Lee, B. C. Ku, and S. P. Jang; "Stability and thermal conductivity characteristics of nanofluids," *Thermochimica Acta,* vol. 455, pp. 70-74, 2007.

[57] S. M. S. Murshed, K. C. Leong, and C. Yang; "Enhanced thermal conductivity of TiO2 - water based nanofluids," *International Journal of Thermal Sciences,* vol. 44, pp. 367-373, Apr 2005.

[58] D. S. Wen and Y. Ding; "Natural convective heat transfer of suspensions of titanium dioxide nanoparticles (Nanofluids)," *IEEE Transactions on Nanotechnology,* vol. 5, pp. 220-227, May 2006.

[59] Y. He, Y. Jin, H. Cheng, Y. Ding, D. Cang, and H. Lu; "Heat transfer and flow behaviour of aqueous suspensions of TiO2 nanoparticles (nanofluids) flowing upward through a verticle pipe," *International Journal of Heat and Mass Transfer,* vol. Article in press, 2006.

[60] A. Turgut, I. Tavman, M. Chirtoc, H. P. Schuchmann, C. Sauter, and S. Tavman; "Thermal Conductivity and Viscosity Measurements of Water-Based TiO2 Nanofluids," *International Journal of Thermophysics,* vol. 30, pp. 1213-1226, 2009.

[61] Y. J. Hwang, Y. C. Ahn, H. S. Shin, C. G. Lee, G. T. Kim, H. S. Park, and J. K. Lee; "Investigation on characteristics of thermal conductivity enhancement of nanofluids," *Current Applied Physics,* vol. 6, pp. 1068-1071, Oct 2006.

[62] M. S. Liu, M. C. C. Lin, C. Y. Tsai, and C. C. Wang; "Enhancement of thermal conductivity with Cu for nanofluids using chemical reduction method," *International Journal of Heat and Mass Transfer,* vol. 49, pp. 3028-3033, Aug 2006.

[63] K. S. Hong, T. K. Hong, and H. S. Yang; "Thermal conductivity of Fe nanofluids depending on the cluster size of nanoparticles," *Applied Physics Letters,* vol. 88, Jan 2006.

[64] S. A. Putnam, D. G. Cahill, P. V. Braun, Z. B. Ge, and R. G. Shimmin; "Thermal conductivity of nanoparticle suspensions," *Journal of Applied Physics,* vol. 99, Apr 2006.

[65] M. J. Assael, C. F. Chen, I. Metaxa, and W. A. Wakeham; "Thermal conductivity of suspensions of carbon nanotubes in water," *International Journal of Thermophysics,* vol. 25, pp. 971-985, 2004.

[66] M. J. Assael, I. N. Metaxa, J. Arvanitidis, D. Christofilos, and C. Lioutas; "Thermal conductivity enhancement in aqueous suspensions of carbon multi-walled and double-walled nanotubes in the presence of two different dispersants," *International Journal of Thermophysics,* vol. 26, pp. 647-664, May 2005.

[67] H. Q. Xie, H. Lee, W. Youn, and M. Choi; "Nanofluids containing multiwalled carbon nanotubes and their enhanced thermal conductivities," *Journal of Applied Physics,* vol. 94, pp. 4967-4971, Oct 2003.

[68] B. Yang and Z. H. Han; "Temperature-dependent thermal conductivity of nanorod-based nanofluids," *Applied Physics Letters,* vol. 89, Aug 2006.

[69] J. A. Eastman, S. R. Phillpot, S. U. S. Choi, and P. Keblinski; "Thermal transport in nanofluids," *Annual Review of Materials Research,* vol. 34, pp. 219-246, 2004.

[70] P. Keblinski, J. A. Eastman, and D. G. Cahill; "Nanofluids for thermal transport," *Materials Today,* vol. 8, pp. 36-44, 2005.

[71] X.-Q. Wang and A. S. Mujumdar; "Heat transfer characteristics of nanofluids: a review," *International Journal of Thermal Sciences,* vol. 46, pp. 1-19, 2007.

[72] S. K. Das, S. U. S. Choi, and H. E. Patel; "Heat transfer in Nanofluids - A review," *Heat Transfer Engineering,* vol. 27, pp. 3-19, Dec 2006.

[73] Y. Ding, H. Chen, Z. Musina, Y. Jin, T. Zhang, S. Witharana, and W. Yang; "Relationship between the thermal conductivity and shear viscosity of nanofluids," *Physica Scripta,* vol. T139, 2010.

[74] S. Ozerinc, S. Kakac, and G. A. Yazicioglu; "Enhanced thermal conductivity of nanofluids:a state-of-the-art review," *Journal of Nanoparticle research,* vol. 8, pp. 145-170, 2010.

[75] S. K. Das and S. U. S. Choi; "A review of heat transfer in nanofluids," *Advances in Heat transfer,* vol. 41, pp. 81-197, 2009.

[76] J. Buongiorno, D. C. Venerus, ..., and S. Witharana; "A benchmark study on the thermal conductivity of nanofluids," *Journal of Applied Physics,* vol. 106, 2009.

[77] Z. L. Wang, D. W. Tang, S. Liu, X. H. Zheng, and N. Araki; "Thermal-Conductivity and Thermal-Diffusivity Measurements of Nanofluids by 3ω Method and Mechanism Analysis of Heat Transport," *International Journal of Thermophysics,* vol. 28, pp. 1255-1268, 2007.

[78] S. H. Kim, S. R. Choi, and D. Kim; "Thermal conductivity of metal-oxide nanofluids: Particle size dependence and effect of laser irradiation," *Journal of Heat Transfer-Transactions of the Asme,* vol. 129, pp. 298-307, Mar 2007.

[79] W. Yu, D. M. France, S. U. S. Choi, and J. L. Routbort; "Review and assessment of Nanofluid technology for Transport and other applications," Argonne National Laboratory ANL/ESD/07-9, 2007.

[80] G. Chen, W. Yu, D. Singh, D. Cookson, and J. Routbort; "Application of SAXS to the study of Particle-size-dependent thermal conductivity in Silica nanofluids," *Journal of Nanoparticle research,* vol. DOI 10.1007/s11051-007-9347-y 2008.

[81] D. C. Venerus and Y. Jiang; "Investigation of thermal transport in colloidal silica dispersions (nanofluids)," *Journal of Nanoparticle research,* vol. DOI 10.1007/s11051-010-0207-9, 2011.

[82] H. Q. Xie, J. C. Wang, T. G. Xi, Y. Liu, and F. Ai; "Dependence of the thermal conductivity of nanoparticle-fluid mixture on the base fluid," *Journal of Materials Science Letters,* vol. 21, pp. 1469-1471, Oct 2002.

[83] S. P. Jang and S. U. S. Choi; "Role of Brownian motion in the enhanced thermal conductivity of nanofluids," *Applied Physics Letters,* vol. 84, pp. 4316-4318, May 2004.

[84] P. Keblinski, S. R. Phillpot, S. U. S. Choi, and J. A. Eastman; "Mechanisms of heat flow in suspensions of nano-sized particles (nanofluids)," *International Journal of Heat and Mass Transfer,* vol. 45, pp. 855-863, Feb 2002.

[85] M. Chandrasekar and S. Suresh; "A Review on the Mechanisms of Heat Transport in Nanofluids," *Heat Transfer Engineering,* vol. 30, pp. 1136-1150, 2009.

[86] Y. Xuan, Q. Li, and W. Hu; "Aggregation structure and thermal conductivity of nanofluids," *AIChE Journal,* vol. 49, pp. 1038-1043, 2003.

[87] J. Koo and C. Kleinstreuer; "A new thermal conductivity model for nanofluids," *Journal of Nanoparticle Research,* vol. 6, pp. 577-588, Dec 2004.

[88] D. H. Kumar, H. E. Patel, V. R. R. Kumar, T. Sundararajan, T. Pradeep, and S. K. Das; "Model for heat conduction in nanofluids," *Physical Review Letters,* vol. 93, Oct 2004.

[89] R. Prasher, P. Bhattacharya, and P. E. Phelan; "Thermal conductivity of nanoscale colloidal solutions (nanofluids)," *Physical Review Letters,* vol. 94, Jan 2005.

[90] W. Yu and S. U. S. Choi; "The role of interfacial layers in the enhanced thermal conductivity of nanofluids: A renovated Maxwell model," *Journal of Nanoparticle Research,* vol. 5, pp. 167-171, Apr 2003.

[91] K. C. Leong, C. Yang, and S. M. S. Murshed; "A model for the thermal conductivity of nanofluids - the effect of interfacial layer," *Journal of Nanoparticle Research,* vol. 8, pp. 245-254, Apr 2006.

[92] H. Q. Xie, M. Fujii, and X. Zhang; "Effect of interfacial nanolayer on the effective thermal conductivity of nanoparticle-fluid mixture," *International Journal of Heat and Mass Transfer,* vol. 48, pp. 2926-2932, Jul 2005.

[93] R. Prasher, P. E. Phelan, and P. Bhattacharya; "Effect of aggregation kinetics on the thermal conductivity of Nanoscale colloidal solutions (Nanofluids)," *Nano Letters,* vol. 6, pp. 1529-1534, 2006.

[94] B.-X. Wang, L.-P. Zhou, and X.-F. Peng; "A fractal model for predicting the effective thermal conductivity of liquid with suspension of nanoparticles," *International Journal of Heat and Mass Transfer,* vol. 46, 2003.

[95] W. Yu and S. U. S. Choi; "The role of interfacial layers in the enhanced thermal conductivity of nanofluids: A renovated Hamilton-Crosser model," *Journal of Nanoparticle Research,* vol. 6, pp. 355-361, Aug 2004.

[96] C. H. Chon, K. D. Kihm, S. P. Lee, and S. U. S. Choi; "Empirical correlation finding the role of temperature and particle size for nanofluid (Al2O3) thermal conductivity enhancement," *Applied Physics Letters,* vol. 87, Oct 2005.

[97] R. Prasher; "Brownian-motion-based convective-conductive model for the thermal conductivity of nanofluids," San Francisco, CA, United States, 2005, pp. 343-353.

[98] R. Prasher, P. Bhattacharya, and P. E. Phelan; "Brownian-motion-based convective-conductive model for the effective thermal conductivity of nanofluids," *Journal of Heat Transfer-Transactions of the Asme,* vol. 128, pp. 588-595, Jun 2006.

[99] R. Prasher, W. Evans, P. Meakin, J. Fish, P. Phelan, and P. Keblinski; "Effect of aggregation on thermal conduction in colloidal nanofluids," *Applied Physics Letters,* vol. 89, Oct 2006.

[100] S. Krishnamurthy, P. Bhattacharya, P. E. Phelan, and R. S. Prasher; "Enhanced mass transport in nanofluids," *Nano Letters,* vol. 6, pp. 419-423, 2006.

[101] C. W. Nan, R. Birringer, D. R. Clarke, and H. Gleiter; "Effective thermal conductivity of Particulate composites with inetrfacial themal resistance," *Journal of Applied Physics,* vol. 81, pp. 6692-6699, 1997.

[102] W. Y. Lai, B. Duculescu, P. E. Phelan, and R. Prasher; "A review of convective heat transfer with nanofluids for electronics packaging," in *Thermal and Thermomechanical Phenomena in Electronics Systems, 2006. ITHERM '06.* , San Diego, California, USA 2006.

[103] S. Kakac and A. Pramuanjaroenkij; "Review of convective heat transfer enhancement with nanofluids," *International Journal of Heat and Mass Transfer,* vol. 52, pp. 3187-3196, 2009.

[104] W. Daungthongsuk and S. Wongwises; "A critical review of convective heat transfer of nanofluids," *Renewable & Sustainable Energy Reviews,* vol. 11, pp. 797-817, Jun 2007.

[105] Y. M. Xuan and Q. Li; "Investigation on convective heat transfer and flow features of nanofluids," *Journal of Heat Transfer-Transactions of the Asme,* vol. 125, pp. 151-155, Feb 2003.

[106] S. Z. Heris, S. G. Etemad, and M. N. Esfahany; "Convective heat transfer of a Cu/Water nanofluid flowing through a circular tube," *Experimental heat transfer,* vol. 22, pp. 217-227, 2009.

[107] B. C. Pak and Y. Cho; "Hydrodynamic and heat transfer studies of dispersed fluids with submicron metallic oxide particles," *Experimental heat transfer,* vol. 11, pp. 151-170, 1998.

[108] S. Z. Heris, S. G. Etemad, and M. N. Esfahany; "Experimental investigation of oxide nanofluids laminar flow convective heat transfer," *International Communications in Heat and Mass Transfer,* vol. 33, pp. 529-535, 2006.

[109] Y. Yang, Z. G. Zhang, E. A. Grulke, W. B. Anderson, and G. F. Wu; "Heat transfer properties of nanoparticle-in-fluid dispersions (nanofluids) in larninar flow," *International Journal of Heat and Mass Transfer,* vol. 48, pp. 1107-1116, Mar 2005.

[110] G. H. Ko, K. Heo, K.Lee, D.S.Kim, C.Kim, Y.Sohn, and M.Choi; "An experimental study of the pressure drop of nanofluids containing Carbon nanotubes in a horizontal tube," *International Journal of Heat & Mass Transfer,* vol. in press, 2007.

[111] T. C. Chien HT, Chen PH, Chen PY; "improvement on thermal performance of a disk shaped miniature heat pipe with nanofluid," *ICEPT Proceedings (IEEE Cat No 03EX750),* p. 389, 2003.

[112] C. H. Tsai CY, PP Ding, B Chan, TY Luh, PH Chen; "effect of structural character of gold nanoparticles in nanofluid on heat pipe thermal performance," *Material Letters,* vol. 58, pp. 1461-1465, 2004.

[113] M. Boudouh, H. L. Gualous, and M. De Labachelerie; "Local convective boiling heat transfer and pressure drop of nanofluid in narrow rectangular channels," *Applied Thermal Engineering,* vol. 30, pp. 2619-2631, 2010.

[114] D. Liu and L. Yu; "Single-Phase Thermal Transport of Nanofluids in a Minichannel," *Journal of Heat Transfer,* vol. 133, pp. 031009-11, 2011.

[115] J. Buongiorno; "Convective transport in nanofluids," *Journal of Heat Transfer-Transactions of the Asme,* vol. 128, pp. 240-250, Mar 2006.

[116] H. Chen, W. Yang, Y. He, Y. Ding, L. Zhang, C. Tan, A. A. Lapkin, and D. V. Bavykin; "Heat transfer and flow behaviour of aqueous suspensions of titanate nanotubes (nanofluids)," *Powder Technology,* vol. 183, pp. 63-72, 2008.

[117] H. Chen, Y. Ding, and A. Lapkin; "Rheological behaviour of nanofluids containing tube / rod-like nanoparticles," *Powder Technology,* vol. 194, pp. 132-141, 2009.

[118] S. Q. Zhou, R. Ni, and S. Funfschilling; "Effects of shear rate and temperature on viscosity of alumina polyalphaolefins nanofluids," *Journal of Applied Physics,* vol. 107, 2010.

[119] Y. He, Y. Men, X. Liu, H. Chen, and Y. Ding; "Study on Forced Convective Heat Transfer of Non-Newtonian Nanofluids," *Journal of Thermal Science,* vol. 18, pp. 20-26, 2009.

[120] A. G. A. Nnanna, T. Fistrovich, K. Malinski, and S. U. S. Choi; "Thermal transport phenomena in buoyancy-driven nanofluids," in *ASME International Mechanical Engineering Congress R&D Expo*, Anaheim, CA, United States, 2004, pp. 571-578.

[121] A. G. A. Nnanna; "Experimental model of Temperature-driven Nanofluids," *Journal of Heat Transfer,* vol. 129, 2007.

[122] N. Putra, W. Roetzel, and S. K. Das; "Natural convection of nano-fluids," *Heat and Mass Transfer,* vol. 39, pp. 775-784, Sep 2003.

[123] S. Witharana, Y. Jin, H. Chen, and Y. Ding; "Title," unpublished.
[124] K. Khanafer, K. Vafai, and M. Lightstone; "Buoyancy-driven heat transfer enhancement in a two-dimensional enclosure utilizing nanofluids," *International Journal of Heat and Mass Transfer,* vol. 46, pp. 3639-3653, Sep 2003.
[125] J. Kim, Y. T. Kang, and C. K. Choi; "Analysis of convective instability and heat transfer characteristics of nanofluids," *Physics of Fluids,* vol. 16, pp. 2395-2401, Jul 2004.
[126] K. S. Hwang, J. H. Lee, and S. P. Jang; "Buoyancy-driven heat transfer of water-based Al2O3 nanofluids," *International Journal of Heat and Mass Transfer,* vol. 50, pp. 4003-4010, 2007.
[127] W. M. Rohsenow and P. Griffith; "Correlation of maximum heat flux data for boiling of saturated liquids," *Chemical Engineering Progress Symposium,* vol. 52, pp. 47-49, 1956.
[128] G. P. Narayan, K. B. Anoop, and S. K. Das; "Mechanism of enhancement/deterioration of boiling heat transfer using stable nanoparticle suspensions over vertical tubes," *Journal of Applied Physics,* vol. 102, Oct 2007.
[129] D. S. Wen and Y. L. Ding; "Experimental investigation into the pool boiling heat transfer of aqueous based gamma-alumina nanofluids," *Journal of Nanoparticle Research,* vol. 7, pp. 265-274, Jun 2005.
[130] S. Witharana; "Boiling of refrigerants on enhanced surfaces & Boiling of nanofluids," Licentiate of Philosophy Thesis, Royal Institute of Technology, Stockholm, Sweden, 2003.
[131] S. K. Das, N. Putra, and W. Roetzel; "Pool boiling characteristics of nano-fluids," *International Journal of Heat and Mass Transfer,* vol. 46, pp. 851-862, Feb 2003.
[132] S. K. Das, N. Putra, and W. Roetzel; "Pool boiling of nano-fluids on horizontal narrow tubes," *International Journal of Multiphase Flow,* vol. 29, pp. 1237-1247, Aug 2003.
[133] P. Vassallo, R. Kumar, and S. D'Amico; "Pool boiling heat transfer experiments in silica-water nano-fluids," *International Journal of Heat and Mass Transfer,* vol. 47, pp. 407-411, Jan 2004.
[134] J. Liu, J. Gu, Z. Lian, and H. Liu; "Experiment and mechanism analysis of pool boiling heat transfer enhancement with water-based magnetic fluid," *Heat Mass Transfer,* vol. 41, pp. 170-175, 2004.
[135] J. P. Tu, N. Dinh, and T. Theofnous; "An experimental study of nanolfuid boiling heat transfer," in *6th international symposium on heat transfer*, China, 2004.
[136] D. Milanova and R. Kumar; "Role of ions in pool boiling heat transfer of pure and silica nanofluids," *Applied Physics Letters,* vol. 87, Dec 2005.
[137] G. P. Narayan, K. B. Anoop, G. Sateesh, and S. K. Das; "Effect of surface orientation on pool boiling heat transfer of nanoparticle suspensions," *International Journal of Multiphase Flow,* vol. 34, pp. 145-160, Feb 2008.
[138] M. Chopkar, A. K. Das, I. Manna, and P. K. Das; "Pool boiling heat transfer characteristics of ZrO2-water nanofluids from a flat surface in a pool," *Heat and Mass Transfer,* vol. 44, pp. 999-1004, 2008.
[139] Z. H. Liu and L. Liao; "Sorption and agglutination phenomenon of nanofluids on a plain heating surface during pool boiling," *International Journal of Heat and Mass Transfer,* vol. 51, pp. 2593-2602, 2008.
[140] S. Khandekar, Y. M. Joshi, and B. Mehta; "Thermal performance of closed two-phase thermosyphon using nanofluids," *International Journal of Thermal Sciences,* vol. 47, pp. 659-667, 2008.

[141] Milanova D. and R. Kumar; "Heat transfer behaviour of Silica Nanoparticles in Pool boiling Experiment," *Journal of Heat Transfer,* vol. 130, 2008.
[142] S. Ujereh, T. Fisher, and I. Mudawar; "Effects of carbon nanotube arrays on nucleate pool boiling," *International Journal of Heat and Mass Transfer,* vol. 50, pp. 4023-4038, Sep 2007.
[143] V. Trisaksri and S. Wongwises; "Nucleate pool boiling heat transfer of TiO2-R141b nanofluids," *International Journal of Heat and Mass Transfer,* vol. 52, pp. 1582-1588, 2009.
[144] S. Soltani, E. Gholamreza, and J. Thibault; "Pool boiling heat transfer performance of Newtonian nanofluids," *Heat and Mass Transfer,* vol. 45, pp. 1555-1560, 2009.
[145] V. Sathyamurthi, H.-S. Ahn, D. Banerjee, and S. C. Lau; "Subcooled Pool Boiling Experiments on Horizontal Heaters Coated With Carbon Nanotubes," *Journal of Heat Transfer,* vol. 131, p. 071501, 2009.
[146] S. M. Kwark, R. Kumar, G. Moreno, J. Yoo, and S. M. You; "Pool boiling characteristics of low concentration nanofluids," *International Journal of Heat and Mass Transfer,* vol. 53, pp. 972-981, 2010.
[147] K. Henderson, Y.-G. Park, L. Liu, and A. M. Jacobi; "Flow-boiling heat transfer of R-134a-based nanofluids in a horizontal tube," *International Journal of Heat and Mass Transfer,* vol. 53, pp. 944-951, 2010.
[148] E. Dominguez-Ontiveros, S. Fortenberry, and Y. A. Hassan; "Experimental observations of flow modifications in nanofluid boiling utilizing particle image velocimetry," *Nuclear Engineering and Design,* vol. 240, pp. 299-304, 2010.
[149] H. Lotfi and M. B. Shafii; "Boiling heat transfer on a high temperature silver sphere in nanofluid," *International Journal of Thermal Sciences,* vol. 48, pp. 2215-2220, 2009.
[150] H. Peng, G. Ding, W. Jiang, H. Hu, and Y. Gao; "Heat transfer characteristics of refrigerant-based nanofluid flow boiling inside a horizontal smooth tube," *International Journal of Refrigeration,* vol. 32, pp. 1259-1270, 2009.
[151] M. A. Kedzierski and M. Gong; "Effect of CuO nanolubricant on R134a pool boiling heat transfer," *International Journal of Refrigeration,* vol. 32, pp. 791-799, 2009.
[152] R. Kathiravan, R. Kumar, A. Gupta, and R. Chandra; "Characterization and Pool Boiling Heat Transfer Studies of Nanofluids," *Journal of Heat Transfer,* vol. 131, 2009.
[153] L. Lun-Chun and L. Zhen-Hua; "Boiling characteristics in small vertical tubes with closed bottom for nanofluids and nanoparticle-suspensions," *Heat and Mass Transfer,* vol. 45, pp. 1-9, 2008.
[154] H. D. Kim, J. Kim, and M. H. Kim; "Effect of nanoparticles on CHF enhancement in pool boiling of nano-fluids," *International Journal of Heat and Mass Transfer,* vol. 49, pp. 5070-5074, Dec 2006.
[155] G. Ding, H. Peng, W. Jiang, and Y. Gao; "The migration characteristics of nanoparticles in the pool boiling process of nanorefrigerant and nanorefrigerant-oil mixture," *International Journal of Refrigeration,* vol. 32, pp. 114-123, 2009.
[156] S. J. Kim, T. McKrell, J. Buongiorno, and L. W. Hu; "Enhancement of flow boiling Critical Heat Flux (CHF) in alumina/water nanofluids.," *Advanced Science Letters,* vol. 2, pp. 100-102, 2009.
[157] H. Kim and M. Kim; "Experimental study of the characteristis nd mechanism of pool boiling CHF enhancement using nanofluids," *Heat and Mass Transfer,* vol. 45, pp. 991-998, 2009.

[158] S. J. Kim, T. McKrell, J. Buongiorno, and L. W. Hu; "Experimental Study of Flow Critical Heat Flux in Alumina-Water, Zinc-Oxide-Water, and Diamond-Water Nanofluids," *Journal of Heat Transfer,* vol. 131, 2009.

[159] M. Golubovic, H. D. M. Hettiarachchi, and W. M. Worek; "Nano fluids and critical heat flux," *Proceedings of the Micro/Nanoscale Heat Transfer International Conference 2008, Pts a and B,* pp. 623-632, 2008.

[160] J. S. Coursey and J. Kim; "Nanofluid boiling: The effect of surface wettability," *International Journal of Heat and Fluid Flow,* vol. 29, pp. 1577-1585, 2008.

[161] I. C. Bang and S. H. Chang; "Boiling heat transfer performance and phenomena of Al2O3-water nano-fluids from a plain surface in a pool," *International Journal of Heat and Mass Transfer,* vol. 48, pp. 2407-2419, Jun 2005.

[162] Z. H. Liu and Y. H. Qiu; "Boiling heat transfer characteristics of nanofluids jet impingement on a plate surface," *Heat and Mass Transfer,* vol. 43, pp. 699-706, May 2007.

[163] H. D. Kim, J. Kim, and M. H. Kim; "Experimental studies on CHF characteristics of nanofluids at pool boiling," *International journal of Multiphase flow,* vol. 33, pp. 691-706, 2007.

[164] S. Kim, H. Kim, H. D. Kim, H. S. Ahn, M. H. Kim, J. Kim, and G. C. Park; "Experimental Investigation of Critical Heat Flux Enhancement by Micro/Nanoscale Surface Modification in Pool Boiling," *Proceedings of the 6th International Conference on Nanochannels, Microchannels, and Minichannels, Pts a and B,* pp. 669-675, 2008.

[165] H. D. Kim and M. H. Kim; "Effect of nanoparticle depositin on Capillary wicking that influences CHF in nanofluids," *Applied physics letters,* vol. 91, 2007.

[166] M. N. Golubovic, H. D. M. Hettiarachchi, W. M. Worek, and W. J. Minkowycz; "Nanofluids and critical heat flux, experimental and analytical study," *Applied Thermal Engineering,* vol. In Press, Corrected Proof, 2008.

[167] A. Suriyawong and S. Wongwises; "Nucleate pool boiling heat transfer characteristics of TiO2-water nanofluids at very low concentrations," *Experimental Thermal and Fluid Science,* vol. 34, pp. 992-999, 2010.

[168] S. B. White, A. J. Shih, and K. P. Pipe; "Effects of nanoparticle layering on nanofluid and base fluid pool boiling heat transfer from a horizontal surface under atmospheric pressure," *Journal of Applied Physics,* vol. 107, pp. 114302-6, 2010.

[169] R. A. Taylor and P. E. Phelan; "Pool boiling of nanofluids: Comprehensive review of existing data and limited new data," *International Journal of Heat and Mass Transfer,* vol. 52, pp. 5339-5347, 2009.

[170] S. M. You, J. H. Kim, and K. H. Kim; "Effect of nanoparticles on critical heat flux of water in pool boiling heat transfer," *Applied Physics Letters,* vol. 83, pp. 3374-3376, Oct 2003.

[171] G. Moreno, S. J. Oldenburg, S. M. You, and J. H. Kim, "Pool boiling heat transfer of alumina-water, zinc oxide-water and alumina-water plus ethylene glycol nanofluids," in *Ht2005: Proceedings of the Asme Summer Heat Transfer Conference 2005, Vol 2*, ed, 2005, pp. 625-632.

[172] K. Sefiane; "On the role of structural disjoining pressure and contact line pinning in critical heat flux enhancement during boiling of nanofluids," *Applied Physics Letters,* vol. 89, Jul 2006.

[173] S. J. Kim, I. C. Bang, J. Buongiorno, and L. W. Hu; "Effects of nanoparticle deposition on surface wettability influencing boiling heat transfer in nanofluids," *Applied Physics Letters,* vol. 89, Oct 2006.

[174] K. J. Park and D. S. Jung; "Enhancement of nucleate boiling heat transfer using carbon nanotubes," *International Journal of Heat and Mass Transfer,* vol. 50, pp. 4499-4502, Oct 2007.

[175] L. C. Lv and Z. H. Liu; "Boiling characteristics in small vertical tubes with closed bottom for nanofluids and nanoparticle-suspensions," *Heat and Mass Transfer,* vol. 45, pp. 1-9, 2008.

[176] B. Fokin, M. Belenkiy, V. Almjashev, V. Khabensky, O. Almjasheva, and V. Gusarov; "Critical heat flux in a boiling aqueous dispersion of nanoparticles," *Technical Physics Letters,* vol. 35, pp. 440-442, 2009.

[177] H. Kim, H. S. Ahn, and M. H. Kim; "On the Mechanism of Pool Boiling Critical Heat Flux Enhancement in Nanofluids," *Journal of Heat Transfer,* vol. 132, pp. 061501-11, 2010.

[178] R. Kathiravan, R. Kumar, A. Gupta, and R. Chandra; "Preparation and pool boiling characteristics of copper nanofluids over a flat plate heater," *International Journal of Heat and Mass Transfer,* vol. 53, pp. 1673-1681, 2010.

[179] S. Soltani, S. G. Etemad, and J. Thibault; "Pool boiling heat transfer of non-Newtonian nanofluids," *International Communications in Heat and Mass Transfer,* vol. 37, pp. 29-33, 2010.

[180] N. Zuber; "Hydrodynamic aspects of boiling heat transfer," PhD thesis, Univeristy of California, Los Angeles, 1959.

[181] P. Sadasivan, P. R. Chappidi, C. Unal, and R. A. Nelson; "Possible mechanisms of macrolayer formation," *Pool and external flow boiling,* p. 135, 1992.

[182] T. G. Theofnous; "The boiling crisis phenomena," *Experimental thermal fluid sciences,* vol. 26, pp. 793-810, 2002.

[183] D. T. Wasan and A. D. Nikolov; "Spreading of nanofluids on solids," *Nature,* vol. 423, pp. 156-159, May 2003.

[184] H. Chon, C , S. Paik, J.B.Tipton Jr, and K. D. Kihm; "effect of nanoparticle sizes and number densities on the evaporation and dryout characteristics for strongly pinned nanofluid droplets," *Langmuir,* vol. 23, 2007.

[185] R. L. Webb; *Principals of Enhanced Heat Transfer*: John Wiley & Sons Inc., 1994.

[186] J. R. Thome; *Enhanced Boiling Heat Transfer*: Hemisphere Publishing Corporation, 1990.

[187] A. E. Bergles; "Enhancement of pool boiling," *International Journal of Refrigeration,* vol. 20, pp. 545-551, 1997.

[188] S. Kim, H. D. Kim, H. Kim, H. S. Ahn, H. Jo, J. Kim, and M. H. Kim; "Effects of nano-fluid and surfaces with nano structure on the increase of CHF," *Experimental Thermal and Fluid Science,* vol. 34, pp. 487-495, 2010.

[189] S. M. Kwark, G. Moreno, R. Kumar, H. Moon, and S. M. You; "Nanocoating characterization in pool boiling heat transfer of pure water," *International Journal of Heat and Mass Transfer,* vol. 53, pp. 4579-4587, 2010.

[190] C. H. Wang and V. K. Dhir; "Effect of surface wettability on active nucleation site density during pool boiling of water on a vertical surface," *Journal of Heat Transfer,* vol. 115, pp. 659-669, 1993.

[191] B. Mikic and W. M. Rohsenow; "A new correlation for pool boiling data including the effect of heating surface characteristics," *Journal of Heat Transfer,* vol. 91, pp. 245-250, 1969.

[192] P. Griffith and J. D. Wallis; "The role of surface conditions in nucleate boiling," *Chem. Eng. Prog. Symp. Series,* vol. 56, pp. 49-63, 1960.

[193] K. Kant and M. E. Weber; "Stability of nucleation sites in pool boiling," *Experimental Thermal and Fluid Science,* vol. 9, pp. 456-465, 1994.
[194] T. D. Rule and J. Kim; "Heat transfer behaviour on small horizontal heaters during pool boiling of FC-72," *Journal of Heat Transfer,* vol. 121, pp. 386-393, 1999.
[195] Z. Yin, A. Prosperetti, and J. Kim; "Buble growth on an impulsively powered microheater," *International Journal of Heat and Mass Transfer,* vol. 47, pp. 1053-1967, 2004.
[196] F. Demiray and J. Kim; "Micro-scale heat transfer measurements during pool boiling of FC-72," *International Journal of Heat and Mass Transfer,* vol. 47, pp. 3257-3268, 2004.
[197] M. Shoji and Y. Takaji; "Bubbling from a single artificial cavity," *International Journal of Heat and Mass Transfer,* vol. 44, pp. 2763-2776, 2001.
[198] L. Zhang and M. Shoji; "Nuclation site interactions in pool boiling," *International Journal of Heat and Mass Transfer,* vol. 46, pp. 513-522, 2003.
[199] R. Rammig and R. Weiss; "Growth of vapour bubbles from artificial nuclation sites," *Cryogenics,* vol. 31, pp. 64-69, 1990.
[200] G. Son, V. K. Dhir, and N. Ramanujapu; "Dynamics and Heat Transfer Associated With a Single Bubble During Nucleate Boiling on a Horizontal Surface," *Journal of Heat Transfer,* vol. 121, pp. 623-631, 1999.
[201] Y. Qi and J. F. Klausner; "Heterogeneous Nucleation With Artificial Cavities," *Journal of Heat Transfer,* vol. 127, pp. 1189-1196, 2005.
[202] Y. Qi and J. F. Klausner; "Comparison of Gas Nucleation and Pool Boiling Site Densities," *ASME Conference Proceedings,* vol. 2004, pp. 663-669, 2004.
[203] S. Siedel, S. Cioulachtjian, and J. Bonjour; "Experimental analysis of bubble growth, departure and interactions during pool boiling on artificial nucleation sites," *Experimental Thermal and Fluid sciences,* vol. 32, pp. 1504-1511, 2008.
[204] E. Wagner and P. Stephan; "High-Resolution Measurements at Nucleate Boiling of Pure FC-84 and FC-3284 and Its Binary Mixtures," *Journal of Heat Transfer,* vol. 131, pp. 121008-12, 2009.
[205] S. Moghaddam and K. Kiger; "Physical mechanisms of heat transfer during single bubble nucleate boiling of FC-72 under saturation conditions. II: Theoretical analysis," *International Journal of Heat and Mass Transfer,* vol. 52, pp. 1295-1303, 2009.
[206] C. Hutter, D. B. R. Kenning, K. Sefiane, T. G. Karayiannis, H. Lin, G. Cummins, and A. J. Walton; "Experimental pool boiling investigations of FC-72 on silicon with artificial cavities and integrated temperature microsensors," *Experimental Thermal and Fluid Science,* vol. 34, pp. 422-433, 2010.
[207] S. H. Bhavani, C. P. Tsai, and R. C. Jaeger; "Pool boiling charactristics of enhanced hybrid silicon surfaces," *Journal of Heat Transfer,* vol. 171, pp. 19-27, 1991.
[208] M. Shoji; "Studies on boiling chaos: a review," *International Journal of Heat and Mass Transfer,* vol. 47, pp. 1105-1128, 2004.
[209] M. Sultan and R. L. Judd; "Interaction of nucleation phenomena at adjacent sites in nucleate boiling," *Journal of Heat Transfer,* vol. 105, pp. 955-962, 1983.
[210] R. L. Judd and A. Chopra; "Interaction of the nucleation processes occurring at adjacent nucleation sites," *Journal of Heat Transfer,* vol. 115, pp. 955-962, 1993.
[211] D. B. R. Kenning and Y. Yan; "Wall temperatures in nucleate boiling: spatial and temporal variations," in *9th International Heat transfer conference*, Jerusalam, 1990, pp. 33-38.

[212] D. B. R. Kenning, I. Golobic, and J. Petkovsek; "Pool boiling: Global correlations and mechanistic studies," presented at the 11th UK national heat transfer conference London, UK, 2009.
[213] I. Golobic, J. Petkovsek, M. Baselj, A. Papez, and D. Kenning; "Experimental determination of transient wall temperature distributions close to growing vapor bubbles," *Heat and Mass Transfer,* vol. 45, pp. 857-866, 2009.
[214] C. Gerardi, J. Buongiorno, L.-w. Hu, and T. McKrell; "Study of bubble growth in water pool boiling through synchronized, infrared thermometry and high-speed video," *International Journal of Heat and Mass Transfer,* vol. 53, pp. 4185-4192, 2010.
[215] O. Glatter and O. Kratky; *Small angle X-ray scattering*: Academic Press, 1982.
[216] S. Mazumder, K. V. Bhagwat, and A. Sequeira; "Estimation of particle size distribution in multiple small-angle scattering," *Journal of Physics: Condensed Matter,* vol. 7, pp. 9737-9746., 1995.
[217] G. Beaucage, H. K. Kammlerb, and S. E. Pratsinis; "Particle size distributions from small-angle scattering using global scattering functions," *Journal of Applied Crystallography,* vol. 37, pp. 523-535, 2004.
[218] J. Bolze, B. Peng, N. Dingenouts, P. Panine, T. Narayanan, and M. Ballauff; "Formation and Growth of Amorphous Colloidal Calcium Carbonate Precursor Particles as Detected by Time-Resolved SAXS," *Langmuir* vol. 18, pp. 8364-8369, 2002.
[219] H.-L. Lee, G. Beaucage, S. E. Pratsinis, and S. Vemury; "Fractal analysis of flame-synthasized nanostructured Silica and Titania powders using Small angle x-ray scattering," *Langmuir* vol. 14, pp. 5751-5756, 1998.
[220] Y. MORI, M. FURUKAWA, T. HAYASHI, and K. NAKAMURA; "Size Distribution of Gold Nanoparticles Used by Small Angle X-ray Scattering," *Particulate Science and Technology,* vol. 24, pp. 97-103, 2006.
[221] M. M. Kostic; "Critical issues and application potentials in nanofluids research," in *Multifunctional Nanocomposites 2006* Honolulu, Hawaii, 2006.
[222] K. Sinkó, V. Torma, and A. Kovács; "SAXS investigation of porous nanostructures " *Journal of Non-Crystalline Solids,* vol. 354, pp. 5466–5474, 2008.
[223] M. Kosmulski and E. Matijevic; "Zeta potential of anatase (TiO2) in mixed solvents," *Colloids and Surfaces,* vol. 64 pp. 57-65, 1992.
[224] M. Kosmulski, S. Durand-Vidal, J. Gustafsson, and J. B. Rosenholm; "Charge interactions in semi-concentrated titania suspensions at very high ionic strengths," *Colloids and Surfaces A,* vol. 157, pp. 145-259, 1999.
[225] J. J. Healy, J. J. d. Groot, and J. Kestin; "The theory of the Transient Hot wire method for measuring thermal conductivity," *Physica* vol. 82C, pp. 392-408, 1976.
[226] H. Poltz; "Die wärmeleitfähigkeit von flüssigkeiten III : Abhängigkeit der wärmeleitfähigkeit von der schichtdicke bei organischen flüssigkeiten," *International Journal of Heat and Mass Transfer,* vol. 8, pp. 609-620, 1965.
[227] P. Vadasz; "Rendering the Transient Hot Wire Experimental Method for Thermal Conductivity Estimation to Two-Phase Systems---Theoretical Leading Order Results," *Journal of Heat Transfer,* vol. 132, pp. 081601-7, 2010.
[228] J. Nanda, C. Maranville, S.C. Bollin, D. Sawall, H. Ohtani, J.T. Remillard, and J. M. Ginder; "Thermal Conductivity of Single-Wall Carbon Nanotube Dispersions: Role of Interfacial Effects," *The Journal of Physical Chemistry C Letters,* vol. 112, pp. 654-658, 2008.
[229] H. Xie and L. Chen; "Adjustable thermal conductivity in carbon nanotube nanofluids," *Physics Letters A* vol. 373, pp. 1861–1864, 2009.

[230] T. Sun and A. S. Teja; "Density, Viscosity and Thermal conductivity of Aqueous Ethylene, Diethylene,and Tryethylene Glycol mixtures between 290K and 450K," *Journal of Chemical Engineering Data,* vol. 48, pp. 198-202, 2003.
[231] H. Chen, S. Witharana, Y. Jin, C. Kim, and Y. Ding; "Predicting thermal conductivity of liquid suspensions of nanoparticles (nanofluids) based on rheology," *Particuology,* vol. 7, pp. 151-157, 2009.
[232] S. Witharana, H. Chen, and Y. Ding; "Shear stability and thermophysical properties of nanofluids," presented at the IEEE-International conference on Information and Automation for Sustainability, Colombo, Sri Lanka, 2010.
[233] H. Chen, Y. Ding, Y. He, and C. Tan; "Rheological behaviour of Ethylene glycol based titania Nanofluids," *Chemical Physics Letters,* 2007.
[234] "KRUSS Easy Drop manual, 2006," ed.
[235] J. Dabrowski and H.-J. Müssig; *Silicon surfaces and fromation of interfaces*: World Scientific Publishing co. Pte. Ltd., 2000.
[236] S. Franssila; *Introduction to Microfabrication* John Wiley & Sons Ltd, 2010.
[237] T. C. Huang, H. Toraya, T. C. Blanton, and Y. Wu; "X-ray powder diffraction analysis of silver behenate, a possible low-angle diffraction standard," *Journal of Applied Crystallography,* vol. Volume 26, pp. 180-184, 1993.
[238] R. D. B. Fraser and T. P. MacRae; "Unit cell and molecular connectivity in tendon collagen," *International Journal of Biological Macromolecules,* vol. 3, pp. 193-200, 1981.
[239] T. D. Waite, J. K. Cleaver, and J. K. Beattie; "Aggregation Kinetics and Fractal Structure of gamma-Alumina Assemblages," *Journal of Colloid and Interface science,* vol. 241, pp. 333-339, 2001.
[240] M. B. Cardoso, H. R. Luckarift, V. S. Urban, H. O'Neill, and G. R. Johnson; "Protein Localization in Silica Nanospheres Derived via Biomimetic Mineralization," *Advanced Functional Materials,* vol. 20, pp. 3031–3038, 2010.
[241] L. B. Lurio, D. Lumma, A. R. Sandy, M. A. Borthwick, P. Falus, S. G. J. Mochrie, J. F. Pelletier, M. Sutton, L. Regan, A. Malik, and G. B. Stephenson; "Absence of Scaling for the Intermediate Scattering Function of a Hard-Sphere Suspension: Static and Dynamic X-Ray Scattering from Concentrated Polystyrene Latex Spheres," *Physical Review Letters,* vol. 84, p. 785, 2000.
[242] P. Salgi and R. Rajagopalan; "Polydispersity in colloids: implications to static structure and scattering," *Advances in Colloid and Interface science,* vol. 43, pp. 169-288, 1993.
[243] C. Munch and J. Kalus; "New shear apparatus for in situ small-angle x-ray scattering experiments," *Review of Scientific Instruments,* vol. 70, pp. 187-192, 1999.
[244] *Buehler Sum-Met Buyer's Guide 2008*. Available: www.mitar.sk/prospekty/katalogbuehler20062007.pdf
[245] A. E. Bergles; "Heat transfer enhancement: The maturing of second generation heat transfer technology. ," *Heat Transfer Engineering,* vol. 18, 1997.
[246] V. P. Carey; *Liquid-Vapour phase change phenomena*: Hemisphere Publishing Corp., 1992.
[247] F. P. Incropera and D. P. DeWitt; *Fundamentals of Heat and Mass Transfer*, 4th ed.: John Wiley & Sons Inc., 1996.
[248] W. M. Rohsenow and Hartnett J.P; *Handbook of Heat transfer*: McGraw Hill, New York, 1973.
[249] W. M. Irvine and J. B. Pollack; "Infrared optical properties of water and ice spheres," *Icarus,* vol. 8, pp. 324-360, 1968.

[250] T. Curley, R. Forsyth, S. Sun, K. Fliszar, G. Colleto, and P. Martin; "Measurement of dissolved Oxygen as a determination of media equilibrium during dissolution testing," *Dissolution Technologies,* vol. November, pp. 6-11, 2004.
[251] J. H. Lienhard and A. Karimi; "Homogeneous Nucleation and the Spinodal Line," *Journal of Heat Transfer,* vol. 103, pp. 61-64, 1981.
[252] M. Blander and J. L. Katz; "Bubble Nucleation in Liquids," *AIChE Journal,* vol. 21, pp. 833-848, 1975.
[253] J. G. Eberhart; "The Thermodynamic and Kinetic Limits of Superheat of a Liquid " *Journal of Colloid and Interface science,* vol. 56, pp. 262-269, 1976.

Appendix B

Published

- **S. Witharana**, H. Chen, Y. Ding; **Nanofluids for heat transfer,** ***Nanophysics Handbook, Taylor and Francis Publishing Corporation, 2011***
- Y. Ding, H. Chen, Z. Musina, Y. Jin, T. Zhang, **S. Witharana**, W. Yang; **Relationship between the thermal conductivity and shear viscosity of nanofluids,** ***Physica Scripta, T139 (2010) 014078***

- D.C. Venerus, J. Buongiorno, R. Christianson, J. Townsend, I.C. Bang, G. Chen, S.J. Chung, M. Chyu, H. Chen, Y. Ding, F. Dubois, G. Dzido, D. Funfschilling, Q. Galand, J. Gao, H. Hong, M. Horton, L. Hu, C.S. Iorio, A.B. Jarzebski, Y. Jiang, S. Kabelac, M. A. Kedzierski, C. Kim, J-H Kim, S. Kim, T. McKrell, R. Ni, J. Philip1 N. Prabhat, P. Song, S. Van Vaerenbergh, D. Wen, **S. Witharana**, X-Z Zhao, S-Q Zhou; **Viscosity measurements on colloidal dispersions (nanofluids) for heat transfer applications,** ***Applied Rheology, 20:4 (2010) 44582***
- J. Buongiorno, D.C. Venerus, N. Prabhat, T. McKrell, J. Townsend, R. Christianson, Y.V. Tolmachev, P. Keblinski, L-W Hu, J.L. Alvarado, I. C. Bang, S. W. Bishno, M. Bonetti, F.Botz, A. Cecere, Y. Chang, G. Chen, H. Chen, S.J. Chung, M.K. Chyu, S.K. Das, R. Di Paola, Y. Ding, F. Dubois, G. Dzido, J. Eapen, W. Escher, D. Funfschilling, Q. Galand, J. Gao, P.E. Gharagozloo, K.E. Goodson, J.G. Gutierrez, H. Hong, M. Horton, K.S. Hwang, C.S. Iorio, S.P. Jang, A.B. Jarzebski, Y. Jiang, L. Jin, S. Kabelac, A. Kamath, M.A. Kedzierski, L.G. Kieng, C. Kim, J-H Kim, S. Kim, S. H. Lee, K. C. Leong, I. Manna, B. Michel, R. Ni, H.E. Patel, J. Philip, D. Poulikakos, C. Reynaud, R. Savino, P.K. Singh, P. Song, T. Sundararajan, E. Timofeeva, T. Tritcak, A.N. Turanov, S. Van Vaerenbergh, D. Wen, **S. Witharana**, C. Yang, W-H Yeh, X-Z Zhao, S-Q Zhou; **A Benchmark Study on the Thermal Conductivity of Nanofluids,** ***Journal of Applied physics*****, *106, 094312 (2009)***
- H. Chen, **S. Witharana**, Y. Jin, C. Kim, Y. Ding; **Predicting thermal conductivity of liquid suspensions of nanoparticles (nanofluids) based on Rheology,** ***Particuology 7 (2009) 151–157***

Accepted

- **S. Witharana**, H. Chen, Y. Ding; **Stability of nanofluids in quiescent and shear flow fields,** ***Accepted by Nanoscale Research Letters (2100)***

Submitted

- G. Okeke, **S. Witharana,** Y. Ding et al.; **Computational analysis of factors influencing the enhancement of thermal conductivity of nanofluids**, ***Submitted to Journal of Nanoparticle Research (2011)***

Under internal review

- **S. Witharana**, C.S. Hodges, Y. Ding et al.; ***Aggregation and settling of polydisperse aqueous alumina suspensions, To be submitted to Industrial & Engineering Chemistry Research***

Manuscripts under preparation

- S. Witharana, J. Buongiorno, Y. Ding et al.; ***Boiling of liquids on nanosmooth heaters***
- Y. Ding, S. Witharana, Z. Musina et al.; ***Manufacturing of Functional Nanofluids, Nanomanufacturing Handbook***